ADVANCED DIGITAL TECHNOLOGIES IN DIGITALIZED SMART GRID

EDITED BY: Xiangjun Zeng, Yan Xu and Dongqi Liu
PUBLISHED IN: Frontiers in Energy Research

frontiers Research Topics

frontiers

ISSN 1664-8714
ISBN 978-2-83250-445-1
DOI 10.3389/978-2-83250-445-1

About Frontiers

Frontiers is more than just an open-access publisher of scholarly articles: it is a pioneering approach to the world of academia, radically improving the way scholarly research is managed. The grand vision of Frontiers is a world where all people have an equal opportunity to seek, share and generate knowledge. Frontiers provides immediate and permanent online open access to all its publications, but this alone is not enough to realize our grand goals.

Frontiers Journal Series

The Frontiers Journal Series is a multi-tier and interdisciplinary set of open-access, online journals, promising a paradigm shift from the current review, selection and dissemination processes in academic publishing. All Frontiers journals are driven by researchers for researchers; therefore, they constitute a service to the scholarly community. At the same time, the Frontiers Journal Series operates on a revolutionary invention, the tiered publishing system, initially addressing specific communities of scholars, and gradually climbing up to broader public understanding, thus serving the interests of the lay society, too.

Dedication to Quality

Each Frontiers article is a landmark of the highest quality, thanks to genuinely collaborative interactions between authors and review editors, who include some of the world's best academicians. Research must be certified by peers before entering a stream of knowledge that may eventually reach the public - and shape society; therefore, Frontiers only applies the most rigorous and unbiased reviews.
Frontiers revolutionizes research publishing by freely delivering the most outstanding research, evaluated with no bias from both the academic and social point of view. By applying the most advanced information technologies, Frontiers is catapulting scholarly publishing into a new generation.

What are Frontiers Research Topics?

Frontiers Research Topics are very popular trademarks of the Frontiers Journals Series: they are collections of at least ten articles, all centered on a particular subject. With their unique mix of varied contributions from Original Research to Review Articles, Frontiers Research Topics unify the most influential researchers, the latest key findings and historical advances in a hot research area! Find out more on how to host your own Frontiers Research Topic or contribute to one as an author by contacting the Frontiers Editorial Office: frontiersin.org/about/contact

ADVANCED DIGITAL TECHNOLOGIES IN DIGITALIZED SMART GRID

Topic Editors:
Xiangjun Zeng, Changsha University of Science and Technology, China
Yan Xu, Nanyang Technological University, Singapore
Dongqi Liu, Changsha University of Science and Technology, China

Citation: Zeng, X., Xu, Y., Liu, D., eds. (2022). Advanced Digital Technologies in Digitalized Smart Grid. Lausanne: Frontiers Media SA.
doi: 10.3389/978-2-83250-445-1

Table of Contents

frontiers in Energy Research

ORIGINAL RESEARCH
published: 31 January 2022
doi: 10.3389/fenrg.2021.793686

A Data-Driven Genetic Algorithm for Power Flow Optimization in the Power System With Phase Shifting Transformer

*Zuohong Li[1], Feng Li[1], Ruoping Liu[1], Mengze Yu[1], Zhiying Chen[2], Zihao Xie[2] and Zhaobin Du[2]**

[1]The Grid Planning and Research Center of Guangdong Power Grid Corporation, Guangzhou, China, [2]School of Electric Power Engineering, South China University of Technology, Guangzhou, China

Phase-shifting transformer (PST) is one of the flexible AC transmission technologies to solve the problem of uneven power transmission. Considering that PST can also be used as a regulation means for the economic operation of the system, it is necessary to study the power flow optimization of power systems with PST. In order to find a more efficient power flow optimization method, an improved genetic algorithm including a data-driven module is proposed. This method uses the deep belief network (DBN) to train the sample set of the power flow and obtains a high-precision proxy model. Then, the calculation of the DBN model replaces the traditional adaptation function calculation link which is very time-consuming due to a great quantity of AC power flow solution work. In addition, the sectional power flow reversal elimination mechanism in the genetic algorithm is introduced and appropriately co-designed with DBN to avoid an unreasonable power flow distribution of the grid section with PST. Finally, by comparing with the traditional model-driven genetic algorithm and traditional mathematical programming method, the feasibility and the validity of the method proposed in this paper are verified on the IEEE 39-node system.

Keywords: phase-shifting transformer, power flow optimization, genetic algorithm, data-driven, deep belief network

OPEN ACCESS

Edited by:
Xiangjun Zeng,
Changsha University of Science and Technology, China

Reviewed by:
Wenjie Zhang,
National University of Singapore, Singapore
Yunhe Hou,
The University of Hong Kong, Hong Kong SAR, China
Fushuan Wen,
Zhejiang University, China

****Correspondence:***
Zhaobin Du
epduzb@scut.edu.cn

Specialty section:
This article was submitted to Smart Grids, a section of the journal Frontiers in Energy Research

Received: *12 October 2021*
Accepted: *20 December 2021*
Published: *31 January 2022*

Citation:
Li Z, Li F, Liu R, Yu M, Chen Z, Xie Z and Du Z (2022) A Data-Driven Genetic Algorithm for Power Flow Optimization in the Power System With Phase Shifting Transformer. Front. Energy Res. 9:793686. doi: 10.3389/fenrg.2021.793686

1 INTRODUCTION

With the formation of interconnection of regional power systems, the power transmission is often done through multiple parallel channels. Due to the differences in transmission distance and line parameters of these channels, the uneven distribution of the power flow in each channel will result in the restriction of the cross-section transmission capacity (Sun, 2011). Considering that the existing transmission network is very complex and mature, improving the transmission capacity of the power grid through the transformation and construction of the transmission network will be restricted by environmental conditions, economic costs, and other factors, so it is necessary to fully tap the transmission potential of the existing transmission network with the minimal investment to improve its power supply stability and reliability (Nadeem et al., 2020). Phase-shifting transformer, as a kind of power flow control equipment, has the characteristics of flexible control and large-range adjustment angle. In addition, it can respond quickly under the help of high-power electronic devices and is expected to be a daily regulation means for the economic operation of the system (Verboomen et al., 2005; Kawaura et al., 2016; Morrell and Eggebraaten., 2019). However, although the phase-shifting transformer (PST) has many advantages, it also increases the complexity of the

power grid structure. It is more important that when it is necessary to perform multiple power flow calculations for the large power grid with the phase-shifting transformer to determine the best phase-shifter gear, the calculation cost is often very large. Thus, some methods to improve the power flow optimization efficiency of power systems with the phase-shifting transformer are proposed. In literature (Zhang et al., 2021), the iteration step of the affine direction is improved, and the key mapping parameters is reconfigured, which improves the efficiency of the multicenter correction interior point method. In literature (Cui et al., 2013), matrix block technology is used to reduce the calculation scale of the nonlinear primal dual interior point method, which improves the efficiency of optimization of power systems with phase-shifting transformer. However, when the scale of the power system is very large, these measures to improve the optimization efficiency are still difficult to adapt to the scale of the optimization problem. Considering the rapidity of data-driven methods, a data-driven approach will be adapted to solve this problem in this paper.

Traditional power flow optimization methods are model-driven. Model-driven optimization methods can be divided into mathematical programming methods, intelligent optimization algorithms, and hybrid methods (Liu, 2021). Common mathematical programming methods include the linear programming method (Mohamed and Venkatesh, 2019), the interior point method (Pan et al., 2018), and so on. Intelligent optimization algorithms include genetic algorithm (Ahmed et al., 2021), particle swarm optimization algorithm (Zhang et al., 2014), and so on. Hybrid methods refer to the combination or collaboration of two (or more) methods to solve an optimization problem and include PSO-sequential quadratic programming (Victoire and Jeyakumar, 2004), seeker optimization algorithm-SQP (Sivasubramani and Swarup, 2010), and so on. However, the model-driven optimization method has obvious bottlenecks in computational efficiency, so the data-driven power flow optimization method has recently aroused the research interest of many scholars due to its high computation efficiency. The data-driven optimization methods can be divided into two categories according to the different functions of the data drive. The first type is data-driven modeling, including deterministic modeling and uncertain modeling—for example, Van Horn *et al.* (2016) applies data-driven injection shift factor matrix to the optimal power flow model so that the real-time security-constrained economic dispatch of the power grid can be robust to various disturbances. Lorca and Sun (2014) and Roldan *et al.* (2018) respectively proposed the construction methods of data-driven polyhedron and ellipsoidal uncertainty sets. The second type is data-driven optimization decisions. Lei et al. (2021) proposed a data-driven optimal power flow method based on stacked extreme learning machine framework, which can directly obtain the optimal scheduling decision scheme of the system without the iterative process. (Liu et al., 2021) presents a novel data-driven approach based on artificial neural networks to enable fast economic dispatch in electricity–gas coupled systems by utilizing simulation data from the piecewise-linearization-based model-driven method. In a word, the purpose of the data-driven optimization method of the first type is to improve the performance of the built model rather than improve the optimization efficiency. The second one is to directly replace the flow optimization process with the neural network, which greatly reduces the time cost of the optimization. However, the mapping between the power system operation state and the optimization decision scheme is complex, especially when the system scale is large. Directly through the black box prediction, it is difficult to apply to the actual optimization decisions in a convincing way. Therefore, an alternative data-driven power flow optimization framework is proposed to balance the relationship between interpretability and optimization efficiency in this paper. We use data drive to replace the calculation of the power flow in the optimization process rather than the whole optimization process, which makes the solution results still retain the physical significance of the optimization. Our approach is still much faster than the model-driven optimization method, although it takes longer than the data-driven optimization method of the second type.

At present, the power flow (PF) calculation methods of power systems can be divided into the model-driven power flow calculation and the data-driven power flow calculation. The former mainly includes the forward–backward method (Butler-Purry, 2013), the Newton–Raphson method (Zhu and Tomsovic, 2007), and the DC power flow method (Stott et al., 2009). With the spread of massive phasor measurement units (PMUs) and supervisory control and data acquisition (SCADA) systems, the latter gradually attracted the interest of scholars. The data-driven power flow method can be divided into three categories. The method of the first type is to calculate the Jacobian matrix of high precision based on measured data (Chen et al., 2016). The method of the second type is to obtain a more accurate linearized power flow calculation model based on the measured data (Liu et al., 2019). The method of the third type uses neural network to replace AC power flow calculation to realize the faster power flow calculation (Liu and Kong, 2021). Obviously, only the third kind of method is used to improve the efficiency of power flow calculation. Therefore, this paper adopts the third method and combines the data-driven power flow calculation into the intelligent optimization algorithm to form the data-driven power flow optimization method.

In Shi et al. (2019), deep belief network (DBN) is seen to be an excellent candidate for the data-driven model, and it is a multilayer probability generation model that extracts features well. In addition, because of its good feature extraction and discrimination ability, DBN is widely used in power prediction and equipment fault diagnosis and shows better results than traditional machine learning methods in power prediction and fault diagnosis accuracy (Xu et al., 2018; Tao et al., 2020; Dong et al., 2021). Therefore, DBN is adopted as the data-driven approach of this paper.

To sum up, this paper proposes a power flow optimization method based on data-driven technology and an improved genetic algorithm for power systems with PST. The method uses DBN to train the sample set, in which the input variables

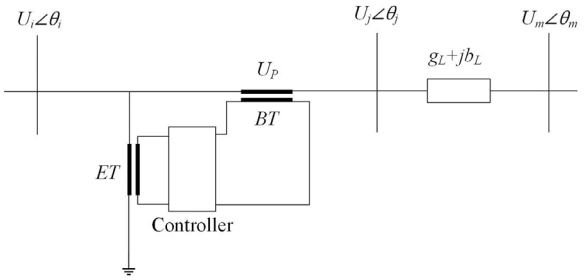

FIGURE 1 | Two-core symmetrical phase-shifting transformer structure diagram.

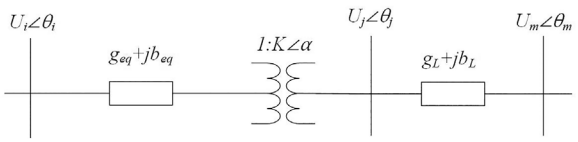

FIGURE 2 | The equivalent circuit of the branch with phase-shifting transformer.

are phase-shift angle, the active power of the generator, and load active and reactive power and the output variables are system loss and the power flow of the lines where the power flow reverse may occur. The calculation link of the fitness function in the genetic algorithm is replaced by the high-precision DBN model, which avoids the time-consuming problem of power flow calculation by the way of iteration and keeps a high accuracy. Moreover, in the process of genetic algorithm optimization, the introduction of the sectional power flow reversal elimination mechanism makes the solutions evolve in an effective optimization direction. So, the method proposed in this paper reduces the difficulty of power flow calculation for power systems with PST and improves the speed of power flow optimization. The main contributions of this paper are as follows:

(1) A new paradigm of data-driven power flow optimization is proposed, which improves the optimization efficiency while ensuring the optimization accuracy and has certain generalization ability.
(2) By adding state variables of optimization models into the output set of the sample of neural networks, the proposed optimization method can completely consider inequality constraints containing the state variables—for example, by adding the active power of the lines prone to power reversal into the output set of the sample, the proposed method can consider the inequality constraints about power reversal and can avoid unreasonable power flow distribution of the grid section with PST.

The structure of this article is as follows: first, **Section 2** introduces the equivalent model of PST and the change in model-based PF calculation of power systems with PST. After that, **Section 3** presents the power flow optimization model of systems with PST. Next, **Section 4** describes the data-driven approach used to replace the traditional PF calculation and highlights the improvements to the genetic algorithm. Subsequently, **Section 5** verifies the effectiveness of the proposed method on the IEEE 39-node modification system with PST by comparing it with the traditional model-driven genetic algorithm and traditional mathematical programming method. Finally, the main findings of this study are summarized with some prospects for future studies in the conclusion section.

2 MATHEMATICAL MODEL OF THE PHASE SHIFTING TRANSFORMER

2.1 The Basic Principle of the Phase Shifting Transformer

Phase shifting transformer adjustment can generally be divided into longitudinal adjustment, lateral adjustment and oblique adjustment (Zhang, 2017). Longitudinal regulation is to adjust the amplitude of the voltage, lateral regulation is to adjust the phase of the voltage, and oblique regulation changes both the voltage amplitude and its phase.

In this paper, the discrete two-core symmetrical PST is selected as the research object, which belongs to the lateral adjustment. Its structure is shown in **Figure 1**.

As can be seen from **Figure 1**, the structure of the controlled PST includes a series booster transformer (BT), an excitation transformer (ET) and a controller (Mehdi, 2010; Bian et al., 2012). First of all, the parallel transformer is used to obtain the terminal voltage of the branch where the PST is located. Then, according to the system's demand, the voltage of a certain amplitude and phase angle is obtained by using the mechanical or power electronic control device. Finally, the voltage is injected into the line by the series transformer to realize the effect of regulating the voltage phase angle.

2.2 Power Flow Models With Phase Shifting Transformer

The equivalent circuit of the branch with PST is shown in **Figure 2**.

In **Figure 2**, $Y_{eq} = g_{eq} + jb_{eq}$ represents the equivalent admittance of the PST, $Y_L = g_L + jb_L$ represents the equivalent admittance of the line, α is the phase-shift angle, and U_i, θ_i, U_j, and θ_j represent the voltage amplitude and phase of node i and j, respectively.

In the power flow calculation of a system with PST, the node admittance matrix of the network is generally symmetrical, and a series of processing and simplifications in the PF calculation is also based on the symmetry of the node admittance matrix. However, because the ratio of PSTs is a complex number, not a scalar, the admittance of the PST branch between node i and node j, as shown in **Figure 2**, in an equivalent circuit form, $Y_{ij} \neq Y_{ji}$, and the node admittance matrix of a system with PST is no longer symmetrical. In order to maintain the symmetry of the node admittance matrix, the PST branch should be pre-treated in order to keep the node admittance matrix of the whole system symmetrical during PF calculation.

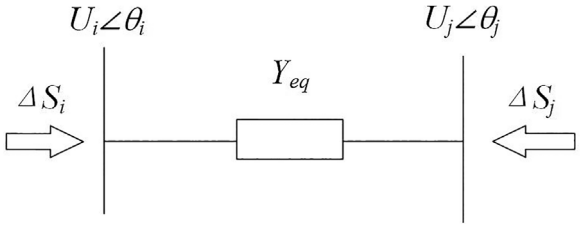

FIGURE 3 | The schematic diagram of equivalent injected power of phase-shifting transformer.

In details, the variable ratio of the PST is firstly removed, and the equivalent admittance becomes Y_{eq}. Then, the injection power of node i and node j needs to be corrected. The schematic diagram of the equivalent injected power of PST is shown in **Figure 3**.

The change of injection power of the nodes at both ends of the derived equivalent PST is as follows (Noroozian and Andersson., 1993; Papazoglou et al., 1999; Eremia et al., 2016):

$$\begin{cases} \Delta P_i = U_i U_j\left\{g_{eq}\left[\cos\left(\alpha+\theta_{ij}\right)-\cos\theta_{ij}\right]+b_{eq}\left[\sin\left(\alpha+\theta_{ij}\right)-\sin\theta_{ij}\right]\right\} \\ \Delta Q_i = U_i U_j\left\{g_{eq}\left[\sin\left(\alpha+\theta_{ij}\right)-\sin\theta_{ij}\right]-b_{eq}\left[\cos\left(\alpha+\theta_{ij}\right)-\cos\theta_{ij}\right]\right\} \\ \Delta P_j = U_i U_j\left\{g_{eq}\left[\cos\left(\alpha-\theta_{ji}\right)-\cos\theta_{ji}\right]-b_{eq}\left[\sin\left(\alpha-\theta_{ji}\right)+\sin\theta_{ji}\right]\right\} \\ \Delta Q_j = -U_i U_j\left\{g_{eq}\left[\sin\left(\alpha-\theta_{ji}\right)+\sin\theta_{ji}\right]+b_{eq}\left[\cos\left(\alpha-\theta_{ji}\right)-\cos\theta_{ji}\right]\right\} \end{cases} \tag{1}$$

where ΔP_i, ΔP_j, ΔQ_i, and ΔQ_j denote the injected active and reactive power of node i and node j, respectively. Moreover, $\theta_{ij} = \theta_i - \theta_j$, $\theta_{ji} = \theta_j - \theta_i$.

It is known by **Equation 1** that the equivalent injection power on both sides of the PST is only related to the parameters of the PST and the voltage amplitude and phase at both ends of it. In each iteration of power flow calculation, as long as the equivalent injection power is calculated through the above-mentioned formula and added to the original injection power of the node, the power flow solution with PST can be solved as usual.

3 OPTIMIZATION MODEL OF POWER SYSTEMS WITH PHASE-SHIFTING TRANSFORMER

The PST changes the phase of the voltage at the installation point of it by stringing the voltage with adjustable amplitude into the transmission line so as to adjust the power flow of the transmission line. In order to better play the power flow regulation ability of PST, the power flow optimization model of power systems with PST is considered as follows (Zhang et al., 2021):

$$\begin{aligned} &\min f(x,u) \\ &s.t.\begin{cases} h(x,u)=0 \\ \underline{g} \le g(x,u) \le \bar{g} \end{cases} \end{aligned} \tag{2}$$

In the expression, $f(x,u)$ is the target function, $h(x,u)$ is an equation constraint, $g(x,u)$ is an inequality constraint, g and $\bar{g}$ respectively represent the lower and upper limits of $g(x,u)$, and x and u respectively represent state variables and control variables. The control variables selected in this paper include phase-shift angle and generator output power (MW).

3.1 Target Function

The objective function of this paper is the active power loss of the system. The expression is as follows:

$$P_{loss} = \sum_{i=1}^{Nl} G_i\left[V_{i1}^2 + V_{i2}^2 - 2V_{i1}V_{i2}\cos\left(\theta_{i1}-\theta_{i2}\right)\right] \tag{3}$$

where P_{loss} is the active power loss of the system, Nl is the total number of branches of the system, G_i is the conductivity of the branch i, V_{i1}, θ_{i1}, and V_{i2}, θ_{i2} are the voltage and phase angle of the bus at the head and tail side of branch i, respectively.

3.2 Equation Constraints

The active and reactive power constraint equations are as follows:

$$P_{Gi} - P_{Di} - \sum_{j=1}^{n} V_i V_j\left(G_{ij}\cos\theta_{ij} + B_{ij}\sin\theta_{ij}\right) = 0 \tag{4}$$

$$Q_{Gi} - Q_{Di} - \sum_{j=1}^{n} V_i V_j\left(G_{ij}\sin\theta_{ij} - B_{ij}\cos\theta_{ij}\right) = 0 \tag{5}$$

where P_{Gi} and Q_{Gi} are the active and reactive power output of the i-bus generator, respectively. P_{Di} and Q_{Di} are the load active and reactive power of the bus i. G_{ij} and B_{ij} are the conductance and the susceptance of the line i–j, respectively. θ_{ij} is the voltage phase difference at both ends of the line i–j.

3.3 Inequality Constraints

3.3.1 Constraints of Control Variables

3.3.1.1 Shift-Phase Angle

In this paper, the phase angle of PST is chosen as the control variable and limited to the range from α_{min} to α_{max}

$$\alpha_{min} \le \alpha \le \alpha_{max} \tag{6}$$

3.3.1.2 The Generator Active Output (MW)

$$P_{Gimin} \le P_{Gi} \le P_{Gimax}, i = 1, \cdots, G_N \tag{7}$$

The active power output of the generator, P_{Gi}, is chosen as another kind of decision-making variable. Among them, P_{Gimin} and P_{Gimax} are the minimum and maximum active power output of the generator i, respectively. G_N indicates the generator node number that is involved in the decision-making variable list.

3.3.2 Constraints of State Variables

The inequality constraints for the voltage amplitude of the load node are as follow:

$$V_{imin} \le V_i \le V_{imax}, i = 1, \cdots, N_D \tag{8}$$

where V_{imin} and V_{imax} are the minimum and maximum voltage of the load node, respectively. N_D represents the total number of load nodes. In this paper, V_{imin} and V_{imax} are set as 0.95 and 1.052 p.u., respectively.

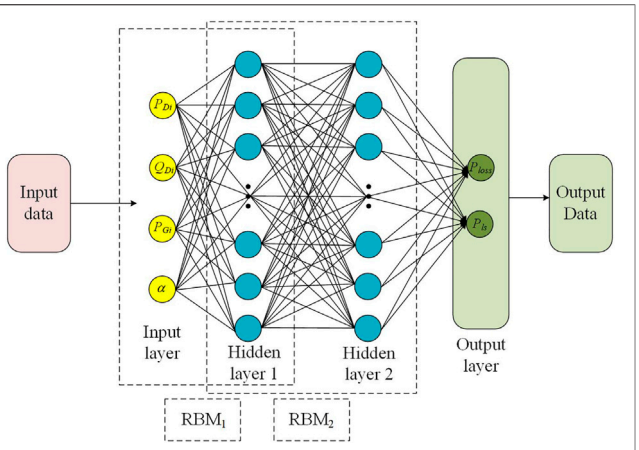

FIGURE 4 | Deep belief network structure diagram.

The inequality constraints of the reactive power output of generators are as follows:

$$Q_{Gkmin} \le Q_{Gk} \le Q_{Gkmax},\ k = 1, \ldots, N_g \tag{9}$$

where Q_{Gkmin} and Q_{Gkmax} are the minimum and maximum reactive powers of the generator k, respectively, and N_g is the number of all generators.

The inequality constraints on the transmission limit are as follow:

$$P_{ijmin} \le P_{ij} \le P_{ijmax} \tag{10}$$

where P_{ij} is the transmission power from node i to j, and P_{ijmin} and P_{ijmax} are respectively the minimum and the maximum permissible powers of line i–j and $P_{ijmin} = -P_{ijmax}$.

4 PROPOSED METHODOLOGY

4.1 Deep Belief Network

DBN is an efficient unsupervised learning algorithm stacked by a series of restricted Boltzmann machines (RBMs) and then adds a layer of back-propagation (BP) neural networks at the bottom level. The DBN topology and training process are shown in **Figure 4**. The DBN training process is divided into unsupervised training and fine-tuning. First of all, individually unsupervised training is given to each layer of the RBM network so as to retain feature information as much as possible when mapping the feature vectors to different feature spaces. Then, the parameters obtained from the unsupervised training phase were uses as the initial value, and the DBN was fine-tuned through BP. This process can avoid local optimization in the training process.

About the structure of the DBN, this paper selects the phase-shift angle, generator active power, and active power and reactive power of the load node as input. The first two kinds of variables are the control variables. In addition, in order to characterize the operating states of the power system, the active power and reactive power of all load nodes are added to the input set of the sample. Notably, when the number of system load nodes is huge and the processing capacity of the learning model is limited, only some key load nodes or cross-section power flow and other characteristics can be selected to characterize the operation mode of the power system. The selection of a specific feature in the operation information of a power system is another interesting topic and will be further studied in the future. The DBN outputs are the active total line loss of the system expressed by P_{loss}, and the power flow value of the branch where the power flow reverse phenomenon may occur which is expressed by P_{ls}.

In the face of unbalanced power in the system for PF calculation in both model-based and data-driven ways, one or more generators are generally assigned to bear the unbalanced power—for example, Mezghani *et al.* (2020) uses multiple generators, as an automatic generation control scheme, to bear the unbalanced power caused by uncertain factors when considering many scenarios. Liu *et al.* (2021) adopts a slack generator to bear the unbalanced power caused by data-driven errors. In this paper, considering that the slack generator needs to bear the unbalanced power of the system, the active power of the slack generator cannot participate in the process of power flow optimization, so the error brought by the data drive in this paper will also be borne by the slack generator as part of the unbalanced power, and the sample input set of this paper does not include the active power of the slack generator.

4.2 Genetic Algorithm Improvement: Elimination of Power Flow Reversal Individuals

First, the concept of the power flow reverse is introduced. The phenomenon of power flow reverse refers to the phenomenon that the power flow direction is opposite to the positive direction assumed in advance—for example, if the power flow reverse occurs on the line i–j, $P_{ij} < 0$.

The generator area and the load area in the network structure are normally determined, and the power delivery pattern between areas through one or more cross-sections is planned and maintained according to operation rules. Thus, in this paper, the phenomenon of the power flow reverse of cross-sections or a line of a section under study is seen as abnormal, contrary to the requirement of power system operation safety—for example, when the power flow in one of the parallel lines in a cross-section is reversed, the resulting loop current/power will make the distribution of the power flow more uneven within the section and will probably lead to the phenomenon of power flow overload in the other lines. Therefore, in this paper, the active powers of the lines, where the power flow reverse may occur, are added into the output of the sample set to monitor whether power flow reverse occurs or not. In this way, the proposed optimization method can consider $P_{ij} > 0$, which is the inequality constraint about the power flow reverse. In order to determine these lines, it is necessary to use simulation data information to determine which lines in the concerned section will be prone to power flow reversal. At the same time, this paper adds the section line power flow direction identification link in the genetic algorithm (GA) adaptation calculation step. Considering that each individual corresponds to an operation state of the power

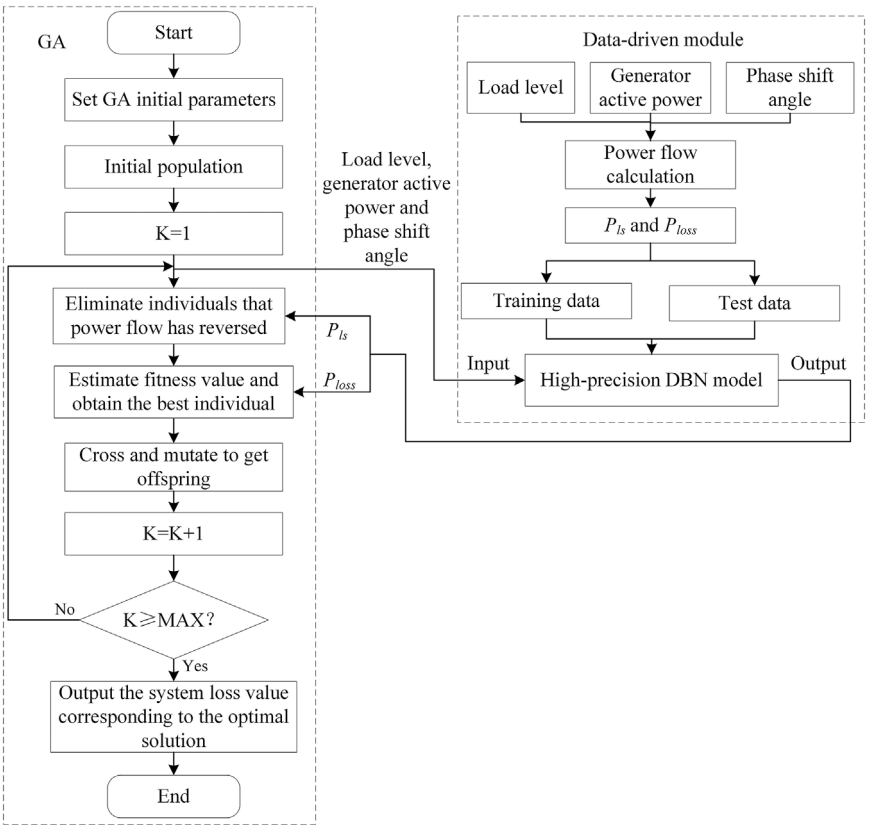

FIGURE 5 | The flow chart of improved genetic algorithm based on data drive.

system in the genetic algorithm, if the lines with power flow reversal in the studied section are identified, the corresponding individuals are eliminated.

4.3 Power Flow Optimization Based on Improved Genetic Algorithm With Deep Belief Network

The calculation link of the fitness function in the improved GA is replaced by the well-trained DBN model, which realizes the rapid calculation of the power flow optimization. The main steps of the improved genetic algorithm based on data drive are shown in **Figure 5**, and the implementation process is as follows:

(1) Construct a quantity of network training samples: The training samples are constructed by randomly selecting different load levels, different active power levels of generators, and different PST gears within a reasonable range. The system loss value is obtained by the calculation of formula (3) as one of the DBN output. Another DBN output is the power flow of the lines in the studied section where the power flow reverse may occur.
(2) The constructed samples are divided into training sets and test sets, which are used for DBN training and the performance testing of the post-training networks, respectively. The DBN parameters are set according to the actual system specifications.
(3) Set the GA parameters, including population size, maximum iteration number, iterative accuracy, cross-probability and variation probability, *etc.*, and initialize the population. The genes of each chromosome consist of the active and reactive load value, the controllable generator power (MW), and the phase angle of the PST.
(4) The DBN is used to predict each individual to get the corresponding fitness value and the active powers of the lines where the power flow reverse may occur, and the power flow reversal judgment is performed on each individual. The individuals with power flow reversal are eliminated, and the others are retained or eliminated through fitness ranking.
(5) Crossover and mutation of the population to obtain the better offspring.
(6) Determine whether the end condition of GA has been met. If the maximum number of iterations or the iterative accuracy is reached, stop the iteration and output the system loss and the optimal power flow scheme, otherwise return to step (4).

Notably, the main work of calculating the adaptation function is actually to calculate a power flow in the power flow optimization problem of a power system. It is very time-consuming to repeatedly

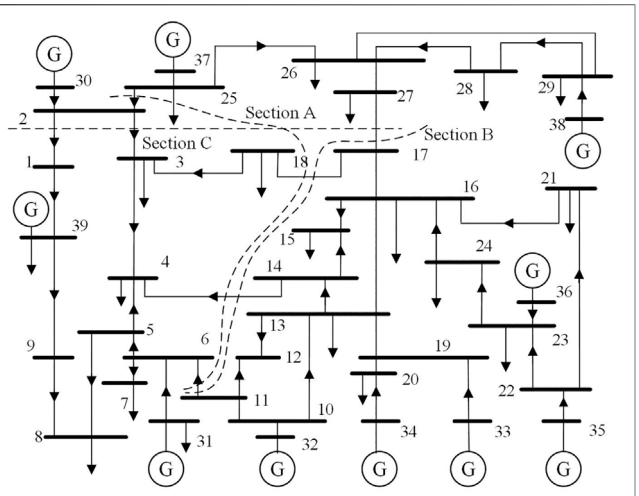

FIGURE 6 | IEEE 39-node system structure diagram.

calculate the power flow in the iterative process, while replacing the power flow calculation with the DBN model can greatly reduce the time cost. Therefore, as long as the learning model is guaranteed within a certain acceptable precision range, the optimization process of the algorithm can be greatly accelerated with almost no loss of optimization accuracy.

5 CASE STUDY

5.1 Phase-Shifting Transformer Installation Position and Parameters

In this paper, the IEEE 39-node system is used as the simulation example, and the diagram is shown in **Figure 6**.

Figure 6 shows three sections of the system (Jia et al., 2010). In this paper, section B is selected for research. In order to determine the installation location of the PST, it is necessary to analyze the power flow distribution of section B, as shown in **Table 1**.

Among them, F and T represent the starting and ending points of the branch, and P represents the active power of the line.

It should be noted that, in order to ensure that the IEEE 39-node system meets the inequality constraint (8), some parameters of the standard IEEE 39-node system are modified in this paper, and the contents of the modifications are shown in **Table 2**. The data in **Table 1** is based on the modified IEEE 39-node system.

For simplicity, only one PST is considered. According to the power flow data shown in **Table 1**, this paper installs the PST between nodes 17 and 27. Because this branch has the smallest power flow, the PST installed on this branch can absorb the power flow of other lines in the section and improve the overall transport capacity of the section.

In order to determine the PST parameters, it is necessary to clarify the active power limit value of the 17–27 branch. This paper assumes that the active power limit value of the branch with PST is 350 MW. In addition, this paper takes [−10°, 10°] as the phase-shift angle adjustment range, and the adjacent phase-shift gears differ by 1°. According to the parameter design method of

TABLE 1 | Power flow distribution of section B.

Branch number	F	T	P (MW)
1	BUS17	BUS 27	36
2	BUS17	BUS18	193.4
3	BUS14	BUS4	264.2
4	BUS11	BUS6	319.1

the PST in literature (Yu et al., 2013), the equivalent reactance of the PST at each tap position can be obtained. Considering that the difference of the PST equivalent reactance at different gears is very small, the equivalent reactance corresponding to the phase-shift angle of 0° is chosen as the equivalent reactance of each gear. The selected equivalent reactance of the PST is 0.04 p.u.

5.2 Sample Set Construction

In this paper, BPA and MATLAB simulation software are used to automatically generate a steady-state power flow sample set, and the GA is implemented on the MATLAB platform. The test computer is configured as Intel Core i7-4790, CPU s3.2 GHz, 8 GB RAM.

According to the analysis of **Section 4.1**, the input of the DBN includes P_{Di}, Q_{Di}, P_{Gi}, and α. In this paper, only one PST is installed, and the dimension of the phase-shift angle variable is one. Then, the generators 30, 32, and 33 are selected to participate in the power flow optimization process, so there are three active power variables of the generators. Considering that the sample system has only 19 load nodes, this paper selects all of the load nodes to reflect the system operation features and test the capability of the DBN, which means that there are 38 load variables of active and reactive power. Totally, the sample input amount is 42. In terms of the range of the input variables, the phase-shift angle is in the range of [−10°, 10°], while the active powers of the generators of BUS30, BUS32, and BUS33 are respectively in the range of [520 MW, 1,040 MW], [362 MW, 725 MW], and [326 MW, 652 MW]. Among them, the upper limit of the active power of each generator is derived from the example of MATPOWER (Zimmerman et al., 2011), and the lower limit is half of the upper limit according to experience. If we set the lower limit value of the active power of each generator as 0 according to the practice of MATPOWER, a large number of samples in the simulation will not converge. In addition, the active and reactive powers of each load node at the load level of 100% are shown in **Table 3**. Specifically, the load levels in the sample set of this paper include 95, 100, 102, and 105%, and the number of samples per load level is 1,000. So, the input dimension of the sample set is 42 × 4,000.

Considering that the power flow of line 17–27 is small and easy to reverse, this paper puts the active power of line 17–27 as one of the outputs of the DBN. Thus, the output of the DBN is of two dimensions: the active power of line 17–27 and the system loss. The sample set used in this paper can be found in the supplementary material.

5.3 Accuracy of Different Learning Models

In order to compare the prediction accuracy of DBN, in terms of system network loss, three extra common machine learning

TABLE 2 | The modified parameters of the IEEE 39-node system.

No.	Before the change	After the change
BUS25	Active load: 224 MW, reactive load: 47.2 MVAR	Active load: 300 MW, reactive load: 150 MVAR
BUS26	Active load: 139 MW, reactive load: 17 MVAR	Active load: 150 MW, reactive load: 30 MVAR
BUS36	Arrange the voltage value or Vmax: 1.063 p.u.	Arrange the voltage value or Vmax: 1.030 p.u

TABLE 3 | The active and reactive power of each load node at the load level of 100%.

No.	P (MW)	Q (MVAR)	No.	P (MW)	Q (MVAR)
BUS3	322	2.4	BUS23	247.5	84.6
BUS4	500	184	BUS24	308.6	–92
BUS7	233.8	84	BUS25	300	150
BUS8	522	176	BUS26	150	30
BUS12	8.5	88	BUS27	281	75.5
BUS15	320	153	BUS28	206	27.6
BUS16	329	32.3	BUS29	283.5	26.9
BUS18	158	30	BUS31	9.2	4.6
BUS20	680	103	BUS39	1,104	250
BUS21	274	115	—	—	—

methods are used for the test: back-propagation neural network (BP), extreme learning machine (ELM), and support vector machine (SVM). In the 4,000 sample sets in **Section 5.2**, 3,000 samples were randomly selected as the training set and 1,000 samples as the test set. Thus, these four models are trained and tested with the same samples. The model parameters are as follows:

1) DBN: We use two hidden layers, which contain 300 and 400 hidden nodes, respectively. The momentum, learning rate, and number of RBM pre-training are chosen as 0.7, 0.03, and 100, respectively.
2) ELM: The number of hidden layer nodes is 60.
3) SVM: 4 polynomial nuclear functions are selected. The penalty function and the nucleus function coefficient is 1.5 and 10, respectively.

The predicted results of different models on the test set are shown in **Figure 7**. It can be seen that the DBN used in this paper has a good prediction effect on the system loss of the test set. The forecast values of DBN and the expectations (the true values) from the simulation cases are basically consistent, which can meet the application requirements of the system loss assessment. The

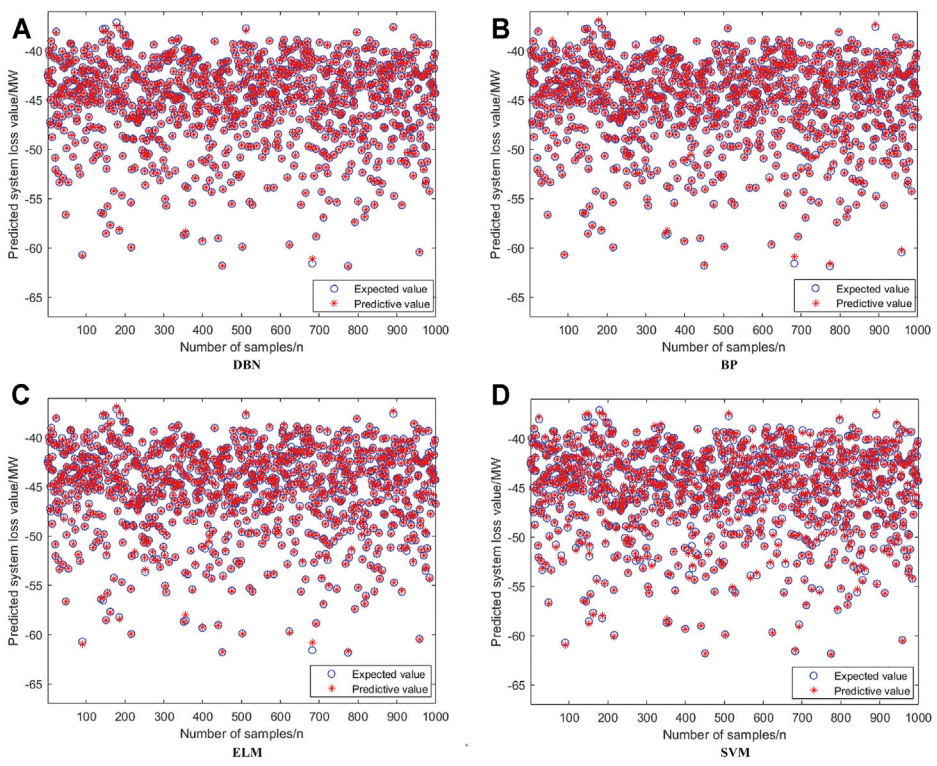

FIGURE 7 | Predicted results of different models on the test set. **(A)** is DBN, **(B)** is BP, **(C)** is ELM, **(D)** is SVM.

TABLE 4 | Predicted results of different models on the test set.

Model	DBN	BP	ELM	SVM
RMSE	0.032363	0.058879	0.094488	0.139440
MAE	0.017190	0.039753	0.069476	0.114470
R^2	0.999946	0.999821	0.999539	0.998996

other three common machine learning methods also show good prediction results.

In addition, to further compare the performance of the models, root mean square error (RMSE), mean absolute error (MAE), and determination coefficients (R^2) are used (Kang et al., 2015; Mohan et al., 2018). The results of the relevant indicators are shown in **Table 4**. Among them, RMSE and MAE are used to evaluate the predictive ability of the model on the test samples. The smaller the value of RMSE and MAE, the better the predicting performance of the model for system loss. In addition, R^2 is used to evaluate the fitting degree of the model with the test set. The closer the value is to 1, the higher the fitting degree is.

As can be seen from **Table 4**, compared with BP, ELM, and SVM methods, all the indicators of DBN are leading, so DBN is recommended as the data-driven module of the GA in this paper.

5.4 Comparison of Data-Driven and Model-Driven Genetic Algorithms

The basic parameters of the GA used in this paper are as follows: the number of maximum iterations is 70, the number of variables is 4, the number of individuals is 40, the generation gap is 0.95, the crossover probability is 0.7, and the mutation probability is 0.01.

In order to test the accuracy of the data-driven GA and the generalization ability of the learning models mentioned above under different load levels of the system, we take the load levels of 93, 95, 97, 99, 101, 103, 105, and 107% for simulation. The simulation results are shown in **Table 5**, where the results of the model-driven genetic algorithm are regarded as true values.

Among them, $P_{\mathrm{loss,GA}}$ represents the optimal system loss value obtained by model-driven GA. $P_{\mathrm{loss,DBN\text{-}GA}}$, $P_{\mathrm{loss,BP\text{-}GA}}$, $P_{\mathrm{loss,ELM\text{-}GA}}$, and $P_{\mathrm{loss,SVM\text{-}GA}}$ respectively represent the optimal system losses obtained by different data-driven GA. The relative error is calculated as follows: ($P_{\mathrm{loss,XX\text{-}GA}}$ - $P_{\mathrm{loss,GA}}$) / $P_{\mathrm{loss,GA}}$, where the expression $P_{\mathrm{loss,XX\text{-}GA}}$ represents the data-driven GA.

As can be seen from **Table 5**, the error of DBN-based GA is smaller than those of other data-driven methods at 97, 101, and 105% load levels. Relatively, the DBN-based GA has less error than other data-driven methods. As a whole, the DBN-based GA shows a stronger generalization of different load levels of the system compared with the other data-driven GA in **Table 5**.

In order to verify the accuracy of data-driven optimization results, the optimization results based on DBN were substituted into BPA (Tao et al., 2013). The active power loss value based on DBN and BPA ($P_{\mathrm{loss,DBN\text{-}BPA}}$) was compared with that based on the model-driven method ($P_{\mathrm{loss,GA}}$), and the results are as shown in **Table 6**. This process is named "state recovery" (Liu et al., 2021) since it is aimed at recovering the system state based on the optimization results of the data-driven method. This approach can also help examine whether the results of the data-driven method can be applicable for practical power flow optimization.

From the data in **Table 6**, the precision of the optimization results based on DBN and BPA is high enough, which means that the results of the data-driven method can be applicable for practical power flow optimization.

5.5 Comparison of Genetic Algorithms and a Mixed-Integer Second-Order Cone Programming Model

In order to further verify the optimization performance of the proposed method, we compared the calculation time and optimization results of different data-driven GA, the model-driven GA, and the traditional mathematical programming method at 100% load level. Considering the discrete characteristics of the PST, the power flow optimization problem of the traditional solution method is transformed into a mixed-integer second-order cone programming (MISOCP) model (Lin et al., 2019). Then, the mature optimization solver GUROBI is used to solve the problem (Lin et al., 2019). The time cost and solution results of various models are shown in **Table 7**. Moreover, the iteration will be terminated if the difference between the optimal objective functions of three adjacent iterations is less than 0.01 when we use the model-driven GA.

As can be seen from the results in **Table 7**, data-driven GA is significantly superior to model-driven GA and MISOCP in time consumption. By comparing the optimization results between

TABLE 5 | Errors of the data-driven genetic algorithm (GA) and model-driven GA.

Load level (%)	$P_{\mathrm{loss,GA}}$ (MW)	$P_{\mathrm{loss,DBN\text{-}GA}}$ (MW)	Relative error (%)	$P_{\mathrm{loss,BP\text{-}GA}}$ (MW)	Relative error (%)	$P_{\mathrm{loss,ELM\text{-}GA}}$ (MW)	Relative error (%)	$P_{\mathrm{loss,SVM\text{-}GA}}$ (MW)	Relative error (%)
93	39.5	38.9838	−1.31	39.1165	−0.97	43.5033	10.13	37.0208	−6.28
95	38.2	38.3535	0.40	38.3811	0.47	38.2034	0.01	38.4691	0.70
97	37.6	37.5784	−0.06	38.0802	1.28	39.0566	3.87	38.3721	2.05
99	37.3	37.5717	0.73	37.3637	0.17	37.7442	1.19	37.8158	1.38
101	37.7	37.7164	0.04	37.0992	−1.59	37.0216	−1.80	37.3028	−1.05
103	38.0	38.1828	0.48	38.0909	0.24	38.1106	0.29	37.6957	−0.80
105	38.8	38.782	−0.05	38.5966	−0.52	38.8291	0.07	38.9025	0.26
107	39.9	39.4093	−1.23	37.3648	−6.35	39.1624	−1.85	40.245	0.86

TABLE 6 | Errors of the optimization results based on deep belief network (DBN) and BPA.

Load level (%)	$P_{loss,GA}$ (MW)	$P_{loss,DBN-BPA}$ (MW)	Relative error (%)
93	39.5	39.01	−1.24
95	38.2	38.19	−0.03
97	37.6	37.35	−0.66
99	37.3	37.31	0.03
101	37.7	37.7	0
103	38.0	38.14	0.37
105	38.8	38.83	0.08
107	39.9	39.94	0.10

TABLE 7 | Comparison of data-driven genetic algorithm (GA), model-driven GA, and MISOCP.

Operation	CPU time (s)	P_{loss} (MW)
DBN-GA	0.637	37.61
BP-GA	1.608	37.28
ELM-GA	0.593	37.33
SVM-GA	0.640	37.72
Model-driven	262.373	37.6
MISOCP	3.857	38.39

different models, it can be seen that the data-driven GA and the model-driven GA can obtain better solutions than the traditional MISOCP algorithm, having better performance in avoiding local optimal in this case. In addition, the accuracy of DBN is the highest at 100% load level when regarding the result of model-driven GA as the truth value. In a word, although the time consumption of DBN is not the shortest, DBN is still a more appropriate choice considering the comprehensive performance of accuracy, generalization ability, and time consumption.

Through the study, it can be seen that the data-driven GA can greatly accelerate the optimization process under the premise of ensuring the optimization accuracy.

5.6 Validation of the Improved GA

In order to verify the correctness and validity of **Section 4.2**, we make a simulation comparison on whether to adopt the power flow reversal elimination mechanism. The simulation example is the IEEE 39-node system with PST at the load level of 100%. The simulation results are shown in **Table 8**.

From the comparison of the data in **Table 8**, it can be seen that, compared with the practice of eliminating the individuals with power flow reversal, the uniformity of power flow distribution in each line of section B is significantly reduced without eliminating the individuals with power flow reversal. It is necessary to point out that, in the scenario studied in this paper, the power flow reverse phenomenon is more likely to occur when the phase-shift angle is in the positive interval.

TABLE 8 | The power flow distribution of section B with or without eliminating individuals of power flow reverse.

F	T	P (MW)	
		Eliminated	Not eliminated
BUS17	BUS27	8.2	−29.8
BUS17	BUS18	18.1	45.3
BUS14	BUS4	144.4	154.5
BUS11	BUS6	72.2	89.5

6 CONCLUSION

1) The optimal power flow model of the power system with the phase-shifting transformer is established, and an efficient data-driven algorithm is proposed to solve it, which not only balances the optimization speed and accuracy but also has certain generalization ability for various power grid operation modes.
2) The sectional power flow reversal elimination mechanism in the genetic algorithm is introduced and appropriately co-designed with DBN to avoid the unreasonable power flow distribution of the grid section with PST.
3) Simulation examples show that the improved genetic algorithm containing data drive process proposed in this paper is effective.

The current research is aimed to optimize the power flow of power systems with PST in a certain load level range. The change of the system topology has not been considered. Therefore, how to apply the proposed method to the power flow optimization of a power system with more variable operation modes is the main topic in future works.

DATA AVAILABILITY STATEMENT

The original contributions presented in the study are included in the article/supplementary material, Further inquiries can be directed to the corresponding author.

AUTHOR CONTRIBUTIONS

All authors listed have made a substantial, direct, and intellectual contribution to the work and approved it for publication.

FUNDING

This research was funded by the Southern Power Grid Corporation's Science and Technology Project (Project No. 037700KK52190015 (GDKJXM20198313)) and the Key-Area Research and Development Program of Guangdong Province (2019B111109001).

REFERENCES

Ahmed, M. K., Osman, M. H., Shehata, A. A., and Korovkin, N. V. (2021). "A Solution of Optimal Power Flow Problem in Power System Based on Multi Objective Particle Swarm Algorithm," in 2021 IEEE Conference of Russian Young Researchers in Electrical and Electronic Engineering (ElConRus), St. Petersburg, Moscow, Russia, January 26-29, 2021 (IEEE), 1349–1353. doi:10.1109/ElConRus51938.2021.9396117

Bian, X., Tse, C. T., Guangyue Li, G., and Yang Fu, Y. (2012). "Study on TCPS Static and Dynamic Modeling in Power System," in IEEE PES Conference on Innovative Smart Grid Technologies, Tianjin, China, May 21-24, 2012 (IEEE). doi:10.1109/ISGT-Asia.2012.6303267

Butler-Purry, K. (2013). Distribution System Modeling and Analysis [Book Reviews]. *IEEE Power Energ. Mag.* 11 (3), 106–108. doi:10.1109/MPE.2013.2245593

Chen, Y. C., Wang, J., Dominguez-Garcia, A. D., and Sauer, P. W. (2016). Measurement-based Estimation of the Power Flow Jacobian Matrix. *IEEE Trans. Smart Grid* 7 (5), 2507–2515. doi:10.1109/TSG.2015.2502484

Cui, Y., Chen, J., and Liu, J. (2013). Optimal Allocation of TCPS for Enhancing Transfer Capability of Electric Power Transmission Section. *Shaanxi Electric Power* 41 (11), 75–79+101. doi:10.3969/j.issn.1673-7598.2013.11.018

Dong, Y., Dong, Z., Zhao, T., Li, Z., and Ding, Z. (2021). Short Term Load Forecasting with Markovian Switching Distributed Deep Belief Networks. *Int. J. Electr. Power Energ. Syst.* 130 (1), 106942. doi:10.1016/j.ijepes.2021.106942

Eremia, M., Liu, C. C., and Edris, A. A. (2016). *Advanced Solutions in Power Systems: HVDC, FACTS, and Artificial Intelligence*. Hoboken, USA: IEEE Press and Wiley.

Jia, H., Mu, Y., and Yu, X. (2010). Directional Control Method to Interface Power Based on DC Power Flow and Sensitivity. *Automation Electric Power Syst.* 34 (2), 34–38.

Kang, B., Ku, Y. H., and Kim, Y. D. (2015). A Case Study for ANN-Based Rainfall-Runoff Model Considering Antecedent Soil Moisture Conditions in Imha Dam Watershed, Korea. *Environ. Earth Sci.* 74 (2), 1261–1272. doi:10.1007/s12665-015-4117-0

Kawaura, Y., Yamanouchi, S., Ichihara, M., Iwamoto, S., Suetsugu, Y., and Higashitani, T. (2016). "Phase-shifting Transformer Application to Power-Flow Adjustment for Large-Scale PV Penetration," in 2016 IEEE Region 10 Conference (TENCON), Singapore, November 22-25, 2016 (IEEE), 3328–3331. doi:10.1109/TENCON.2016.7848668

Lei, X., Yang, Z., Yu, J., Zhao, J., Gao, Q., and Yu, H. (2021). Data-Driven Optimal Power Flow: A Physics-Informed Machine Learning Approach. *IEEE Trans. Power Syst.* 36 (1), 346–354. doi:10.1109/TPWRS.2020.3001919

Lin, S., Yang, Z., Fan, G., Liu, M., He, S., Tang, Z., et al. (2019). A Mixed-Integer Second-Order Cone Programming Algorithm for the Optimal Power Distribution of AC-DC Parallel Transmission Channels. *Energies* 12 (19), 3605. doi:10.3390/en12193605

Liu, G. (2021). Modeling and Solution Research on Dynamic Economic Dispatch of Power System with Wind Power. Master's thesis/dissertation. Beijing(China): North China Electric Power University.

Liu, H., ShenGuo, X. Q., and Sun, H. (2021). A Data-Driven Approach towards Fast Economic Dispatch in Electricity–Gas Coupled Systems Based on Artificial Neural Network. *Appl. Energ.* 286, 116480. doi:10.1016/j.apenergy.2021.116480

Liu, X., and Kong, X. (2021). Fast Load Flow Calculation of N-2 Contingency Based on Convolutional Neural Network. *Electric Power Eng. Tech.* 40 (4), 95–100. doi:10.12158/j.2096-3203.2021.04.013

Liu, Y., Zhang, N., Wang, Y., Yang, J., and Kang, C. (2019). Data-Driven Power Flow Linearization: A Regression Approach. *IEEE Trans. Smart Grid* 10 (3), 2569–2580. doi:10.1109/TSG.2018.2805169

Lorca, A., and Sun, X. A. (2015). Adaptive Robust Optimization with Dynamic Uncertainty Sets for Multi-Period Economic Dispatch under Significant Wind. *IEEE Trans. Power Syst.* 30 (4), 1702–1713. doi:10.1109/TPWRS.2014.2357714

Mehdi, P. (2010). Improvement of Transient Stability of Power System by Thyristor Controlled Phase Shifter Transformer. *Am. J. Appl. Sci.* 7 (11), 1495–1499. doi:10.3844/ajassp.2010.1495.1499

Mezghani, I., Misra, S., and Deka, D. (2020). Stochastic AC Optimal Power Flow: A Data-Driven Approach. *Electric Power Syst. Res.* 189, 106567. doi:10.1016/j.epsr.2020.106567

Mohamed, A. A., and Venkatesh, B. (2019). Line-Wise Optimal Power Flow Using Successive Linear Optimization Technique. *IEEE Trans. Power Syst.* 34, 2083–2092. doi:10.1109/TPWRS.2018.2881254

Mohan, N., Soman, K. P., and Sachin Kumar, S. (2018). A Data-Driven Strategy for Short-Term Electric Load Forecasting Using Dynamic Mode Decomposition Model. *Appl. Energ.* 232, 229–244. doi:10.1016/j.apenergy.2018.09.190

Morrell, T. J., and Eggebraaten, J. G. (2019). "Applications for Phase-Shifting Transformers in Rural Power Systems," in 2019 IEEE Rural Electric Power Conference (REPC), Bloomington, MN, USA, April 28-May 1, 2019 (IEEE), 70–74. doi:10.1109/REPC.2019.00020

Nadeem, M., Imran, K., Khattak, A., Ulasyar, A., Pal, A., Zeb, M. Z., et al. (2020). Optimal Placement, Sizing and Coordination of FACTS Devices in Transmission Network Using Whale Optimization Algorithm. *Energies* 13 (3), 753–776. doi:10.3390/en13030753

Noroozian, M., and Andersson, G. (1993). Power Flow Control by Use of Controllable Series Components. *IEEE Trans. Power Deliv.* 8 (3), 1420–1429. doi:10.1109/61.252669

Pan, S., Jian, J., and Yang, L. (2018). A Hybrid MILP and IPM Approach for Dynamic Economic Dispatch with Valve-Point Effects. *Int. J. Electr. Power Energ. Syst.* 97, 290–298. doi:10.1016/j.ijepes.2017.11.004

Papazoglou, T. M., Popovic, D. P., and Mijailovic, S. V. (1999). "Phase Shifting Transformers in an Efficient Power Flow Control Method," in International Conference on Electric Power Engineering, Budapest, Hungary, August 29-September 2, 1999 (IEEE). doi:10.1109/PTC.1999.826439

Roldan, C., Minguez, R., Garcia-Bertrand, R., and Arroyo, J. M. (2019). Robust Transmission Network Expansion Planning under Correlated Uncertainty. *IEEE Trans. Power Syst.* 34 (3), 2071–2082. doi:10.1109/TPWRS.2018.2889032

Shi, T., Mei, F., Lu, J., Lu, J., Pan, Y., Zhou, C., et al. (2019). Phase Space Reconstruction Algorithm and Deep Learning-Based Very Short-Term Bus Load Forecasting. *Energies* 12 (22), 4349–4366. doi:10.3390/en12224349

Sivasubramani, S., and Swarup, K. S. (2010). Hybrid SOA-SQP Algorithm for Dynamic Economic Dispatch with Valve-Point Effects. *Energy* 35 (12), 5031–5036. doi:10.1016/j.energy.2010.08.018

Stott, B., Jardim, J., and Alsac, O. (2009). DC Power Flow Revisited. *IEEE Trans. Power Syst.* 24 (3), 1290–1300. doi:10.1109/TPWRS.2009.2021235

Sun, W. (2011). Optimal Phase Shifter Calculation Based on Adaptive Genetic Algorithm. *J. Mech. Electr. Eng.* 28 (7), 901–904.

Tao, C., Wang, X., Gao, F., and Wang, M. (2020). Fault Diagnosis of Photovoltaic Array Based on Deep Belief Network Optimized by Genetic Algorithm. *Chin. J. Electr. Eng.* 6 (3), 106–114. doi:10.23919/CJEE.2020.000024

Tao, H., Xu, J., and Zou, W. (2013). Model Conversion from BPA to PSCAD. *Electric Power Automation Equipment* 33 (8), 152–156. doi:10.3969/j.issn.1006-6047.2013.08.026

Van Horn, K. E., Dominguez-Garcia, A. D., Sauer, P. W., Alejandro, D., and SauerPeter, W. (2016). Measurement-Based Real-Time Security-Constrained Economic Dispatch. *IEEE Trans. Power Syst.* 31 (5), 3548–3560. doi:10.1109/TPWRS.2015.2493889

Verboomen, J., Van Hertem, D., Schavemaker, P. H., Kling, W. L., and Belmans, R. (2005). Phase Shifting Transformers: Principles and Applications," in 2005," in International Conference on Future Power Systems, Amsterdam, Netherlands, November 18, 2005 (IEEE). doi:10.1109/FPS.2005.204302

Victoire, T. A. A., and Jeyakumar, A. E. (2004). Hybrid PSO-SQP for Economic Dispatch with Valve-Point Effect. *Electric Power Syst. Res.* 71 (1), 51–59. doi:10.1016/j.epsr.2003.12.017

Xu, D., Li, Z., Yang, S., Lu, Z., Zhang, H., Chen, W., et al. (2018). "A Classified Identification Deep-Belief Network for Predicting Electric-Power Load," in 2018 2nd IEEE Conference on Energy Internet and Energy System Integration (EI2), Beijing, China, October 20-22, 2018 (IEEE). doi:10.1109/EI2.2018.8582314

Yu, H., Zhou, F., and Yang, Z. (2013). Parameter Design and Steady State Characteristic Analysis of TCPSTs in a EHV-Grid. *Electric Power* 46 (11), 36–41. doi:10.3969/j.issn.1004-9649.2013.11.008

Zhang, N., Zhang, K., Li, Q., Liu, J., Zhao, J., and Sun, G. (2021). Optimal Power Flow Calculation of Power System Containing TCPST Based on Improved MCCIPM. *Electric Power Eng. Tech.* 40 (5), 144–150. doi:10.12158/j.2096-3203.2021.05.020

Zhang, Y., Gong, D.-w., Geng, N., and Sun, X.-y. (2014). Hybrid Bare-Bones PSO for Dynamic Economic Dispatch with Valve-point Effects. *Appl. Soft Comput.* 18 (4), 248–260. doi:10.1016/j.asoc.2014.01.035

Zhang, Z. (2017). Application of Phase Shifting Measures in Emergency Control of Power System. Master's thesis/dissertation. Hangzhou(China): Zhejiang University.
Zhu, Y., and Tomsovic, K. (2002). Adaptive Power Flow Method for Distribution Systems with Dispersed Generation. *IEEE Trans. Power Deliv.* 17 (5), 822–827. doi:10.1109/TPWRD.2002.1022810
Zimmerman, R. D., Murillo-Sanchez, C. E., and Thomas, R. J. (2011). MATPOWER: Steady-State Operations, Planning, and Analysis Tools for Power Systems Research and Education. *IEEE Trans. Power Syst.* 26 (1), 12–19. doi:10.1109/TPWRS.2010.2051168

Conflict of Interest: ZL, FL, RL and MY are employees of Guangdong Power Grid Corporation and a fee for service was provided to ZC, ZX and ZD for their contribution.

The remaining authors declare that the research was conducted in the absence of any commercial or financial relationships that could be construed as a potential conflict of interest.

The authors declare that this study received funding from Guangdong Power Grid Corporation. The funder had the following involvement in the study: the writing of this article and the decision to submit it for publication.

Publisher's Note: All claims expressed in this article are solely those of the authors and do not necessarily represent those of their affiliated organizations or those of the publisher, the editors, and the reviewers. Any product that may be evaluated in this article or claim that may be made by its manufacturer is not guaranteed or endorsed by the publisher.

frontiers in Energy Research

HYPOTHESIS AND THEORY
published: 03 February 2022
doi: 10.3389/fenrg.2022.803142

Distribution Network Voltage Arc Suppression Method Based on Flexible Regulation of Neutral Point Potential of the New Grounding Transformer

Wu Lifang[1], Bai Hao[2], Zhou Ke[1], Yuan Zhiyong[2], Yu Xiaoyong[1], Lei Jinyong[2], Zou Yu[3] and Zhang Yuan[4]*

[1]Electric Power Research Institute of Guangxi Power Grid, Nanning, China, [2]Electric Power Research Institute, China Southern Power Grid, Guangzhou, China, [3]Qinzhou Power Supply Bureau of Guangxi Power Grid Co. Ltd, Qinzhou, China, [4]Chongzuo Power Supply Bureau of Guangxi Power Grid Co. Ltd, Chongzuo, China

OPEN ACCESS

Edited by:
Xiangjun Zeng,
Changsha University of Science and Technology, China

Reviewed by:
Junhua Xu,
Guangxi University, China
Narottam Das,
Central Queensland University, Australia

***Correspondence:**
Wu Lifang
837674977@qq.com

Specialty section:
This article was submitted to Smart Grids, a section of the journal Frontiers in Energy Research

Received: *27 October 2021*
Accepted: *04 January 2022*
Published: *03 February 2022*

Citation:
Lifang W, Hao B, Ke Z, Zhiyong Y, Xiaoyong Y, Jinyong L, Yu Z and Yuan Z (2022) Distribution Network Voltage Arc Suppression Method Based on Flexible Regulation of Neutral Point Potential of the New Grounding Transformer. Front. Energy Res. 10:803142. doi: 10.3389/fenrg.2022.803142

Aiming at the problems that the existing arc suppression cabinet technology cannot adjust the zero sequence voltage flexibly and the control and hardware implementation of active arc suppression equipment based on power electronics are difficult, a new method of voltage arc suppression in the distribution network based on the flexible regulation of the neutral point potential of the new grounding transformer is proposed. From the perspective of the sequence component, the variation law of the neutral point voltage before and after the closing of the tapped grounding branch of the new grounding transformer is analyzed. By selecting the appropriate initial tap position of the tap-to-ground switch, the fault phase voltage is flexibly controlled so that the fault phase voltage is reduced to below the reignition voltage to quickly solve the influence of the single-phase grounding fault, and the risk of non-fault phase insulation breakdown is reduced to ensure the stable operation of the distribution network. According to the ratio of the fault phase current to the zero sequence voltage before and after the gear inputs, whether the arc suppression of the single-phase grounding fault is completed is judged. Compared with power electronic products, the new grounding transformer has the advantages of high reliability, long service life, and low cost and has strong economy and applicability in engineering. The single-phase grounding fault model of the 10kV distribution network is built in the PSCAD/EMTDC simulation environment, and the new method of the distribution network voltage arc suppression based on the flexible regulation of neutral point potential of the new grounding transformer is verified. The simulation results show that the proposed method can effectively reduce the fault phase voltage to achieve the reliable arc suppression of the single-phase grounding fault.

Keywords: distribution networks, single-phase grounding fault, neutral point potential, flexible pressure regulating, the voltage arc suppression

INTRODUCTION

The grounding modes of a neutral point in a power system include direct grounding of the neutral point and non-effective grounding of the neutral point. Among them, neutral non-effective grounding includes non-grounding, arc suppression coil grounding, and high impedance grounding (Li, 2019a). Non-effective grounding method accounts for more than 85% of the voltage levels of 6kV–110 kV in the Chinese power grid (Xue, 2015a). In the long-term power system operation, insulation aging, environmental changes, and other conditions are easy to cause short circuit and other problems. Among them, the proportion of the single-phase short-circuit fault is the largest, accounting for more than 60% of the short-circuit fault types (Choi et al., 2010; Fang, 2017). The single-phase grounding fault is often accompanied by the arc grounding fault (Xiao, 2021), which is harmful to personal and equipment safety for a long time, and the arc grounding fault has complex characteristics such as frequent flameout, small arc current, and strong randomness affected by the environment. Therefore, it is difficult to identify and inhibit the single-phase arc grounding fault, and failing to deal with them in time is easy to cause economic losses and personal safety accidents (Zeng, 2000; Liu, 2016).

The existing arc suppression methods of the distribution network mainly use the neutral point arc suppression coil to compensate the capacitive current of the grounding fault point. According to the compensation object, the arc suppression methods of the distribution network can be divided into the current arc suppression method and voltage arc suppression method, and the current arc suppression law can be subdivided into the passive current arc suppression method and active current arc suppression method. The principle of the passive current arc suppression method is that the neutral point of the power grid and the earth are connected by adjustable inductance. When a grounding fault occurs, the inductive current is output through the adjustable inductance to compensate the capacitive current of the fault point system (Jin, 2010; Elombo et al., 2013; Xue, 2015b; Wang, 2018; Chen, 2020). The principle of active current arc suppression is to measure and calculate the fault current through the transformer and inject a zero sequence current with the same size and opposite direction under the premise of the known fault current so as to realize full current compensation arc suppression (Wang, 2015; Xie, 2015; Guo, 2017; Peng, 2018; Wu, 2018; Xu, 2018; Ze-Yin Zheng, 2020). Based on the principle of the current arc suppression method, the team of Li Jinglu of the Changsha University of Science and Technology developed a set of neutral point dynamic grounding devices to inject the compensation current (Li, 2019b), the team of Guo Moufa of Fuzhou University developed the three-phase cascaded H-bridge current converter to inject the compensation current (You, 2016), and the team of Yang Tingsheng of China Ocean Petroleum International Co., Ltd. developed a power electronic switch turn-regulation arc suppression coil to reduce the fault current (Yang, 2021). For the compensation method of the passive arc coil, some scholars have developed a pre-adjusted arc coil (National Development Reform Commission, 2007), air-gap inductive arc suppression coil, and arc suppression coil composed of three cores and five coils (Cai, 2004; Pang, 2006). However, the essence of the current arc cancellation method needs to obtain the fault current value (Zheng, 2021), while it is difficult to obtain the fault current value accurately in the power system engineering application. At the same time, there are problems; for example, the arc residual current is large (Zhang, 2019), and the arc suppression effect is affected by the control mode and the change of the operation state of the distribution network, so it is not widely promoted.

Aiming at the problems of the current arc suppression methods, voltage arc suppression methods came into being. At present, the voltage arc suppression method mostly used on the market is the fault phase transfer arc suppression technology (Grifflel, 1997; Chen, 2019), and its principle is to set up a grounding branch in the station. When a grounding fault occurs, the short-circuit current of the grounding branch is transferred by short-circuiting the fault phase bus in the station, thereby reducing the fault phase voltage to zero. On the basis of the fault phase transfer technology, the State Grid Corporation puts forward the active intervention arc suppression technology (Wang, 2020). The fault phase transfer technology can alleviate insulation deterioration, improve the accuracy of fault location, and it is simple and easy to operate when operating overvoltage occurs. But when metal grounding fault occurs, the grounding fault current is large (Fan, 2019), and there is a risk of the interphase fault under the condition of phase selection failure (Hänninen and Lehtonen, 1998; Xiang, 2020), so its arc suppression effect will be affected (Yao, 2009).

In view of the above problems, based on the principle of suppressing fault phase voltage re-ignition, a voltage arc suppression method for the distribution network based on flexible regulation of the neutral point potential of the new grounding transformer is proposed. The initial gear size is determined by the ceiling function, and then, the initial gear of the primary side of the new grounding transformer is closed; the tapped grounding branch is divided so that the zero potential is offset, and the zero sequence voltage is adjusted. Then, the ratio of the fault phase current to the zero sequence voltage is used to determine whether the arc suppression is completed so as to achieve rapid and flexible regulation of the fault phase voltage and reliable arc suppression. Furthermore, the single-phase grounding fault model of the 10kV distribution network is built in the PSCAD/EMTDC simulation environment to verify the reliability of the new voltage arc suppression method of the distribution network with a flexible voltage control.

THE PRINCIPLE OF NEUTRAL POINT POTENTIAL CONTROLLING STEP-DOWN ARC SUPPRESSION FLEXIBLY

System Equivalent Circuit After Closed Tap Grounding Branch

According to the extinguishing mechanism of the grounding arc, the resistance of a grounding medium is inversely proportional to the fault phase voltage (Huang, 2020), and when the maximum

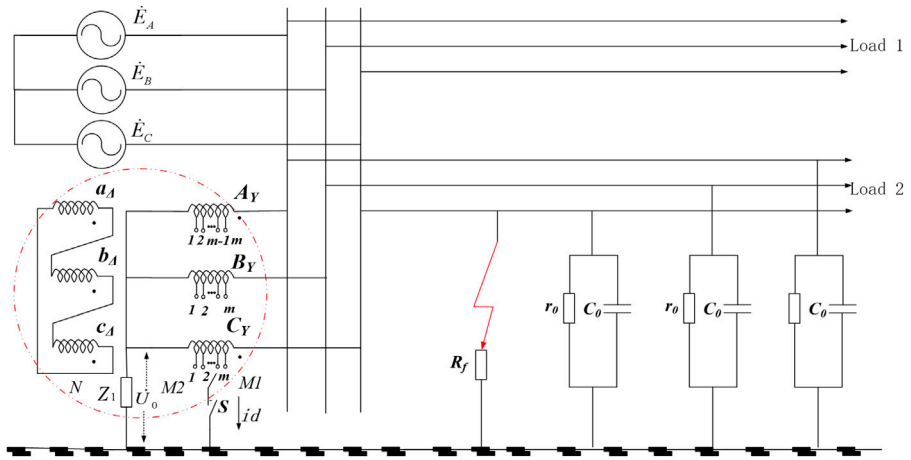

FIGURE 1 | Principle diagram of voltage arc suppression with flexible control of neutral point potential of the grounding transformer.

re-ignition voltage is less than the recovery speed of the grounding medium resistance, the arc is no longer reignited. According to the long-term operation experience of the distribution grid, the critical value of the maximum reignition voltage is between 0.22 and 0.36 times of the phase voltage in the 10kV distribution network (Yao, 2009).

The principle diagram of voltage arc suppression flexibly controlled by neutral point potential of the grounding transformer is shown in **Figure 1**. *EA*, *EB*, and *EC* are electromotive forces of three-phase power supply in the distribution network, *C*0 is the equivalent capacitance of the system to the ground, *r*0 is the equivalent resistance of the system to the ground, and Rf is the grounding fault resistance. AY, BY, and C_Y are the high-voltage side windings of the transformer. Ground taps are set on this side, and m taps are set in total. The taps rise from the neutral point of the high-voltage side transformer to the system in turn, which are 1, 2,. . ., m, respectively. aΔ, bΔ, and cΔ are low-voltage side windings of the transformer, and the neutral point lead of the system is grounded through impedance *Z*1. In addition, $\dot{I}_d$ is the grounding branch current, and the reference direction is the tap flow to the grounding point.

In **Figure 1**, it is defined that the tap-to-system side is defined as the *M*1 side, the tap to the neutral point of the high-voltage side of the transformer side is defined as the*M*2 side, and the transformer low-voltage side is defined as the *N* side. Then, the original dual-winding transformer can be equivalent to a three-winding transformer.

When a single-phase grounding fault occurs, the grounding branch switches of taps with different tap positions are closed, and the phase and amplitude of the zero-sequence voltage change so that the fault phase voltage changes according to different tap positions. The amplitude of the fault phase voltage is determined by the number of turns of windings contained in different tap positions, and the system line voltage remains unchanged in the process of mobilizing taps with different tap positions.

The transformer is a static component, and its positive and negative sequence impedances are equal, ignoring the line loss. The equivalent circuit diagrams of the positive sequence, negative sequence, and zero sequence of the system are drawn as shown in **Figure 2**. The 1-1′ port corresponds to the grounding transformer and the ground, and the 2-2′ port corresponds to the fault point and the ground.

In **Figure 2**, $X1a$, $X1b$, and$X2$ are the *M*1, *M*2, and *N* side winding leakage reactance, ZL is the arc suppression coil impedance value, Zs is the power supply impedance, and Xc is the line to the ground positive sequence or negative sequence reactance. The power supply impedance is far less than the line to the ground positive and negative sequence reactance. In addition, $Xc(0)$ is the line to the ground zero sequence reactance. $\dot{U}1(1)$, $\dot{U}1(2)$, and $\dot{U}1(0)$ are the voltages of the 1-1′ terminal, and $\dot{I}1(1)$, $\dot{I}1(2)$, and $\dot{I}1(0)$ are the currents of the 1-1′ terminal.

For the positive order circuit in **Figure 2A**, it can be described as

$$\begin{bmatrix} \dot{U}_{1(1)} \\ \dot{U}_{2(1)} \end{bmatrix} = \begin{bmatrix} Z_{11} & Z_{12} \\ Z_{21} & Z_{22} \end{bmatrix} \begin{bmatrix} \dot{I}_{1(1)} \\ \dot{I}_{2(1)} \end{bmatrix} + \begin{bmatrix} \dot{U}_{Z1} \\ \dot{U}_{Z2} \end{bmatrix}, \tag{1}$$

For the negative order circuit in **Figure 2B**, it can be described as

$$\begin{bmatrix} \dot{U}_{1(2)} \\ \dot{U}_{2(2)} \end{bmatrix} = \begin{bmatrix} Z_{11} & Z_{12} \\ Z_{21} & Z_{22} \end{bmatrix} \begin{bmatrix} \dot{I}_{1(2)} \\ \dot{I}_{2(2)} \end{bmatrix}, \tag{2}$$

For the zero-order circuit in **Figure 2C**, it can be described as

$$\begin{bmatrix} \dot{U}_{1(0)} \\ \dot{U}_{2(0)} \end{bmatrix} = \begin{bmatrix} Z_{11(0)} & Z_{12(0)} \\ Z_{21(0)} & Z_{22(0)} \end{bmatrix} \begin{bmatrix} \dot{I}_{1(0)} \\ \dot{I}_{2(0)} \end{bmatrix}, \tag{3}$$

The relevant parameters are as follows:

$$Z_{11} = X_{1a} + X_{1b} + \frac{jX_C Z_S}{Z_S + jX_C} \approx X_{1a} + X_{1b} + Z_S, \tag{4}$$

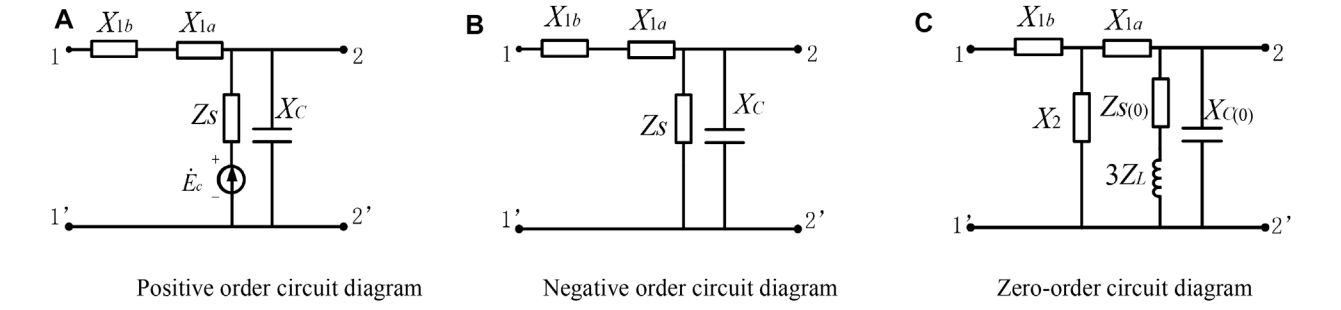

FIGURE 2 | Positive, negative, and zero-sequence equivalent circuit diagrams. **(A)** Positive-order circuit diagram **(B)** Negative-order circuit diagram **(C)** Zero-order circuit diagram

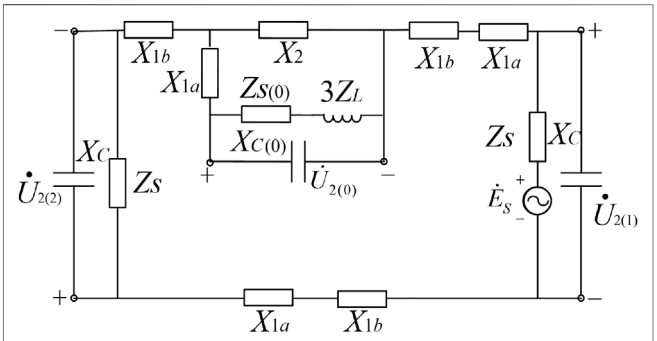

FIGURE 3 | Equivalent sequence diagram of the system.

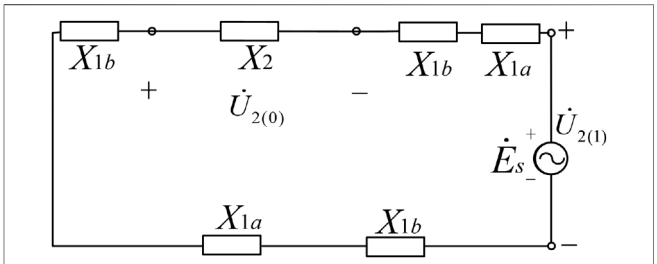

FIGURE 4 | Simplified equivalent sequence diagram.

$$Z_{12} = Z_{21} = Z_{22} = \frac{jX_C Z_S}{Z_S + jX_C} \approx Z_S, \tag{5}$$

$$\dot{U}_{Z1} = \dot{U}_{Z2} \approx \dot{E}_c. \tag{6}$$

As $Z_{S(0)}$ is far less than $3Z_L$ in **Figure 2C**, $Z_{S(0)}$ can be ignored, and then, the relevant parameters in **Eq. 3** are

$$Z_{11(0)} = X_{1b} + \frac{X_2\left[X_{1a}(3Z_L + jX_{C(0)}) + 3Z_L jX_{C(0)}\right]}{(X_2 + X_{1a})(3Z_L + jX_{C(0)}) + 3Z_L jX_{C(0)}}, \tag{7}$$

$$Z_{12(0)} = Z_{21(0)} = \frac{Z_L X_2 X_{C(0)}}{X_{C(0)}(X_2 + X_{1a}) - j3Z_L(X_2 + jX_{C(0)} + X_{1a})}, \tag{8}$$

$$Z_{22(0)} = \frac{X_2\left[X_{1a}(3Z_L + jX_{C(0)}) + 3Z_L jX_{C(0)}\right]}{(X_2 + X_{1a})(3Z_L + jX_{C(0)}) + 3Z_L jX_{C(0)}}, \tag{9}$$

When the transformer tap is grounded, there are

$$\dot{U}_{1(1)} + \dot{U}_{1(2)} + \dot{U}_{1(0)} = 0, \tag{10}$$

$$\dot{I}_{1(1)} = \dot{I}_{1(2)} = \dot{I}_{1(0)}, \tag{11}$$

According to the positive, negative and zero-sequence equivalent circuit diagrams in **Figure 2** and **Eqs 10, 11**, the equivalent sequence network of the system is obtained, as shown in **Figure 3**.

In the positive and negative sequence circuit diagrams, the capacitive reactance Xc is greatly large and the internal resistance Zs is greatly small, which can be approximately ignored; when there is no arc suppression coil in the zero-sequence circuit diagram, the capacitance reactance of zero-sequence capacitance to ground is greatly large, which can be approximately ignored. If there is an arc suppression coil, since the detuning of the system generally does not exceed ±15%, the admittance value after parallel connection is relatively small, and the current value flowing over $X1a$ is greatly small. At this time, the branch in series with $X1a$ after parallel connection of the arc suppression coil and ground capacitance can be regarded as an open circuit, and $\dot{U}2(0)$ can be approximately regarded as the voltage at both ends of $X2$. Therefore, the equivalent sequence network diagram of the system in **Figure 3** can be simplified to obtain the simplified equivalent sequence network diagram of the system, as shown in **Figure 4**.

Zero-Sequence Voltage Phase After Closed Tap Grounding Branch

It can be seen from **Figure 4** that $\dot{U}2(1) = \dot{E}s$. It can be seen from **Eq. 2** that $\dot{U}2(2) = Z21\dot{I}1(2) + Z22\dot{I}2(2)$. It can be seen from **Eq. 5** that $Z21 = Z22 = Zs$, and internal resistance Zs is extremely small, so $\dot{U}2(2) \approx 0$, that is, the negative sequence voltage at the fault point is very small, so the fault phase voltage is the sum of the positive sequence voltage and zero sequence voltage, namely, $\dot{U}f = \dot{E}s + \dot{U}2(0) = \dot{E}s + X2\dot{I}1(0)$. Assuming that the phase of $\dot{E}s$ is θ since all components in the series circuit in **Figure 4** are

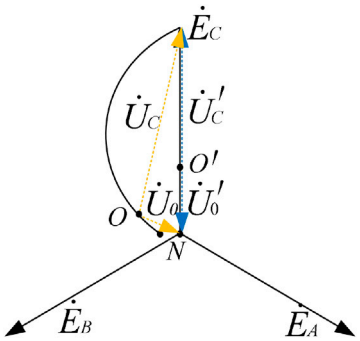

FIGURE 5 | Diagram of the system voltage variation before and after closure of the tap earthing branch.

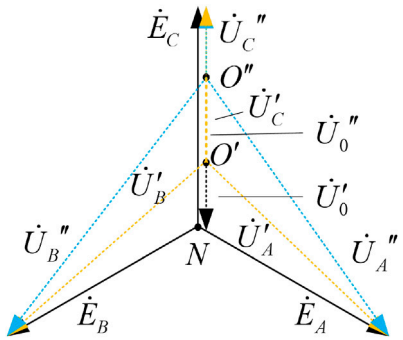

FIGURE 6 | Diagram of the system voltage change with the change of the grounding tap of the transformer.

TABLE 1 | Maximum reignition voltage under different detuning degrees of the distribution network.

Take-off of concordance	Maximum reignition voltage/kV	The peak time/s
−0.1	1.74	0.25
−0.05	1.47	0.43
0	0.86	0.01
0.05	1.52	0.36
0.1	1.83	0.23

inductive, the voltage phase of the two ends of $\dot{U}2(0)$ is $(\theta+180^{\circ})$, that is, the zero-sequence voltage phase at the fault point after closing the tapped grounding switch will be approximately opposite to the positive-sequence voltage phase.

Therefore, it is known that after closing the primary side of the new type of the grounding transformer–tapped grounding branch from the perspective of sequence component analysis, the zero potential point offsets making the phase of the zero sequence voltage and phase voltage opposite and reducing the fault phase voltage so as to achieve the arc suppression. The voltage phasors of the system before and after the closing of the tap grounding branch after the single-phase grounding fault occurs are shown in **Figure 5**.

In **Figure 5**, N is the neutral point of the system, O is the zero potential point when the single-phase grounding fault occurs, $\dot{U}0$ is the zero sequence voltage, that is, the neutral point voltage of the system, and the fault phase voltage is $\dot{U}C$. After closing the tap grounding branch to adjust the fault voltage, zero potential will shift to point O', the neutral point voltage of the system is $\dot{U}'0$, and the fault phase voltage will be reduced to $\dot{U}'c$. Furthermore, the phase of $\dot{U}'0$ is opposite to that of $\dot{U}'c$.

Zero-Sequence Voltage Amplitude Under Different Gears

It can be seen from **Figure 4** that the zero-sequence impedance $Z0 = X2$ of the system. According to the transformer short-circuit grounding formula (Jiale, 2010), the expression of $Z0$ is:

$$Z_0 = \omega(1-x)^2 N_1^2 \left(\frac{S}{\rho L} - \lambda 0\right), \tag{12}$$

where x is the ratio of turns of the$M2$ side winding to turns of the primary side winding, and its value range is [0,1]. ω is the angular frequency, $\lambda 0$ is the magnetic conductivity of the iron core, S is the cross-sectional area of magnetoresistance, ρ is the magnetic leakage magnetoresistance, and L is the length of the magnetic circuit. As the gear is adjusted, it changes x. Therefore, taking x as the independent variable and deriving $Z0$, we get

$$Z_0' = 2\omega N_1^2 (x-1)\left(\frac{S}{\rho L} - \lambda 0\right), \tag{13}$$

It can be seen from **Eq. 13** that with the increase of x in the value range, the zero-sequence impedance decreases monotonically. With the continuous increase of gear, the system zero-sequence impedance decreases, resulting in the increase of the loop zero-sequence current and system zero-sequence voltage $\dot{U}2(0) = 3\dot{I}0Z1$. Adjust the gear size of the tap grounding branch, and the change of relevant voltage phasors of the system are shown in **Figure 6**.

It can be seen from **Figure 6** that when a fault occurs, the tap grounding branches of different gears are closed, and the zero potential point shifts and moves in the direction of the phase voltage. Therefore, the zero-sequence voltage changes after closing the tap grounding branches of different gears. So with the increase of gears, the zero potential point gradually increases, and the fault phase voltage decreases.

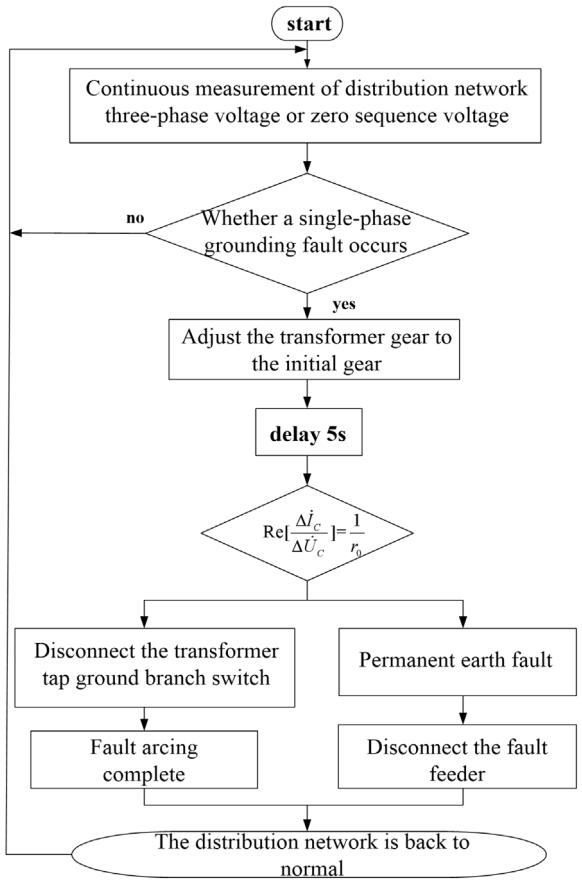

FIGURE 7 | Voltage arc suppression flow chart with flexible voltage control.

INITIAL GEAR SELECTION AND THE ARC SUPPRESSION CRITERION

In order to quickly extinguish the arc in case of a fault, it is necessary to set an appropriate initial gear. Under the initial gear, the critical value of the maximum reburning voltage should be greater than or equal to the fault phase voltage, and the maximum reburning voltage $Ucrm$is made, that is, $Ucrm \geq Uf$. According to the practical application of the project, in the 10kV distribution network, the maximum reignition voltage is different under different detuning conditions. Therefore, after selecting the initial gear, the arc extinguishing effect will be significantly affected under different detuning degrees. The detuning and maximum reburning voltage are shown in **Table.1**.

It can be seen from **Table 1** that the maximum reignition voltage varies with different detuning degrees. Therefore, in order to determine the initial tap position, $Ucrm = Uf = 0.3\dot{E}x$is considered, and $\dot{E}x$ is taken as the x-phase fault phase voltage. When the initial tap grounding switch is closed, the zero-sequence voltage $\dot{U}2(0)$ can be obtained from the equivalent sequence network diagram in **Figure 4**:

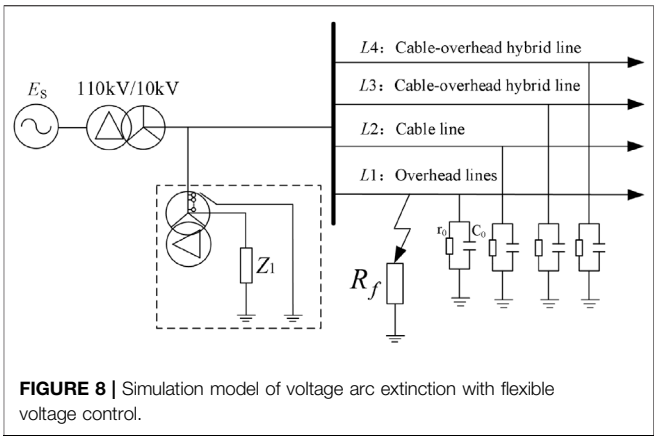

FIGURE 8 | Simulation model of voltage arc extinction with flexible voltage control.

$$\dot{U}_f = \dot{U}crm = \dot{E}c - \dot{U}_{2(0)}, \tag{14}$$

Make the initial gear n; n shall meet

$$\frac{\dot{E}c - \dot{U}crm}{\dot{E}c} = \frac{n \times \frac{N}{m}}{N}, \tag{15}$$

Furthermore, n obtained from **Eqs 14, 15**

$$n = 0.7m, \tag{16}$$

This is because the maximum reburning voltage is different under different detuning degrees. For example, when the detuning degree is 0.1, it can be seen from **Table 1** that the maximum reburning voltage is about 0.32 times the fault phase voltage. At this time, after the initial gear is determined according to **Eq. 16** for arc suppression, there is still weak arc light leading to reignition, so the initial gear obtained according to **Eq. 16** cannot meet all the actual operating conditions on site. Therefore, in order to ensure that arc suppression can be effectively carried out under different operating conditions and the gear adjustment is step-by-step adjustment, round it up by one time along the absolute value through the ceiling function. At this time, the initial gear n is

$$CEILING(\frac{\dot{E}x - \dot{U}crm}{\dot{E}x} \times m, 1), \tag{17}$$

After determining the initial gear, in order to improve the safe and stable operation ability, one can be added to the initial gear adjustment to ensure the complete arc suppression. Therefore, it is necessary to determine whether the arc is completely eliminated after adjusting the initial gear, that is, whether the fault phase voltage is zero. If it is not zero, one should be added to the actual initial gear to ensure the complete arc suppression. According to the ratio of the fault phase voltage and the fault phase current before and after the tap connection, the judgment method can determine whether the arc suppression is completed.

Since the line voltage of the system remains unchanged before and after the fault, ignoring the loss on the line, the current $\dot{I}C$ of the fault phase C before the initial gear is put into operation is

TABLE 2 | Circuit parameters.

The line type	The length of the line/km	The damping ratio/*d* (%)	Ground capacitance/μF	Resistance to ground/kΩ
Overhead line	16	4.00	0.063	1,053
Cable line	16	3.00	0.910	121
Cable-overhead hybrid line	27	3.10	0.875	130
Cable-overhead hybrid line	23	3.21	0.720	163

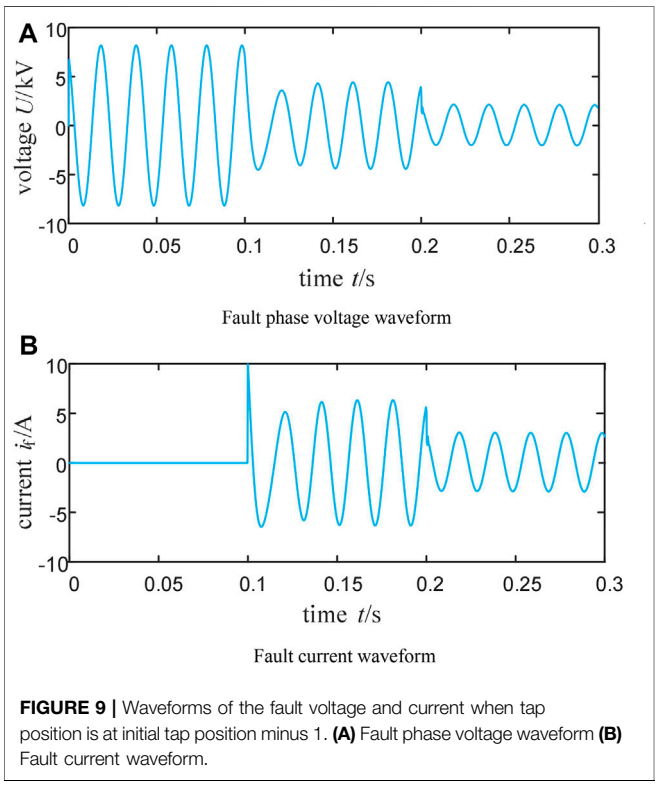

FIGURE 9 | Waveforms of the fault voltage and current when tap position is at initial tap position minus 1. **(A)** Fault phase voltage waveform **(B)** Fault current waveform.

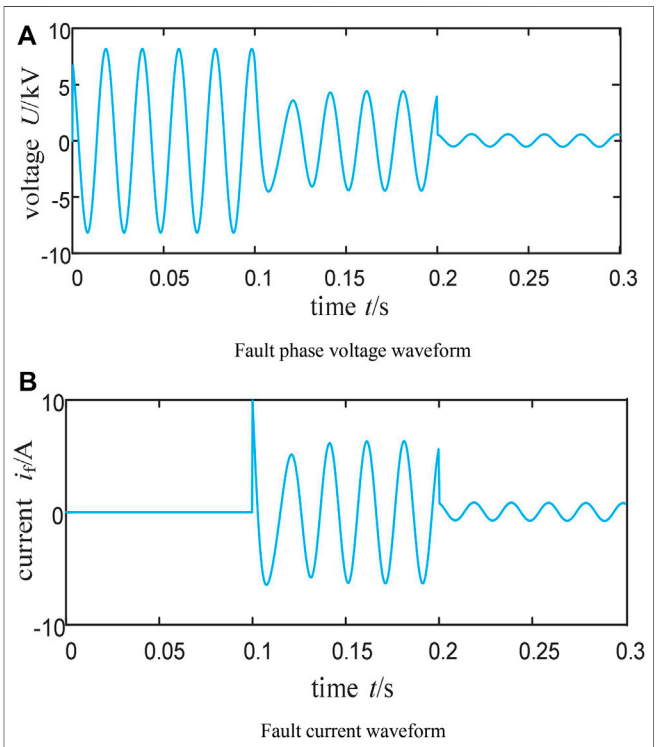

FIGURE 10 | Waveforms of the fault voltage and current when the tap is at the initial tap. **(A)** Fault phase voltage waveform **(B)** Fault current waveform.

$$\dot{I}c = (\dot{E}c - \dot{U}_0)\left(\frac{1}{R_f} + \frac{1}{r_0} + j\omega C_0\right) + \dot{I}_{TC}, \tag{18}$$

$\dot{I}TC$ is the current of phase C of the grounding transformer. After the initial gear is put into operation, the current $\dot{I}'C$ of the fault phase C is

$$\dot{I}'c = (\dot{E}c - \dot{U}'0)\left(\frac{1}{R_f} + \frac{1}{r_0} + j\omega C_0\right) + \dot{I}Tc, \tag{19}$$

$\dot{U}'0$ is the zero-sequence voltage after the initial gear inputs, and subtract from **Eqs 18, 19** to obtain

$$\Delta\dot{I}C = \Delta\dot{U}_0\left(\frac{1}{R_f} + \frac{1}{r_0} + j\omega C_0\right), \tag{20}$$

where $\Delta\dot{I}C = \dot{I}'C - \dot{I}C$ and $\Delta\dot{U}0 = \dot{U}'0 - \dot{U}0$, and **Eq. 21** can be changed as follows:

$$\mathrm{Re}\left[\frac{\Delta\dot{I}_C}{\Delta\dot{U}_0}\right] = \frac{1}{R_f} + \frac{1}{r_0}. \tag{21}$$

It can be seen from **Eq. 21** that the real part of the fault phase current voltage ratio before and after the initial gear inputs is $\frac{1}{r0}$, and then, the arc suppression is completed. Therefore, when a fault occurs, in order to quickly carry out the arc suppression, turn on the initial gear switch. According to the above analysis, the fault phase voltage is equal to the sum of the positive sequence voltage and zero sequence voltage; the positive sequence voltage is opposite to the zero sequence voltage, and the fault phase voltage is lower than the reburning voltage. The completion of the arc suppression is determined by judging the real value of the ratio of the fault phase current and voltage before and after the initial gear inputs. The new voltage arc suppression method proposed in this study only needs to set tap on the high-voltage side winding of the

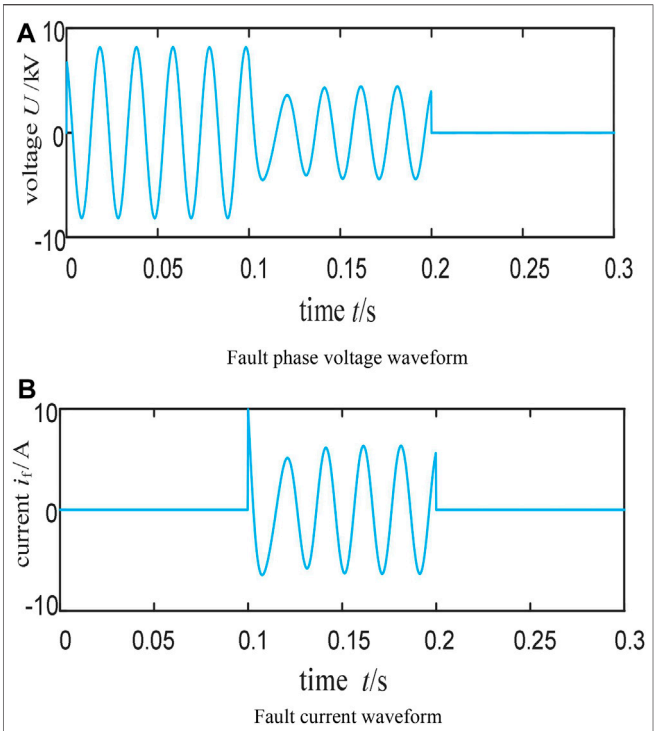

FIGURE 11 | Waveforms of the fault voltage and current when tap position is at initial tap position plus 1. **(A)** Fault phase voltage waveform **(B)** Fault current waveform.

grounding transformer at the head end of the distribution network to realize flexible voltage control, make the fault phase voltage change with the change of the zero-sequence voltage, reduce the fault phase voltage, realize the arc suppression, and solve the single-phase grounding fault with high reliability, fast response, low investment cost, and easy implementation.

REALIZATION PROCESS OF THE VOLTAGE ARC SUPPRESSION

The implementation method of the single-phase grounding fault voltage arc suppression in the distribution network is shown in **Figure 7**. The three-phase voltage or the zero sequence voltage of the distribution network is measured in real time through the measuring elements. When the measurement results show that the 3% phase voltage is less than the change of the zero-sequence voltage or 15% phase voltage is less than the zero-sequence voltage, it is considered that a single-phase grounding fault has occurred in the distribution network. Adjust the gear of the grounding transformer to the initial gear. Then, after a delay of 5 s, judge whether the real part value of the fault phase current voltage ratio before and after the initial gear inputs is equal to $\frac{1}{r0}$. If it is not equal, it is judged as a permanent grounding fault and disconnect the fault feeder. And, if it is equal, disconnect the grounding branch switch of the transformer gear so that the fault arc suppression completes and the normal operation of the distribution network restores.

In the early design scheme of the distribution network, the requirements for transformer capacity are high, resulting in high energy consumption and high actual power cost. At present, the distribution network has innovated the transformer. For the 10 kV distribution network, a section of bus is generally equipped with 12 lines. Using typical distribution network parameters, the system capacitance current is about 100 A, and the transformer capacity *Sb* is

$$Sb \approx UIc = \frac{10.5}{\sqrt{3}} \times 100 = 606.2\text{kVA}, \tag{22}$$

Therefore, using a voltage source with small capacity to make the transformer capacity slightly larger than the load can not only reduce loss and improve power efficiency but also realize the flexible control of the zero-sequence voltage.

SIMULATION ANALYSIS

In order to verify the effectiveness of the proposed new voltage arc suppression method based on the flexible voltage control of the grounding transformer, a single-phase grounding fault simulation model of the 10 kV distribution network is built in PSCAD/EMTDC software, as shown in **Figure 8**.

Taps at different positions are set at the primary winding side of the transformer. Build various line hybrid models in the PSCAD/EMTDC simulation environment, including the cable line, overhead line, and cable and overhead line hybrid. Their parameters are shown in **Table 2**.

In the 10 kV distribution network system, the maximum reburning voltage is $Ucrm \approx 0.3 \times Uc \approx 1.75$kV. At 0.1s, a single-phase grounding fault occurs in phase C, and the grounding resistance is 700Ω. Adjust the gear at 0.2s, and

TABLE 3 | Comparison of the voltage and current of the fault phase before and after the adjustment of the gear position in different gear positions.

Gear	State of the gear	Maximum fault phase voltage/kV	Maximum fault current/A
The initial gear minus 1	Before shifting gear	5.372	6.057
	After shifting gear	2.146	3.066
The initial gear	Before shifting gear	5.119	6.474
	After shifting gear	0.610	0.871
The initial gear plus 1	Before shifting gear	5.020	6.535
	After shifting gear	0	0

simulation analysis is carried out at initial gear minus 1, initial gear and initial gear plus 1, respectively. The waveform diagrams of the fault phase voltage and fault current are obtained, as shown in **Figures 9**, **10**, **11**.

From **Figures 9**, **10**,**11**, it can be seen that the single-phase grounding fault occurs in 0.1 s, and the system is asymmetric, resulting in the zero-sequence voltage and fault current. In 0.2 s, adjust the gear. According to the changes of the fault phase voltage and fault current when adjusting different gears, it can be seen that with the adjustment of the gear, the fault phase voltage and fault current decrease accordingly, and when the gear is adjusted to the initial gear, the fault phase voltage is lower than the maximum reignition voltage, which can effectively prevent arc reignition. Record the fault phase voltage and fault current before and after the switch is closed in different gears in **Table 3**.

It can be seen from **Table 3** that the ratio of the fault phase current to the zero-sequence voltage increases gradually before and after gear adjustment under different gears. When it is below the initial gear, the ratio of the fault phase current to the zero-sequence voltage is about 0.93, and when it is at the initial gear plus 1, the ratio of the fault phase current to the zero-sequence voltage is about 1.3. Therefore, with the gradual increase of the gear, the fault phase voltage becomes smaller and smaller, and the fault arc suppression effect is gradually enhanced. When adjusted to the appropriate gear, the fault phase voltage is less than the arc reburning voltage to prevent fault reburning, fundamentally destroy the reburning conditions, and complete the voltage arc suppression.

CONCLUSION

Aiming at the problem of the single-phase grounding fault, a new method of voltage arc suppression in the distribution network based on the flexible regulation of neutral point potential of the new grounding transformer is proposed in this study. Taps at different positions are set on the winding of the grounding transformer. By turning on and off taps at different gears, the fault phase voltage is flexibly adjusted. A single-phase grounding fault model of the 10kV distribution network is built in the PSCAD/EMTDC simulation environment. In case of the single-phase grounding fault, turn on the tap to check the change of the fault phase voltage, and then, effectively verify the arc suppression principle of the flexible control voltage proposed in this study. Finally, draw conclusions as follows:

1) From the perspective of a sequence component, a new method of voltage arc suppression in the distribution network based on the flexible regulation of neutral point potential of the new grounding transformer is proposed. By adjusting the initial position of the tap, achieve the arc suppression without measuring the ground parameters. Compared with the current distribution network arc suppression cabinet technology and active arc suppression equipment based on power electronics, zero-sequence voltage regulation is more flexible, control and hardware implementation are more simple, and it has stronger economy and applicability in engineering.
2) Through the selection of the initial tap position by the ceiling function, the zero potential point can be offset after the grounding of the tapped position so that the phase of the power supply voltage of the ground phase is opposite to that of the neutral point voltage, which is beneficial to the arc suppression of the fault. Without directly reducing the fault phase voltage to zero, the non-fault phase voltage does not need to rise to the line voltage, which reduces the risk of the non-fault phase voltage insulation breakdown.
3) Selecting the appropriate initial tap position can reduce the fault phase voltage to below the arc reignition voltage in a short time so as to effectively prevent the arc reignition to realize the rapid arc suppression of the single-phase grounding fault voltage in the distribution network. The arc suppression equipment is of great significance in preventing wildfires, protecting personal safety, and so on. The fault treatment method has theoretical and engineering reference values in the field of grounding fault treatment of the distribution network.

DATA AVAILABILITY STATEMENT

The original contributions presented in the study are included in the article/Supplementary Material, further inquiries can be directed to the corresponding author.

AUTHOR CONTRIBUTIONS

All authors listed have made a substantial, direct, and intellectual contribution to the work and approved it for publication.

FUNDING

This study was funded by Guangxi Power Grid Technology Project (ZBKJXM20190061).

REFERENCES

Cai, X. S. (2004). New Resonance Earth System with Magnetic Bias and its protection. *Proc. CSEE* 4 (6), 44–49. doi:10.13334/j.0258-8013.pcsee.2004.06.009 (in Chinese).

Chen, Y. S. (2019). Effects of Load on Arc-Suppression Method Based on Grounded-Fault Transfer Device. *Electr. Meas. Instrumentation* 56 (23), 24–30. doi:10.19753/j.issn1001-1390.2019.023.004

Chen, W. D. (2020). Research on Active Arc Elimination Method for Grounding Fault of Distribution Network Based on Current Injection. dissertation/master's thesis. China University of Mining and Technology.

Choi, Y. J, Choi, M. S, and Lee, S (2010). The Advanced Protection Coordination Scheme using Phase Angle of Zero-Sequence Current in Ungrounded System. *Trans. Korean Inst. Electr. Eng.* 59 (1), 19-25.

Elombo, A. I., Holtzhausen, J. P., Vermeulen, H. J., Pieterse, P. J., and Vosloo, W. L. (2013). Comparative Evaluation of the Leakage Current and Aging

Performance of Htv Sr Insulators of Different Creepage Lengths when Energized by Ac, Dc+ or Dc- in a Severe marine Environment. *IEEE Trans. Dielect. Electr. Insul.* 20 (2), 421–428. doi:10.1109/tdei.2013.6508743

Fan, S. S. (2019). Arc-Suppression Method Based on Transferring the Residual Current of Single Phase Grounding Fault in Distribution Network. *Electr. Meas. Instrumentation* 56 (11), 20–25. doi:10.19753/j.issn1001-1390.2019.011.004

Fang, W. L. (2017). *Transient Analysis of Power System*. China Electric Power Press.

Grifflel, D. J. (1997). A New deal for Safety and Quality on MV Networks. *IEEE Trans. Power Deliv.* 12 (4), 1428–1433.

Guo, M. S. (2017). Flexible Arc-Suppression Potimization Method for Distribution Network Adaptable to Variation of Line Parameters and Load. *Automation Electric Power Syst.* 41 (8), 138–145. doi:10.7500/AEPS20160621001

Hänninen, S., and Lehtonen, M. (1998). Characteristics of Earth Faults in Electrical Distribution Networks with High Impedance Earthing. *Electric Power Syst. Res.* 44 (3), 155–161. doi:10.1016/s0378-7796(97)01193-0

Huang, J. S. (2020). Study on Compression Arcing and Lightning Protection of Distribution Network. *Insulators and Surge Arresters* (01), 111–117. doi:10.16188/j.isa.1003-8337.2020.01.019

Jiale, S. (2010). Study of Zero-Sequence Differential protection for Transformer with Yn/Δ Connection. *Power Syst. Prot. Control.* 38 (16), 54–61. doi:10.3969/j.issn.1674-3415.2010.16.011 (in Chinese)

Jin, W. S. (2010). A Novel IGBT Based Arc-Suppression Coil Automatic Tuning System. *J. Electric Power Sci. Tech.* 25 (2), 56–60. doi:10.3969/j.issn.1673-9140.2010.02.011 (in Chinese).

Li, Z. S. (2019a). Multifunctional Safety Earthing Treatment Device for Distribution Network Based on Intelligent Earthing Method of Fault Phase. *Insulators and Surge Arresters* (01), 116–119. doi:10.16188/j.isa.1003-8337.2019.01.019

Li, Z. S. (2019b). Development and Application of a Complete Set of Neutral Grounding System for Distribution Network Based on the Judgment of Fault. *Nature* (01), 180–183. doi:10.16188/j.isa.1003-8337.2019.01.030

Liu, B. S. (2016). New Flexible Control System of Full Compensation Single-Phase Ground Fault Fundamental Current. *Proc. CSEE* 36 (9), 2322–2330. doi:10.13334/j.0258-8013.pcsee.2016.09.002

National Development Reform Commission (2007). *PRC.DL/T1057-2007.The Technical Condition of Complete Set of Automatic Tracking Compensation Arc Suppression Coil*. China Electric Power Press.

Pang, Q. S. (2006). Design of Air gap Inductance Regulation Arc-Suppression Coil Control System. *High Voltage Eng.* 32 (4), 5–10. doi:10.13336/j.1003-6520.hve.2006.04.004 (in Chinese)

Peng, S. (2018). Active Arc-Suppression Method of Grounding Fault for Distribution Network Based on Secondary Injection. *Power Syst. Prot. Control.* 46 (20), 142–149. doi:10.7667/PSPC171503

Wang, Y. S. (2015). Earth Fault Neutralizer Full Compensation Technology and Application. *Distribution & Utilization* 06, 24–29. doi:10.19421/j.cnki.1006-6357.2015.06.004

Wang, P. S. (2018). Steady-state Modeling and Optimal Design Method of Magnetic Controllable Petersen Coil with Discontinuous Core Structure. *Proc. CSEE* 38 (18), 5606–5614. doi:10.13334/j.0258-8013.pcsee.170821

Wang, P. S. (2020). Additional Resistance Based Fault Phase Identification Method Suitable for Active Interference Arc Suppression Device. *Electric Power Eng. Tech.* 39 (04), 180–186.doi:10.12158/j.2096-3203.2020.04.025

Wu, B. S. (2018). A New Type of Arc-Suppression Coil Automatic Tracking Compensation Device. *Power Syst. Prot. contro* 46 (20), 142–149.doi:10.7667/PSPC171411

Xiang, G. S. (2020). Phase Selection Method for Grounding Faults of Asymmetric Distribution Network Based on Phase Difference. *Electr. Meas. Instrumentation* 57 (22), 70–76. doi:10.19753/j.issn1001-1390.2020.22.010

Xiao, Z. S. (2021). Single-Phase Grounding Arc Based on Parameter Fitting. *Insulators and Surge Arresters* (02), 190–197. doi:10.16188/j.isa.1003-8337.2021.02.029

Xie, J. S. (2015). An Active Compensation and Control Method of Asymmetrical Voltage in Non-Solidly Grounded System. *Automation Electric Power Syst.* 39 (5), 115–121. doi:10.7500/AEPS20140303006

Xu, M. S. (2018). Model Recognition Based Single-Phase Earthed Faulty Line Selection Method of Petersen Coil Grounded System. *Power Syst. Prot. Control.* 46 (2), 73–78. doi:10.7667/PSPC162117

Xue, Y. S. (2015a). Transient Equivalent Circuit and Transient Analysis of Single-Phase Earth Fault in Arc Suppression Coil Grounded System. *Proc. CSEE* 35 (22), 5703–5714. doi:10.13334/j.0258-8013.pcsee.2015.22.004

Xue, Y. S. (2015b). Selection Problems of Neutral Grounding Mode in Active Distribution Networks. *Automation Electric Power Syst.* 39 (13), 129–136. doi:10.7500/AEPS20140717003

Yang, T. S. (2021). Fast Adjustable Arc Suppression Coil Based on Power Electronic Switch. *Electr. Meas. Instrumentation* 58 (5), 62–69. doi:10.19753/j.issn1001-1390.2021.05.009

Yao, H. L. (2009). *Resonant Grounding of Power System*. Beijing: China Electric Power Press.

You, J. D. (2016). Research of Flexible Arc-Suppression and Fault Line Selection Methods of Earth-Fault in Distribution Systems Based on Cascaded H-Bridge Converter. dissertation/master's thesis. Fuzhou university.

Zeng, X. S. (2000). New Methods for Control and protection Relay in a Compensated Medium Voltage Distribution Network Based on Injecting Various Frequency Current. *Proc. CSEE* 20 (1), 30–33. doi:10.13334/j.0258-8013.pcsee.2000.01.008

Ze-Yin Zheng, S. (2020). Flexible Arc-Suppression Method Based on Improved Distributed Commutations Modulation for Distribution Networks. *Int. J. Electr. Power Energ. Syst.* 116, 105580. ISSN 0142-0615. doi:10.1016/j.ijepes.2019.105580

Zhang, H. S. (2019). Discussion on Earthing Mode of Neutral Point through Arc Suppression Coil in Distribution Network. *Insulators and Surge Arresters* (03), 87–91. doi:10.16188/j.isa.1003-8337.2019.03.015

Zheng, Z. Y. S.(2021).A novel method of insulation parameters measurement based on hybrid flexible arc suppression device in distribution networks. *Int. J. Electr. Power Energy Syst.* 130, 106982. doi:10.1016/j.ijepes.2021.106982

Conflict of Interest: ZY was employed by the Qinzhou Power Supply Bureau of Guangxi Power Grid Co. Ltd. ZHY was employed by the Chongzuo Power Supply Bureau of Guangxi Power Grid Co. Ltd.

The remaining authors declare that the research was conducted in the absence of any commercial or financial relationships that could be construed as a potential conflict of interest.

Publisher's Note: All claims expressed in this article are solely those of the authors and do not necessarily represent those of their affiliated organizations, or those of the publisher, the editors, and the reviewers. Any product that may be evaluated in this article, or claim that may be made by its manufacturer, is not guaranteed or endorsed by the publisher.

frontiers in Energy Research

ORIGINAL RESEARCH
published: 04 February 2022
doi: 10.3389/fenrg.2022.829934

A Spatial Assessment of Wildfire Risk for Transmission-Line Corridor Based on a Weighted Naïve Bayes Model

Kunxuan Xiang[1], You Zhou[1], Enze Zhou[2], Junhan Lu[1], Hui Liu[1] and Yu Huang[1]*

[1]School of Electrical and Information Engineering, Changsha University of Science and Technology, Changsha, China, [2]Electric Power Research Institute, Guangdong Power Grid, Guangzhou, China

In order to improve the wildfire prevention capacity of transmission lines, a wildfire risk assessment method for transmission-line corridors based on Weighted Naïve Bayes (WNB) is proposed in this paper. Firstly, the importance of 14 collected types of wildfire-related factors is analyzed based on the information gain ratio. Then, the optimal factors set and the most accurate sampling table are constructed by deleting the factors in the lowest order of importance one by one. Finally, the performance of the WNB model is compared to that of NB and BNW models according to the ROC curve and visualization. A total of 76.36% of fire events in 2020 fell in high-risk and very-high-risk regions, indicating the acceptable accuracy of the proposed assessment method of wildfire risk.

Keywords: wildfire, risk assessment, weighted naïve bayes, transmission-line corridors, risk visualization

OPEN ACCESS

Edited by:
Yan Xu,
Nanyang Technological University, Singapore

Reviewed by:
Wu Lu,
Shanghai University of Electric Power, China
Lujia Wang,
China University of Mining and Technology, China

****Correspondence:***
You Zhou
zhouyou243@csust.edu.cn

Specialty section:
This article was submitted to Smart Grids, a section of the journal Frontiers in Energy Research

Received: *06 December 2021*
Accepted: *03 January 2022*
Published: *04 February 2022*

Citation:
Xiang K, Zhou Y, Zhou E, Lu J, Liu H and Huang Y (2022) A Spatial Assessment of Wildfire Risk for Transmission-Line Corridor Based on a Weighted Naïve Bayes Model. Front. Energy Res. 10:829934. doi: 10.3389/fenrg.2022.829934

INTRODUCTION

The continuously growing economy has brought a higher demand for electricity in China in recent years. Under the background of "power transmission from west to east", cross-regional high-voltage transmission lines achieve the demand for long-distance power transmission. However, transmission-line corridors have to extend to and/or through areas suffering from high risks of wildfires (Song et al., 2012; Zeng, 2009). Once a wildfire is ignited near a transmission line, the burning of vegetation produces high temperatures and a high concentration of soot cover, which causes the dramatic decrease of air insulation under the transmission line. Undere these conditions, breakdowns are prone to happen between phase-to-phase or phase-to-ground and cause a tripping failure in the transmission line (Huang et al., 2015). Under the effect of wildfire combustion, the automatic reclosing is difficult to operate successfully, and may even cause multiple trips of transmission lines to induce a cascading grid failure (Hu et al., 2014; Wu et al., 2012).

To reduce the effect of wildfire on transmission lines, a series of wildfire prevention measures have been proposed and carried out domestically and abroad, such as quantitative forecasting, wide-area real-time satellite monitoring, fire-fighting measures, and so on (Lu et al., 2017; Ye et al., 2014). Compared to passive prevention methods, the assessment of the wildfires risk level can effectively improve the implementation efficiency of key wildfire preventions in high-risk areas and reduce the hazards and economic losses caused by wildfires (Wang and Fan, 2016; Liu et al., 2016).

The outbreak of wildfire generally stems from the combined effects of multiple wildfire-related factors. Scholars have formulated a series of quantitative risk assessments based on wildfire-related factors. Early forest fire risk assessments in China are only focused on meteorological factors. The temperature, humidity, precipitation, and wind speed are used to predict the weather and wildfire behaviors (Xu et al., 2016). However, besides the meteorological factors, other wildfire-related

factors, such as vegetation types, land-usage types, and fire-spot density also contribute significantly to assessing fire risk. State Grid Corporation of China has issued drawing guidelines for regional distribution maps of wildfires near overhead transmission lines. In this guideline, fire-spot density factors combined with vegetation burning hazard levels are used to assess and classify the risk level of wildfires in the transmission-line corridors (QGDW11643, 2016). However, these three wildfire-related factors are considered to have the same contribution to the risk assessment of wildfires. The Analytic Hierarchy Process is widely used to differentiate the importance of factors, but it relies too heavily on the subjective experiences gathered by questionnaires (Wang and Wang, 2016; Zhu et al., 2016). BP neural network can improve the accuracy of the model by continuously correcting the weight of factors. Liu et al. proposed a wildfire risk assessment method based on the BP neural network (Liu C. X. et al., 2017), but this method requires a huge amount of data as the basis for modeling. The Bayesian Network (BNW) can effectively integrate prior knowledge and objective evidence to solve the uncertainty of wildfire risk assessments based on mathematical statistics and graph theory. However, its complex network structure also easily leads to a reduction in computational efficiency (Dlamini, 2010). The use of Naïve Bayes (NB) based on conditional independence has the advantage of promoting computational efficiency, but neglecting the relationship between the wildfire-related factors could bring the curse of dimensionality and reduce the evaluation accuracy (Chen et al., 2021).

In this paper, a method is established based on Weighted Naïve Bayes (WNB) for assessing the wildfire risk of transmission-line corridors. First, 14 types of wildfire-related factors are screened out. The data of wildfire-related factors is collected and pre-processed in the four southern provinces of China (Yunnan, Guizhou, Guangxi, Guangdong) with grids of 1 km × 1 km. Then the weights of factors are obtained based on the entropy method to weaken the independence assumption of Naïve Bayes (NB). Combining with the most accurate sampling table (MAST), an optimal WNB model is constructed to calculate the wildfire risk probability of the grids in the research area. For visualization, the wildfire risks are graded based on the geometric interval classification. Finally, the performance of WNB is compared to that of BNW and NB models.

STUDY AREA AND DATA COLLECTION

Study Area

Four provinces in the south of China, Yunnan, Guizhou, Guangxi, and Guangdong, were selected as the study area. They all belong to subtropical and tropical monsoon climates, being generally rainy with high temperatures which, are suitable climatic conditions for the growth of multiple forests. Specifically, the Yunnan-Guizhou plateau has high vegetation coverage and extensive karst landforms with a sparse population. From January to December in 2020 a total of 825 fire-spots were monitored.

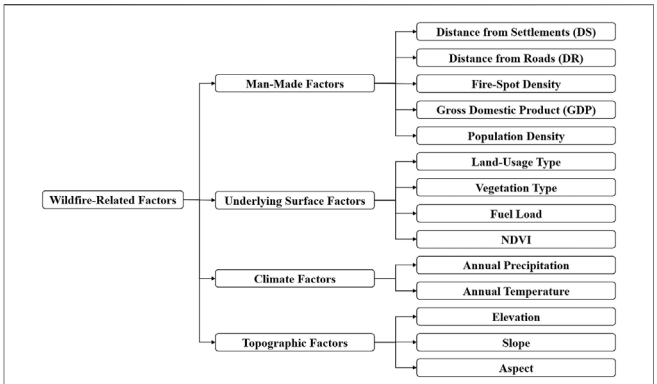

FIGURE 1 | Wildfire-related factors classification.

Once a fire is ignited, it is difficult to put it out quickly and is prone to spread.

Wildfire-Related Factors

Wildfire ignition requires three preconditions: a fire source, sufficient combustibles, and a suitable environment for fire. Fire sources are generally divided into artificial and natural fire sources. Statistics show that more than 90% of wildfires are caused by human activities, both intentionally and unintentionally. Therefore, this paper chooses five factors to represent the impact of human activities, including Distance from Settlements (DS), Distance from Roads (DR), fire-spot density, Gross Domestic Product (GDP), and population density. Combustibles means vegetation types and their coverage on the underlying surface. This paper selects four factors, land-usage type, vegetation type, fuel load, and Normalized Difference Vegetation Index (NDVI), to represent the influence of the underlying surface. Fire-environment mainly refers to weather conditions and topography. Annual precipitation and annual temperature are selected. And elevation, slope and aspect are used to represent the topographic factors. The chosen factors are listed in **Figure 1**.

Data Pre-Processing and Discrete Classification

The study area is first divided into 1 km × 1 km grids. The data of wildfire-related factors are provided by the Resource and Environmental Science and Data Center and the National Meteorological Center, which are extracted by using ArcGIS software. Among them, land-usage type and vegetation type are discrete variables, and the remaining factors are continuous variables. The sample set of fire spots is formed by the latitude and longitude of monitored fire-spots from 2010 to 2019, which are provided by the National Meteorological Center. The sample set of non-fire-spots is constructed by random sampling within the study area. To avoid the overlap of fire-spot and non-fire-spot samples, only grids at least 3 km away from fire-spot samples can be used as non-fire-spot samples.

During the factor collection procedure, the data of DS, DR, elevation, slope, and aspect are calculated by using Digital

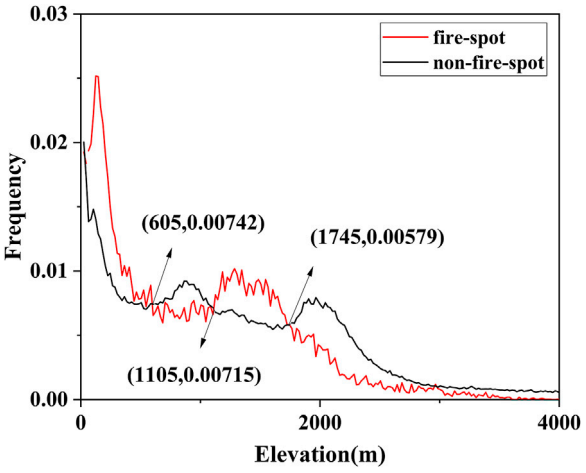

FIGURE 2 | The frequency distribution of elevation.

Elevation Model (DEM). And the data of fire-spot density needs further calculation (Chen et al., 2021), as follows.

step 1 The study area is meshed with 0.25 km × 0.25 km precision. The area of a single grid is calculated based on its longitude and latitude, as shown in formula **(1–3)**.

$$S = d_1 \times d_2 = 0.617\pi R_0 \delta^2 cos\alpha \tag{1}$$

$$d_1 = 111 \times \delta \tag{2}$$

$$d_2 = \frac{\pi R_0 \delta cos\alpha}{180} \tag{3}$$

where d_1 and d_2 are the distance spanned by the grid along the longitude and latitude in km. δ is the latitude span of the grid. R_0 = 6.371 km, which is the average radius of the Earth. α is the central latitude of the grid.

Step 2 The number of fire spots falling on each grid is counted as F_x. And the calculation formula of fire-spot density D_x is as formula **(4)**.

$$D_x = \frac{F_x}{100SY} \tag{4}$$

where the Y is the year of fire-spots.

Step 3 To meet the requirement of spatial resolution, the fire-spot density to a resolution of 1 km × 1 km by using the Kriging interpolation algorithm.

To accelerate the calculation efficiency of Bayes models, the data of all wildfire-related factors for both fire-spot and non-fire-spot samples are graded into four classes. The grading standard is to maximize the difference between the groups of samples. Taking the data of elevation as an example, the frequency distributions of wildfire-related factors are firstly calculated and compared for the two groups of samples, as shown in **Figure 2**. Secondly, all intersections of the distribution curves were found. These intersections can divide data distribution into several intervals, which means the change of probability for wildfire occurrence. For example, when the elevation is lower than 605 m, or between 1,105 m and 1,745 m, there is a greater probability of wildfire occurrence. Thirdly, for the factors of which the number of intersections is more than three, the adjacent intervals are then combined to reduce the final classes number into four.

For the wildfire-related factors with discrete data, the classes are simply formed by their natural property or their attribution to wildfire occurrence. The specific grading standards are summarized in **Supplementary Tables S1, S2, S3**.

IMPORTANCE OF WILDFIRE-RELATED FACTORS

Among the selected 14 wildfire-related factors, some of the factors may contribute little to the risk assessment and cause data redundancy, which increases the model complexity and decrease the accuracy. Thus, the factors are ranked by contribution importance based on the information gain ratio. By deleting the lowest factors of the rank singly, the optimal factor set is selected according to the accuracy results of the model.

Information Entropy and Information Gain Entropy

In 1948, the mathematician C. E. Shannon first proposed the concept of Information Entropy. The larger the information entropy is, the larger the uncertainty of the information source it represents. However, the size of information entropy often cannot reflect the importance of the information contained in the system.

In order to reflect the degree of characteristic information brought to the system, the Information Gain Entropy, which is the difference between the entropy of the set to be classified and the conditional entropy of a selected feature, was used.

Information Entropy

To calculate information entropy, the fire-spot samples, as well as the same amount of non-fire-spot samples are selected. And the information entropy of wildfires is calculated by formula **(5)**:

$$H(Y) = -(p(y_1)log_2(p(y_1)) + p(y_0)log_2(p(y_0))) \tag{5}$$

where $p(y_1)$ and $p(y_0)$ represent the occurrence and non-occurrence probability of wildfires, respectively. And there is $\sum p(y_i) = 1$.

Information Gain Entropy

In a wildfire event, the information gain entropy represents the reduced uncertainty degree of the factor information, which is recorded as $G(Y|X)$.

$$G(Y|X) = H(Y) - H(Y|X) \tag{6}$$

$$H(Y|X) = -\sum_{i=1}^{n} p(x_i)(p(x_{i1})log_2(p(x_{i1})) + p(x_{i0})log_2(p(x_{i0}))) \tag{7}$$

where $H(Y|X)$ is the conditional information entropy of the wildfire event Y with the given factor X. $p(x_i)$ represents the distribution probability under each factor. $p(x_{i1})$ and $p(x_{i0})$

TABLE 1 | Importance of wildfire-related factors.

Factors	Information gain entropy	Information gain ratio
Vegetation types	0.512	0.3447
Land-usage types	0.4893	0.2962
Historical fire-spot density	0.562	0.2654
Population density	0.5142	0.2454
Fuel load	0.5781	0.2203
GDP	0.6698	0.1864
Annual temperature	0.7076	0.1853
DS	0.7794	0.1699
Annual precipitation	0.8394	0.1693
Elevation	0.8073	0.1686
NDVI	0.735	0.1655
Slope	0.8446	0.1642
DR	0.8892	0.1483
Aspect	0.9319	0.1482

represent the proportion of fire-spot samples and non-fire-spot samples of the same level under each factor, respectively.

Information Gain Ratio

When the number of factor samples data is large, the information gain entropy is also larger. In order to eliminate the influence of the number of samples, the information gain ratio is proposed (Xiong et al., 2014). It avoids the overfitting of factor data by offsetting the complexity of factor variables.

$$\boldsymbol{G_R(Y|X)} = \frac{\boldsymbol{G(Y|X)}}{\boldsymbol{H_X(Y)}} \tag{8}$$

where $G(Y|X)$ represents the information gain entropy corresponding to factor X. $H_X(Y)$ is the information entropy of mountain wildfire event Y about factor X.

Importance Rank of Wildfire-Related Factors

The calculated information gain entropy and information gain ratio of factors are listed in **Table 1**.

Vegetation type, land-usage type, and historical fire-spot density are the three most important factors in affecting the occurrence risk of wildfire. It is because that the vegetation type and land-usage type can indicate the degree of fuel whereas the historical fire-spot density represents the high incidence of wildfires. The DR and the aspect are the factors with the least influence on the wildfire occurrence.

METHODOLOGY

Weighted Naïve Bayes

Bayes theorem calculates the posterior probability of events by combining the prior probability and conditional probability, as follows (Qu et al., 2016; Zhao et al., 2013; Ma et al., 2013).

$$\boldsymbol{P(X_i|Y)} = \frac{\boldsymbol{P(Y|X_i)\cdot P(X_i)}}{\boldsymbol{P(Y)}} \tag{9}$$

where $P(X_i)$ is the prior probability of event X_i, which is obtained according to the data distribution difference of fire-spot and non-fire-spot samples. $P(Y|X_i)$ is the conditional probability of event Y occurring under the occurrence of event X_i. $P(Y) = \sum P(Y|X_i)\cdot P(X_i)$ is the probability of event Y occurring under the condition with the occurrence of all events $X_1\ X_2 \cdots X_i$. $P(X_i|Y)$ is the posterior probability that the given Y is caused by the event X_i.

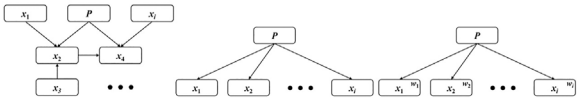

FIGURE 3 | WNB, NB, and WNB classifier structure.

Due to the conditional independence, the NB model has advantages of higher operating efficiency, faster speed, and a simple structure compared to BNW. But absolute independence does not exist in reality. The WNB model assigns different weights to nodes to strengthen the connections between nodes. In this way, the assumption of the independence of NB can be weakened (Huang et al., 2015; Lee, 2015; Liu R. et al., 2017; Tang et al., 2018; Ji et al., 2019). The structures of BNW, NB, and WNB models are shown in **Figure 3**.

The posterior probability in WNB is defined as the weighted product of the conditional probabilities of factors, as shown in formula **(10)**.

$$\boldsymbol{P\left(y_j\middle|x_1, x_2\cdots x_n\right) = P\left(y_j\right)\prod P\left(x_i\middle|y_j\right)^{\omega_i}} \tag{10}$$

According to the wildfire risk assessment of the transmission corridor based on NB [16], the conditional probability of factors under fire or non-fire conditions is obtained.

$$\boldsymbol{P\left(x_{ij}\middle|y_j\right) = \frac{n_{ij} + 100}{\sum_{k=1}^{4} n_{ij} + 400}} \tag{11}$$

where x_{ij} represent the factor x_i at the j^{th} level. n_{ij} is the sample size of x_{ij}. The distributions of $P(x_{ij}|y_0)$ and $P(x_{ij}|y_1)$ represent the conditional probability of a non-fire event and a fire event.

Finally, the weighted Bayesian posterior probability of wildfire occurrence $P(Y)$ is determined.

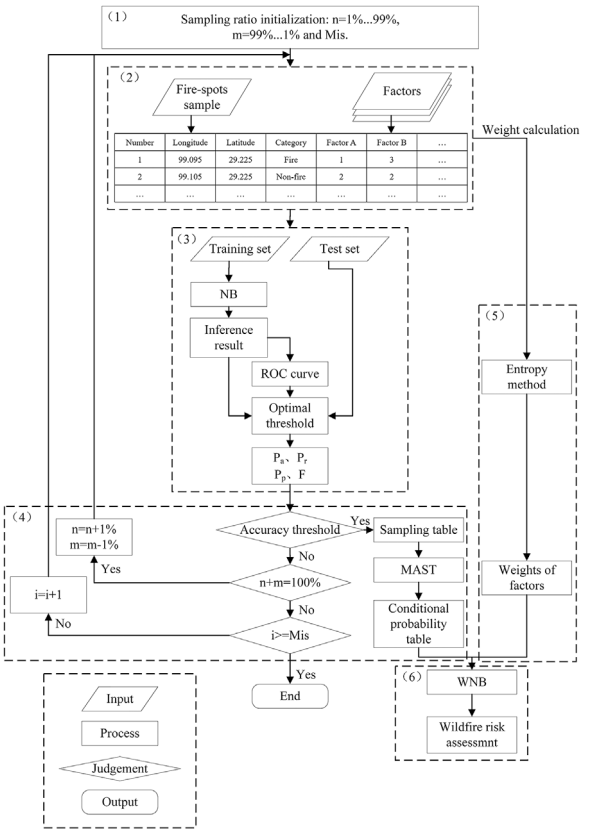

FIGURE 4 | The wildfire risk assessment model framework on WNB.

$$P(Y) = \frac{P(y_1|x_1, x_2 \cdots x_n)}{P(y_1|x_1, x_2 \cdots x_n) + P(y_0|x_1, x_2 \cdots x_n)} \tag{12}$$

Weight Calculation

The weights are often obtained by subjective or objective methods. With subjective methods, the value of weights is strongly affected by the knowledge and experience of surveyed experts, which may introduce larger errors to the model. Therefore, the entropy method is used to objectively evaluate and weight the factors in the WNB model.

In the information entropy theory, a smaller information entropy indicates a larger variation of the factor value with more information. Based on the information entropy theory, the weight is determined by the information entropy of the factor.

Step 1 The data of factors is normalized by

$$x_{ij}^{'} = \frac{x_{ij} - x_{max}}{x_{max} - x_{min}} \tag{13}$$

where x_{ij} represents the value of the j^{th} factor of the i^{th} object. x_{max} and x_{min} are the maximum and minimum values among the x_{ij}.

Step 2 The entropy value e_i of the i^{th} factor is:

$$e_i = -ln(n)^{-1} \sum_{j=1}^{n} P_{ij} \cdot \ ln P_{ij} \tag{14}$$

$$P_{ij} = \frac{x_{ij}^{'}}{\sum_{i=1}^{n} x_{ij}^{'}} \tag{15}$$

where P_{ij} represents the proportion of the j^{th} evaluation object of the i^{th} factor.

Step 3 According to the information entropy e_i of factors, the initial weight f_i is determined, and the entropy weight w_i is obtained after normalization.

The entropy weight w_i of the i^{th} factor is calculated as:

$$f_i = \frac{1 - e_i}{m - \sum_{i=1}^{m} e_j} \tag{16}$$

$$w_i = \frac{f_i}{\sum_{i=1}^{m} f_i} \tag{17}$$

Framework Conceptualization

The framework of the WNB-based wildfire risk assessment model is as shown in **Figure 4**.

1) Initialize the sample table, that is the proportion n of fire-spot samples and the proportion m of non-fire-spot samples, in which n + m = 100%. And set the maximum sampling times, Mis = 100.

2) Extract the fire-spot samples and non-fire-spot samples, and the value of wildfire-related factors in 1 km × 1 km grids by using ArcGIS 10.4.

3) Establish a training set and a test set for the model. The training set is formed by randomly selecting 75% of the fire-spot and non-fire-spot samples. The test set is formed by the remaining 25% of the samples. Naïve Bayes conditional probability is estimated based on the training set. And the optimal threshold is determined by observing the Receiver Operating Characteristic (ROC) curve to establish the confusion matrix, as shown in **Supplementary Table S4**.

The accuracy P_a, recall P_r, precision P_p and F_β score of the test set under this sampling ratio are calculated, according to **Eqs 18–21**.

$$P_a = \frac{TP + TN}{TP + TN + FP + FN} \tag{18}$$

$$P_r = \frac{TP}{TP + FN} \tag{19}$$

$$P_p = \frac{TP}{TP + FP} \tag{20}$$

$$F_\beta = \frac{(1 + \beta^2) P_r P_p}{\beta^2 P_p + P_r} \tag{21}$$

Considering the higher tolerance of the fake wildfire events for power grids, $\beta = 3$ is used.

4) Set the thresholds of P_a, P_r, P_p and F_β as 0.75 to find the Most Accurate Sampling Table (MAST) by using the forward sorting algorithm. Only the sampling tables whose performance meets the requirement of thresholds can be included in the sampling table database. The conditional probabilities of factors under the fire and non-fire conditions are then evaluated.
5) Calculate the factor weights by using the entropy method.

TABLE 2 | Entropy weight under different factors.

Number	14	13	12	11	10	9	8	7	6
Vegetation types	0.1138	0.1210	0.1303	0.1378	0.1477	0.1576	0.1682	0.1875	0.2034
Land-usage types	0.1304	0.1387	0.1493	0.1580	0.1693	0.1806	0.1927	0.2149	0.2331
Fire-spot density	0.0866	0.0922	0.0992	0.1050	0.1125	0.1200	0.1280	0.1428	0.1549
Population density	0.0980	0.1042	0.1121	0.1186	0.1271	0.1357	0.1447	0.1614	0.1750
Fuel load	0.0799	0.0850	0.0914	0.0967	0.1037	0.1106	0.1180	0.1316	0.1427
GDP	0.0509	0.0541	0.0582	0.0616	0.0660	0.0705	0.0752	0.0838	0.0909
Annual temperature	0.0473	0.0503	0.0541	0.0573	0.0614	0.0655	0.0699	0.0779	0
DS	0.0699	0.0744	0.0800	0.0847	0.0908	0.0969	0.1033	0	0
Annual precipitation	0.0452	0.0481	0.0517	0.0547	0.0586	0.0626	0	0	0
Elevation	0.0485	0.0516	0.0555	0.0587	0.0629	0	0	0	0
NDVI	0.0552	0.0588	0.0631	0.0668	0	0	0	0	0
Slope	0.0480	0.0511	0.0550	0	0	0	0	0	0
DR	0.0666	0.0709	0	0	0	0	0	0	0
Aspect	0.0598	0	0	0	0	0	0	0	0

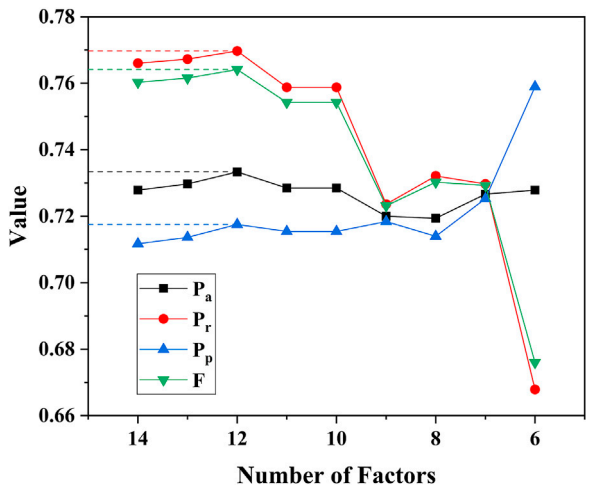

FIGURE 5 | The accuracy P_a, recall P_r, precision P_p and F_β score of the model under different factor sets.

6) Establish the WNB-based wildfire risk assessment model, by combining the conditional probability and factor weight.

RESULTS AND DISCUSSION

According to the importance rank of information gain ratio, some factors contribute little to the wildfire risk assessment. Therefore, the factor with the lowest information gain ratio is deleted one by one to obtain the Optimal Factor Set (OFS). The optimal WNB model is then established by the OFS. At the same time, an NB model, as well as a BNW model with the same factors, are established for comparison.

The Optimal Factors Set and the Most Accurate Sampling Table

The entropy weights of wildfire-related factors during the formation of OFS are shown in **Table 2**.

The performance of the WNB models under different factor sets is compared by using the 825 new fire-spot samples and an equal number of non-fire-spot samples in 2020. With the optimal threshold, the performance measures of the model under different factor sets are shown in **Figure 5**.

As can be seen from **Figure 5**, the two factors of aspect and DR have been deleted, and the P_a, P_r, P_p and F_β scores of the model have improved to a certain extent. They all reach the optimal state. As more factors are reduced, the P_r and F_β scores of the model reduce stepwise. Therefore, the top 12 factors of the information gain ratio are selected to form the OFS, and the MAST is obtained through 100 iterations. By using the OFS and MAST, the final accuracy P_a is 0.7566, recall P_r is 0.7661, precision P_p is 0.7728, and F_β the score is 0.7667. The prior probability of fire and non-fire is 0.53 and 0.47, respectively. The conditional probability table is shown in **Figure 6**.

The conditional probabilities of factors under fire and non-fire conditions differ from each other, indicating different effects on the wildfire. Therefore, these 12 types of wildfire-related factors can be used to evaluate the wildfire risk of the research area.

Comparison of BWN, NB, and WNB

The BNW can solve the uncertainty of evaluating wildfires by combining the prior conditional probability and the relationship between factors (Jiang et al., 2016; Albuquerque et al., 2017; Bates et al., 2021). However, the network complexity may be time-consuming and storage-consuming of the model. The NB, based on the assumption of conditional independence, can improve computational efficiency but sacrifices the predicting accuracy. By adding the different weights into factors, the WNB could compensate for the influence of different factors on the results and form a budget method with both plausibility and efficiency. In order to compare the assessment performance of the proposed WNB model, a BWN model and an NB model are also established based on OFS.

Wildfire Risk Assessment Model Based on BNW and NB

To build a BNW-based wildfire risk assessment model, the appropriate BNW structure should be established firstly

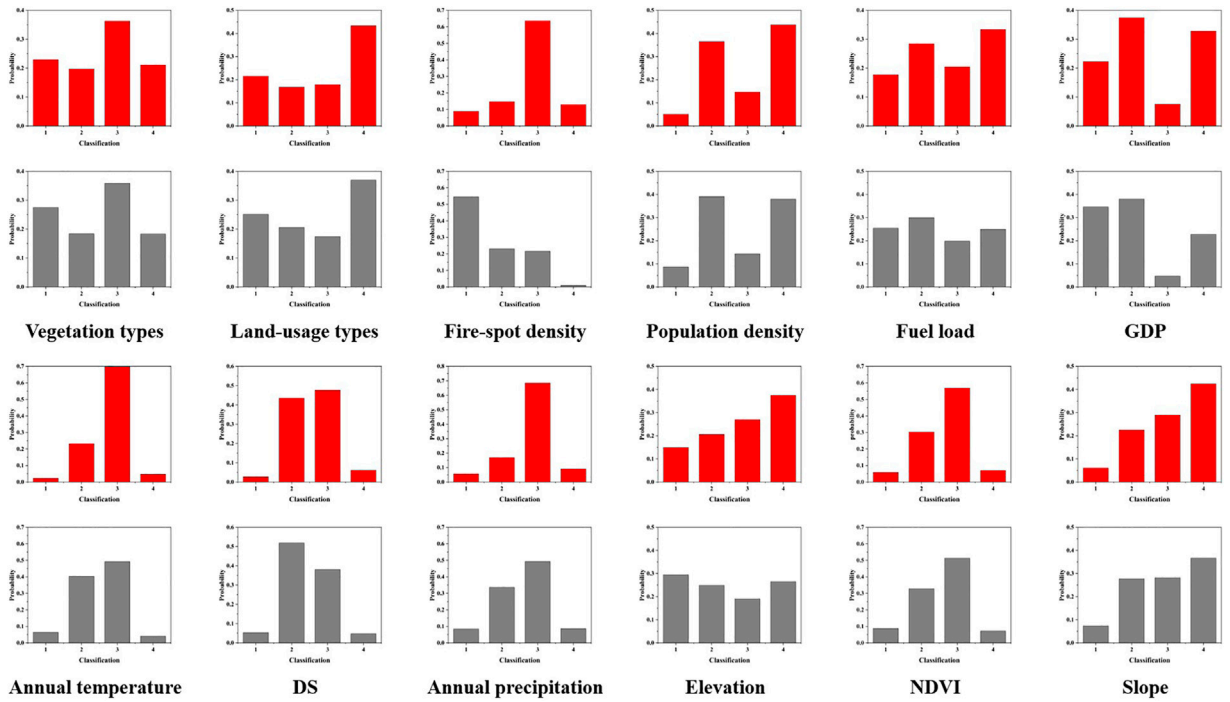

FIGURE 6 | The conditional probability table of fire and non-fire (Red is fire and gray is non-fire).

(Sevinc et al., 2020; Penman et al., 2020; Wu et al., 2018). The BNW structure consists of factor nodes, connecting lines, and arrows. The data of factor nodes are provided by the most accurate sampling table, which guarantees the optimal state of nodes. The connection line and arrow are determined by the causal correlation of two nodes. The relationship between wildfire-related factors is obtained by Pearson correlation analysis (**Supplementary Table S5**). When the absolute value of a Pearson coefficient is higher than 0.1, it is considered to have a certain relationship between two factors. For example, the Pearson coefficient between GDP and population density is 0.719, indicating a strong positive correlation between the two factors. According to the literature, population density affects the distribution of

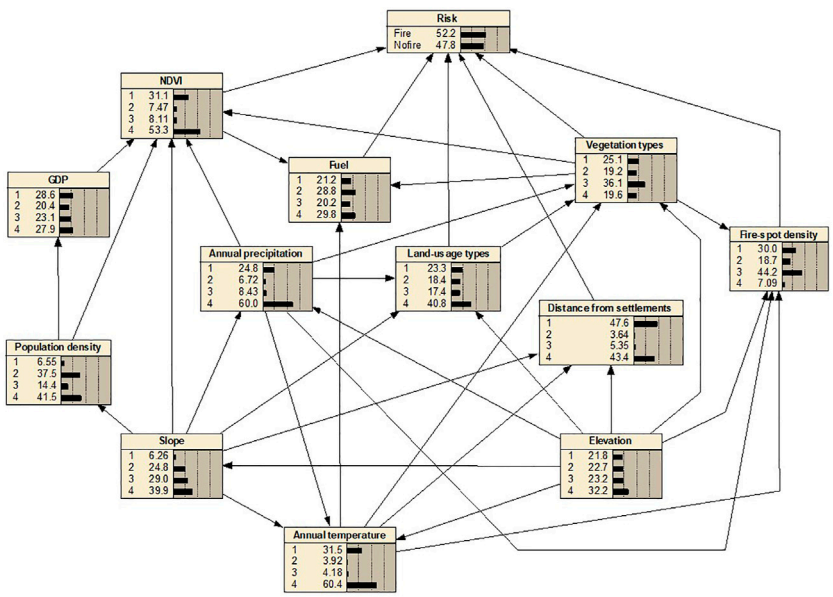

FIGURE 7 | The model framework based on BNW.

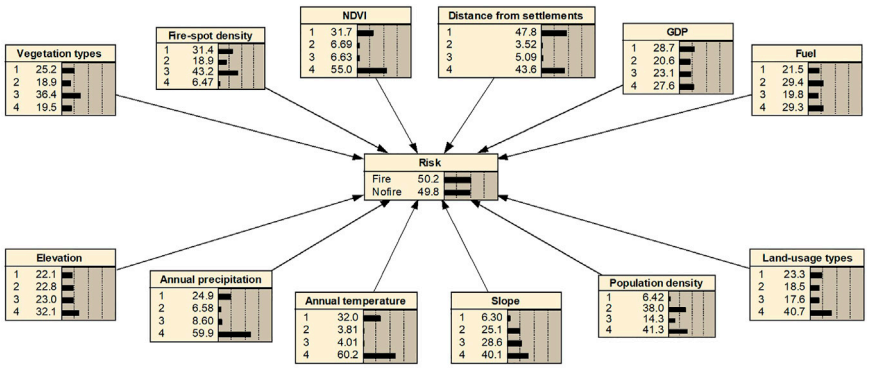

FIGURE 8 | The model framework based on NB.

GDP, so the arrow points from population density to GDP. The connecting lines and arrows between the factors in BNW, as well as the prior probability between factor nodes, are obtained, shown in **Figure 7**.

The structure of the NB model is much simpler, in which all factor nodes only points to fire events node, as shown in **Figure 8**.

Receiver Operating Characteristic Curve

The Receiver Operating Characteristic (ROC) curve is drawn based on a series of binary classification results. In the ROC curve, the True Positive Rate (TPR) is the ordinate whereas the False Positive Rate (FPR) is the abscissa. The Area Under ROC Curve (AUC) can be used to represent the classification performance of the model. The performance of the classifier is better when the AUC is larger. The TPR and FPR are calculated as:

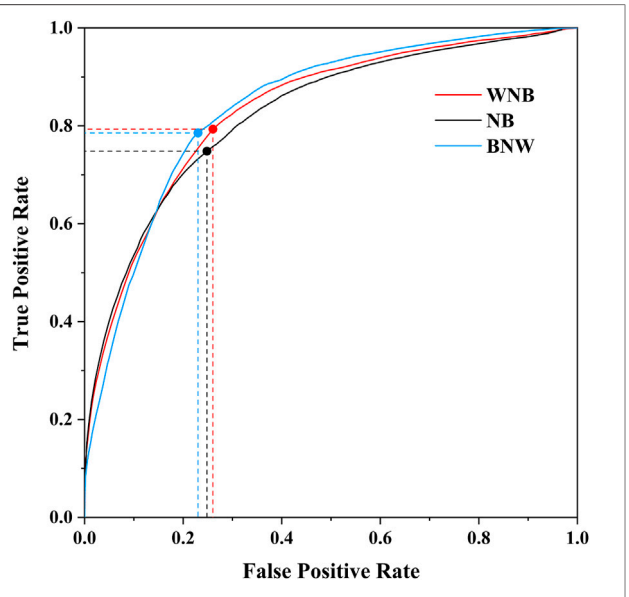

FIGURE 9 | The ROC curve of WNB, NB, and BNW.

$$TPR = \frac{TP}{TP + FN} \tag{22}$$

$$FPR = \frac{FP}{FP + TN} \tag{23}$$

In order to compare the performance of three Bayesian models, fire-spots from 2010 to 2019 and non-fire-spots are randomly extracted in equal proportions to calculate the probability of wildfire. According to the threshold of fire and non-fire, the ROC curves are constructed, as shown in **Figure 9**.

It can be clearly seen that the AUC of the NB model is the smallest, indicating the worst classification effect. The AUC of the BNW, NB, and WNB classifiers are 0.8446, 0.7973, and 0.8383 respectively. The points marked in curves are the Optimal Division Threshold (ODT). Under the ODT, the TPR of the WNB model and BNW model is nearly identical and is higher than that of the NB model. The FPRs of WNB, NB, and BNW are relatively similar.

According to the analysis of the ROC curves, both WNB and BNW models have a good performance in classifying the fire and non-fire events. But the intercoupling of factors, the establishment, and calculation processes of the BNW analysis is complicated and time-consuming, andthe classification performance of the model strongly depends on the reasonability of structure. The WBN strengthens the effects of important factors and weakens the influence of redundant relationships on model performance by assigning different weights to the factors. It not only considers the interrelationship of factors but also reduces the complexity of calculation. Therefore, the classification performance of the WNB model is similar to that of BNW but has a simple structure and shortened calculation speed.

Wildfire Risk Assessment

By using the established WNB, NB, and BNW models, the posterior probabilities of wildfire risk of the grids in the research area are estimated. And the statistics of probability results are shown in **Supplementary Table S6**.

The distribution of estimated probabilities by different models is very different in the research area, indicating that the grading method may have an important impact on wildfire risk assessment. Therefore, four different grading methods, that

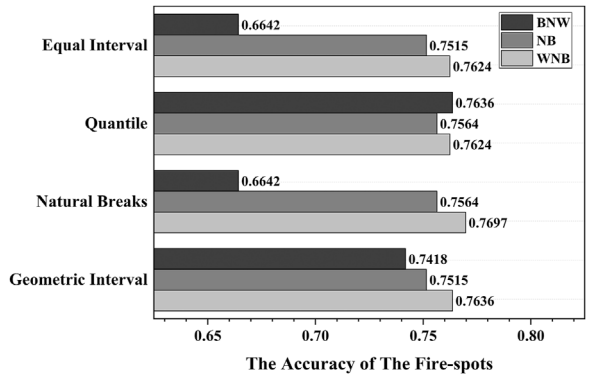

FIGURE 10 | The accuracy comparison of the four grading methods.

is equal interval, quantile, natural breaks, and geometric interval, are compared. Among them, the equal interval method divides the probability distribution of wildfire risk into four equal sub-ranges. The quantile method allocates division intervals into an equal proportion. The natural breaks method, which was proposed by Jenks (Anchang et al., 2016, suggests that the distribution can be divided into groups with similar nature by the natural turning points or breakpoints between any series of populations. It collects the greatest similarities inside the groups, and used the greatest difference to separate the groups. The principle of the geometric interval method is to establish segmentation hyperplanes by maximizing the distance between the hyperplane and the nearest sample (Peng and Wang, 2009).

By using the grading methods, the wildfire risk of grids is then classified into four levels, Low-risk, Medium-risk, High-risk, and Very-high-risk, based on the results of poster probability. For comparison, the fire spots in 2020 are used as the criterion to identify whether they fall into a region with high-risk or very-high-risk levels. The accuracy of the four grading methods is shown in **Figure 10**.

With the four grading methods, the accuracy of the BNW model differs remarkably. The accuracy reaches the highest (0.7636) by using the quantile method, whereas it is only 0.6642 using the grading methods of equal intervals and natural breaks. This means the predicting performance of the BNW-based wildfire risk assessment model is sensitive to the grading method. On the other hand, the accuracy results of the NB and WNB models are relatively stable with different grading methods. Specifically, the accuracy of the WNB model is all above 0.76 with either grading method, indicating that the WNB model is stable and adaptable.

Compared to the other three grading methods, the geometric interval method ensures an approximate same number of values in each grading range and a consistent variation between intervals. It is believed to be a compromise between the equal interval method, the quantile method, and the natural breaks method. Therefore, the geometric interval method is selected as the grading standard for visualizing the wildfire risks of the research area. By using the geometric interval method, the accuracy of the three Bayesian models is 0.7418, 0.7515, and 0.7636, respectively.

The Visualization of Wildfire Risk Assessment Models

Based on the grading results of the geometric interval method, the distribution of wildfire risk levels based on BNW, NB, and WNB models are visualized by using ArcGIS Software, as shown in **Figure 11**.

It can be found that no matter which Bayesian model is adopted, the overall risk distribution of the study area is roughly similar. This is mainly because the three kinds of Bayesian networks all use the same OFS and MAST and the sampling results objectively reflect the actual situation of the study area. The High-risk and Very-high-risk regions are generally distributed at the south and southeast of the study area. However, in some local areas, the assessment results of different models differ. For instance, in the result of the BNW model, the regions of a, b, and c have a larger area that is assessed to be the Very-high-risk. The Very-high-risk areas in NB and WNB models are much more scattered in the local regions, as shown in **Figure 12**. This may be caused by the mutual coupling of factors considered in the BNW model. Most factors have spatial continuity and surrounding relevance, so when the BNW model is used for assessment, the results would be smoothed. The NB model treats the factors independently, so the results are more scattered. Since WNB emphasizes some wildfire-related factors, the dispersion of the results lies between the NB model and the BNW model.

The proportions of grid areas and the fire spots from 2015 to 2021 under the four levels are summarized in **Table 3**. When using the geometric interval method for grading the poster probabilities of risk assessment, the low-risk and very high-risk occupy a larger proportion than the rest two risk level in

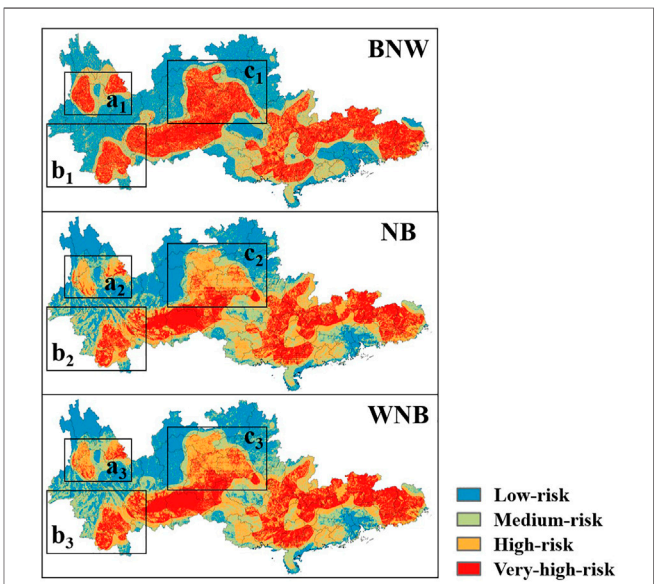

FIGURE 11 | The distributions of wildfire risk levels based on BNW, NB, and WNB.

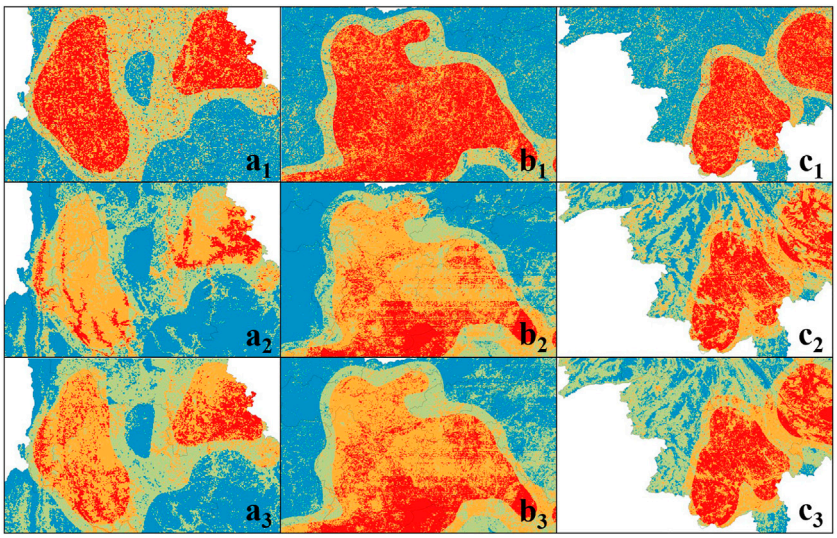

FIGURE 12 | The distribution of wildfire risk levels in local regions **(a, b, and c)**.

TABLE 3 | The proportions of the grids under the four levels.

Risk level	BNW		NB		WNB	
	Fire-spots proportion (%)	Area proportion (%)	Fire-spots proportion (%)	Area proportion (%)	Fire-spots proportion (%)	Area proportion (%)
Low	7.55	31.83	6.70	28.40	4.69	26.11
Medium	16.02	20.82	10.52	22.80	9.02	23.91
High	27.86	18.82	23.27	26.50	25.80	25.56
Very-high	48.57	28.53	59.51	22.30	60.47	24.42

the BNW model. The total area of these two risk levels accounts for 60.36% of the whole region. The area proportions of the four risk levels are more evenly distributed in the results of the NB and WNB models. In WNB-based risk assessment, 86.28% of the fire-spots fall in the high-risk and very high-risk region, which is much higher than that of BNW (76.43%) and NB (82.78%).

Considering the area and accuracy at the same time, the assessment performance of the BNW model is the worst. In total, 48.57% of fire spots falls in the High-risk and Very-high-risk area, which accounts for 47.35% of the total research region. By defining the predicting efficiency as the ratio of accuracy and the area proportion of the High-risk and Very-high-risk area, the predicting efficiencies for BNW, NB, and WNB models are 1.61, 1.69, and 1.73, separately. The WNB model exhibits the highest efficiencies for wildfire risk assessment, which is very helpful for the monitoring, inspection, and prevention of wildfires by relevant departments.

CONCLUSION

1) The importance of 14 types of wildfire-related factors is ranked through the information gain ratio. The vegetation type, land-usage type, and fire-spot density are the three most important factors that affect the occurrence of wildfires. The aspect and DR have few effects on the risk assessment of wildfire occurrence.
2) The deletion of less important factors and establishment of a Most Accurate Sampling Table can improve the assessment performance of the WNB model. The best accuracy of the WNB model is 0.7566 by deleting the aspect and DR factors.
3) Compared to the BNW and NB model, the WNB model has the best predicting efficiency for fire-spots assessment. By using the geometric interval grading method, a total of 86.44% of the fire-spots fall in the high-risk and very high-risk regions, and the predicting efficiency is 1.72.

DATA AVAILABILITY STATEMENT

The original contributions presented in the study are included in the article/**Supplementary Materials**, further inquiries can be directed to the corresponding author.

AUTHOR CONTRIBUTIONS

Funding acquisition, JL; Investigation, EZ; Methodology, HL; Project administration, YZ; Software, HL; Supervision, JL;

Writing—original draft, KX; Writing—review and editing, KX and YH. All authors have read and agreed to the published version of the manuscript. And all authors agree to be accountable for the content of the work.

FUNDING

The research was funded by the Science and technology projects funded by China Southern Power Grid Corporation for supporting this research under Contract No. GDKJXM20198386, by the Scientific Research Foundation of Hunan Education Department under Grant No.20B007 for scientific research, by the Changsha University of Science and Technology Professional Master's Innovation Project SJCX202045, by the Changsha University of Science and Technology Academic Master's Research and Innovation Project CX2020SS56, by the Changsha University of Science and Technology Academic Master's Research and Innovation Project CX2021SS47.

ACKNOWLEDGMENTS

The authors would like to thank Weijie Chen from the Changsha University of Science and Technology for his helpful suggestions. The authors also would like to thank the reviewers for their constructive suggestions and comments.

SUPPLEMENTARY MATERIAL

The Supplementary Material for this article can be found online at: https://www.frontiersin.org/articles/10.3389/fenrg.2022.829934/full#supplementary-material

REFERENCES

Albuquerque, M. T. D., Gerassis, S., Sierra, C., Taboada, J., Martín, J. E., Antunes, I. M. H. R., et al. (2017). Developing a New Bayesian Risk Index for Risk Evaluation of Soil Contamination. *Sci. Total Environ.* 603-604, 167–177. doi:10.1016/j.scitotenv.2017.06.068

Anchang, J. Y., Ananga, E. O., and Pu, R. (2016). An Efficient Unsupervised index Based Approach for Mapping Urban Vegetation from IKONOS Imagery. *Int. J. Appl. Earth Observation Geoinformation* 50, 211–220. doi:10.1016/j.jag.2016.04.001

Bates, B. C., Dowdy, A. J., and McCaw, L. (2021). A Bayesian Approach to Exploring the Influence of Climate Variability Modes on Fire Weather Conditions and Lightning-Ignited Wildfires. *Clim. Dyn.* 57, 1207–1225. doi:10.1007/s00382-021-05764-2

Chen, W., Zhou, Y., Zhou, E., Xiang, Z., Zhou, W., and Lu, J. (2021). Wildfire Risk Assessment of Transmission-Line Corridors Based on Naïve Bayes Network and Remote Sensing Data. *Sensors* 21 (2), 634. doi:10.3390/s21020634

Dlamini, W. M. (2010). A Bayesian Belief Network Analysis of Factors Influencing Wildfire Occurrence in Swaziland. *Environ. Model. Softw.* 25, 199–208. doi:10.1016/j.envsoft.2009.08.002

Hu, Y., Liu, K., and Wu, T. (2014). Analysis of Influential Factors on Operation Safety of Transmission Line and Countermeasures. *High Voltage Eng.* 40 (11), 3491–3499.

Huang, D. C., Li, P., Ruan, J. J., Zhang, Y., and Wu, T. (2015). Review on Discharge Mechanism and Breakdown Characteristics of Transmission Line Gap under Forest Fire Condition. *High Voltage Eng.* 41 (2), 622–632. doi:10.13336/j.1003-6520.hve.2015.02.040

Ji, H., Huang, S., Wu, Y., Hui, Z., and Zheng, C. (2019). A New Weighted Naive Bayes Method Based on Information Diffusion for Software Defect Prediction. *Softw. Qual J* 27 (3), 923–968. doi:10.1007/s11219-018-9436-4

Jiang, L., Li, C., Wang, S., and Zhang, L. (2016). Deep Feature Weighting for Naive Bayes and its Application to Text Classification. *Eng. Appl. Artif. Intelligence* 52, 26–39. doi:10.1016/j.engappai.2016.02.002

Lee, C.-H. (2015). A Gradient Approach for Value Weighted Classification Learning in Naive Bayes. *Knowledge-Based Syst.* 85, 71–79. doi:10.1016/j.knosys.2015.04.020

Liu, C. X., Fan, P., Wang, H. T., and Guo, J. (2017). Modeling forest Fire Risk Assessment Based on BP Neural Network of Transmission Line. *Power Syst. Prot. Control.* 45 (17), 100–105. doi:10.7667/PSPC161228

Liu, M. J., Shao, Z. C., and Shangguan, T. (2016). Study on Models and Methods of Risk Assessment of Transmission Line Fault Caused by Fire. *Power Syst. Prot. Control.* 44 (6), 82–89. doi:10.7667/PSPC150844

Liu, R., Chen, Y., Wu, J., Gao, L., Barrett, D., Xu, T., et al. (2017). Integrating Entropy-Based Naïve Bayes and GIS for Spatial Evaluation of Flood Hazard. *Risk Anal.* 37 (4), 756–773. doi:10.1111/risa.12698

Lu, J. Z., Liu, Y., Xu, X. J., and Yang, L. (2017). Prediction and Early Warning Technology of Wildfire Nearby Overhead Transmission Lines. *High Voltage Eng.* 43 (1), 314–320. doi:10.13336/j.1003-6520.hve.20161227041

Ma, D. Z., Ding, W. F., and Liu, S. N. (2013). Risk Assessment Method for Fire in Underground Space Based on Bayesian Network. *China Saf. Sci. J.* 23 (11), 151–156. doi:10.16265/j.cnki.issn1003-3033.2013.11.027

Peng, X. J., and Wang, Y. F. (2009). Total Margin V-Support Vector Machine and its Geometric Problem. *Pattern Recognition Artif. Intelligence* 22 (1), 8–16. doi:10.16451/j.cnki.issn1003-6059.2009.01.021

Penman, T. D., Cirulis, B., and Marcot, B. G. (2020). Bayesian Decision Network Modeling for Environmental Risk Management: A Wildfire Case Study. *J. Environ. Manage.* 270, 110735. doi:10.1016/j.jenvman.2020.110735

QGDW11643 (2016). *Guidelines for Drawing Wildfire Distribution on Overhead Transmission Lines*. Beijing: State Grid Corporation.

Qu, Z. Y., Yang, Q., and Yang, J. M. (2016). Risk Association Model of Smart Substation Based on Bayesian Network. *Automation Electric Power Syst.* 40 (2), 95–99. doi:10.7500/AEPS20150518003

Sevinc, V., Kucuk, O., and Goltas, M. (2020). A Bayesian Network Model for Prediction and Analysis of Possible forest Fire Causes. *For. Ecol. Manag.* 457, 117723. doi:10.1016/j.foreco.2019.117723

Song, G. B., Cai, X. L., Gao, S. P., and Zhang, J-K. (2012). Survey of Fault Location Research for HVDC Transmission Lines. *Power Syst. Prot. Control.* 40 (5), 133–137. doi:10.3969/j.issn.1674-3415.2012.05.026

Tang, X., Shu, Y., Lian, Y., Zhao, Y., and Fu, Y. (2018). A Spatial Assessment of Urban Waterlogging Risk Based on a Weighted Naïve Bayes Classifier. *Sci. Total Environ.* 630, 264–274. doi:10.1016/j.scitotenv.2018.02.172

Wang, K., and Fan, C. (2016). Electric Transmission Lines Fire Risk Impact Factor Weighting Analysis Based on Analytic Hierarchy Process. *Geomatics Spat. Inf. Tech.* 39 (12), 116–119. doi:10.3969/j.issn.1672-5867.2016.12.035

Wang, S., and Wang, F. (2016). Research of Forest Fire Risk Distribution of Transmission Line and its Application. *Hubei Electric Power* 40 (2), 23–27+32. doi:10.19308/j.hep.2016.02.005

Wu, J., Hu, Z., Chen, J., and Li, Z. (2018). Risk Assessment of Underground Subway Stations to Fire Disasters Using Bayesian Network. *Sustainability* 10 (10), 3810. doi:10.3390/su10103810

Wu, T., Ruan, J. J., and Zhang, Y. (2012). Study on the Statistic Characteristics and Identification of AC Transmission Line Trips Induced by forest Fires. *Power Syst. Prot. Control.* 40 (10), 138–143+148. doi:10.3969/j.issn.1674-3415.2012.10.025

Xiong, P., Zhu, T. Q., and Gu, X. (2014). Data Anonymization Based on Restriction of Information Gain Ratio: Method and Evaluation. *Appl. Res. Comput.* 31 (3), 819–824. doi:10.3969/j.issn.1001-3695.2014.03.044

Xu, K., Zhang, X., Chen, Z., Wu, W., and Li, T. (2016). Risk Assessment for Wildfire Occurrence in High-Voltage Power Line Corridors by Using Remote-Sensing Techniques: a Case Study in Hubei Province, China. *Int. J. Remote Sensing* 37 (20), 4818–4837. doi:10.1080/01431161.2016.1220032

Ye, L. P., Chen, X. Y., He, Z. L., and Xie, C-Z. (2014). Present Situation of forest Fire Early Warning Technology Used for Transmission Line. *Power Syst. Prot. Control.* 42 (6), 145–153.

Zeng, Q. F. (2009). The Spatial Distribution Characteristics and Cluster Analysis of forest Fires in Guangdong Province. *For. Fire Prev.* 4, 29–32. doi:10.3969/j.issn.1002-2511.2009.04.009

Zhao, Y., Li, H. Q., and Wang, Y. M. (2013). A Complex Network Theory and Conditional Probability Based Risk Assessment Method for Disastrous Accidents. *Power Syst. Tech.* 37 (11), 3190–3196. doi:10.13335/j.1000-3673.pst.2013.11.035

Zhu, Q., Guo, J., and Zeng, B. (2016). An Early-Warning Evaluation Model against Mountain Fire of Transmission Line Based on Analytic Hierarchy Process. *Electr. Meas. Instrumentation* 55 (6), 71–75+88. doi:10.3969/j.issn.1001-1390.2018.06.012

Conflict of Interest: The author EZ is employed by the company Guangdong Power Grid.

The remaining authors declare that the research was conducted in the absence of any commercial or financial relationships that could be construed as a potential conflict of interest.

This study received funding from China Southern Power Grid Corporation under Contract No. GDKJXM20198386. The funder had the following involvement with the study: Data Calculation of Fire-spot Density.

Publisher's Note: All claims expressed in this article are solely those of the authors and do not necessarily represent those of their affiliated organizations, or those of the publisher, the editors and the reviewers. Any product that may be evaluated in this article, or claim that may be made by its manufacturer, is not guaranteed or endorsed by the publisher.

frontiers in Energy Research

ORIGINAL RESEARCH
published: 07 February 2022
doi: 10.3389/fenrg.2022.796325

A Reduced-Order RNN Model for Solving Lyapunov Equation Based on Efficient Vectorization Method

Zhiying Chen[1], *Zhaobin Du*[1]*, *Feng Li*[2] *and Chengjun Xia*[1]

[1]School of Electric Power Engineering, South China University of Technology, Guangzhou, China, [2]The Grid Planning and Research Center of Guangdong Power Grid Corporation, Guangzhou, China

With the trend of electronization of the power system, a traditional serial numerical algorithm is more and more difficult to adapt to the demand of real-time analysis of the power system. As one of the important calculating tasks in power systems, the online solution of Lyapunov equations has attracted much attention. A recursive neural network (RNN) is more promising to become the online solver of the Lyapunov equation due to its hardware implementation capability and parallel distribution characteristics. In order to improve the performance of the traditional RNN, in this study, we have designed an efficient vectorization method and proposed a reduced-order RNN model to replace the original one. First, a new vectorization method is proposed based on the special structure of vectorized matrix, which is more efficient than the traditional Kronecker product method. Second, aiming at the expanding effect of vectorization on the problem scale, a reduced-order RNN model based on symmetry to reduce the solution scale of RNN is proposed. With regard to the accuracy and robustness, it is proved theoretically that the proposed model can maintain the same solution as that of the original model and also proved that the proposed model is suitable for the Zhang neural network (ZNN) model and the gradient neural network (GNN) model under linear or non-linear activation functions. Finally, the effectiveness and superiority of the proposed method are verified by simulation examples, three of which are standard examples of power systems.

Keywords: Lyapunov equation, vectorization, reduced-order RNN, symmetry, ZNN, GNN

OPEN ACCESS

Edited by:
Yan Xu,
Nanyang Technological University, Singapore

Reviewed by:
Yushuai Li,
University of Oslo, Norway
Dazhong Ma,
Northeastern University, China

***Correspondence:**
Zhaobin Du
epduzb@scut.edu.cn

Specialty section:
This article was submitted to Smart Grids, a section of the journal Frontiers in Energy Research

Received: *16 October 2021*
Accepted: *03 January 2022*
Published: *07 February 2022*

Citation:
Chen Z, Du Z, Li F and Xia C (2022) A Reduced-Order RNN Model for Solving Lyapunov Equation Based on Efficient Vectorization Method. Front. Energy Res. 10:796325. doi: 10.3389/fenrg.2022.796325

INTRODUCTION

With the trend of the electronic power system, the scale of system computing is increasing day by day, while the demand of real-time analysis and calculation in the process of system operation remains unchanged. Traditional serial algorithms cannot solve this contradiction well, so various parallel algorithms and distributed methods appear successively. In power system state estimation, Chen et al. (2017) have used the SuperLU_MT solver to estimate the state of the actual power grid, making full use of the parallel characteristics of multicore and multi-thread solver. Liu Z. et al. (2020) have fully explored the parallelism in the calculation of continuous power flow and applied the continuous Newton method power flow model to realize the parallel solution algorithm of continuous power flow based on GPU in large scale and multiple working conditions. Moreover, a novel distributed dynamic event-triggered Newton–Raphson algorithm is proposed to solve the double-mode energy management problem in a fully distributed fashion (Li et al., 2020). Similarly, Li Y. et al. (2019) proposed an event-triggered distributed algorithm with some desirable

features, namely, distributed execution, asynchronous communication, and independent calculation, which can solve the issues of day-ahead and real-time cooperative energy management for multienergy systems. Given that software algorithms are essentially run by hardware, implementing functions directly from hardware is also an option for real-time computing. For example, Hafiz et al. (2020) proposed a real-time stochastic optimization of energy storage management using deep learning–based forecasts for residential PV applications, where the key of the real-time computation is the hardware controller. It is worth pointing out that compared with the aforementioned methods, the neural dynamics method has greater potential in the field of real-time calculation of power systems (Le et al., 2019), and its time constant can reach tens of milliseconds (Chicca et al., 2014) because of its parallel distribution characteristics and the convenience of hardware implementation.

The Lyapunov equation is widely used in some scientific and engineering fields to analyze the stability of dynamic systems (He et al., 2017; He and Zhang, 2017; Liu J. et al., 2020). In addition, the Lyapunov equation plays an important role in the controller design and robustness analysis of non-linear systems (Zhou et al., 2009; Raković and Lazar, 2014). In the field of power systems, the balanced truncation method, controller design, and stability analysis are also inseparable from the solution of the Lyapunov equation (Zhao et al., 2014; Zhu et al., 2016; Shanmugam and Joo, 2021). Therefore, many solving algorithms have been proposed to solve the Lyapunov equation. For example, Bartels and Stewart proposed the Bartels–Stewart method (Bartels and Stewart, 1972), which is a numerically stable solution. Lin and Simoncini (Lin and Simoncini, 2013) proposed the minimum residual method for solving the Lyapunov equation. Stykel (2008) used the low-rank iterative method to solve the Lyapunov equation and verified the effectiveness of the method through numerical examples. However, the efficiency of these serial processing algorithms is not high in large-scale applications and related real-time processing (Xiao and Liao, 2016).

Recently, due to its parallelism and convenience of hardware implementation, recurrent neural networks have been proposed and designed to solve the Lyapunov equation (Zhang et al., 2008; Yi et al., 2011; Yi et al., 2013; Xiao et al., 2019). The RNN mainly includes the Zhang neural network (ZNN) and gradient neural network (GNN) (Zhang et al., 2008). Most of the research studies on RNN focus on the improvement of model convergence. For example, Yi et al. (2013) point out that when solving a stationary or a non-stationary Lyapunov equation, the convergence of the ZNN is better than that of GNN. Yi et al. (2011) used a power-sigmoid activation function (PSAF) to build an improved GNN model to accelerate the iterative convergence of Lyapunov equation. In (Xiao and Liao, 2016), the sign-bi-power activation function (SBPAF) is used to accelerate the convergence of the ZNN model for solving the Lyapunov equation and the proposed ZNN model has finite-time convergence, which is obviously better than the previous ZNN and GNN models. In recent years, some studies have considered the noise-tolerant ZNN model. In Xiao et al. (2019), two robust non-linear ZNN (RNZNN) are established to find the solution of the Lyapunov equation under various noise conditions. Different from previous ZNN models activated by the typical activation functions (such as the linear activation function, the bipolar sigmoid activation function, and the power activation function), these two RNZNN models have predefined time convergence in the presence of various noises.

However, both GNN and ZNN need to transform the solution matrix from the matrix form to the vector form through the Kronecker product, which is called vectorization of the RNN model (Yi et al., 2011). The use of the Kronecker product will make the scale of the problem to be solved larger. As the size of the problem increases, the scaling effect of the Kronecker product becomes more obvious. The enlargement effect of the Kronecker product on the model size will not only lead to insufficient memory when the RNN is simulated on software but also make the hardware implementation of the RNN model need more devices and wiring, which increases the volume of hardware, the complexity of hardware production, and the failure rate of hardware. However, no study has discussed the order reduction of the RNN model.

It should be pointed out that the vectorized RNN model needs to be solved using a hardware circuit. However, as the relevant research of the RNN for solving the Lyapunov equation is still in the stage of theoretical exploration and improvement, there are no reports about hardware products of the RNN solver of the Lyapunov equation. Relevant studies (Zhang et al., 2008; Yi et al., 2011; Yi et al., 2013; Xiao and Liao, 2016; Xiao et al., 2019) simulate the execution process of the RNN hardware circuit through the form of software simulation, and this study also adopts this form. It is undeniable that the results of software simulation are consistent with those of hardware implementation. Therefore, the theoretical derivation and simulation results of the RNN in this article and in the literature (Zhang et al., 2008; Yi et al., 2011; Yi et al., 2013; Xiao and Liao, 2016; Xiao et al., 2019) can be extended to the scenarios of hardware implementation.

The RNN is used to solve the Lyapunov equation, and the ultimate goal is to develop an effective online calculation model to solve the Lyapunov equation, so it is of great significance to improve the calculation speed of the RNN. Current studies focus on improving the computational speed of the RNN by improving the convergence of RNN. However, how to efficiently realize vectorization of the RNN model is also a breakthrough to improve the computational efficiency of the RNN method. At present, the Kronecker product is generally used to transform the solution matrix into the vector form (Horn and Johnson, 1991). The Kronecker product actually performs multiple matrix multiplication operations, and the time complexity of multiplying two n×n matrices is O (n^3), so the time complexity of the Kronecker product increases rapidly as the scale increases. This means that the traditional matrix vectorization method based on the Kronecker product still has room for optimization.

In summary, this article proposes an efficient method for vectorizing the RNN model based on the special structure of the vectorized matrix, which is more efficient than the traditional

expansion method by the Kronecker product. Aiming at the expanding effect of vectorization on the problem scale, a reduced-order RNN model based on symmetry was proposed for solving the time-invariant Lyapunov equation, and the validity and applicability of the reduced-order RNN model were proved theoretically. The main contributions of this article are as follows.

1) An efficient method for vectorization of RNN model is proposed. Compared with the traditional vectorization method, this method has higher efficiency and less time consumption.
2) The reduced-order RNN model for solving the Lyapunov equation based on symmetry is proposed, which greatly reduces the solution scale. It is proved theoretically that the proposed model can maintain the same solution as that of the original model. Meanwhile, it is proved theoretically that the proposed model is suitable for the ZNN model and GNN model under linear or non-linear activation functions.
3) Several simulation examples are given to verify the effectiveness and superiority of the proposed efficient method for vectorization of the RNN and the reduced-order RNN model. It is also verified that the neural dynamics method is suitable for solving the Lyapunov equation of power systems through three standard examples of power systems.

In order to show the contributions of this study more clearly, the logical graph using the RNN model for solving the Lyapunov equation is shown in **Figure 1**, and the main novelties and differences of this article from Refs Yi et al. (2011); Yi et al. (2013); Xiao and Liao (2016); Xiao et al. (2019) are shown in **Table 1**.

In **Table1**, items and numbers correspond to the three steps of **Figure 1**. The relevant references include Yi et al. (2011); Yi et al. (2013); Xiao and Liao (2016); Xiao et al. (2019).

In conclusion, Refs (Yi et al., 2011; Yi et al., 2013; Xiao and Liao, 2016; Xiao et al., 2019) focus on constructing a stronger RNN model to improve the convergence and noise-tolerant ability, including using different activation functions and neural networks. However, this study focuses on the vectorization method and the reduced-order RNN model.

PROBLEM FORMULATION AND RELATED WORK

Problem Formulation

Consider the following well-known Lyapunov equation (Yunong Zhang and Danchi Jiang, 1995)

$$A^{\mathrm{T}}X(t) + X(t)A = -C, \tag{1}$$

where $A \in \mathbb{R}^{n\times n}$ is a constant stable real matrix and $C \in \mathbb{R}^{n\times n}$ is a constant symmetric positive-definite matrix. The objective is to find the unknown matrix $X(t) \in \mathbb{R}^{n\times n}$ to make the Lyapunov matrix **Eq. 1** hold true. Let $X^* \in \mathbb{R}^{n\times n}$ denote the theoretical solution of **Eq. 1**.

In addition, two of the most relevant works (i.e., GNN and ZNN models) are presented to solve the Lyapunov **Eq. 1** in the following.

GNN

According to the principle of GNN (Yi et al., 2011) and combined with the characteristics of Lyapunov equation, a corresponding GNN model can be designed to solve the Lyapunov equation. The design steps are as follows:

First, construct an energy function based on norm as follows:

$$\Delta = \frac{\|A^{\mathrm{T}}X(t) + X(t)A + C\|_{\mathrm{F}}^2}{2} \tag{2}$$

where $\|.\|_{\mathrm{F}}$ means F-norm. The minimum value of the energy function is the solution of the Lyapunov equation.

Second, based on the principle of the negative gradient descent of the GNN, the following formula can be constructed:

$$-\frac{\partial\Delta}{\partial X} = -A\left(A^{\mathrm{T}}X(t) + X(t)A + C\right) - \left(A^{\mathrm{T}}X(t) + X(t)A + C\right)A^{\mathrm{T}} \tag{3}$$

By introducing the adjustable positive parameter γ, the following GNN model can be obtained:

$$\begin{aligned}\dot{X}(\mathrm{t}) = &-\gamma A\left(A^{\mathrm{T}}X(t) + X(t)A + C\right)\\ &-\gamma\left(A^{\mathrm{T}}X(t) + X(t)A + C\right)A^{\mathrm{T}}\end{aligned} \tag{4}$$

where $\gamma > 0$, $X(t) \in \mathbb{R}^{n\times n}$, and $X(0) \in \mathbb{R}^{n\times n}$ is the initial value of $X(t)$.

Finally, the conventional linear GNN (**Eq. 4**) can be improved into the following non-linear expression by employing a non-linear activation function array $\mathcal{F}(\cdot)$:

$$\begin{aligned}\dot{X}(\mathrm{t}) = &-\gamma\left(A\mathcal{F}\left(A^{\mathrm{T}}X(t) + X(t)A + C\right)\right.\\ &\left.+\mathcal{F}\left(A^{\mathrm{T}}X(t) + X(t)A + C\right)A^{\mathrm{T}}\right)\end{aligned} \tag{5}$$

where $\mathcal{F}(\cdot)$: $\mathbb{R}^{n\times n} \to \mathbb{R}^{n\times n}$ denotes a matrix-valued activation function array of the GNN models. In this study, the bipolar sigmoid activation function (BPAF) is selected as the representative of the non-linear activation function of the GNN model for simulation because of its strong convergence (Yi et al., 2011). The expression of BPAF is as follows:

$$\mathcal{F}(x) = \frac{1 - \exp(-\delta x)}{1 + \exp(-\delta x)} \tag{6}$$

where δ is a constant and $\delta > 1$.

ZNN

First, following Zhang et al.'s design method (Zhang et al., 2002), we can define the following matrix-valued error function to monitor the solution process of Lyapunov **Eq. 1**:

$$E(t) = A^{\mathrm{T}}X(t) + X(t)A + C \tag{7}$$

Then in view of the definition of $E(t)$ and the design formula $\mathrm{d}E(t)/dt = -\gamma\varphi(E(t))$, the dynamic equation of the ZNN model for solving the online Lyapunov **Eq. 1** is derived as follows:

$$A^{\mathrm{T}}\dot{X}(\mathrm{t}) + \dot{X}(\mathrm{t})A = -\gamma\varphi\left(A^{\mathrm{T}}X(t) + X(t)A + C\right) \tag{8}$$

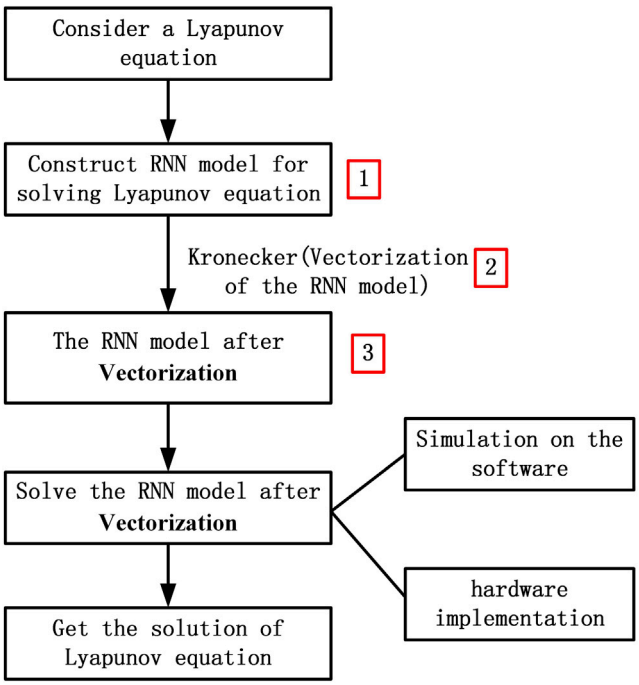

FIGURE 1 | Logical graph of using a RNN model for solving the Lyapunov equation.

TABLE 1 | Main novelties and differences of this article from the relevant references.

Number	Item	Refs. [9,15-17]	This article
1	Constructing RNN model	✓	✗
2	Vectorization	✗	✓
3	Reduced-order RNN model	✗	✓

where $\varphi(\cdot)$: $\mathbb{R}^{n\times n} \to \mathbb{R}^{n\times n}$ denotes a matrix-valued activation function array of the ZNN models. The definition of γ in the ZNN model is the same as that in the GNN model.

In this study, the RNZNN-1 model is selected as the representative of the non-linear activation function of the ZNN model for simulation because of its strong convergence (Xiao et al., 2019). The expression of the non-linear activation function in the RNZNN-1 model is as follows:

$$\varphi(x) = \left(a_1|x|^{\eta} + a_2|x|^{\omega}\right)\operatorname{sign}(x) + a_3 x + a_4 \operatorname{sign}(x) \tag{9}$$

where design parameters $0 < \eta < 1$, $\omega > 1$, $a_1 > 0$, $a_2 > 0$, $a_3 \geq 0$, $a_4 \geq 0$, and $\operatorname{sign}(x)$ denotes the signum function.

AN EFFICIENT METHOD FOR VECTORIZATION OF RNN MODEL

General Method of Vectorizing RNN Model

The RNN model needs to be transformed to the vector form so that it can be used for software simulation (Li X. et al., 2019) and hardware implementation.

Vectorization of the GNN Model

Yi et al. (2011) pointed out that the vectorization of GNN model is as follows:

$$\begin{aligned}\operatorname{vec}\dot{X}(t) &= -\gamma\big((A\otimes I)\mathcal{F}\big((A^{\mathrm{T}}\otimes I)\operatorname{vec}X(t) + (I\otimes A^{\mathrm{T}})\\ &\quad \operatorname{vec}X(t) + \operatorname{vec}C\big) + (I\otimes A)\mathcal{F}\big((A^{\mathrm{T}}\otimes I)\operatorname{vec}X(t)\\ &\quad + (I\otimes A^{\mathrm{T}})\operatorname{vec}X(t) + \operatorname{vec}C\big)\big)\\ &= -\gamma\big((A\oplus A)\mathcal{F}\big((A^{\mathrm{T}}\oplus A^{\mathrm{T}})\operatorname{vec}X(t) + \operatorname{vec}C\big)\big)\end{aligned} \tag{10}$$

where

$$A \oplus A = A\otimes I + I\otimes A \tag{11}$$

$$A^{\mathrm{T}} \oplus A^{\mathrm{T}} = A^{\mathrm{T}}\otimes I + I\otimes A^{\mathrm{T}} \tag{12}$$

where ⊗ means the Kronecker product. Given $X = [x_{ij}] \in \mathbb{R}^{n\times n}$, we can vectorize X as a column vector, $\operatorname{vec}(X) \in \mathbb{R}^{n^2\times 1}$, which is defined as $\operatorname{vec}(X) = [x_{11},\ldots,x_{1n},x_{21},\ldots,x_{n1},\ldots,x_{nn}]^{\mathrm{T}}$.

Since the order of matrix addition and matrix transpose is interchangeable (Cheng and Chen, 2017),

$$(Y+Z)^{\mathrm{T}} = Y^{\mathrm{T}} + Z^{\mathrm{T}} \tag{13}$$

Applying this property to **Eq. 11**, we can get

$$(A\otimes I + I\otimes A)^{\mathrm{T}} = (A\otimes I)^{\mathrm{T}} + (I\otimes A)^{\mathrm{T}} \tag{14}$$

According to Chen and Zhou (2012), the relationship between the matrix transpose and Kronecker product is as follows:

$$(Y\otimes Z)^{\mathrm{T}} = Y^{\mathrm{T}}\otimes Z^{\mathrm{T}} \tag{15}$$

Applying this property to **Eq. 14**, we can get

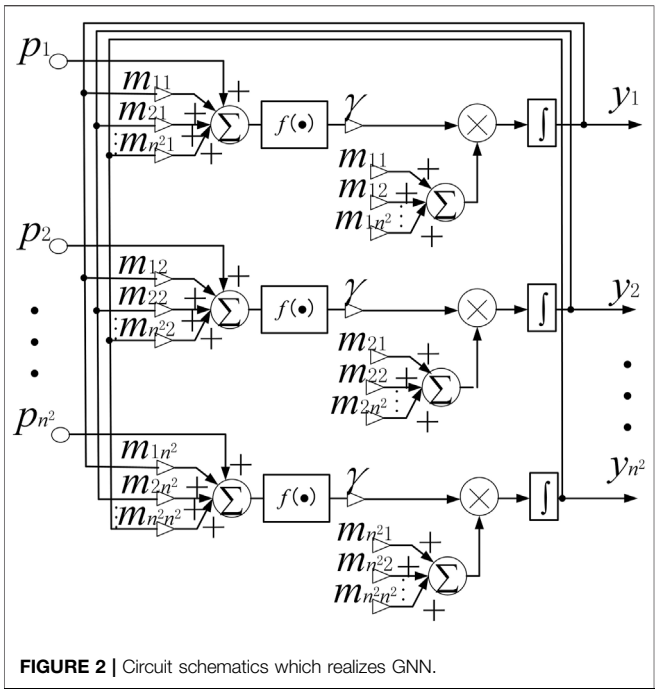

FIGURE 2 | Circuit schematics which realizes GNN.

$$(A \otimes I)^{\mathrm{T}} + (I \otimes A)^{\mathrm{T}} = A^{\mathrm{T}} \otimes I^{\mathrm{T}} + I^{\mathrm{T}} \otimes A^{\mathrm{T}} \tag{16}$$

Considering $I = I^{\mathrm{T}}$ and combining **Eqs 11**, **12**, **14** and **16**, we can get

$$(A \oplus A)^{\mathrm{T}} = A^{\mathrm{T}} \oplus A^{\mathrm{T}} \tag{17}$$

Vectorization of the ZNN Model

The vectorization process of the ZNN model is similar to that of the GNN. Carry out Kronecker product on **Eq. 8**, and we can get:

$$\begin{aligned}(A^{\mathrm{T}} \oplus A^{\mathrm{T}})\mathrm{vec}\dot{X}(t) &= -\gamma\varphi\left((A^{\mathrm{T}} \otimes I)\mathrm{vec}X(t) + (I \otimes A^{\mathrm{T}})\mathrm{vec}X(t) + \mathrm{vec}C\right) \\ &= -\gamma\varphi\left((A^{\mathrm{T}} \oplus A^{\mathrm{T}})\mathrm{vec}X(t) + \mathrm{vec}C\right)\end{aligned} \tag{18}$$

Vectorization of the RNN Model

By comparing **Eqs 10**, **17** and **18**, it can be seen that the key of vectorization of the RNN model is to solve $A^{\mathrm{T}} \oplus A^{\mathrm{T}}$.

According to **Eq. 12**, the calculation of $A^{\mathrm{T}} \oplus A^{\mathrm{T}}$ can be divided into three steps:

1) Calculate $A^{\mathrm{T}} \otimes I$

$$A^{\mathrm{T}} \otimes I = \begin{bmatrix} a_{11} & \cdots & 0 & \cdots & \cdots & \cdots & a_{n1} & \cdots & 0 \\ \vdots & \ddots & \vdots & \cdots & \cdots & \cdots & \vdots & \ddots & \vdots \\ 0 & \cdots & a_{11} & \cdots & \cdots & \cdots & 0 & \cdots & a_{n1} \\ \vdots & \vdots & \vdots & \ddots & & & \vdots & \vdots & \vdots \\ \vdots & \vdots & \vdots & & \ddots & & \vdots & \vdots & \vdots \\ \vdots & \vdots & \vdots & & & \ddots & \vdots & \vdots & \vdots \\ a_{1n} & \cdots & 0 & \cdots & \cdots & \cdots & a_{nn} & \cdots & 0 \\ \vdots & \ddots & \vdots & \cdots & \cdots & \cdots & \vdots & \ddots & \vdots \\ 0 & \cdots & a_{1n} & \cdots & \cdots & \cdots & 0 & \cdots & a_{nn} \end{bmatrix} \tag{19}$$

where $\begin{bmatrix} a_{ij} & \cdots & 0 \\ \vdots & \ddots & \vdots \\ 0 & \cdots & a_{ij} \end{bmatrix}$ is a diagonal matrix with n rows and n columns. $A^{\mathrm{T}} \otimes I$ is a matrix with n^2 rows and n^2 columns.

2) Calculate $I \otimes A^{\mathrm{T}}$

$$\begin{aligned} I \otimes A^{\mathrm{T}} &= \begin{bmatrix} a_{11} & \cdots & a_{n1} & \cdots & \cdots & \cdots & 0 & \cdots & 0 \\ \vdots & \ddots & \vdots & \cdots & \cdots & \cdots & \vdots & \ddots & \vdots \\ a_{1n} & \cdots & a_{nn} & \cdots & \cdots & \cdots & 0 & \cdots & 0 \\ \vdots & \vdots & \vdots & \ddots & & & \vdots & \vdots & \vdots \\ \vdots & \vdots & \vdots & & \ddots & & \vdots & \vdots & \vdots \\ \vdots & \vdots & \vdots & & & \ddots & \vdots & \vdots & \vdots \\ 0 & \cdots & 0 & \cdots & \cdots & \cdots & a_{11} & \cdots & a_{n1} \\ \vdots & \ddots & \vdots & \cdots & \cdots & \cdots & \vdots & \ddots & \vdots \\ 0 & \cdots & 0 & \cdots & \cdots & \cdots & a_{1n} & \cdots & a_{nn} \end{bmatrix} \\ &= \begin{bmatrix} A^{\mathrm{T}} & 0 & \cdots & 0 \\ 0 & A^{\mathrm{T}} & \cdots & 0 \\ \vdots & \vdots & \ddots & \vdots \\ 0 & 0 & \cdots & A^{\mathrm{T}} \end{bmatrix} \end{aligned} \tag{20}$$

where $I \otimes A^{\mathrm{T}}$ is a matrix with n^2 rows and n^2 columns.

3) Add $A^{\mathrm{T}} \otimes I$ to $I \otimes A^{\mathrm{T}}$

$$A^{\mathrm{T}} \otimes I + I \otimes A^{\mathrm{T}} = \begin{bmatrix} 2a_{11} & \cdots & a_{n1} & \cdots & a_{n1} & \cdots & 0 \\ \vdots & \ddots & \vdots & \cdots & \vdots & \ddots & \vdots \\ a_{1n} & \cdots & a_{nn} + a_{11} & \cdots & 0 & \cdots & a_{n1} \\ \vdots & \vdots & \vdots & \ddots & \vdots & \vdots & \vdots \\ a_{1n} & \cdots & 0 & \cdots & a_{11} + a_{nn} & \cdots & a_{n1} \\ \vdots & \ddots & \vdots & \cdots & \vdots & \ddots & \vdots \\ 0 & \cdots & a_{1n} & \cdots & a_{1n} & \cdots & 2a_{nn} \end{bmatrix} \tag{21}$$

TABLE 2 | Comparison of the original-order RNN and the reduced-order RNN under Example 1.

	Linearity		Non-linearity	
	Original-order RNN	Reduced-order RNN	Original-order RNN	Reduced-order RNN
Scale	9	6	9	6
Proportion	66.7%			
ZNN F-norm	2.8400e-5	2.4700e-5	3.1127e-4	1.9507e-4
GNN F-norm	5.4000e-5	1.5208e-4	3.4400e-5	4.0500e-5

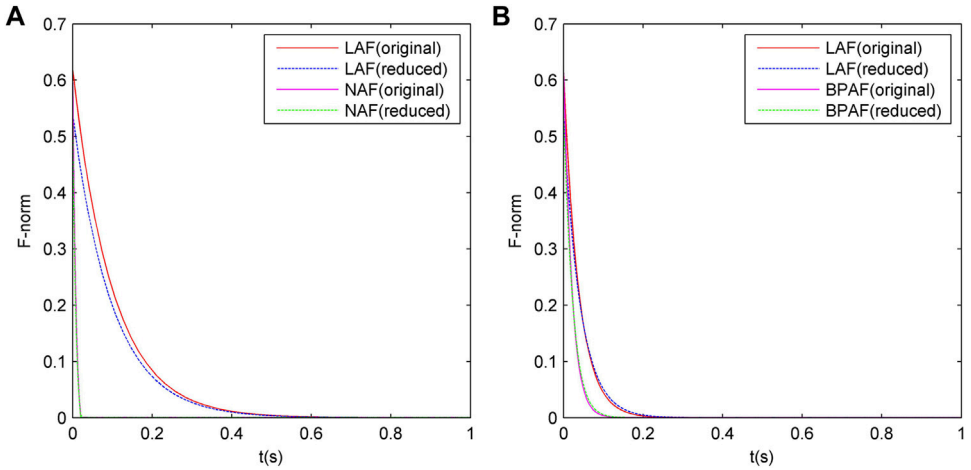

FIGURE 3 | Comparison of the convergence between the original-order and the reduced-order RNN models under Example 1. **(A)** is ZNN, **(B)** is GNN.

TABLE 3 | Comparison of the original-order RNN and the reduced-order RNN under Example 2.

	Linearity		Non-linearity	
	Original-order RNN	**Reduced-order RNN**	**Original-order RNN**	**Reduced-order RNN**
Scale	25	16	25	16
Proportion	64%			
ZNN F-norm	2.6800e-5	2.1400e-5	3.1300e-5	5.1600e-6
GNN F-norm	8.1400e-5	1.7200e-5	1.6487e-4	1.8600e-5

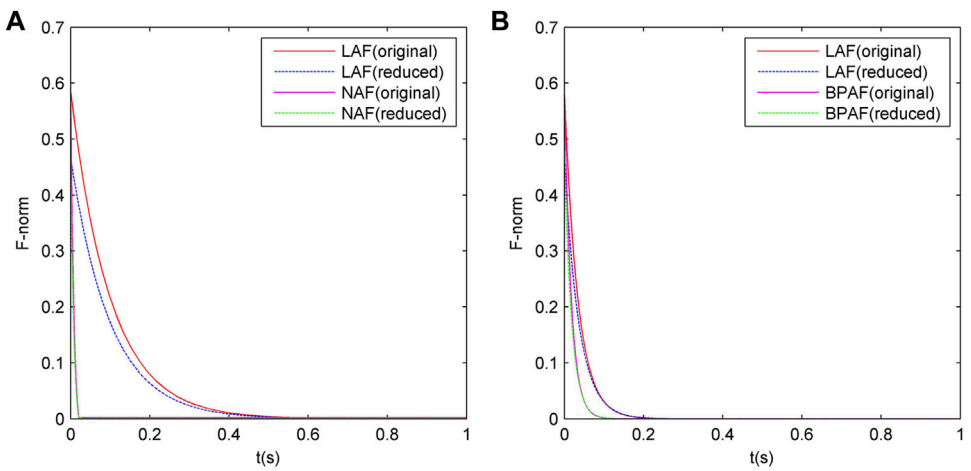

FIGURE 4 | Comparison of the convergence between the original-order and the reduced-order RNN models under Example 2. **(A)** is ZNN, **(B)** is GNN.

TABLE 4 | Comparison of the original-order RNN and the reduced-order RNN under Example 3.

	Linearity		Non-linearity	
	Original-order RNN	**Reduced-order RNN**	**Original-order RNN**	**Reduced-order RNN**
Scale	100	55	100	55
Proportion	55%			
ZNN F-norm	5.4400e-5	4.0800e-5	5.1745e-4	6.9400e-5
GNN F-norm	9.8582e-4	9.9281e-4	3.8700e-5	8.3900e-5

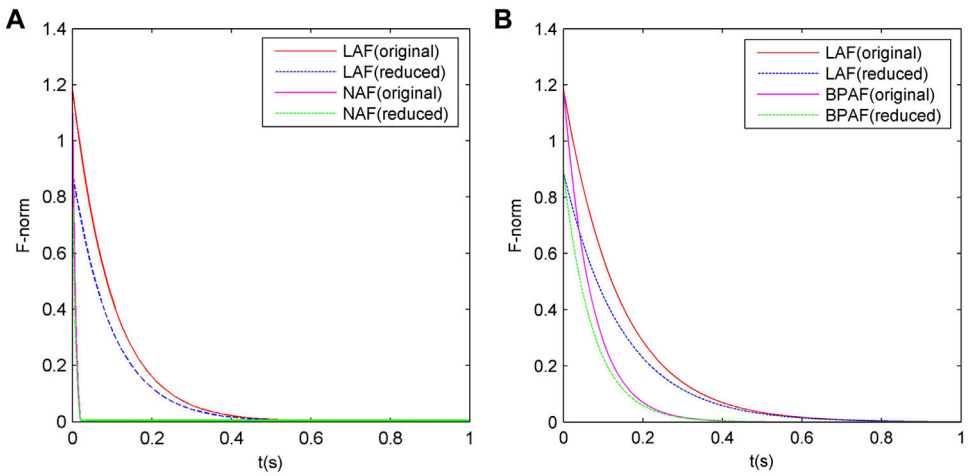

FIGURE 5 | Comparison of the convergence between the original-order and the reduced-order RNN models under Example 3. **(A)** is ZNN, **(B)** is GNN.

TABLE 5 | Comparison of the original-order ZNN and the reduced-order ZNN under Examples 4-6.

	Linearity (15)		Linearity (35)		Linearity (97)	
	Original-order ZNN	**Reduced-order ZNN**	**Original-order ZNN**	**Reduced-order ZNN**	**Original-order ZNN**	**Reduced-order ZNN**
Scale	225	120	1225	630	9409	4753
Proportion	53.3%		51.4%		50.5	
ZNN F-norm	3.3541e-2	3.2454e-2	3.4016e-2	1.5757e-2	1.6214e-3	3.1051e-3

An Efficient Method for Vectorization of RNN Model

According to the previous analysis, no matter how the matrix A is changed, the matrix structure of $A^{\mathrm{T}} \oplus A^{\mathrm{T}}$ is fixed. Based on the special structure of $A^{\mathrm{T}} \oplus A^{\mathrm{T}}$, an efficient method for vectorization of the RNN model is proposed in this article. The steps are as follows.

1) Create a matrix with n^2 rows and n^2 columns named K and fill K with the elements of A according to **Eq. 19**.
2) Fill K with the elements of A according to **Eq. 20**.
3) Add the corresponding element of A to the diagonal element of K according to **Eq. 21**.

The vectorization method of the RNN model proposed in this article is still based on the Kronecker product, but the time complexity is greatly reduced. Because the vectorization method proposed in this article replaces matrix multiplication with assignment and addition.

THE REDUCED-ORDER RNN MODEL FOR SOLVING LYAPUNOV EQUATIONS BASED ON SYMMETRY

Since the solution of **Eq. 1**, X^*, is always symmetric, as long as the upper trigonometric elements of X^* are solved, the

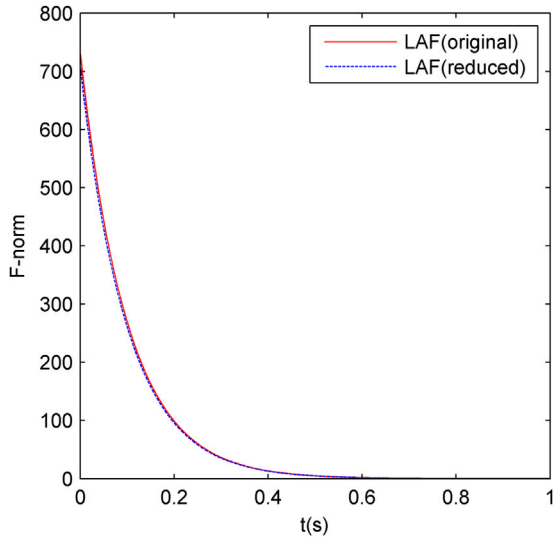

FIGURE 6 | Comparison of the convergence between the original-order and the reduced-order ZNN models under Example 4.

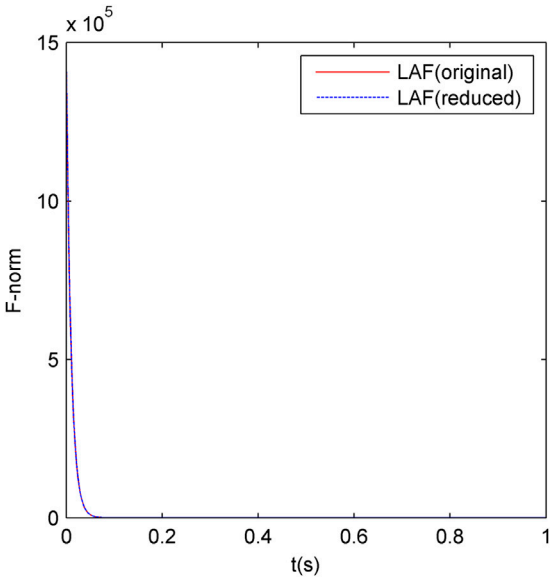

FIGURE 7 | Comparison of the convergence between the original-order and the reduced-order ZNN models under Example 5.

lower trigonometric elements of X^* can be obtained correspondently, which can greatly reduce the computational amount of solving the Lyapunov equations. Based on this idea, a reduced-order RNN model for solving the Lyapunov equation based on symmetry is proposed in this article.

The Reduced-Order ZNN Model With Linear Activation Function

Vectorization

Let's consider a ZNN model with linear activation function after vectorization. The formula is as follows:

$$\begin{bmatrix} k_{11} & k_{12} & \cdots & k_{1,n+1} & \cdots & k_{1,n^2} \\ k_{21} & k_{22} & \cdots & k_{2,n+1} & \cdots & k_{2,n^2} \\ \vdots & \vdots & \ddots & \vdots & \vdots & \vdots \\ k_{n+1,1} & k_{n+1,2} & \cdots & k_{n+1,n+1} & \cdots & k_{n+1,n^2} \\ \vdots & \vdots & \vdots & \vdots & \ddots & \vdots \\ k_{n^2,1} & k_{n^2,2} & \cdots & k_{n^2,n+1} & \cdots & k_{n^2,n^2} \end{bmatrix} \begin{bmatrix} \dot{x}_1 \\ \dot{x}_2 \\ \vdots \\ \dot{x}_{n+1} \\ \vdots \\ \dot{x}_{n^2} \end{bmatrix} = -\gamma \left(\begin{bmatrix} k_{11} & k_{12} & \cdots & k_{1,n+1} & \cdots & k_{1,n^2} \\ k_{21} & k_{22} & \cdots & k_{2,n+1} & \cdots & k_{2,n^2} \\ \vdots & \vdots & \ddots & \vdots & \vdots & \vdots \\ k_{n+1,1} & k_{n+1,2} & \cdots & k_{n+1,n+1} & \cdots & k_{n+1,n^2} \\ \vdots & \vdots & \vdots & \vdots & \ddots & \vdots \\ k_{n^2,1} & k_{n^2,2} & \cdots & k_{n^2,n+1} & \cdots & k_{n^2,n^2} \end{bmatrix} \begin{bmatrix} x_1 \\ x_2 \\ \vdots \\ x_{n+1} \\ \vdots \\ x_{n^2} \end{bmatrix} + \begin{bmatrix} c_1 \\ c_2 \\ \vdots \\ c_{n+1} \\ \vdots \\ c_{n^2} \end{bmatrix} \right) \tag{22}$$

where $K = A^{\mathrm{T}} \oplus A^{\mathrm{T}}$.

For the convenience of later discussion, $S \in \mathbb{R}^{n \times n}$ is constructed. Assign the following values to S as follows:

$$S = \begin{bmatrix} 1 & 2 & \cdots & n \\ n+1 & n+2 & \cdots & 2n \\ \vdots & \vdots & \ddots & \vdots \\ n(n-1)+1 & n(n-1)+2 & \cdots & n^2 \end{bmatrix} \tag{23}$$

Each element of S is the index number of the element of A at the same position.

We can expand X^* to $\mathrm{vec}X^* \in \mathbb{R}^{n^2 \times 1}$. Assuming that x_2^* and x_{n+1}^* are, respectively, the elements of the 1st row and the $n+1$th row of $\mathrm{vec}X^*$. Due to the symmetry, x_2^* will be equal to x_{n+1}^*.

Reduce the Column Number of *K*

If the Kronecker product is directly carried out on **Eq. 1**, then

$$\begin{bmatrix} k_{11} & k_{12} & \cdots & k_{1,n+1} & \cdots & k_{1,n^2} \\ k_{21} & k_{22} & \cdots & k_{2,n+1} & \cdots & k_{2,n^2} \\ \vdots & \vdots & \ddots & \vdots & \vdots & \vdots \\ k_{n+1,1} & k_{n+1,2} & \cdots & k_{n+1,n+1} & \cdots & k_{n+1,n^2} \\ \vdots & \vdots & \vdots & \vdots & \ddots & \vdots \\ k_{n^2,1} & k_{n^2,2} & \cdots & k_{n^2,n+1} & \cdots & k_{n^2,n^2} \end{bmatrix} \begin{bmatrix} x_1 \\ x_2 \\ \vdots \\ x_{n+1} \\ \vdots \\ x_{n^2} \end{bmatrix} = - \begin{bmatrix} c_1 \\ c_2 \\ \vdots \\ c_{n+1} \\ \vdots \\ c_{n^2} \end{bmatrix} \tag{24}$$

We can use $K\mathrm{vec}X = -\mathrm{vec}C$ to express **Eq. 24**. Lan (2017) points out that if A is stable and C is symmetrically positive definite, then the Lyapunov **Eq. 1** has a unique symmetric positive definite solution. Therefore, the K matrix of **Eq. 24** must be invertible.

Multiply both sides of **Eq. 22** by the inverse matrix of K, then we get

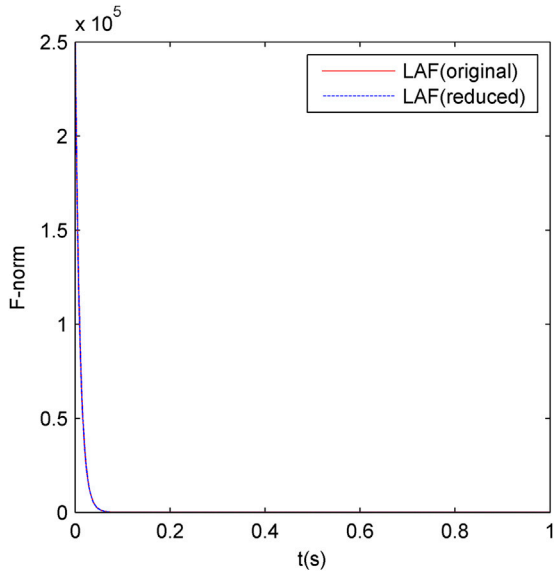

FIGURE 8 | Comparison of the convergence between the original-order and the reduced-order ZNN models under Example 6.

$$\begin{bmatrix} \dot{x_1} \\ \dot{x_2} \\ \vdots \\ \dot{x_{n+1}} \\ \vdots \\ \dot{x_{n^2}} \end{bmatrix} = -\gamma \left(\begin{bmatrix} x_1 \\ x_2 \\ \vdots \\ x_{n+1} \\ \vdots \\ x_{n^2} \end{bmatrix} + K^{-1} \begin{bmatrix} c_1 \\ c_2 \\ \vdots \\ c_{n+1} \\ \vdots \\ c_{n^2} \end{bmatrix} \right) \tag{25}$$

From **Eq. 25**, we can see that $K^{-1}\text{vec}C$ is the solution of the Lyapunov **Eq. 1**, which means $K^{-1}\text{vec}C = \text{vec}X^*$. Since X^* is a symmetric matrix, the differential equations of $x_2(t)$ and $x_{n+1}(t)$ are the same. If $x_2(0)$ and $x_{n+1}(0)$ are equal, then the time domain trajectories of $x_2(t)$ and $x_{n+1}(t)$ are the same, namely, $\dot{x_2}(t) = \dot{x_{n+1}}(t)$ and $x_2(t) = x_{n+1}(t)$. Therefore, for **Eq. 22**, the column $n+1$ of K can be added to the second column. Similarly, the same operation of column addition can be performed on the other columns in the symmetric positions. So the column number of K reduces to $0.5(n+1)n$. **Eq. 22** becomes

$$\begin{bmatrix} k_{11} & k_{12} & \dots & k_{1,0.5(n+1)n} \\ k_{21} & k_{22} & \dots & k_{2,0.5(n+1)n} \\ \vdots & \vdots & \ddots & \vdots \\ k_{n+1,1} & k_{n+1,2} & \dots & k_{n+1,0.5(n+1)n} \\ \vdots & \vdots & \vdots & \vdots \\ k_{n^2,1} & k_{n^2,2} & \dots & k_{n^2,0.5(n+1)n} \end{bmatrix} \begin{bmatrix} \dot{x_1} \\ \dot{x_2} \\ \vdots \\ \dot{x}_{0.5(n+1)n} \end{bmatrix} =$$
$$-\gamma \left(\begin{bmatrix} k_{11} & k_{12} & \dots & k_{1,0.5(n+1)n} \\ k_{21} & k_{22} & \dots & k_{2,0.5(n+1)n} \\ \vdots & \vdots & \ddots & \vdots \\ k_{n+1,1} & k_{n+1,2} & \dots & k_{n+1,0.5(n+1)n} \\ \vdots & \vdots & \vdots & \vdots \\ k_{n^2,1} & k_{n^2,2} & \dots & k_{n^2,0.5(n+1)n} \end{bmatrix} \begin{bmatrix} x_1 \\ x_2 \\ \vdots \\ x_{0.5(n+1)n} \end{bmatrix} + \begin{bmatrix} c_1 \\ c_2 \\ \vdots \\ c_{n+1} \\ \vdots \\ c_{n^2} \end{bmatrix} \right), \tag{26}$$

Reduce the Row Number of *K*

When the steady state is considered, the differential term of **Eq. 26** is 0, and we can get:

$$\begin{bmatrix} k_{11} & k_{12} & \dots & k_{1,0.5(n+1)n} \\ k_{21} & k_{22} & \dots & k_{2,0.5(n+1)n} \\ \vdots & \vdots & \ddots & \vdots \\ k_{n+1,1} & k_{n+1,2} & \dots & k_{n+1,0.5(n+1)n} \\ \vdots & \vdots & \vdots & \vdots \\ k_{n^2,1} & k_{n^2,2} & \dots & k_{n^2,0.5(n+1)n} \end{bmatrix} \begin{bmatrix} x_1 \\ x_2 \\ \vdots \\ x_{0.5(n+1)n} \end{bmatrix} = -\begin{bmatrix} c_1 \\ c_2 \\ \vdots \\ c_{n+1} \\ \vdots \\ c_{n^2} \end{bmatrix} \tag{27}$$

As mentioned before, if A is stable and C is symmetrically positive definite, then Lyapunov **Eq. 1** has a unique symmetric positive definite solution. Therefore, the number of equations should be the same as the number of variables (Cheng and Chen, 2017), namely, the rank of the coefficient matrix of **Eq. 27** is equal to $0.5(n+1)n$, which means the row vector set of the coefficient matrix of **Eq. 27** is linearly correlated.

We can construct the augmented matrix of **Eq. 27** and name it as G. If we define the first row of G as the vector α_1, the second

TABLE 6 | Comparison of the time cost of two vectorization methods for RNN models.

Scale	Method A (ms)	Method B (ms)	Proportion (%)
3	0.032	0.117	19.7
5	0.049	0.132	37.1
10	0.117	0.225	52.0
15	0.221	9.677	2.3
20	0.811	2.245	36.1
30	1.818	9.349	19.4
35	2.070	28.916	7.2
40	3.206	28.254	11.3
50	5.106	71.949	7.1
97	34.983	921.778	3.8

row as the vector α_2, and so on, the row n^2 is defined as the vector α_{n^2}.

According to the knowledge of linear algebra, the vector set $\alpha_1, \alpha_2, \ldots, \alpha_{n^2}$ is linearly dependent only if at least one of the vectors in the set can be represented linearly by the other vectors.

Let us define the vectors which can be represented linearly by the other vectors as the redundant vectors. Suppose that

$$\alpha_{n^2} = h_1\alpha_1 + h_2\alpha_2 + \ldots + h_{n^2-1}\alpha_{n^2-1} \tag{28}$$

where $h_1, h_2, \ldots, h_{n^2-1}$ are real numbers and at least one of them is not equal to 0. Then α_{n^2} is a redundant vector. As long as the redundant vectors are found out and the equations of their corresponding rows are deleted, a new augmented matrix with full row rank can be obtained.

According to the aforementioned analysis, as long as A is stable and C is symmetrically positive definite, then the redundant vectors must exist, which means there are always some vectors that satisfy **Eq. 28**. However, A and C are independent of each other. Considering there are always some vectors satisfying **Eq. 28** in the case of any stable A and any symmetrically positive definite C, there is only one possibility that for some redundant vector, there is another vector that is equal to it, and the row indexes of both of them are symmetric in the matrix S. Only in this way, based on the symmetric characteristics of matrix C, can the redundant vectors always satisfy **Eq. 28** when A and C are independent of each other.

For a redundant vector, its own row index and the row index of another vector equal to it can form a pair of indexes. We can use these index pairs to find the redundant vectors and delete the corresponding rows. In general, in an index pair, the equation corresponding to the index whose value is larger is selected for deletion.

After the row deletion, the row number of K also reduces to $0.5(n+1)n$. **Eq. 26** becomes

$$\begin{bmatrix} k_{11} & k_{12} & \cdots & k_{1,0.5(n+1)n} \\ k_{21} & k_{22} & \cdots & k_{2,0.5(n+1)n} \\ \vdots & \vdots & \ddots & \vdots \\ k_{0.5(n+1)n,1} & k_{0.5(n+1)n,2} & \cdots & k_{0.5(n+1)n,0.5(n+1)n} \end{bmatrix} \begin{bmatrix} \dot{x}_1 \\ \dot{x}_2 \\ \vdots \\ \dot{x}_{0.5(n+1)n} \end{bmatrix}$$
$$= -\gamma\left(\begin{bmatrix} k_{11} & k_{12} & \cdots & k_{1,0.5(n+1)n} \\ k_{21} & k_{22} & \cdots & k_{2,0.5(n+1)n} \\ \vdots & \vdots & \ddots & \vdots \\ k_{0.5(n+1)n,1} & k_{0.5(n+1)n,2} & \cdots & k_{0.5(n+1)n,0.5(n+1)n} \end{bmatrix} \times \begin{bmatrix} x_1 \\ x_2 \\ \vdots \\ x_{0.5(n+1)n} \end{bmatrix} + \begin{bmatrix} c_1 \\ c_2 \\ \vdots \\ c_{0.5(n+1)n} \end{bmatrix}\right) \tag{29}$$

We can use $K_r\mathrm{vec}\dot{X}_r = -\gamma(K_r\mathrm{vec}X_r + \mathrm{vec}C_r)$ to express **Eq. 29**.

Reduced-Order GNN Model With Linear Activation Function

Consider a GNN model with linear activation function after vectorization. The formula is as follows:

$$\begin{bmatrix} \dot{x}_1 \\ \dot{x}_2 \\ \vdots \\ \dot{x}_{n+1} \\ \vdots \\ \dot{x}_{n^2} \end{bmatrix} = -\gamma \begin{bmatrix} k_{11} & k_{12} & \cdots & k_{1,n+1} & \cdots & k_{1,n^2} \\ k_{21} & k_{22} & \cdots & k_{2,n+1} & \cdots & k_{2,n^2} \\ \vdots & \vdots & \ddots & \vdots & \vdots & \vdots \\ k_{n+1,1} & k_{n+1,2} & \cdots & k_{n+1,n+1} & \cdots & k_{n+1,n^2} \\ \vdots & \vdots & \vdots & \vdots & \ddots & \vdots \\ k_{n^2,1} & k_{n^2,2} & \cdots & k_{n^2,n+1} & \cdots & k_{n^2,n^2} \end{bmatrix}^{\mathrm{T}}$$
$$\left(\begin{bmatrix} k_{11} & k_{12} & \cdots & k_{1,n+1} & \cdots & k_{1,n^2} \\ k_{21} & k_{22} & \cdots & k_{2,n+1} & \cdots & k_{2,n^2} \\ \vdots & \vdots & \ddots & \vdots & \vdots & \vdots \\ k_{n+1,1} & k_{n+1,2} & \cdots & k_{n+1,n+1} & \cdots & k_{n+1,n^2} \\ \vdots & \vdots & \vdots & \vdots & \ddots & \vdots \\ k_{n^2,1} & k_{n^2,2} & \cdots & k_{n^2,n+1} & \cdots & k_{n^2,n^2} \end{bmatrix} \begin{bmatrix} x_1 \\ x_2 \\ \vdots \\ x_{n+1} \\ \vdots \\ x_{n^2} \end{bmatrix} + \begin{bmatrix} c_1 \\ c_2 \\ \vdots \\ c_{n+1} \\ \vdots \\ c_{n^2} \end{bmatrix}\right) \tag{30}$$

When the steady state is considered, the differential term of **Eq. 30** is 0, and **Eq. 30** is changed into **Eq. 24**. From the aforementioned derivation, it can be known that both $K\mathrm{vec}X = -\mathrm{vec}C$ and $K_r\mathrm{vec}X_r = -\mathrm{vec}C_r$ can obtain the solution of Lyapunov **Eq. 1**. On this basis, an attempt is made to construct a reduced-order GNN model with linear activation function after vectorization, as follows:

$$\begin{bmatrix} \dot{x}_1 \\ \dot{x}_2 \\ \vdots \\ \dot{x}_{0.5(n+1)n} \end{bmatrix} = -\gamma \begin{bmatrix} k_{11} & k_{12} & \cdots & k_{1,0.5(n+1)n} \\ k_{21} & k_{22} & \cdots & k_{2,0.5(n+1)n} \\ \vdots & \vdots & \ddots & \vdots \\ k_{0.5(n+1)n,1} & k_{0.5(n+1)n,2} & \cdots & k_{0.5(n+1)n,0.5(n+1)n} \end{bmatrix}^{T}$$
$$\left(\begin{bmatrix} k_{11} & k_{12} & \cdots & k_{1,0.5(n+1)n} \\ k_{21} & k_{22} & \cdots & k_{2,0.5(n+1)n} \\ \vdots & \vdots & \ddots & \vdots \\ k_{0.5(n+1)n,1} & k_{0.5(n+1)n,2} & \cdots & k_{0.5(n+1)n,0.5(n+1)n} \end{bmatrix} \begin{bmatrix} x_1 \\ x_2 \\ \vdots \\ x_{0.5(n+1)n} \end{bmatrix} + \begin{bmatrix} c_1 \\ c_2 \\ \vdots \\ c_{0.5(n+1)n} \end{bmatrix}\right). \tag{31}$$

When the steady state is considered, **Eq. 31** is changed into $K_r\mathrm{vec}X_r = -\mathrm{vec}C_r$, which means the solution of Lyapunov **Eq. 1** can be finally obtained by solving **Eq. 31**.

Reduced-Order RNN Model With Non-Linear Activation Functions

Before every non-linear activation function is introduced into the linear RNN, it will be theoretically proved that their introduction can guarantee the correct convergence of RNN. However, the reduced-order RNN in this article does not change the structure of RNN, but only changes the size of RNN. Because both the problem scale and the specific values of the matrix are generally expressed in symbolic form in the theoretical derivation (Xiao and Liao, 2016; Xiao et al., 2019), and the reduced-order RNN model in this article is still applicable to the relevant theoretical proof of introducing the non-linear activation functions into the linear RNN. In other words, the reduced-order method in this article can be applied to the RNN model with non-linear activation functions.

The Generation of the Reduced-Order RNN Model

The steps for generating the reduced-order RNN model are as follows:

1) S is constructed, and the construction logic is as described above.
2) Considering that the indexes in the symmetric positions of S can form $\frac{n(n-1)}{2}$ index pairs, we construct a matrix L and fill L with $\frac{n(n-1)}{2}$ index pairs. It is important to note that all of the elements in the first column of L must be the upper trigonometric elements (excluding diagonal elements) of S. For the convenience of presentation, suppose M is the first column of L, and N is the second column of matrix L.
3) For K and vec$C$ of RNN model, the rows corresponding to the element values of N are deleted.
4) For K and vec$C$ obtained in step 3, add the symmetric columns according to the element values of M and N, and the columns obtained by the addition will replace the columns corresponding to the element values of M, while the columns corresponding to the element values of N will be deleted. For vec$\dot{X}(t)$ and vec$X(t)$, the rows corresponding to the element values of N will be deleted.

It should be pointed out that in mathematical proof, if the order of row reduction and column reduction is exchanged, the correctness of the reduced-order RNN model cannot be proved or another proof method is needed to complete the proof. However, in the case that the mathematical proof has been completed, the order of row reduction and column reduction does not affect the final result, since we know in advance which rows and columns are to be deleted. In the aforementioned steps of generating the reduced-order RNN model, the reason why we carry out step 3 first is that it can reduce the computational amount of the column addition to achieving higher computational efficiency.

The Significance of the Reduced-Order RNN Model

In order to better explain the value and significance of the reduced-order RNN model proposed in this article, the differences before and after the order reduction are shown from the perspectives of software simulation and hardware implementation, respectively. For the convenience of discussion, the GNN is taken as an example to illustrate.

Simulation on the Software

We use the ode45 function of MATLAB to solve the GNN model after vectorization. By comparing **Eq. 30** and **Eq. 31**, it can be seen that the memory requirement of the reduced-order GNN model is much smaller than that of the original GNN model. Therefore, the reduced-order GNN model greatly alleviates the problem of insufficient memory that may occur in the software simulation of the GNN.

Hardware Implementation

When we use the traditional GNN model, the structure of the circuit diagram is shown as **Figure 2** (Yi et al., 2011).

Where $M = [m_{ij}] \in R^{n^2\times n^2} = A \oplus A$, $P = [p_1, p_2, \ldots, p_{n^2}]^{\mathrm{T}} = \mathrm{vec}C \in R^{n^2\times 1}$, $Y = [y_1, y_2, \ldots, y_{n^2}]^{\mathrm{T}} = \mathrm{vec}X \in R^{n^2\times 1}$.

When we use the reduced-order GNN model, the structure of the circuit diagram is shown as **Figure 2**, except that the n^2 in the diagram becomes $0.5(n+1)n$.

So the reduced-order GNN model greatly reduces the number of devices and wiring required for the hardware realization of GNN model, which is conducive to reducing the volume of hardware, the complexity of hardware production, and the failure rate of hardware.

ILLUSTRATIVE VERIFICATION

The simulation examples in this article are all completed on the MATLAB 2013b platform. In this article, the ode45 function of MATLAB is used to simulate the iterative process of RNN (Zhang et al., 2008). The corresponding computing performance is tested on a personal computer with Intel Core i7-4790 CPU @3.2GHz and 8 GB RAM.

Since there are great differences between software and hardware in the principle of realizing the integral function, there will be a big gap between the time cost in simulating the RNN process using software and the time cost in implementing the RNN model using hardware. Considering the research on the RNN model used to solve the Lyapunov equation is still in the stage of theoretical exploration, and has not reached the stage of hardware production for the time being, this article does not discuss the influence of the proposed reduced-order RNN model on the time consuming of RNN.

The Reduced-Order RNN Model for Solving Lyapunov Equation Based on Symmetry

Example 1

Let us consider the Lyapunov **Eq. 1** with the following coefficient matrices:

$$A = \begin{bmatrix} -11 & 2 & 3 \\ 4 & -7 & 6 \\ 1 & 8 & -12 \end{bmatrix} \text{ and } C = I^{3\times 3}$$

where A is similar to Example II in Xiao et al. (2019). However, A and C of Example II in Xiao et al. (2019) do not fit the definition of **Eq. 1**, so we change A a little bit and set C to be the identity matrix.

In this example, we set $\gamma = 10$, $\eta = 0.25$, $\omega = 4$, $a_1 = a_2 = a_3 = a_4 = 1$, and $\delta = 4$ (Yi et al., 2011; Xiao et al., 2019).

In order to demonstrate the advantages of the reduced-order RNN model, this article compares the performance of the reduced-order RNN and the original-order RNN, as shown in **Table 2**. In **Table 2**, linearity and non-linearity, respectively, mean the linear activation function and the non-linear activation function. Scale means the row number of vec$X$ or vecX_r. Proportion means the row number of vecX_r divided by the row number of vec$X$. The ZNN F-norm and GNN F-norm, respectively, mean $\| A^{\mathrm{T}}X + XA + C \|_F$ at the end of the simulation of ZNN and GNN.

In order to study the effect of order reduction method proposed in this article on the convergence of the RNN model, the F-norm curves of the original-order RNN model and the reduced-order RNN model are drawn, as shown in **Figure 3**. In **Figure 3A**, LAF means the ZNN model with linear activation functions. NAF means the ZNN model with the non-linear activation function of **Eq. 9**. In **Figure 3B**, LAF means the GNN model with linear activation functions. BPAF means the GNN model with the non-linear activation function of **Eq. 6**. In both **Figure 3A** and **Figure 3B**, F-norm refers to $\| A^{\mathrm{T}}X(t) + X(t)A + C \|_F$.

Example 2

To enlarge the scale of the example, we consider Lyapunov **Eq. 1** with the following coefficient matrices:

$$A = \begin{bmatrix} -17 & 3 & 4 & 5 & 6 \\ 3 & -17 & 3 & 4 & 5 \\ 4 & 3 & -17 & 3 & 4 \\ 5 & 4 & 3 & -17 & 3 \\ 6 & 5 & 4 & 3 & -17 \end{bmatrix} \text{ and } C = I^{5\times 5}$$

where A is similar to Example III in Xiao et al. (2019). However, A and C of Example III in Xiao et al. (2019) do not fit the definition of **Eq. 1**, so we change A a little bit and set C to be the identity matrix.

In this example, RNN's model parameters are the same as Example 1. Similar to Example 1, we can get **Table 3** and **Figure 4**. The definitions of all nouns in **Table 3** are the same as those in **Table 2**, and the definitions of all nouns in **Figure 4** are the same as those in **Figure 3**.

Example 3

$$A = \begin{bmatrix} -50 & 5 & 2 & 5 & 9 & 5 & 8 & 3 & 6 & 10 \\ 8 & -51 & 10 & 10 & 7 & 1 & 4 & 4 & 3 & 8 \\ 4 & 3 & -51 & 2 & 4 & 10 & 3 & 9 & 8 & 5 \\ 6 & 10 & 8 & -49 & 6 & 10 & 5 & 1 & 2 & 5 \\ 2 & 2 & 9 & 2 & -47 & 5 & 1 & 1 & 7 & 5 \\ 7 & 9 & 9 & 2 & 1 & -47 & 2 & 2 & 2 & 4 \\ 3 & 6 & 1 & 9 & 3 & 4 & -42 & 7 & 4 & 6 \\ 7 & 10 & 4 & 6 & 2 & 10 & 10 & -44 & 7 & 6 \\ 7 & 1 & 3 & 6 & 2 & 4 & 6 & 7 & -44 & 9 \\ 8 & 5 & 9 & 2 & 3 & 2 & 1 & 5 & 1 & -44 \end{bmatrix} \text{ and } C = I^{10\times 10}$$

A 10*10 matrix is randomly generated and then α-shift is applied to the matrix to make it stable (Yang et al., 1993), which is the generation process of A of Example 3 in this article. C is set to be the identity matrix.

In this example, RNN's model parameters are the same as Example 1. Similar to Example 1, we can get **Table 4** and **Figure 5**. The definitions of all nouns in **Table 4** are the same as those in **Table 2**, and the definitions of all nouns in **Figure 5** are the same as those in **Figure 3**.

Based on the information in the aforementioned three tables, we can draw the following conclusions:

a) The reduced-order RNN model has a very obvious effect, with the scale reduced by about 33–45%. Moreover, the effect of the reduced-order RNN model becomes more obvious with the increase in the size of the example. According to $\lim_{n\to\infty} \frac{0.5n(n+1)}{n^2} = 0.5$, it can be seen that when the size of the example is larger, the percentage of the scale decrease is closer to 50%. The reduced-order RNN model not only greatly alleviates the problem of insufficient memory in the software simulation of RNN but also greatly reduces the number of devices and wiring required for the hardware realization of RNN model, which is conducive to reducing the volume of hardware, the complexity of hardware production, and the failure rate of hardware.
b) Under different case scales, whether it is ZNN or GNN, whether it is linear activation function or non-linear activation function, the steady-state errors of the reduced-order RNN model are very close to 0, which means the reduced-order RNN model can always converge to the correct solution of the Lyapunov equation. This indicates that the reduced-order RNN model is applicable to ZNN and GNN, as well as the scenarios of linear activation function and non-linear activation function, which is consistent with the theoretical derivation results above.
c) Under different case scales, the difference in the steady-state accuracy between the reduced-order RNN and the original-order RNN is very small, indicating that the reduced-order RNN basically does not affect the steady-state accuracy of RNN.

Based on the information in the aforementioned three figures, we can draw the following conclusions:

a) Under different case scales, the reduced-order RNN models with linear or non-linear activation functions either have a little effect on the iterative convergence characteristics or enhance the convergence at the beginning of the iteration process and have a little effect on the convergence at the end of it.
b) Under the non-linear activation functions, the convergence of the ZNN model is always stronger than that of the GNN model when other conditions are fixed.
c) Under the linear activation function, the convergence of the ZNN model is weaker than that of the GNN model when the size of the examples is small (e.g., Example 1 and Example 2). The convergence of the linear ZNN model is stronger than that of the linear GNN model when the size of the examples is large (e.g., Example 3).
d) For both ZNN and GNN, the convergence of the RNN model with non-linear activation function is always stronger than that of the linear RNN model.
e) With the increase in the size of the examples, the convergence of ZNN is basically unchanged, while the convergence of GNN will become significantly worse.

Example 4

In order to verify the applicability of neural dynamics method to the power system, the corresponding Lyapunov equation describing system controllability is generated for the IEEE three-machine nine-node system according to the principle of the balanced truncation method in (Zhao et al., 2014). The input signal is the rotor speed deviation and the output signal is the auxiliary stabilizing signal (Zhu et al., 2016). It should be noted that the IEEE standard systems used in this article come from the examples of the PST toolkit (Lan, 2017), and the linearization process of the system is realized by the svm_mgen.m of PST toolkit. We set $\gamma = 10$. $A \in \mathbb{R}^{15\times 15}$ and $C \in \mathbb{R}^{15\times 15}$ of the Lyapunov equation are detailed in **Supplementary Material**.

In this example, the linear ZNN was selected for testing. Similar to Example 1, we can get **Table 5** and **Figure 6**. The definitions of all nouns in **Table 5** are the same as those in **Table 2** and the definitions of all nouns in **Figure 6** are the same as those in **Figure 3**.

Example 5

Similar to Example 4, we generate the corresponding Lyapunov equation describing system controllability of the IEEE 16-machine

system. $A \in \mathbb{R}^{35\times35}$ and $C \in \mathbb{R}^{35\times35}$ of the Lyapunov equation are detailed in **Supplementary Material**. We set $\gamma = 100$. The simulation results are shown in **Table 5** and **Figure 7**. The definitions of all nouns in **Figure 7** are the same as those in **Figure 3**.

Example 6

Similar to Example 4, we generate the corresponding Lyapunov equation describing system controllability of the IEEE 48-machine system. $A \in \mathbb{R}^{97\times97}$ and $C \in \mathbb{R}^{97\times97}$ of the Lyapunov equation are detailed in **Supplementary Material**. We set $\gamma = 100$. The simulation results are shown in **Table 5** and **Figure 8**. The definitions of all nouns in **Figure 8** are the same as those in **Figure 3**.

It can be seen from **Table 5** and **Figures 6–8** that the neural dynamics method used to solve Lyapunov equations is also suitable for solving Lyapunov equations in power systems, and the reduced-order RNN mosdels proposed in this article is effective in the example of power systems. Moreover, with the increase in the power system scale, the convergence and steady-state accuracy of ZNN model are almost unchanged, indicating the applicability of the RNN model to power systems of different scales.

It is worth mentioning that the integration between the electric power and natural gas systems has been steadily enhanced in recent decades. The incorporation of natural gas systems brings, in addition to a cleaner energy source, greater reliability and flexibility to the power system (Liu et al., 2021). Since the dynamic model of the electricity–gas coupled system can be expressed by differential-algebraic equations (Zhang, 2005; Yang, 2020), which means the dynamic model of the electricity–gas coupled system is the same as that of the power system, the aforementioned applicability analysis of the methods proposed in this article for large power systems are also applicable to large electricity–gas coupled systems.

An Efficient Method for Vectorization of RNN Model

Table 6 compares the time cost of the RNN model vectorization method proposed in this article and the traditional RNN model vectorization method. For the sake of convenience, the former is called method A and the latter is called method B. In order to better demonstrate the effect of the vectorization method of RNN model proposed in this article, four examples are added, as shown in **Table 6**. Four newly added examples are generated in the same way as Example 3 and are detailed in **Supplementary Material**, where ms means millisecond; scale means the order of A; and proportion refers to the time taken by method A divided by the time taken by method B.

It can be seen from **Table 6** that method A is significantly better than method B in terms of time cost, with the decrease in time cost between 48 and 98%. With the increase in the size of the examples, the proportion of time cost improvement generally increases. It should be pointed out that when the system sizes are 15, 35, and 97, the corresponding examples are the IEEE standard systems mentioned before, which indicates that the vectorization method proposed in this article is also effective in the example of power systems.

CONCLUSION

1) We propose an efficient method for vectorizing RNN models, which can achieve higher computational efficiency than the traditional method of vectorizing RNN based on the Kronecker product.
2) In order to reduce the solving scale of the RNN model, a reduced-order RNN model for solving the Lyapunov equation was proposed based on symmetry. At the same time, it is proved theoretically that the proposed model can maintain the same solution as that of the original model, and it is also proved that the proposed model is suitable for both the ZNN model and GNN model under linear or non-linear activation functions.
3) Several simulation examples are given to verify the effectiveness and superiority of the proposed method, while three standard examples of power systems are given to verify that the neural dynamics method is suitable for solving the Lyapunov equation of power systems.

Because the neural dynamics method has parallel distribution characteristics and hardware implementation convenience, its convergence and computation time are not sensitive to the system scale. Considering the current development level and trend of the very large-scale integration (VLSI) chip and the ultra large-scale integration (ULSI) chip, the wide application of the neural dynamics method in large-scale systems is expected.

In addition, the research on the RNN model used to solve the Lyapunov equation is mainly in the stage of theoretical improvement and exploration, and there are few reports about hardware products. The hardware product design will be the main content of the next stage.

DATA AVAILABILITY STATEMENT

The original contributions presented in the study are included in the article/**Supplementary Material**, further inquiries can be directed to the corresponding author.

AUTHOR CONTRIBUTIONS

All authors listed have made a substantial, direct, and intellectual contribution to the work and approved it for publication.

FUNDING

This work was supported in part by the Key-Area Research and Development Program of Guangdong Province (2019B111109001), the National Natural Science Foundation of China (51577071), and the Southern Power Grid Corporation's Science and Technology Project (Project No. 037700KK52190015 (GDKJXM20198313)).

SUPPLEMENTARY MATERIAL

The Supplementary Material for this article can be found online at: https://www.frontiersin.org/articles/10.3389/fenrg.2022.796325/full#supplementary-material

REFERENCES

Bartels, R. H., and Stewart, G. W. (1972). Solution of the Matrix Equation AX + XB = C [F4]. *Commun. ACM* 15 (9), 820–826. doi:10.1145/361573.361582

Chen, Z., and Zhou, J. (2012). *Introduction to Matrix Theory*. Beijing: Beihang University Press.

Chen, Q., Gong, C., Zhao, J., Wang, Y., and Zou, D. (2017). Application of Parallel Sparse System Direct Solver Library Super LU_MT in State Estimation. *Automation Electric Power Syst.* 41 (3), 83–88. doi:10.7500/AEPS20160607008

Cheng, K., and Chen, X. (2017). *Linear Algebra*. Chongqing: Chongqing University Press.

Chicca, E., Stefanini, F., Bartolozzi, C., and Indiveri, G. (2014). Neuromorphic Electronic Circuits for Building Autonomous Cognitive Systems. *Proc. IEEE* 102 (9), 1367–1388. doi:10.1109/JPROC.2014.2313954

Hafiz, F., Awal, M. A., Queiroz, A. R. d., and Husain, I. (2020). Real-Time Stochastic Optimization of Energy Storage Management Using Deep Learning-Based Forecasts for Residential PV Applications. *IEEE Trans. Ind. Applicat.* 56 (3), 2216–2226. doi:10.1109/TIA.2020.2968534

He, W., and Zhang, S. (2017). Control Design for Nonlinear Flexible Wings of a Robotic Aircraft. *IEEE Trans. Contr. Syst. Technol.* 25 (1), 351–357. doi:10.1109/TCST.2016.2536708

He, W., Ouyang, Y., and Hong, J. (2017). Vibration Control of a Flexible Robotic Manipulator in the Presence of Input Deadzone. *IEEE Trans. Ind. Inf.* 13 (1), 48–59. doi:10.1109/TII.2016.2608739

Horn, R. A., and Johnson, C. R. (1991). *Topics in Matrix Analysis*. Cambridge: Cambridge University Press.

Lan, X. (2017). *Research on Model Order Reduction Method and Predictive Control Algorithm of Grid Voltage Control System* (Beijing: North China Electric Power University). [dissertation/master's thesis].

Le, X., Chen, S., Li, F., Yan, Z., and Xi, J. (2019). Distributed Neurodynamic Optimization for Energy Internet Management. *IEEE Trans. Syst. Man. Cybern, Syst.* 49 (8), 1624–1633. doi:10.1109/TSMC.2019.2898551

Li, X., Yu, J., Li, S., Shao, Z., and Ni, L. (2019a). A Non-linear and Noise-Tolerant ZNN Model and its Application to Static and Time-Varying Matrix Square Root Finding. *Neural Process. Lett.* 50 (2), 1687–1703. doi:10.1007/s11063-018-9953-y

Li, Y., Zhang, H., Liang, X., and Huang, B. (2019b). Event-Triggered-Based Distributed Cooperative Energy Management for Multienergy Systems. *IEEE Trans. Ind. Inf.* 15 (4), 2008–2022. doi:10.1109/TII.2018.2862436

Li, Y., Gao, D. W., Gao, W., Zhang, H., and Zhou, J. (2020). Double-Mode Energy Management for Multi-Energy System via Distributed Dynamic Event-Triggered Newton-Raphson Algorithm. *IEEE Trans. Smart Grid* 11 (6), 5339–5356. doi:10.1109/TSG.2020.3005179

Lin, Y., and Simoncini, V. (2013). Minimal Residual Methods for Large Scale Lyapunov Equations. *Appl. Numer. Maths.* 72, 52–71. doi:10.1016/j.apnum.2013.04.004

Liu, J., Zhang, J., and Li, Q. (2020a). Upper and Lower Eigenvalue Summation Bounds of the Lyapunov Matrix Differential Equation and the Application in a Class Time-Varying Nonlinear System. *Int. J. Control.* 93 (5), 1115–1126. doi:10.1080/00207179.2018.1494389

Liu, Z., Chen, Y., Song, Y., Wang, M., and Gao, S. (2020b). Batched Computation of Continuation Power Flow for Large Scale Grids Based on GPU Parallel Processing. *Power Syst. Techn.* 44 (3), 1041–1046. doi:10.13335/j.1000-3673.pst.2019.2050

Liu, H., Shen, X., Guo, Q., and Sun, H. (2021). A Data-Driven Approach towards Fast Economic Dispatch in Electricity-Gas Coupled Systems Based on Artificial Neural Network. *Appl. Energ.* 286, 116480. doi:10.1016/j.apenergy.2021.116480

Raković, S. V., and Lazar, M. (2014). The Minkowski-Lyapunov Equation for Linear Dynamics: Theoretical Foundations. *Automatica* 50 (8), 2015–2024. doi:10.1016/j.automatica.2014.05.023

Shanmugam, L., and Joo, Y. H. (2021). Stability and Stabilization for T-S Fuzzy Large-Scale Interconnected Power System with Wind Farm via Sampled-Data Control. *IEEE Trans. Syst. Man. Cybern, Syst.* 51 (4), 2134–2144. doi:10.1109/TSMC.2020.2965577

Stykel, T. (2008). Low-rank Iterative Methods for Projected Generalized Lyapunov Equations. *Electron. Trans. Numer. Anal.* 30 (1), 187–202. doi:10.1080/14689360802423530

Xiao, L., and Liao, B. (2016). A Convergence-Accelerated Zhang Neural Network and its Solution Application to Lyapunov Equation. *Neurocomputing* 193, 213–218. doi:10.1016/j.neucom.2016.02.021

Xiao, L., Zhang, Y., Hu, Z., and Dai, J. (2019). Performance Benefits of Robust Nonlinear Zeroing Neural Network for Finding Accurate Solution of Lyapunov Equation in Presence of Various Noises. *IEEE Trans. Ind. Inf.* 15 (9), 5161–5171. doi:10.1109/TII.2019.2900659

Yang, J., Chen, C. S., Abreu-garcia, J. A. D., and Xu, Y. (1993). Model Reduction of Unstable Systems. *Int. J. Syst. Sci.* 24 (12), 2407–2414. doi:10.1080/00207729308949638

Yang, H. (2020). *Dynamic Modeling and Stability Studies of Integrated Energy System of Electric, Gas and Thermal on Multiple Time Scales* (Hunan: Changsha University of Science & Technology). [dissertation/master's thesis].

Yi, C., Chen, Y., and Lu, Z. (2011). Improved Gradient-Based Neural Networks for Online Solution of Lyapunov Matrix Equation. *Inf. Process. Lett.* 111 (16), 780–786. doi:10.1016/j.ipl.2011.05.010

Yi, C., Chen, Y., and Lan, X. (2013). Comparison on Neural Solvers for the Lyapunov Matrix Equation with Stationary & Nonstationary Coefficients. *Appl. Math. Model.* 37 (4), 2495–2502. doi:10.1016/j.apm.2012.06.022

Yunong Zhang, Z., and Danchi Jiang, M. T. J. (1995). *A Recurrent Neural Network for Solving Sylvester Equation with Time-Varying Coefficients*. New York: Academic Press.

Zhang, Y., Jiang, D., and Wang, J. (2002). A Recurrent Neural Network for Solving Sylvester Equation with Time-Varying Coeffificients. *IEEE Trans. Neural Netw.* 13 (5), 1053–1063. doi:10.1109/TNN.2002.1031938

Zhang, Y., Chen, K., Li, X., Yi, C., and Zhu, H. (2008). "Simulink Modeling and Comparison of Zhang Neural Networks and Gradient Neural Networks for Time-Varying Lyapunov Equation Solving," in Proceedings of IEEE International Conference on Natural Computation. Jinan. IEEE, 521–525. doi:10.1109/ICNC.2008.47

Zhang, Y. (2005). *Study on the Methods for Analyzing Combined Gas and Electricity Networks* (Beijing: China Electric Power Research Institute). [dissertation/master's thesis].

Zhao, H., Lan, X., Xue, N., and Wang, B. (2014). Excitation Prediction Control of Multi-machine Power Systems Using Balanced Reduced Model. *IET Generation, Transm. Distribution* 8 (6), 1075–1081. doi:10.1049/iet-gtd.2013.0609

Zhou, B., Duan, G.-R., and Li, Z.-Y. (2009). Gradient Based Iterative Algorithm for Solving Coupled Matrix Equations. *Syst. Control. Lett.* 58 (5), 327–333. doi:10.1016/j.sysconle.2008.12.004

Zhu, Z., Geng, G., and Jiang, Q. (2016). Power System Dynamic Model Reduction Based on Extended Krylov Subspace Method. *IEEE Trans. Power Syst.* 31 (6), 4483–4494. doi:10.1109/TPWRS.2015.2509481

Conflict of Interest: The authors declare that the research was conducted in the absence of any commercial or financial relationships that could be construed as a potential conflict of interest.

frontiers in Energy Research

ORIGINAL RESEARCH
published: 07 February 2022
doi: 10.3389/fenrg.2022.794191

Adaptive Balancing Control of Cell Voltage in the Charging/Discharging Mode for Battery Energy Storage Systems

Yanfeng Wang[1], *Di Liu*[1], *Yongpeng Shen*[1]*, *Yaohua Tang*[2], *Yanhui Chen*[3] *and Junmin Zhang*[3]

[1]College of Electrical and Information Engineering, Zhengzhou University of Light Industry, Zhengzhou, China, [2]Rundian Energy Science and Technology Co., Ltd., Zhengzhou, China, [3]Pinggao Group Intelligent Power Technology Co., Ltd., Pingdingshan, China

To improve the balancing time of battery energy storage systems with "cells decoupled and converters serial-connected," a new cell voltage adaptive balancing control method in both charging and discharging modes is proposed in this study. The overall system architecture and basic operating principle of the active balancing system with "cells decoupled and converters serial-connected" are presented first. Then, by dynamically regulating the balancing acceleration coefficient of each cell according to the cell voltage deviation, the adaptive balancing control of cell voltage in charging and discharging modes is analyzed. An experimental prototype consisting of six smart cells is developed, and experiments in charging and discharging modes were carried out. The experiment results demonstrate that compared with the balancing process with a static acceleration coefficient, the proposed adaptive balancing control of cell voltage shows significant improvement in balancing speed and smaller cell voltage discrepancy.

Keywords: energy storage system, adaptive balancing control, acceleration coefficient, cell voltage discrepancy, charging/discharging

OPEN ACCESS

Edited by:
Yan Xu,
Nanyang Technological University, Singapore

Reviewed by:
Jichao Hong,
University of Science and Technology Beijing, China
Ke Wang,
Chongqing University, China

***Correspondence:**
Yongpeng Shen
shenyongpeng@zzuli.edu.cn

Specialty section:
This article was submitted to Smart Grids, a section of the journal Frontiers in Energy Research

Received: *13 October 2021*
Accepted: *03 January 2022*
Published: *07 February 2022*

Citation:
Wang Y, Liu D, Shen Y, Tang Y, Chen Y and Zhang J (2022) Adaptive Balancing Control of Cell Voltage in the Charging/Discharging Mode for Battery Energy Storage Systems. Front. Energy Res. 10:794191. doi: 10.3389/fenrg.2022.794191

INTRODUCTION

In grid-connected energy storage systems and electric vehicles, battery packs are made from long strings of parallel cells in series to achieve higher operating voltages, while each parallel cell consists of several individual cells in parallel to achieve the desired capacity or power levels. For example, the standard 50 kWh Tesla Model three-battery pack is made of aaaa2,976 of 2170-size individual lithium-ion cells that are connected in the form of 31 individual cells in parallel and 96 parallel cells in series to provide 350 V output voltage and 211 kW output power (Lambert, 2017).

Since cells are charged and discharged by equal currents in multicell battery chains, small differences between cells due to production tolerances or operating conditions tend to be magnified with each charge/discharge cycle. During a charge/discharge cycle, if there is a degraded cell in the chain with diminished capacity, it will be subject to overcharging or overdischarging and will tend to

Abbreviations: k_{pv}, proportional coefficient of voltage loop; k_{iv}, integral coefficient of voltage loop; k_{dv}, differential coefficient of voltage loop; k_{pi}, proportional coefficient of current loop; k_{ii}, integral coefficient of current loop; k_{di}, differential coefficient of current loop; I^*, current demand; V_{cell}, cell port voltage; V_{out}, DC bus port voltage; DC/DC, bidirectional buck–boost DC/DC converter; PID, proportional integral derivative control; PWM, pulse width modulation; CAN, controller area network bus; SOC, state of charge.

fail before the others. That is, with every charge/discharge cycle, the weaker cells will get weaker until they fail. Overall, in an unmanaged string of cells in series, the capacities of cells are likely to diverge from one another during a charge/discharge cycle, which can result in degraded battery energy utilization and even damage or explosions (Huang and Qahouq, 2015). Cell balancing is a way to compensate for weaker cells by equalizing the charge on all the cells in the chain, thus extending battery life.

Various methods of cell balancing have been developed to address this problem by equalizing the stress on the cells and are broadly divided into two categories: passive methods and active methods (Omariba et al., 2019; Pinto et al., 2016; Gallardo et al., 2014; Ouyang et al., 2018). Passive methods are also known as "resistor bleeding balancing" methods (Ye and Cheng, 2017); they remove excess energy from the cell that has higher cell voltage through a bypass resistor until the voltage or charge matches the voltage of the weaker cells (Daowd et al., 2011). Passive methods have the advantages of low cost, simple circuit configurations, and ease of implementation. However, this causes dissipation of additional energy (Huang and Qahouq, 2015), and because low bypass currents are used, equalization times are very long.

Active cell balancing methods remove charge from higher energy cells and deliver it to lower energy cells through active cell equalizing circuits. They have different topologies according to the circuit and active element used to store energy, such as capacitors and/or inductive components (Daowd et al., 2011; Cao et al., 2008; Yu et al., 2019; Tang et al., 2019; Zhang et al., 2019; Tavakoli et al., 2019). There are three subcategories of active balancing methods sorted by circuit topology, namely, charge shunting (Hsieh et al., 2002; Shibata et al., 2001), charge shuttling (Cao et al., 2008; Baughman and Ferdowsi, 2008; Ye and Cheng, 2015; Shousha et al., 2017), and energy converting method–based balancing techniques, among which the energy converter–based balancing method is the most widely used technique. As a typical energy converter–based balancing approach, Evzelman et al. (2016) proposed an architecture that uses modular DC/DC bypass converters to perform active battery cell balancing and to supply current to auxiliary loads, eliminating the need for a separate HV-to-LV high step-down DC/DC converter. Based on a two-stage bidirectional equalization circuit with energy transferring inductors, Ma et al. (2018) proposed a fuzzy logic-controlled equalization scheme to reduce energy consumption and equalization time, and the simulation results show that the standard deviation of the final SOC reduces by 18.5%, and the equalization time decreases by 23%. Similar approaches include those of Zhang et al., (2017); Zheng et al., (2014). An optimized sliding mode control (OSMC) based on the current dynamics model was proposed, which tracks the load current and uses it as a reference to realize the self-balancing of the capacitor voltage (Babaie et al., 2021). Owing to the capacity estimation error of about 5–10% caused by battery degradation, active balance architecture of the hierarchical model predictive control was proposed (Gong et al., 2020). In order to realize the active balance control strategy, by utilizing the low-voltage bypass DC–DC converter and the shared low-voltage DC bus, a new cell balancing system for electric vehicle battery packs was proposed (Trimboli et al., 2022). An MPCP and MPVP control scheme was proposed, which realizes the stability of the DC bus current (Shan et al., 2019). In order to keep the capacitor voltage ripple within a reasonable range, Ma et al., (2021) proposed a new battery integration method which can reduce the capacitor voltage ripple effectively.

For the active cell balancing methods, balancing time and accuracy are two important performance indicators that deserve equal attention (Baronti et al., 2014). Most of the existing methods only pay attention to balancing accuracy and show little sensitivity to balancing time. As the main innovation of this study, by dynamically regulating the balancing acceleration coefficient of each cell according to the voltage deviation, the adaptive balancing control of cell voltage in charging and discharging mode is proposed for the active balancing system with "cells decoupled and converters serial connected," which effectively accelerates the balancing speed and improves the balancing accuracy.

This article is organized as follows. In **Section 2**, the overall system architecture and basic operating principle of the active balancing system with "cells decoupled and converters serial-connected" are described. In **Section 3**, the dynamic balancing acceleration coefficient adaptive mechanisms in charging and discharging modes are analyzed successively. In **Section 4**, experiments carried out and the results of the analysis are presented. Finally, the conclusion is stated in **Section 5**.

RESEARCH AND CONTRIBUTION OF THE STUDY

1) Different from the traditional analysis of the "cells decoupled and converters serial-connected" battery energy storage system, this article explores the deeper influence on the balance time of the battery energy storage system.
2) By dynamically adjusting the balance acceleration coefficient of each cell according to the cell voltage deviation, the adaptive balance control of the cell voltage in the charge and discharge modes is analyzed, and a new adaptive balance control method of the cell voltage in the charge and discharge modes is proposed.
3) An experimental device comprising six smart batteries connected in series is built, and the superiority of the proposed battery voltage adaptive balance control strategy is verified.

SYSTEM DESCRIPTION

The system architecture of the proposed cell voltage adaptive balancing control mechanism in charging/discharging modes is shown in **Figure 1**. In **Figure 1**, the active balancing system is named "cells decoupled and converters serial connected," where the battery pack comprises N battery cells. The blue background area shows the general system structure, where N battery cells are decoupled from one another by N distributed converters, and distributed converters are connected in series output to generate a desired DC bus voltage. The output voltage of each distributed

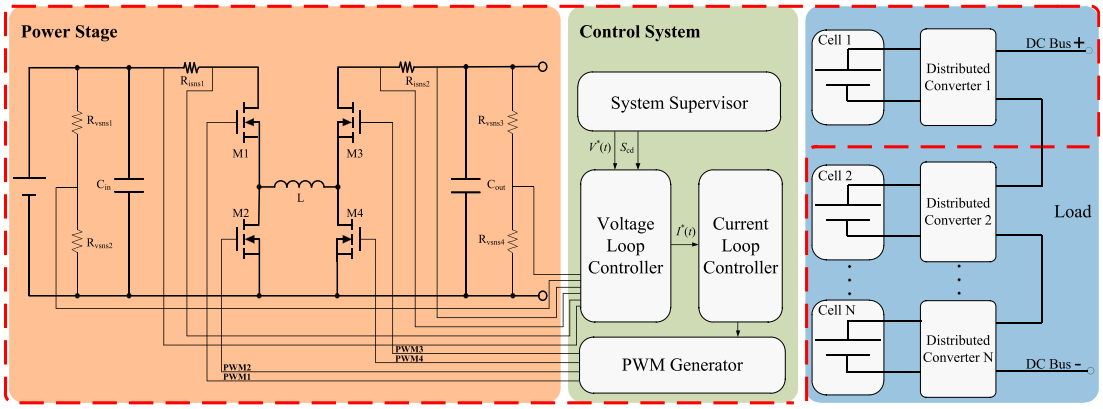

FIGURE 1 | System architecture of the active balancing system with "cells decoupled and converters serial-connected."

converter is adjustable in both the buck and boost modes, and thus, the DC bus voltage is adjustable too. Each combination of a battery cell and a distributed converter is referred to as a "smart cell."

Bidirectional DC/DC conversion between the cell port and DC bus port of the smart cell is accomplished by the power stage of a synchronous 4-switch bidirectional buck–boost DC/DC converter; its main circuit structure is shown in the yellow background area of **Figure 1**, where four switching FETs, M1 to M4, and only one power inductor, L, is utilized. By utilizing the abovementioned structure, bidirectional power conversion between the cell port and DC bus port is achievable, both in the buck and boost modes.

As shown in the green background area of **Figure 1**, to ensure the stability, accuracy, and dynamic characteristics of the output voltage of the 4-switch bidirectional buck–boost DC/DC converter, a capacitor voltage and an inductor current dual closed loop feedback control system are designed, where proportional–integral–differential (PID) control in the outer loop is utilized to realize output voltage control, with k_{pv}, k_{iv}, and k_{dv} as the corresponding proportional, integral, and differential coefficients, respectively, while in the inner loop, PID control is used to improve the transient response of the converter, with k_{pi}, k_{ii}, and k_{di} as the corresponding proportional, integral, and differential coefficients, respectively. In **Figure 1**, the inner loop is responsible for sensing the actual current and then accordingly generating a PWM pulse to achieve current regulation, while the outer loop is responsible for sensing the battery cell port voltage, V_{cell}, and DC bus port voltage, V_{out}, and then sending current demand I^* to the current loop to achieve voltage regulation (Xu and Xu, 2013). Moreover, the system supervisor of the smart cell controls the charging/discharging mode switch signal S_{cd}. Communication between each smart cell is accomplished by the system supervisor through the CAN bus, and then, each smart cell shares the cell voltage, charge voltage, and SOC information. The parameter description utilized in this article is listed in *11 Acronyms and Abbreviations*.

In the discharging mode, the output voltage of each smart cell is adjustable, while current flowing through the DC bus port is dependent on the load for a specific DC bus voltage. The discharging current of the nth cell I_{ncell} at t follows the following equation:

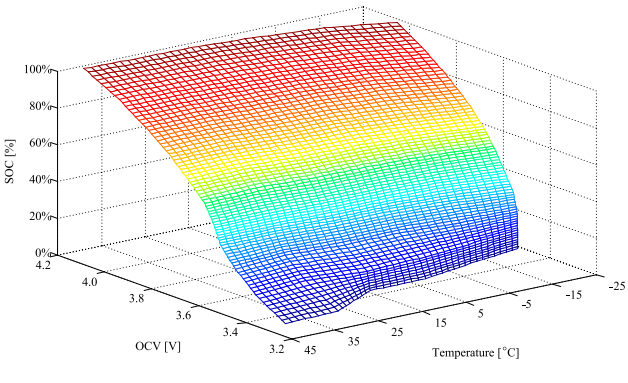

FIGURE 2 | Curved surface of the SOC versus temperature and OCV.

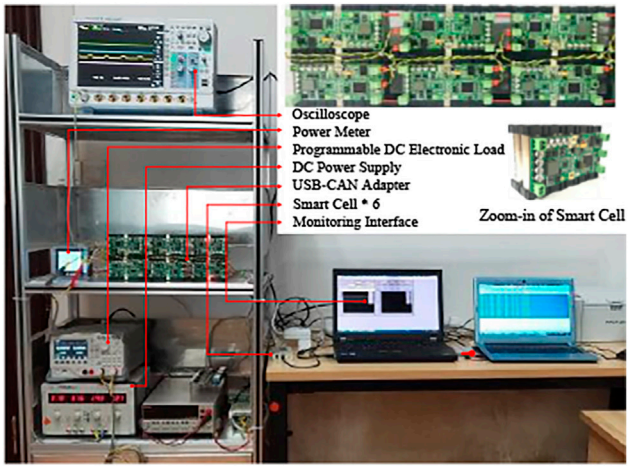

FIGURE 3 | Photograph of the experimental facility.

TABLE 1 | Experimental facility information.

Facility	Model	Parameter	Value
Battery cell	ZH-ISR 18650	Type	$LiCoMnNiO_2$
		Nominal Voltage	3.7 V
		Nominal Capacity	2600 mAh
DC Electronic Load	DL3021	Max voltage and current	150 V/40 A
		Resolution	1m V/1 mA
Oscilloscope	DLM4058	Sample rate	2.5 GS/S
		Bandwidth	500 MHz
DC Power supply	SK1731SL2A	Max current	10 A (Multichannel in parallel)
Converter	Key components	Switching devices	NVMFS5C670NLT3G
		Inductor	ASPI-1367-3R3M-T
		Controller	MC9S12XET256

$$I_{\mathrm{ncell}}(t) = \frac{V_{\mathrm{nout}}(t) \cdot I_{\mathrm{load}}(t)}{V_{\mathrm{ncell}}(t) \cdot \eta[V_{\mathrm{nout}}(t), I_{\mathrm{nout}}(t)]}, \tag{1}$$

where $\mathbf{n} \in \{1, 2, 3, \cdots N\}$, $I(t)$ is the load current at time t and $\eta[V_{\mathrm{nout}}(t), I_{\mathrm{nout}}(t)]$ is the conversion efficiency of the smart cell under $V_{\mathrm{nout}}(t)$ and $I_{\mathrm{nout}}(t)$. $V_{\mathrm{nout}}(t)$ and $V_{\mathrm{ncell}}(t)$ are the voltages of the cell port and DC bus port of the nth smart cell at t, respectively.

Equation 1 shows that I_{ncell} can be arbitrarily controlled by regulating $V_{\mathrm{nout}}(t)$, regardless of the load current. That is, the cell current is decoupled from the load current by utilizing the smart cell, and the discharge rate of each smart cell can be controlled by regulating the output voltage of the corresponding smart cell. The output voltage for a lower discharge rate is lower, the output voltage for a higher discharge rate is higher, and the discharge/charge rate of each smart cell is proportional to its output voltage.

In the charging mode, the bidirectional buck–boost converter works in the current control mode, where the current of each cell is controlled independently by the current loop controller of each smart cell.

According to the desired DC bus voltage and SOC of every cell, the smart cell is able to regulate the discharge/charge rate of the battery cell for SOC balancing and to simultaneously maintain the desired DC bus voltage in both the discharging and charging modes.

ADAPTIVE BALANCING CONTROL OF CELL VOLTAGE

SOC Estimation

The combined OCV (open circuit voltage) and CC (Coulombic counting) method is utilized for SOC estimation. The real-time $SOC_{rt}(t)$ is obtained by the following equation:

$$SOC_{\mathrm{rt}}(t) = SOC_{\mathrm{ini}} - \int_0^t \eta_{\mathrm{i}} I(\tau) / (C_{\mathrm{n}} \cdot SOH_{\mathrm{rt}}) d\tau, \tag{2}$$

where η_i is cell Coulombic efficiency, $\eta_i = 1$ for discharge and $\eta_i \leq 1$ for charge; $I(t)$ is instantaneous cell current (assumed positive for discharge, negative for charge); C_n is the cell nominal capacity in A hour (AH); and SOH_{rt} is the real-time state of health (SOH) of the cell.

In **Equation 2**, the real-time current $I(t)$ is sampled by the current shunt; the initial SOC value SOC_{ini} is predicted according to the relations among cell terminal voltage, temperature, and SOC. **Figure 2** shows the averaged test data of eight 2600-mAH

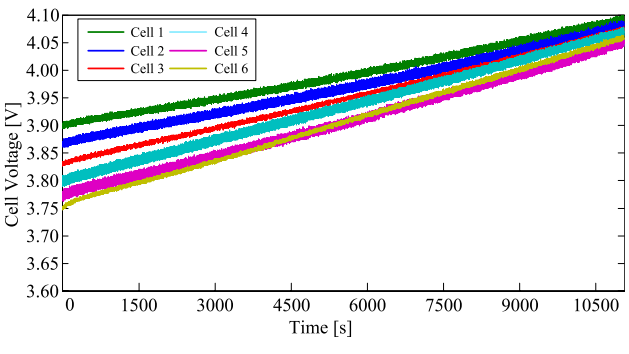

FIGURE 4 | Terminal voltages of six cells during the charging process with a static acceleration coefficient.

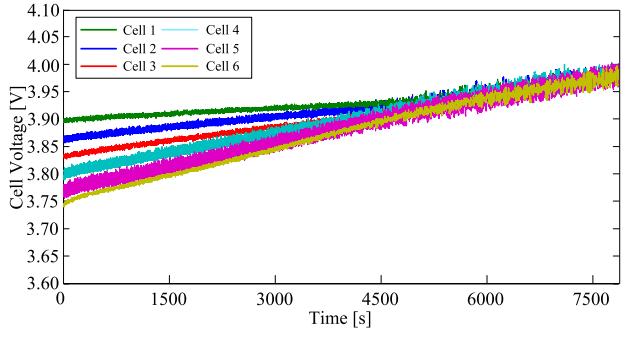

FIGURE 5 | Terminal voltages of six cells during the charging process with a dynamic acceleration coefficient adaptive mechanism.

18650 $LiCoMnNiO_2$ battery cells under different temperature conditions.

Dynamic Balancing Acceleration Coefficient Adaptive Mechanism in the Charging Mode

As described above, the principle of the active balancing system with "cells decoupled and converters serial-connected" is to independently regulate the discharge/charge rate of each cell. Thus, the primary task is to calculate the discharge or charge rate in real time according the status of each cell.

In the charging mode, to characterize the SOC difference at t, $\gamma_n(t)$ is defined as follows:

$$\begin{bmatrix} \gamma_1(t) \\ \gamma_2(t) \\ \vdots \\ \gamma_N(t) \end{bmatrix} = \begin{bmatrix} \rho_1(t) & & & \\ & \rho_2(t) & & \\ & & \ddots & \\ & & & \rho_N(t) \end{bmatrix} \begin{bmatrix} SOC_1(t) - \overline{SOC(t)} \\ SOC_2(t) - \overline{SOC(t)} \\ \vdots \\ SOC_N(t) - \overline{SOC(t)} \end{bmatrix} + \begin{bmatrix} V_{1cell}(t) \\ V_{2cell}(t) \\ \vdots \\ V_{Ncell}(t) \end{bmatrix}, \tag{3}$$

where SOCn(t) is the real-time SOC of the nth cell at t and $\overline{SOC(t)}$ is the average SOC of all cells at t, that is, $\overline{SOC(t)} = \sum_{n=1}^{N} SOC_n(t)/N$. $\rho_n(t)$ is the dynamic balancing acceleration coefficient of the nth cell and is a dynamic adaptive parameter that determines the balancing speed while the SOC deviation is detected.

$$\begin{bmatrix} \rho_1(t) \\ \rho_2(t) \\ \vdots \\ \rho_N(t) \end{bmatrix} = \begin{bmatrix} \frac{V_{1cell}(t)}{V_{cell}^{max}(t) - V_{cell}^{min}(t)} & 0 & 0 & 0 \\ 0 & \frac{V_{2cell}(t)}{V_{cell}^{max}(t) - V_{cell}^{min}(t)} & 0 & 0 \\ 0 & 0 & \vdots & 0 \\ 0 & 0 & 0 & \frac{V_{Ncell}(t)}{V_{cell}^{max}(t) - V_{cell}^{min}(t)} \end{bmatrix}, \tag{4}$$

where $V_{cell}^{max}(t)$ and $V_{cell}^{min}(t)$ are the maximum and minimum cell voltages of all N cells at t, respectively. According to **Eqs. 3, 4**, in the process of cell balancing, the charging current of the nth cell at t+1 results according to **Eq. 5**.

$$I_{ncell}(t+1) = \frac{\gamma_n(t) - \overline{V_{cell}(t)}}{\overline{V_{cell}(t)}} + I_{cset}, \tag{5}$$

where $\overline{V_{cell}(t)} = \sum_{n=1}^{N} V_{ncell}(t)/N$ and I_{cset} is the set value of the charging current. Moreover, $I_{ncell}(t+1)$ should satisfy **Eq. 6**,

$$I_{cmin} \le I_{ncell}(t+1) \le \min(I_{cmax}, C_{imax}), \tag{6}$$

where C_{imax} is the acceptable maximum charging current of the battery cell, and I_{cmin} and I_{cmax} are the minimum and maximum charging currents of the smart cell, respectively.

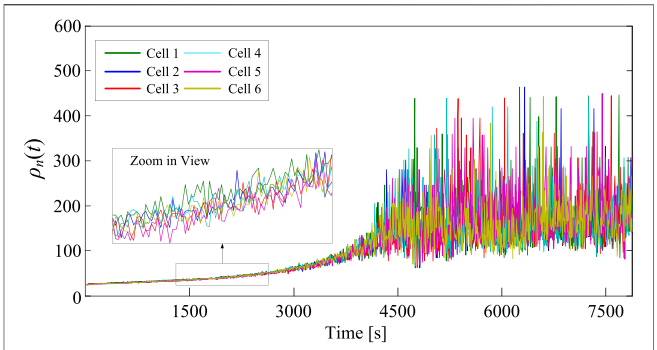

FIGURE 6 | Dynamic acceleration coefficient in the charging process.

Dynamic Balancing Acceleration Coefficient Adaptive Mechanism in the Discharging Mode

In the discharging mode, **Eq. 2** still holds, and now, the adaptive law of $\rho_n(t)$ is shown in **Eq. 7**.

$$\begin{bmatrix} \rho_1(t) \\ \rho_2(t) \\ \vdots \\ \rho_N(t) \end{bmatrix} = \begin{bmatrix} \frac{V_{1cell}(t) - V_{out}^{min}}{\overline{V_{cell}(t)} - V_{cell}^{min}(t)} & 0 & 0 & 0 \\ 0 & \frac{V_{2cell}(t) - V_{out}^{min}}{\overline{V_{cell}(t)} - V_{cell}^{min}(t)} & 0 & 0 \\ 0 & 0 & \vdots & 0 \\ 0 & 0 & 0 & \frac{V_{Ncell}(t) - V_{out}^{min}}{\overline{V_{cell}(t)} - V_{cell}^{min}(t)} \end{bmatrix}, \tag{7}$$

where V_{out}^{min} is the minimum output voltage of the smart cell. Since $\rho_n(t)$ is the dynamic balancing acceleration coefficient of the nth cell in the discharging mode, at any time, it should satisfy **Eq. 8**.

$$V_{out}^{min} \le \left\{ \left[SOC_n(t) - \overline{SOC(t)} \right] \cdot \rho_n(t) + V_{ncell} \right\} \cdot \lambda(t) \le V_{out}^{max}, \tag{8}$$

where $V_{max\,out}$ is the maximum output voltage of the smart cell and $\lambda(t)$ is the DC bus voltage regulation coefficient at t.

$$\lambda(t) = \frac{V_{bus}(t)}{\sum_{n=1}^{N} V_{ncell}(t)}, \tag{9}$$

where $V_{bus}(t)$ is the desired DC bus voltage at t. According to **Eqs. 3, 9**, the discharge current at t+1 is shown in **Eq. 10**.

$$\begin{bmatrix} I_{1cell}(t+1) \\ I_{2cell}(t+1) \\ \vdots \\ I_{Ncell}(t+1) \end{bmatrix} = \begin{bmatrix} \chi_1(t) & & & \\ & \chi_2(t) & & \\ & & \ddots & \\ & & & \chi_N(t) \end{bmatrix}^{-1} \begin{bmatrix} \lambda(t) \cdot I(t) & & & \\ & \lambda(t) \cdot I(t) & & \\ & & \ddots & \\ & & & \lambda(t) \cdot I(t) \end{bmatrix} \begin{bmatrix} \gamma_1(t) \\ \gamma_2(t) \\ \vdots \\ \gamma_N(t) \end{bmatrix}, \tag{10}$$

where $I(t)$ is the DC bus load current at t and $\chi_n(t)$ is defined as follows:

$$\chi_n(t) = V_{ncell}(t) \cdot \eta[V_{nout}(t), I(t)], \tag{11}$$

where $\eta[V_{nout}(t), I(t)]$ is the conversion efficiency of the smart cell under $V_{nout}(t)$ and $I(t)$. The real-time output voltage of every smart cell can be derived by the following equation:

$$\begin{bmatrix} V_{1out}(t+1) \\ V_{2out}(t+1) \\ \vdots \\ V_{Nout}(t+1) \end{bmatrix} = \lambda(t) \cdot \begin{bmatrix} \gamma_1(t) \\ \gamma_2(t) \\ \vdots \\ \gamma_N(t) \end{bmatrix}. \tag{12}$$

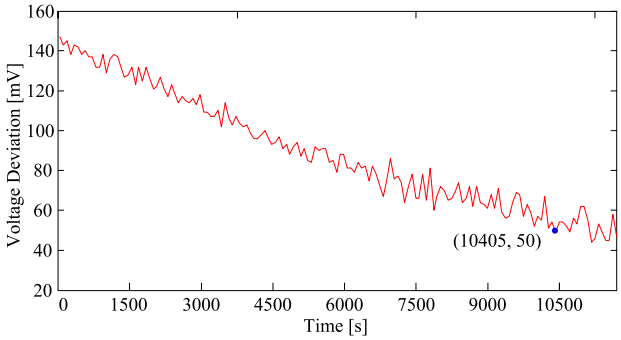

FIGURE 7 | Voltage deviation of six cells during the charging process with a static acceleration coefficient.

ANALYSIS OF EXPERIMENTS AND RESULTS

Experimental Facility

To validate the effectiveness of the proposed dynamic balancing acceleration coefficient adaptive mechanism in charging and discharging modes, experiments were carried out with an experimental setup consisting of six serially connected smart cells, a DC power supply, a programmable DC electronic load, an oscilloscope, a power meter, a USB-CAN adapter, and a monitoring interface implemented on a computer. The photograph of the experimental facility is shown in **Figure 3**. Each smart cell consisted of four parallel 2,600 mAh $LiCoMnNiO_2$ cells connected in parallel to achieve a higher overall capacity. Detailed information of the abovementioned facilities is listed in **Table 1**. The bidirectional buck–boost converter was built around Freescale's 16-bit microcontroller MC9S12XET256, where each smart cell was implemented with an independent converter. The power stage, controller, CAN bus, and peripheral components were integrated in a high-density custom PCB board, as shown in the upper right corner of **Figure 3**.

In Charging Mode

To demonstrate the effectiveness of the dynamic balancing acceleration coefficient adaptive mechanism in the charging mode, the experimental process in the charging mode is designed as follows.

1) At room temperature of 15°C, six smart cells are charged to the initial states with OCVs ranging from 3.75 to 3.90 V. That is, the SOC ranged from 62.7 to 80.0%.
2) The default charging current is set to I_{cset} = 0.75 A.
3) The charging cutoff voltage is set to 4.1 V.
4) Adaptive balancing control is enabled in the charging mode. As a comparison, the charge balancing that utilizes the static acceleration coefficient is performed under the same initial condition, where the coefficient is set to 13.3.

The terminal voltages of six cells during the charging process with a static acceleration coefficient and a dynamic acceleration coefficient adaptive mechanism are shown in **Figures 4**, **5**, respectively. The charging process with a static acceleration coefficient lasts 11,717 s, the voltage discrepancy decreases from 150 to 50 mV, and the charging process is terminated when one of the cells reaches the cutoff voltage of 4.1 V. The charging process with a dynamic acceleration coefficient adaptive mechanism takes 7873s to bring cell voltages to the equilibrium state. **Figure 6** shows that the acceleration coefficient ρ_n of six smart cell values is dynamically regulated according to the cell terminal voltages in the charging process.

The maximum voltage deviation between cells is recorded in periods of 1 s during the charging process. The charging process with a static acceleration coefficient takes 10,405 s to decrease the voltage discrepancy from the initial value of 150–30 mV, while the charging process with a dynamic acceleration coefficient adaptive mechanism takes only 3,860 s, as shown in **Figures 7**, **8** respectively. Furthermore, **Figure 8** shows that the charging process with a dynamic acceleration coefficient adaptive mechanism takes only 4,600 s to decrease the voltage discrepancy to 30 mV, and the final voltage discrepancy is approximately 20 mV.

In Discharging Mode

In the discharging mode, the following experimental processes are designed.

1) At room temperature of 15°C, six smart cells are charged to the initial states with OCVs ranging from 3.77 to 3.95 V, that is, the SOC ranged from 63.9 to 83.8%.
2) The discharging cutoff voltage is set to 3.5 V.
3) The DC electric load is set to 30-Ω constant resistant loading mode, and the DC bus voltage of the smart cell pack is set to V_{bus} = 30 V.
4) Adaptive balancing control is enabled in the discharging mode. Similarly, the discharge balancing operation that utilizes a static acceleration coefficient is performed under the same initial condition.

The terminal voltages of six cells during the discharging processes with a static acceleration coefficient and a dynamic acceleration coefficient adaptive mechanism are shown in **Figures 9**, **10**, respectively. The discharging process with a

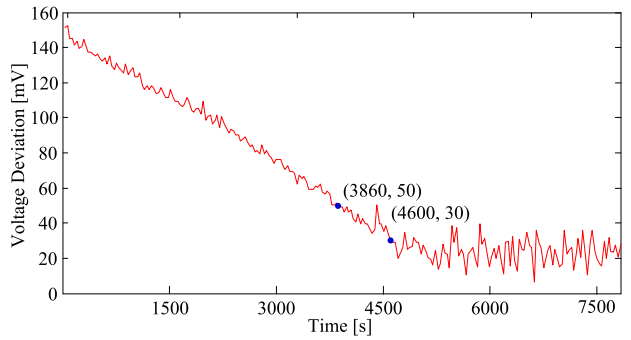

FIGURE 8 | Voltage deviation of six cells during the charging process with a dynamic acceleration coefficient adaptive mechanism.

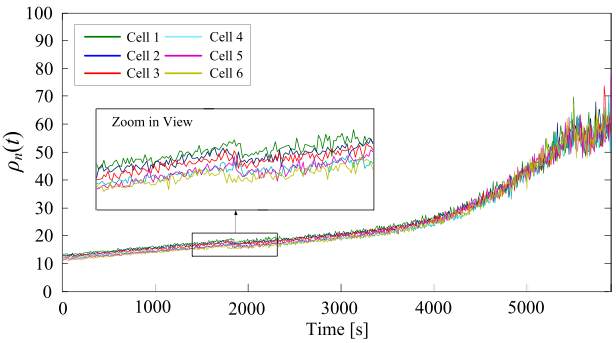

FIGURE 11 | Dynamic acceleration coefficient in the discharging process.

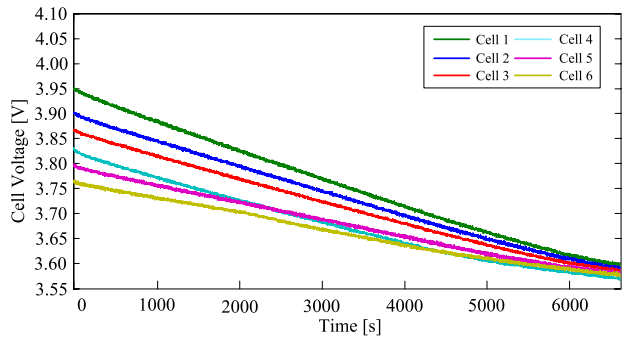

FIGURE 9 | Terminal voltages of six cells during the discharging process with a static acceleration coefficient.

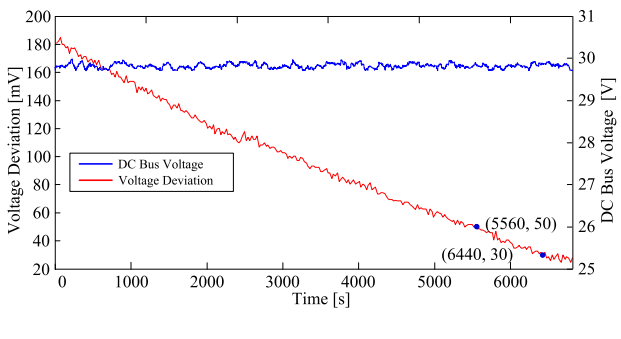

FIGURE 12 | Voltage deviation of six cells and DC bus voltage during the discharging process with a static acceleration coefficient.

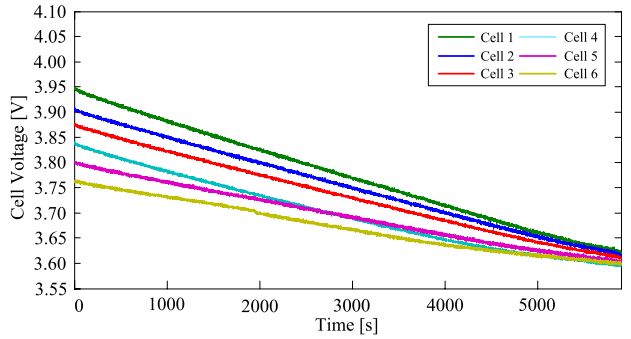

FIGURE 10 | Terminal voltages of six cells during the discharging process with a dynamic acceleration coefficient adaptive mechanism.

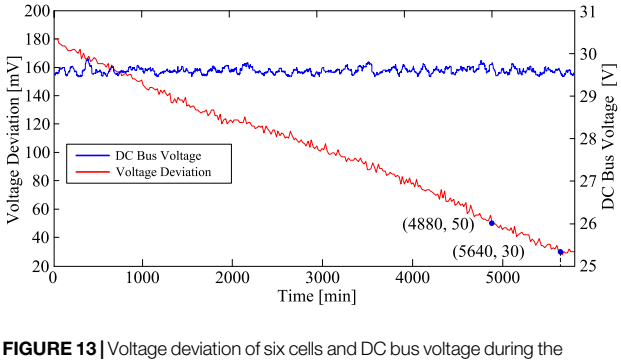

FIGURE 13 | Voltage deviation of six cells and DC bus voltage during the discharging process with a dynamic acceleration coefficient adaptive mechanism.

static acceleration coefficient lasts 6,820 s, and the voltage discrepancy reduced from 180 to 30 mV. The discharging process with a dynamic acceleration coefficient adaptive mechanism lasts 5,800 s. The acceleration coefficient ρ_n values of six smart cells are shown in **Figure 11**.

In **Figures 12**, **13**, the discharging process with a static acceleration coefficient takes 5,560 s to decrease the voltage discrepancy from the initial 180–50 mV, and the final balancing accuracy is 28 mV, while the discharging process with a dynamic acceleration coefficient adaptive mechanism takes only 4,880 s. Furthermore, **Figure 13** shows that the discharging process with a dynamic acceleration coefficient adaptive mechanism takes 5,640 s to decrease the voltage discrepancy to 30 mV, and the final voltage discrepancy is approximately 29 mV. For the DC bus voltage fluctuation during the discharging process shown in **Figures 12**, **13**, the maximum deviation between the set value and actual value is

0.25 V for the static acceleration coefficient and 0.5 V for the dynamic acceleration coefficient adaptive mechanism.

CONCLUSION

By dynamically regulating the balancing acceleration coefficient of each cell according to the voltage deviation, the adaptive balancing control of cell voltage in charging and discharging modes is proposed for the active balancing system with "cells decoupled and converters serial connected." The effectiveness of the proposed method for achieving the adaptive balancing control of cell voltage in the charging/discharging mode can be summarized as follows:

1) In both charging and discharging modes, the active balancing speed is effectively accelerated. The proposed dynamic acceleration coefficient adaptive mechanism decreases the balancing time from 10405 to 3,860 s in the charging mode and from 5,560 s to 4,880 s in the discharging mode.
2) The balancing accuracy is improved significantly in the charging mode. The proposed dynamic acceleration coefficient adaptive mechanism decreases the maximum cell voltage deviation from 50 to 20 mV in the charging mode. Nevertheless, the dynamic acceleration coefficient adaptive mechanism does not show significant improvements in balancing accuracy in the discharging mode.

The shortcoming of the proposed method for achieving the adaptive balancing control of cell voltage in the charging/discharging mode is that it slightly decreases the voltage stability of the DC bus.

DATA AVAILABILITY STATEMENT

The original contributions presented in the study are included in the article/Supplementary Material; further inquiries can be directed to the corresponding author.

AUTHOR CONTRIBUTIONS

YW contributed to resources and funding acquisition; DL contributed to writing, data analysis, and visualization; YS contributed to conceptualization, methodology, and writing—original draft; YT contributed to editing; YC and JZ contributed to resources and editing.

FUNDING

The authors gratefully acknowledge the support by the National Natural Science Foundation of China (Grant No. 61803345) and the Science and Technology Development Project of Henan Province (No. 202102210303).

REFERENCES

Babaie, M., Sharifzadeh, M., Kanaan, H. Y., and Al-Haddad, K. (2021). Switching-Based Optimized Sliding-Mode Control for Capacitor Self-Voltage Balancing Operation of Seven-Level PUC Inverter. *IEEE Trans. Ind. Electron.* 68 (4), 3044–3057. doi:10.1109/tie.2020.2978704

Baronti, F., Roncella, R., and Saletti, R. (2014). Performance Comparison of Active Balancing Techniques for Lithium-Ion Batteries. *J. Power Sourc.* 267, 603–609. doi:10.1016/j.jpowsour.2014.05.007

Baughman, A. C., and Ferdowsi, M. (2008). Double-tiered Switched-Capacitor Battery Charge Equalization Technique. *IEEE Trans. Ind. Electron.* 55 (6), 2277–2285. doi:10.1109/tie.2008.918401

Cao, J., Schofield, N., and Emadi, A. (2008). "Battery Balancing Methods: A Comprehensive Review," in IEEE Vehicle Power & Propulsion Conference (Harbin, China: IEEE). doi:10.1109/vppc.2008.4677669

Daowd, M., Omar, N., Bossche, P. V. D., and Mierlo, J. V. (2011). "Passive and Active Battery Balancing Comparison Based on Matlab Simulation," in IEEE Vehicle Power & Propulsion Conference (Chicago,USA: IEEE). doi:10.1109/vppc.2011.6043010

Evzelman, M., Ur Rehman, M. M., Hathaway, K., Zane, R., Costinett, D., Maksimovic, D., et al. (2016). Active Balancing System for Electric Vehicles with Incorporated Low-Voltage Bus. *IEEE Trans. Power Electron.* 31 (11), 7887–7895. doi:10.1109/tpel.2015.2513432

Gallardo-Lozano, J., Romero-Cadaval, E., Milanes-Montero, M. I., and Guerrero-Martinez, M. A. (2014). Battery Equalization Active Methods. *J. Power Sourc.* 246 (3), 934–949. doi:10.1016/j.jpowsour.2013.08.026

Gong, Z., van de Ven, B. A. C., Gupta, K. M., da Silva, C., Amon, C. H., Bergveld, H. J., et al. (2020). Distributed Control of Active Cell Balancing and Low-Voltage Bus Regulation in Electric Vehicles Using Hierarchical Model-Predictive Control. *IEEE Trans. Ind. Electron.* 67 (12), 10464–10473. doi:10.1109/tie.2019.2956396

Hsieh, Y. C., Moo, C. S., Tsai, I. S., and Cheng, J. C. (2002). "Dynamic Charge Equalization for Series-Connected Batteries," in IEEE International Conference on Industrial Technology (Bankok, Thailand: IEEE).

Huang, W., and Abu Qahouq, J. A. (2015). Energy Sharing Control Scheme for State-Of-Charge Balancing of Distributed Battery Energy Storage System. *IEEE Trans. Ind. Electron.* 62 (5), 2764–2776. doi:10.1109/tie.2014.2363817

Lambert, F. (2017). Tesla Model 3: Exclusive First Look at Tesla's New Battery Pack Architecture. Available at: https://electrek.co/2017/08/24/tesla model 3 exclusive battery pack architecture/.

Ma, Y., Duan, P., Sun, Y., and Chen, H. (2018). Equalization of Lithium-Ion Battery Pack Based on Fuzzy Logic Control in Electric Vehicle. *IEEE Trans. Ind. Electron.* 65 (8), 6762–6771. doi:10.1109/tie.2018.2795578

Ma, Y., Xiao, J., Lin, H., and Wang, Z. (2021). A Novel Battery Integration Method of Modular Multilevel Converter with Battery Energy Storage System for Capacitor Voltage Ripple Reduction. *IEEE Trans. Ind. Electron.* 68 (12), 12250–12261. doi:10.1109/tie.2020.3044780

Omariba, Z. B., Zhang, L., and Sun, D. (2019). Review of Battery Cell Balancing Methodologies for Optimizing Battery Pack Performance in Electric Vehicles. *IEEE Access* 7, 129335–129352. doi:10.1109/access.2019.2940090

Ouyang, Q., Chen, J., Zheng, J., and Fang, H. (2018). Optimal Cell-To-Cell Balancing Topology Design for Serially Connected Lithium-Ion Battery Packs. *IEEE Trans. Sustain. Energ.* 9 (1), 350–360. doi:10.1109/tste.2017.2733342

Pinto, C., Barreras, J. V., Schaltz, E., and Rui, E. A. (2016). Evaluation of Advanced Control for Li-Ion Battery Balancing Systems Using Convex Optimization. *IEEE Trans. Sust. Energ.* 7 (4), 1. doi:10.1109/tste.2016.2600501

Shan, Y., Hu, J., Chan, K. W., Fu, Q., and Guerrero, J. M. (2019). Model Predictive Control of Bidirectional DC-DC Converters and AC/DC Interlinking Converters-A New Control Method for PV-Wind-Battery Microgrids. *IEEE Trans. Sustain. Energ.* 10 (4), 1823–1833. doi:10.1109/tste.2018.2873390

Shibata, H., Taniguchi, S., Adachi, K., Yamasaki, K., Ariyoshi, G., Kawata, K., et al. (2001). "Management of Serially- Connected Battery System Using Multiple

Switches" in IEEE International Conference on Power Electronics & Drive Systems. (Indonesia: DenpasarIEEE).

Shousha, M., Mcrae, T., Prodic, A., Marten, V., and Milios, J. (2017). Design and Implementation of High Power Density Assisting Step-Up Converter with Integrated Battery Balancing Feature. *IEEE J. Emerg. Sel. Top. Power Electron.* 5 (3), 1068–1077. doi:10.1109/jestpe.2017.2665340

Tang, X., Zou, C., Wik, T., Yao, K., Xia, Y., Wang, Y., et al. (2019). Run-to-run Control for Active Balancing of Lithium Iron Phosphate Battery Packs. *IEEE Trans. Power Elect.* 35 (2), 1499–1512.

Tavakoli, A., Khajehoddin, S. A., and Salmon, J. (2019). A Modular Battery Voltage Balancing System Using a Series Connected Topology. *IEEE Trans. Power Elect*.

Trimboli, M. S., de Souza, A. K., and Xavier, M. A. (2022). Stability and Control Analysis for Series-Input/Parallel-Output Cell Balancing System for Electric Vehicle Battery Packs. *IEEE Control. Syst. Lett.* 6, 1388–1393. doi:10.1109/lcsys.2021.3097875

Xu, S., Wang, J., and Xu, J. (2013). A Current Decoupling Parallel Control Strategy of Single-phase Inverter with Voltage and Current Dual Closed-Loop Feedback. *IEEE Trans. Ind. Electron.* 60 (4), 1306–1313. doi:10.1109/tie.2011.2161660

Ye, Y., and Cheng, K. W. E. (2017). Analysis and Design of Zero-Current Switching Switched-Capacitor Cell Balancing Circuit for Series-Connected Battery/supercapacitor. *IEEE Trans. Vehicular Tech.* 67 (2), 948–955.

Ye, Y., and Cheng, K. W. E. (2015). Modeling and Analysis of Series-Parallel Switched-Capacitor Voltage Equalizer for Battery/Supercapacitor Strings. *IEEE J. Emerg. Sel. Top. Power Electron.* 3 (4), 977–983. doi:10.1109/jestpe.2015.2418339

Yu, Y., Saasaa, R., Khan, A. A., and Eberle, W. (2019). A Series Resonant Energy Storage Cell Voltage Balancing Circuit. *IEEE J. Emerging Selected Top. Power Elect*.

Zhang, C., Shang, Y., Li, Z., and Cui, N. (2017). An Interleaved Equalization Architecture with Self-Learning Fuzzy Logic Control for Series-Connected Battery Strings. *IEEE Trans. Veh. Technol.* 66 (12), 10923–10934. doi:10.1109/tvt.2017.2737401

Zhang, H., Wang, Y., Qi, H., and Zhang, J. (2019). Active Battery Equalization Method Based on Redundant Battery for Electric Vehicles. *IEEE Trans. Veh. Technol.* 68 (8), 7531–7543. doi:10.1109/tvt.2019.2925742

Zheng, Y., Ouyang, M., Lu, L., Li, J., Han, X., and Xu, L. (2014). On-line Equalization for Lithium-Ion Battery Packs Based on Charging Cell Voltages: Part 2. Fuzzy Logic Equalization. *J. Power Sourc.* 247 (2), 460–466. doi:10.1016/j.jpowsour.2013.09.012

Conflict of Interest: Author YT is employed by Rundian Energy Science and Technology Co., Ltd. Authors YC and JZ are employed by Pinggao Group Intelligent Power Technology Co., Ltd.

The remaining authors declare that the research was conducted in the absence of any commercial or financial relationships that could be construed as a potential conflict of interest.

Publisher's Note: All claims expressed in this article are solely those of the authors and do not necessarily represent those of their affiliated organizations, or those of the publisher, the editors, and the reviewers. Any product that may be evaluated in this article, or claim that may be made by its manufacturer, is not guaranteed or endorsed by the publisher.

frontiers | Frontiers in Energy Research

ORIGINAL RESEARCH
published: 08 April 2022
doi: 10.3389/fenrg.2022.809127

Study on Oil Flow Surging and Protection Optimization for on Load Tap Changer of Converter Transformer

Haibin Zhou[1], Zhicheng Xie[1], Xing Chen[2], Qinggang Guan[2], Jun Deng[1], Guanwei Liu[3] and Xiaojiang Yan[3]*

[1]Extra-High Voltage Transmission Company of China Southern Power Grid, Guangzhou, China, [2]Shenyang Transformer Research Institute Co., Ltd., Shenyang, China, [3]School of Energy and Power Engineering, Xi'an Jiaotong University, Xi'an, China

The on-load tap changer (OLTC) is one of the key components of converter transformer. The energy generated during tap switching process of the OLTC will cause thermal expansion and surging of the insulating oil in the chamber, resulting in the mis-operation of protective relay and threatening the safe and stable operation of the power system as well. Therefore, taking the typical dual-transition resistance-type OLTC as an example, a numerical modeling method of OLTC oil flow surging based on the realizable k-ε model is proposed, and the fluid simulation model is established based on the FLUENT software. The quantitative relationship between the OLTC transition resistance value and the oil velocity and oil pressure at the top of the oil chamber is analyzed, that is, the smaller the transition resistance, the greater the oil flow velocity and oil pressure during switching. In addition, an equivalent experimental platform is built to carry out the static action characteristic experiment of OLTC oil flow relay, the corresponding relationship between the change range of oil pressure at the top of the chamber, and the oil velocity under typical value (1.5 m/s, 2.0 m/s, and 2.5 m/s) are revealed. Based on which, the optimization suggestions on the protection relay threshold configuration of OLTC oil velocity and oil pressure are put forward.

Keywords: on-load tap changer, fluid simulation, oil flow surging, protection optimization, transformer

OPEN ACCESS

Edited by:
Dongqi Liu,
Changsha University of Science and Technology, China

Reviewed by:
Nasir Ahmed Algeelani,
Al-Madinah International University, Malaysia
Jian Hao,
Chongqing University, China

****Correspondence:***
Zhicheng Xie
xiezhicheng0921@foxmail.com

Specialty section:
This article was submitted to Smart Grids, a section of the journal Frontiers in Energy Research

Received: *04 November 2021*
Accepted: *28 February 2022*
Published: *08 April 2022*

Citation:
Zhou H, Xie Z, Chen X, Guan Q, Deng J, Liu G and Yan X (2022) Study on Oil Flow Surging and Protection Optimization for on Load Tap Changer of Converter Transformer. Front. Energy Res. 10:809127. doi: 10.3389/fenrg.2022.809127

1 INTRODUCTION

On-load tap changer (OLTC) is one of the key components of converter transformer, which plays the role of compensating power grid voltage change and optimizing the control angle. The OLTC of a converter transformer has a wide voltage regulation range, has frequent operation, has a high recovery voltage during voltage regulation, and bears severely working conditions such as harmonics. Therefore, its fault rate is higher than that of a AC power transformer (Zhu and Shen, 2012; Zhu and Shen, 2016).

The OLTC is composed of a tap selector and changer switch, whose position in the converter transformer is shown in **Figure 1**. The tap selector connects the tap in advance according to the tap sequence and makes it bear continuous load. The changer switch is placed in a separate oil chamber and can transfer the load current between different taps. Besides, the OLTC has a separate conservator, and the pipeline from the oil chamber to the conservator has a protective relay (oil flow velocity relay and oil pressure relay).

During tap changing, the insulating oil in the chamber will be heated, expanded, and surged by the energy generated from arc breaking. Normally, the two relays should send alarm/trip signals at the same time or within a certain period of time (may be milliseconds). Actually, there have been many cases of relay malfunctions, especially oil flow velocity relay. However, it can only modify the protection setting value based on experience to deal with the mis-operation case, due to a lack of mechanism research (Liang et al., 2016).

The oil flow surging is related to the energy generated during the tap changing process, the volume of the oil chamber, the height difference between the oil chamber and the conservator, and the diameter of the pipe.

For the operation characteristics and fault diagnosis of the OLTC, scholars have carried out extensive research. In terms of OLTC operation characteristics analysis, electromagnetic transient simulation research has been carried out for the switching process of the OLTC, and quantitative analysis has been obtained from the two aspects of amplitude and phase. The particularity of the operating conditions of the commutator tap changer is revealed, and the technical points of the selection of the commutator tap changer are proposed (Lei et al., 2018; Fan et al., 2018). Yang et al. (2014) simulated the action process of the mechanical OLTC and that with power electronic devices, and calculated the energy loss in the process of on-load voltage regulation under the two modes. A new hybrid on-load tap changer scheme has been given by Shi (2015) and a 110-/35-kV single-phase on-load tap changer model has been built. The feasibility of the proposed scheme is further verified by simulating the transient characteristics of the primary side in the switching process. A new on-load tap changer, which triggers the thyristor circuit through overvoltage and realizes the switching process of uninterrupted current has been proposed by Li (2017). Shen et al. (2015) improved the on-load tap changer of the double transition resistance branch triggered by micro-arc and established a new model of active trigger combined with the double transition resistance branch. Rivas-Trujilo et al. (2010) proposed a modeling structure of on-load tap changer based on the arc model. In each operation of the tap changer, there are a series of switching events with specific timings, and these switching operations are modeled according to the accuracy of the proposed on-load tap changer model that is verified by the measurement of results obtained from computer simulations and the on-load tap changer operation real-time test. Castro et al. (2017) puts forward the measurement method of the on-load tap changer current during transformer operation, and models and simulates the transformer and on-load tap changer in ATP-draw.

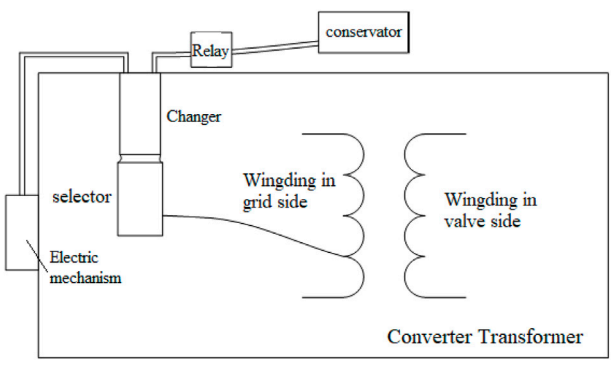

FIGURE 1 | Location diagram of the OLTC in the converter transformer.

In terms of OLTC fault diagnosis, the abnormal physical information of on-load tap changer before and after fault occurrence has been discussed, the joint mapping relationship between the vibration sound and arc has been revealed (Seo et al., 2018), and the joint detection technology has been based on the vibration sound fingerprint and driving motor current (sound and electricity) (Yu et al., 2020), acyclic graph support vector machine fault diagnosis model (Xu et al., 2019), arc detection method of on-load tap changer based on energy conservation principle (Song et al., 2019a), fault identification method based on the multi-resolution feature extraction algorithm, and the genetic optimization support vector machine (Duan et al., 2017). Some scholars have explored the cooperation between OLTC oil flow surge and nonelectric protection by means of the equivalent test. For example, Xu et al. (2021) built a short-circuit arcing test platform and carried out the short-circuit arcing test, and put forward a proposal for the standardized configuration of on-load tap changer nonelectric protection device. Song et al. (2019b) carried out typical test analysis and research on the arc waveform generated by different types of changeover switches, which provided guidance for the optimal design of OLTC. Ding et al. (2016) compared and analyzed the differences of heavy gas protection setting values of different models of on-load tap changer and carried out the static action characteristic test on the gas relay of an on-load tap changer, so as to put forward suggestions on the threshold settings of the gas relay of large capacity transformers.

However, these studies were carried out on the basis of experiments, and the research conclusions have certain limitations. The quantitative mechanism research is insufficient, so it has not formed a unified conclusion. This article focuses on the key operation problems of an OLTC, that is, how to optimize the threshold of oil flow relay and oil pressure relay to ensure the correct action of protection, thus, the refined modeling, oil flow characteristic analysis, and protection threshold optimization are not only the difference between this article and the existing literature but also the key technical innovation of this article.

In this article, in Section 2, the mathematical simulation model of OLTC is established; in Section 3, the simulation result is analyzed, and besides the experimental method, the result is proposed; the change law of the oil speed and oil pressure at the top of the chamber when the OLTC operating under different transition resistances is analyzed, so as to provide guidance for the OLTC protection configuration.

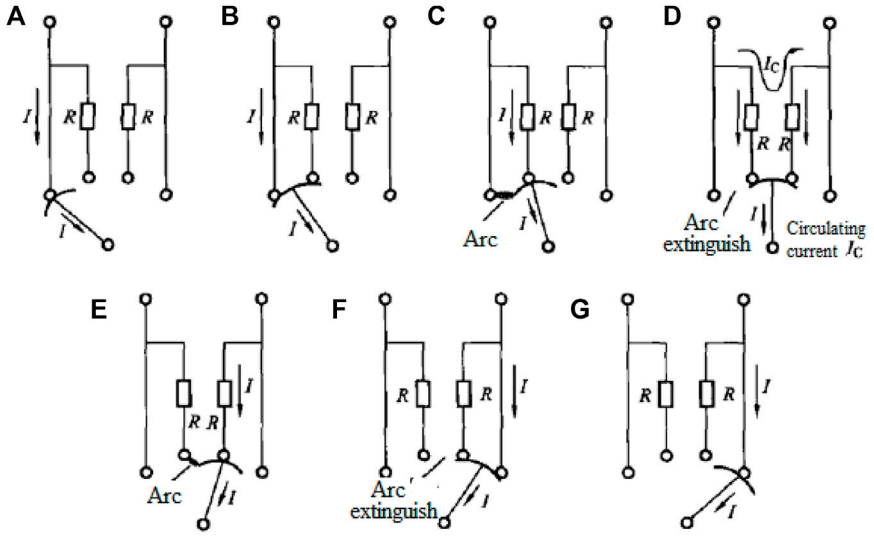

FIGURE 2 | Switching process of dual-transition resistance-type OLTC.

TABLE 1 | Characteristic variables in tap changing process of OLTC.

Contact	Breaking Current	Recovery Voltage	Switching Capacity
Main contact	I	IR	I^2R
Transition contact	$(U_S \pm IR)/2R$	$U_S + IR$	$(U_S \pm IR)^2/2R$

Note: I *represents the breaking current;* U_S, *represents the stage voltage;* R *represents the transition resistance, which can also be represent as* $R = n^*U_S/I$ *(n is the coefficient of transition resistance).*

2 MATHEMATICAL SIMULATION MODELING OF ON-LOAD TAP CHANGER

2.1 Simulation Object

Taking a double transition resistance type OLTC as the simulation object, of which the rated stage voltage is 4037 V and the rated current is 2 × 643 A. The complete tap changing process is shown in **Figure 2**, which includes two arc extinguishing processes (in step d and step f, respectively), and the breaking current, recovery voltage, and switching capacity of the two arc extinguishing processes are shown in **Table 1**.

It can be seen from **Table 1** that 1) the recovery voltage of the auxiliary contact is greater than that of the main contact; 2) the breaking current and the recovery voltage of the main contact is independent of the transition resistance R and the stage voltage, respectively, while those of the auxiliary contact are related to the transition resistance R and stage voltage.

In order to reduce the breaking capacity of the main contact, the value of transition resistance should be lower. However, in order to reduce the switching capacity of the auxiliary contact, the transition resistance value should be higher, in order to reduce the circulating current in the switching process. Therefore, the transition resistance shall be appropriate so that the recovery voltage can be withstood between the actual contacts, and the arc will not rekindle after it is extinguished when the main contact or transition contact is disconnected.

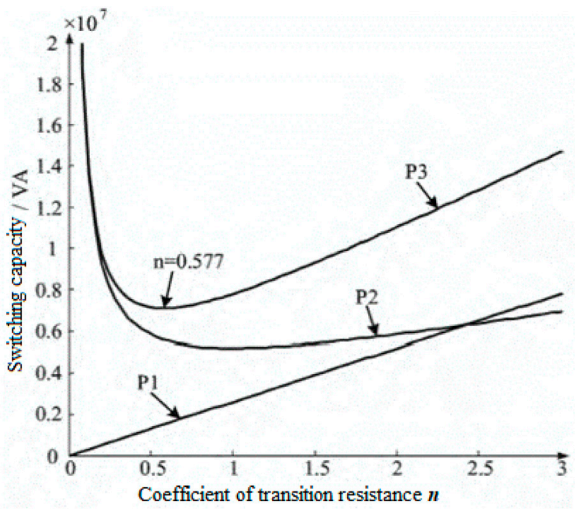

FIGURE 3 | Relationship curve between capacity and transition resistance coefficient.

The transition resistance is generally selected according to the principle of minimizing the breaking capacity of the transition contact. The corresponding breaking capacity P1 of the main contact, the switching capacity P2 of the transition contact and the total breaking capacity P3 can be expressed as:

$$P_1 = I^2R = I^2 \times n \times \frac{U_S}{I} = n \times U_S \times I \quad (1)$$

$$P_2 = \frac{1}{2}I^2R + \frac{U_S^2}{2R} = \left(\frac{n}{2} + \frac{1}{2n}\right) \times U_S \times I \quad (2)$$

$$P_3 = \left(\frac{3n}{2} + \frac{1}{2n}\right) \times U_S \times I \quad (3)$$

The relationship between the switching capacity P1 of the main contact and P2 of the auxiliary contact, total switching capacity P3, and coefficient n of transition resistance is shown in **Figure 3**.

It can be seen that the transition resistance value has a great impact on the OLTC switching capacity. For the dual-transition resistance OLTC studied in this article, when the coefficient of transition resistance n = 0.577, the total switching capacity is the smallest, and when n = 1, the switching capacity of the main contact equals that of the transition contact.

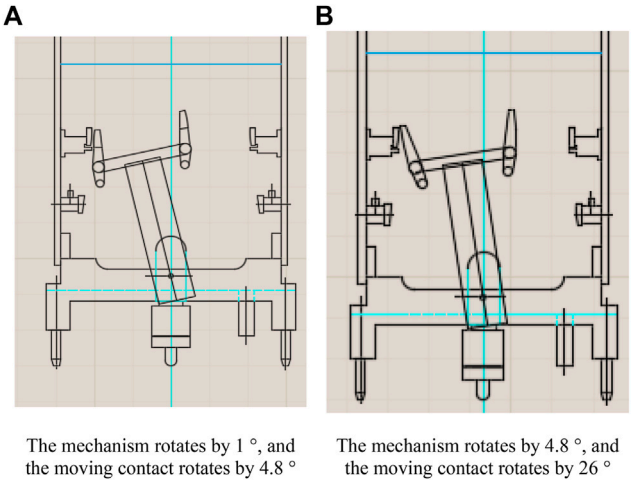

FIGURE 4 | The dynamic and static contacts of the main contact are from contact to separation. **(A)** The mechanism rotates by 1°, and the moving contact rotates by 4.8°. **(B)** The mechanism rotates by 4.8°, and the moving contact rotates by 26°

2.2 Model Established

Firstly, the 3D parameter of the OLTC is measured accurately, and the relative position of each component of the OLTC is drawn in AutoCAD according to the measurement results. Besides, taking the center of the calculation area as the model origin, each component is modeled and assembled by the ProE software.

The OLTC has a complex structure and a large number of components, which is a great challenge to modeling. Therefore, this article proposes an optimization modeling method:

1) In the process of switching, the moving contact and its fast mechanism swing between the two diaphragms, where the flow mainly occurs. Therefore, all structures outside the diaphragms are removed during modeling.
2) Because the movement of the tension spring at the lower part of the moving contact is difficult to simulate, while it has little effect on the transformer oil flow caused by the switching process, all the tension springs at the lower part of the moving contact are therefore removed during modeling.
3) The quick mechanism of transition contact is connected with that of the main contact through the connecting rod mechanism. During the numerical simulation, if the modeling is based on the actual structure, the motion equations of the main contact, transition contact, contact quick mechanism and connecting rod mechanism will become very complex, and the structure has little effect on the transformer oil flow caused by the switching process. Therefore, the connecting rod mechanism is removed during the modeling, The motion equation of the main contact, the transition contact and the fast mechanism are comprehensively determined according to the contact structure of the dynamic and static contacts, the structure of the fast mechanisms, and the current change law in the switching process, such that it can simulate the motion of the moving contact and its fast mechanism in the switching process.
4) The movement speed of the driving mechanism is much smaller than that of the changeover switch, and its influence on the flow of transformer oil is far less than that of the changeover switch. Therefore, the action of the driving mechanism is not considered in modeling.

In the process of switching, when the moving and static contacts are separated from contact, the main contact and transition contact not only rotate with their own rapid mechanism but also rotate around their own rotating shaft under the action of the spring at the bottom of the contact. Therefore, it is necessary to determine the process from contact to separation of the dynamic and static contacts in order to ensure normal operation of the numerical simulation. According to the structure of on-load tap changer provided by the actual converter station and the field measured results, the separation process of the dynamic and static contacts of the main contact and transition contact is finally determined as follows:

1) During the switching process, the main contact quick mechanism rotates a total of 28° (14° on one side), and the rotation angle of its moving contacts during the separation of the moving and static contacts is 26°. According to the structure of the main contact, it is assumed that both the active contact and the fast mechanism rotate at a uniform speed around their respective rotating axes. When the active contact rotates 26°, the fast mechanism rotates 5.42°, that is, when the fast mechanism of the main contact rotates 1°, the moving contact rotates 4.8°, and after the fast mechanism of the main contact rotates 8.58°, the moving contact begins to contact with the static contact. **Figure 4** schematic diagram of

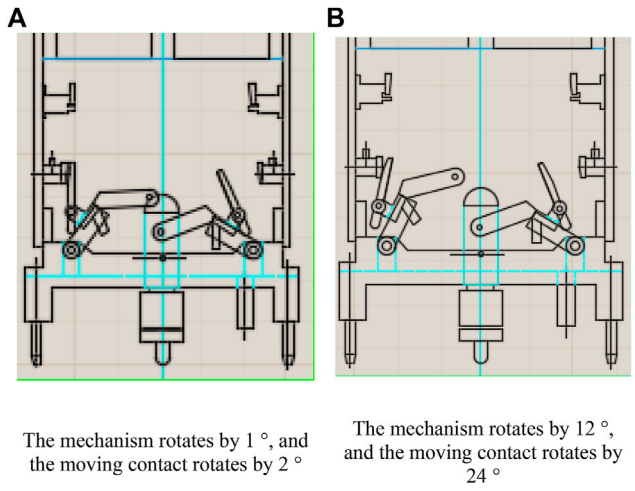

FIGURE 5 | The contact process of dynamic and static contact of transition contact. **(A)** The mechanism rotates by 1°, and the moving contact rotates by 2°. **(B)** The mechanism rotates by 12°, and the moving contact rotates by 24°

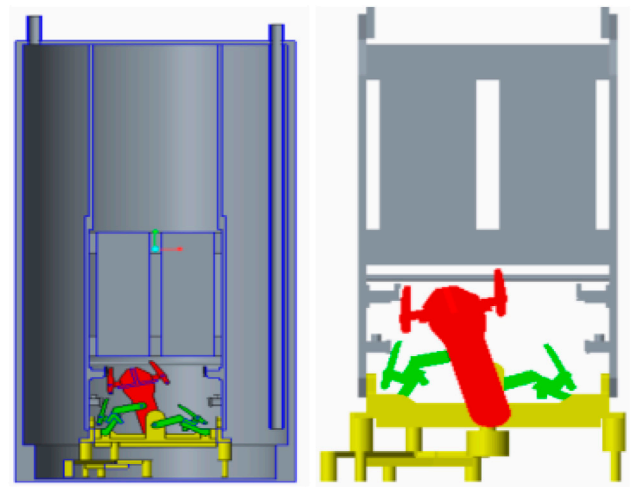

FIGURE 6 | Integral model of the OLTC.

the process from the contact to the initial separation of the moving and stationary contacts of the main contact. The process from the initial separation position to the contact is opposite to this process.

2) The transition contact quick mechanism rotates 34° in total during the switching process, and the rotation angle of its moving contact during the separation of the moving and static contacts is 24°. According to the structure of the transition moving and static contacts, when the transition moving contact rotates 24°, its fast mechanism rotates 12°, that is, when the transition contact fast mechanism rotates 1°, its moving contact rotates 2°, and after the transition contact fast mechanism rotates 22°, its moving contact begins to contact with the static contact. **Figure 5** shows the process diagram of the dynamic and static contacts of the transition contact from the initial contact to full contact (left transition contact). The process from contact to separation is the opposite.

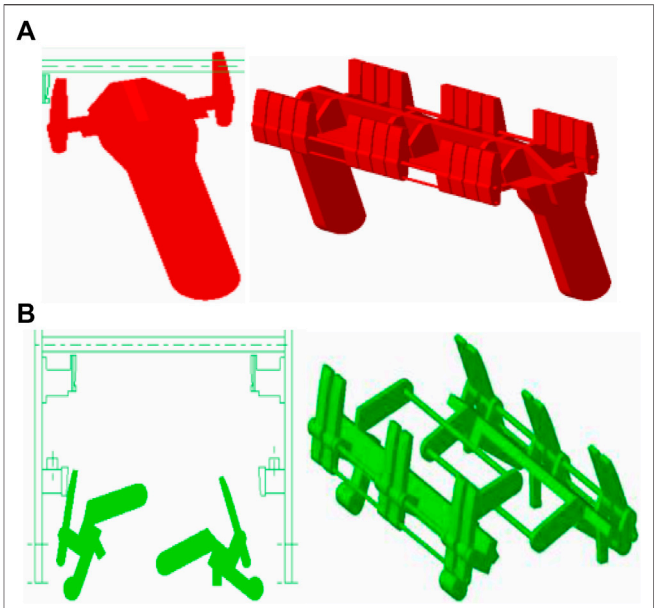

FIGURE 7 | Model of contacts and its fast mechanism. **(A)** Model of the main contact and its fast mechanism. **(B)**Model of the auxiliary contact and its fast mechanism.

The whole and contacts modeling results of the OLTC are shown in **Figures 6**, **7**, respectively.

In **Figure 6**, the two circular pipes on the upper part of the changer are oil flow in–out ports of the on-line oil filter, whose diameters are both 25 mm. Among that, the right part is the in port of oil flow, and its pipe extends into the changer cylinder for 1.15 m; the left part is the out port of oil flow, while its pipe does not extend into the changer cylinder.

2.3 Turbulence Model

The flow field of oil chamber is simulated by realizable k-ε model (Wang, 2004; Wen, 2010), which is improved based on the standard k-ε model, that is, the k equation remains unchanged, while the equation of dissipation rate ε and the eddy viscosity equation are improved mainly. The corresponding transport equation is:

$$\rho\frac{Dk}{Dt}=\frac{\partial}{\partial x_j}\left[\left(\mu+\frac{\mu_t}{\sigma_k}\right)\frac{\partial k}{\partial x_j}\right]+G_k+G_b-\rho\varepsilon-Y_M \tag{4}$$

$$\frac{\partial}{\partial t}(\rho\varepsilon)+\frac{\partial}{\partial x_i}(\rho\varepsilon u_i)=\frac{\partial}{\partial x_i}\left[\left(\mu+\frac{\mu_t}{\sigma_\varepsilon}\right)\frac{\partial\varepsilon}{\partial x_i}\right]+\rho C_1 S\varepsilon - \rho C_2\frac{\varepsilon^2}{k+\sqrt{\nu\varepsilon}}+C_{1\varepsilon}\frac{\varepsilon}{k}C_{3\varepsilon}G_b \tag{5}$$

where $C_1=\max[0.43,\frac{\eta}{\eta+5}]$, $\eta=Sk/\varepsilon$, G_k represents the turbulent kinetic energy due to the average velocity gradient, G_b represents the turbulent kinetic energy caused by buoyancy, and Y_M

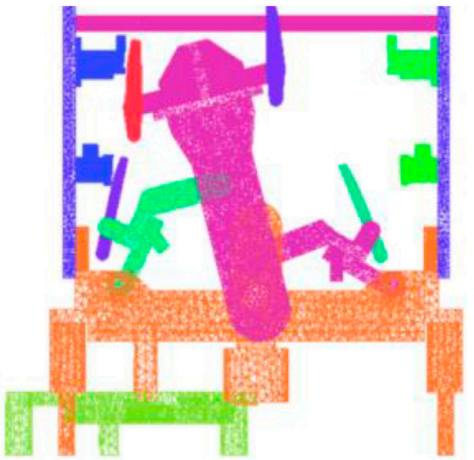

FIGURE 8 | Overall grid of OLTC.

represents the effect of fluctuating expansion of compressible turbulence on the total dissipation rate. The Prandtl number of turbulent kinetic energy k and dissipation rate ε is taken as $\sigma_k = 1.0$ and $\sigma_\varepsilon = 1.2$, respectively. Other default constants are $C_{1\varepsilon} = 1.44$ and $C_2 = 1.9$.

The generation term of the dissipation rate ε in **Equation 5** (the second term on the right) does not include the turbulent kinetic energy G_k, which can reflect the transmission of energy spectrum better. Furthermore, another obvious feature is that the third term on the right side of the equation does not have singularity.

The viscosity coefficient formula is $\mu_t = \rho C_\mu \frac{k^2}{\varepsilon}$, while C_μ is not a constant, and it can be calculated by:

$$C_\mu = \frac{1}{A_0 + A_S \frac{kU^*}{\varepsilon}} \tag{6}$$

where $U^* = \sqrt{S_{ij}S_{ij} + \tilde{\Omega}_{ij}\tilde{\Omega}_{ij}}$, $\tilde{\Omega}_{ij} = \Omega_{ij} - 2\varepsilon_{ijk}\omega_k$, and $\Omega_{ij} = \bar{\Omega}_{ij} - \varepsilon_{ijk}\omega_k$; $\bar{\Omega}_{ij}$ is the ratio between the rotational force tensor and the angular velocity ω_k in the rotating coordinate system. The other variable is constant, that is, $A_0 = 4.04$, $A_S = \sqrt{6}\cos\varphi$, $\varphi = \frac{1}{3}\arccos(\sqrt{6}W)$, where $W = \frac{S_{ij}S_{jk}S_{kj}}{\tilde{S}}$, $\tilde{S} = \sqrt{S_{ij}S_{ij}}$, and $S_{ij} = \frac{1}{2}(\frac{\partial u_j}{\partial x_i} + \frac{\partial u_i}{\partial x_j})$.

For the action of the OLTC, the swing arm will form many vortices, and the improved model has high reliability and accuracy in the flow field simulation.

2.4 Meshing

One of the key factors for fluid computing is the quality of the computational grid. Actually, the structure of the OLTC is extremely complex, including a large amount of transition area of large space and local irregular small areas. Therefore, how to mesh the transition areas becomes very important.

To meet the requirement of the complex geometric model of the oil chamber, the unstructured tetrahedral grid with strong adaptability to complex boundaries is adopted (Baker and Ying, 1994), whose grid distortion rate is less than 0.6, and the total number of grids is 22.68 million. **Figure 8** shows the overall grid of the OLTC. The grid at the contact between the moving and static contacts of the main contact and the transition contact has been densified.

Among them, the maximum volume grid scale of the computational domain is 24 mm; since the gap between the moving and stationary contacts is only 1 mm at the beginning and end of the switching process, the grid scale of the corresponding moving and stationary contact surface is set to 0.5 mm, and the grid of the adjacent surface is set to 1 mm; for the quick mechanism of the main contact and transition contact, the face grid adjacent to the main contact, transition contact, and rotating shaft is set as 2 mm, and the other face grids are set as 4 mm; for the switch base, the face grid adjacent to the rotating shaft is set as 2 mm, and the other face grids are set as 4 mm; for the transition resistance, since the distance between the resistance and the isolation plate is 5.7 mm, the front and rear surface grid is set as 4 mm, and the grid between the four sides and the tightening bolt surface is set as 2 mm; due to the large area of the two diaphragms and insulating cylinder, the grid scale of the outer wall of the diaphragm and the inner wall of the insulating cylinder is set to 16 mm to reduce the number of grids. At the same time, in order to take into account the calculation accuracy and the number of grids, the surface grid scale of the inner wall of the diaphragm (surface mounted static contact) is set to 8 mm.

During the switching process of the OLTC, the movement of the contact will change the flow domain, and the motion of the boundary will also change along with time. The motion form of boundary is predefined through User-Defined-Function (UDF), and its angular velocity is specified before calculation. The updating process of the mesh is completed automatically according to the change in boundary at each iteration step. Because the displacement of the moving boundary is much larger than the grid size, to avoid the grid with negative values, or the calculation that does not converge due to excessive grid distortion, the grids with excessive distortion rates or excessive size changes are concentrated together and redivided in the calculation process, to meet the requirements of the distortion rate and size.

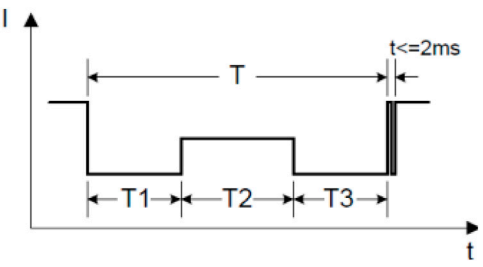

FIGURE 9 | Switching sequence diagram of OLTC.

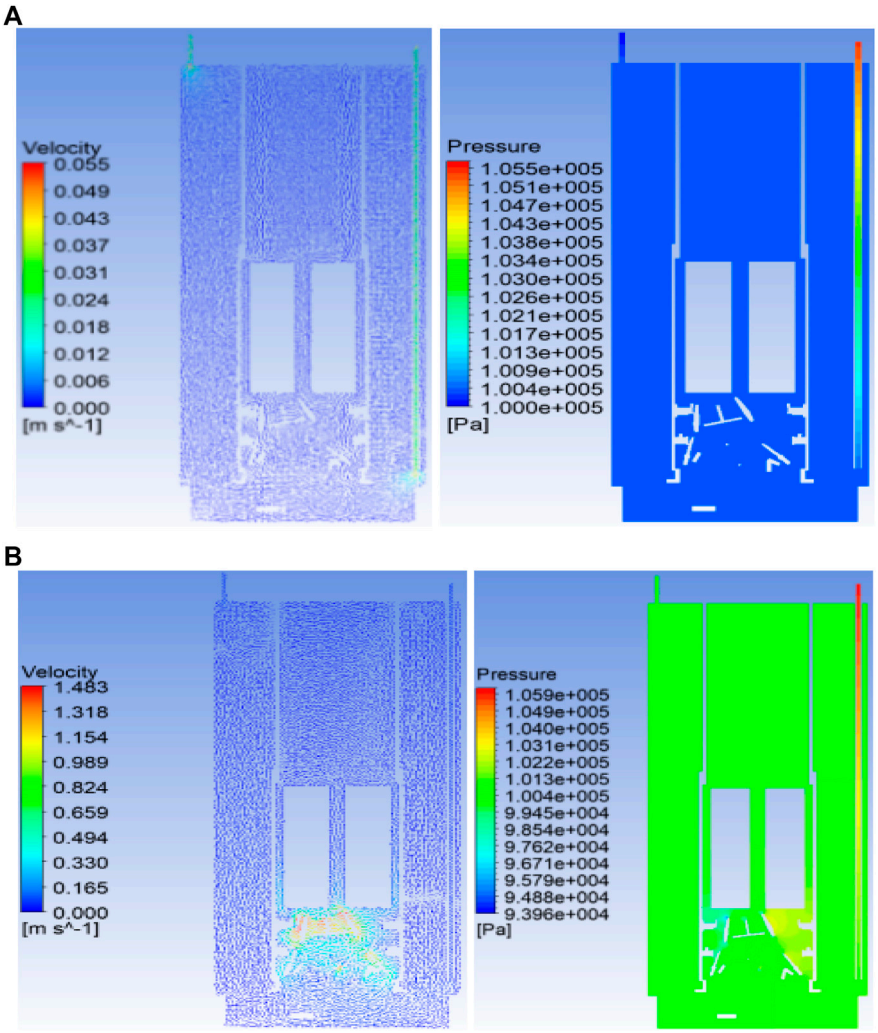

FIGURE 10 | Velocity field and pressure field of OLTC. **(A)** Velocity field and pressure field before action. **(B)** Velocity field and pressure field before arcing.

2.5 Boundary Conditions and Parameter Determination

2.5.1 Condition Setting of Flow Boundary

Normally, the OLTC is placed in a sealed cylinder filled with insulating oil. Therefore, the calculation area is set to be filled with transformer oil (#25), with oil pressure of 100 kP A and oil temperature of 40°C. The oil density is 895 kg/m^3, the dynamic viscosity is 0.97 kg/(ms), the thermal conductivity is 0.128 W/(mK), and the specific heat capacity at constant pressure is 1.8 kJ/(kgK). Owing to the high density of the insulating oil, the influence of its own gravity should be considered in numerical simulation. Each solid wall is set as an adiabatic nonslip boundary, without the consideration of the influence of wall roughness.

2.5.2 Setting of Contact Speed

The OLTC switching sequence diagram is shown in **Figure 9**. The total flow duration T during the switching process is about 44 ms.

The active contact not only moves with the fast mechanism but also rotates around its own rotating shaft when the moving contact starts to contact with the static contact. Similarly, assuming that the moving contact rotates at a uniform speed around its own rotating shaft, it has been determined during modeling that when the fast mechanism rotates 1°, the moving contact rotates 4.8° around its own rotating shaft. Therefore, it can be calculated that the angular speed of the moving contact rotating around its own rotating shaft is 1872°/S = 3.1416 rad/s.

The fast mechanism of transition contact rotates 22° in the noncontact stage of dynamic and static contacts, and its angular speed is 774.65°/S = 6.76 rad/s; in the contact stage, it rotates 12°, and its angular velocity is 76.5°/S = 2.413 rad/s; in the contact stage, when the fast mechanism of the transition contact rotates by 1°, the moving contact rotates by 2° around its own rotating shaft. Therefore, the angular speed of the transition moving contact rotating around its own rotating shaft is 553°/S = 4.826 rad/s.

TABLE 2 | Oil flow velocity and oil pressure under different transition resistors.

Parameters	Value						
Transition resistance coefficient, *n*	0.2	0.3	0.4	0.5	0.6	0.8	1.0
Arcing energy (J)	4099	3293	2890	2649	2486	2285	2164
Oil flow (m/s)	1.11	0.86	0.81	0.74	0.67	0.64	0.62
Oil pressure (kPa)	61.4	47.8	44.1	40.5	35.9	34.1	33.2

2.5.3 Setting of Arcing Time, Arcing Position, and Released Energy

According to the test report, the arcing time does not exceed 12 ms, with an average of 6 ms. According to OLTC stage voltage and rated current, AC arc energy during switching can be calculated by:

$$W = \int u(t)i(t)dt \tag{7}$$

where $u(t)$ is the voltage of electric arc, whose value is:

$$u = El(t) + U_0 \tag{8}$$

where, E is the electric field intensity of the arc column, with the value of 200 V/cm. $l(t)$ is the length of the electric arc, which is the function of time. U_0 is the voltage drop of the electric arc near the cathode area, the value of which is 50 V.

The main contact and transition contact of the OLTC are swing rod devices with one end fixed, then the value of $l(t)$ can be represented by:

$$l = 2Rsin\frac{\omega t}{2} \tag{9}$$

where R is the length of the swing rod, and ω is the rotational angular velocity.

The arcing current is the periodic current, which can be expressed by:

$$i = \sqrt{2}Isin(2\pi ft + \varphi_0) \tag{10}$$

Putting **Equations 8–10** into **Equation 7**, we get:

$$W = \int \sqrt{2}Isin(2\pi ft + \varphi_0)\left(2ERsin\frac{\omega t}{2} + U_0\right)dt \tag{11}$$

The arcing energy can be obtained by integrating **Equation 11** in the arcing time.

3 ANALYSIS OF SIMULATION RESULTS

3.1 Characteristics of Oil Flow Surge Before Switching and During Unburned Arc

Figure 10A shows the velocity field and pressure field at the section 11 mm away from the cylinder's center before OLTC action, after the calculation of unsteady flow field converges.

Before switching, the flow in the switch cylinder is smooth, the speed is very low, and the maximum speed is just about 0.055 m/s. The oil pressure in the cylinder is basically the same and that on the cylinder's wall is about 100.4 kPa. The temperature difference in the whole cylinder is very small, only 0.5°C.

TABLE 3 | Oil flow velocity and oil pressure under different loads.

Parameters	Value						
Load current multiple	0.5	0.6	0.7	0.8	1.0	1.1	1.2
Arcing energy (J)	3011	3178	3345	3512	3849	4016	4187
Oil flow (m/s)	0.83	0.85	0.88	0.925	0.99	1.09	1.13
Oil pressure (kPa)	45.3	46.3	48.5	51.3	55.5	60.2	63.1

Figure 10B shows the velocity field and pressure field at the central section of the oil barrel of the OLTC before the arc energy of the main contact is added, after the moving contact and fast mechanism act for 13.9 ms.

Before adding the arcing energy of the main contact, the oil flow rate near the moving contact and the fast mechanism increases obviously, but the flow in other areas is still gentle and the flow rate is very low. The oil pressure on the cylinder wall changes little, about 100.6 kPa. The temperature difference in the whole cylinder is very small, only 1.8°C. It shows that the influence of switching action on the flow field in the cylinder is mainly concentrated near the moving contact and fast mechanism.

3.2 Characteristics of Oil Flow Surge During Switching

3.2.1 Characteristics of Oil Flow Surge Under Different Transition Resistance

After the stage voltage and rated current are determined, the transition resistance has the greatest impact on the OLTC breaking performance.

The different transition resistance coefficients are selected, the arcing energy of the main contact, arcing energy of the transition contact, and total arcing energy under various working conditions according to **Equation 11** are calculated, and the arcing time is then set as 10 ms. Based on the OLTC simulation model, the oil pressure and oil flow velocity of insulating oil in the oil chamber under different transition resistance values are obtained. The results are summarized in **Table 2**.

Through the correlation analysis of the transition resistance coefficient, the arcing energy, oil flow, and oil pressure data are shown in **Table 2**, and it can be found that the correlation coefficients of transition resistance coefficient–arcing energy, transition resistance coefficient–oil flow, and transition resistance coefficient–oil pressure are −0.89, −0.86, and −0.87, respectively, showing a negative correlation. The correlation

TABLE 4 | Oil flow velocity and oil pressure under switching times.

Parameters	Value						
Arcing time of main contact (ms)	10	9	8	7	6	5	4
Arcing time of transition contact (ms)	10	9.5	8.5	7.5	6.5	5.5	4.5
Arcing energy (J)	3849	3472	2880	2284	1717	1206	775
Oil flow (m/s)	0.99	0.92	0.81	0.64	0.49	0.38	0.28
Oil pressure (kPa)	55.5	50.8	43.9	34.1	25.1	18.5	12.5

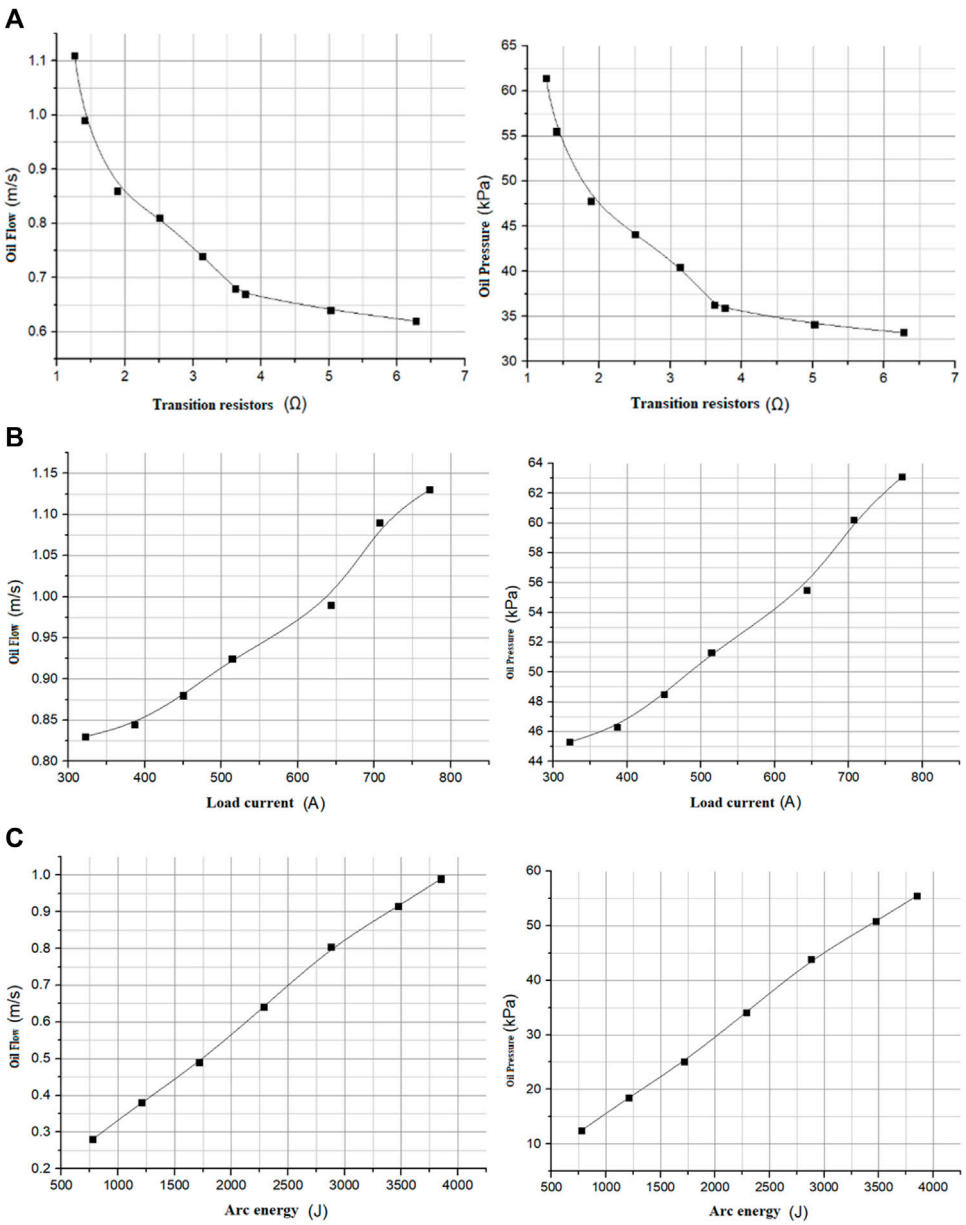

FIGURE 11 | Variation curve of oil flow and oil pressure with transition resistance, load and total arc energy. **(A)** Variation curve of oil flow and oil pressure with transition resistance. **(B)** Variation curve of oil flow and oil pressure with load. **(C)** Variation curve of oil flow and oil pressure with total arc energy.

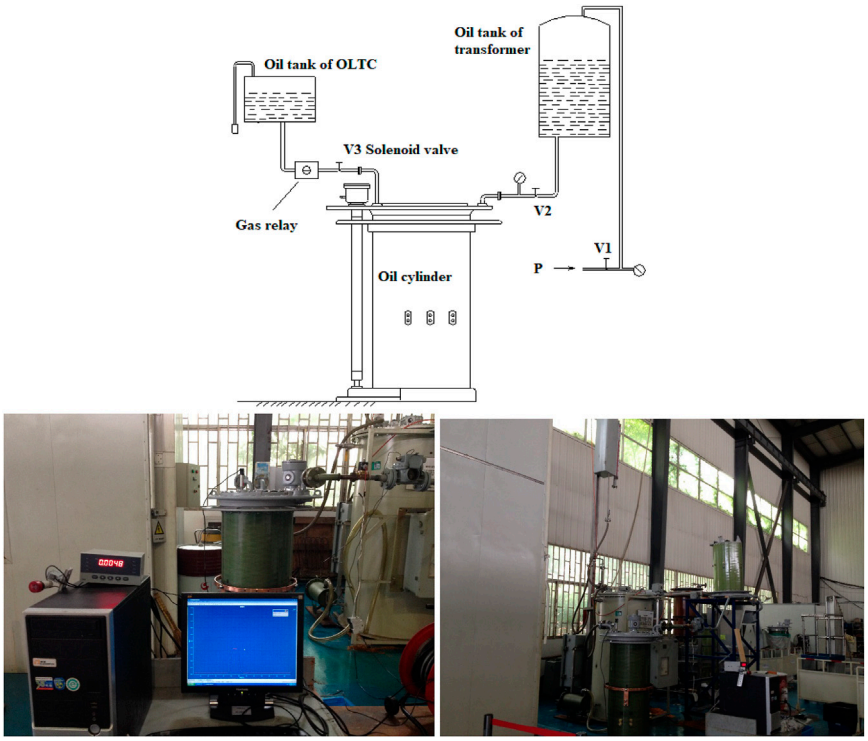

FIGURE 12 | Schematic diagram and physical picture of oil flow relay experiment.

coefficients of both the arcing energy–oil flow and arcing energy–oil pressure are 0.99, indicating that the effect of arcing energy on oil flow and oil pressure is basically linear. The correlation coefficient between oil flow and oil pressure is 0.99, that is, the quantitative relationship between them can be expressed by a linear function.

3.2.2 Characteristics of Oil Flow Surge Under Different Loads

The oil pressure and oil flow speed of insulating oil in the switch oil chamber during OLTC switching under different loads are shown in **Table 3**.

It can be seen from **Table 3** that the arcing energy of the main contact, the arcing energy of the transition contact, and the total arcing energy increase with the increase of the load, and result in the increase of oil flow and oil pressure with the increase of the load. When the load is 1.2 times the rated load, the oil flow speed reaches 1.13 m/s, which is close to the preset 1.5 m/s. Since the gasification of transformer oil caused by arcing is not considered in the simulation, the actual oil flow velocity should be higher than that of the numerical simulation, so it is necessary to consider increasing the setting value of oil flow relay.

3.2.3 Characteristics of Oil Flow Surge Under Different Switching Times

Select different T1, T2, and T3 to simulate the changes of oil flow speed and pressure in the oil chamber of the transfer switch when the on-load tap changer is switched under various combinations, as shown in **Table 4**.

It can be seen from **Table 4** that different switching times lead to differences in arc energy, but the oil flow speed and oil pressure increase with the increase of arc energy.

The curve drawn according to the above simulation data is shown in **Figure 11**.

It can be seen that the smaller the transition resistance, the greater the oil flow speed and oil pressure; the greater the load, the greater the oil flow speed and oil pressure; and the greater the arcing energy, the greater the oil flow velocity and oil pressure.

3.3 Experimental Method

For the OLTC with both oil flow relay and pressure relay, to match the threshold values of the two relays, it is also necessary to carry out the static action characteristic experiment of oil flow relay, to further analyze the corresponding relationship between oil flow and oil pressure. The test principle is shown in **Figure 12**.

A certain pressure is applied to the oil chamber of the OLTC, to simulate the rise of the internal pressure of the oil chamber under OLTC failure, and then the solenoid valve installed in the oil flow relay pipeline is opened to release the pressure immediately, to make the insulating oil surge. Test the action of the oil flow relay to obtain the corresponding relationship between the internal pressure value of the oil chamber and the action of the oil flow relay. Meanwhile, according to the successive approximation principle, the critical pressure

TABLE 5 | Results of oil flow relay static pressure test.

Oil flow speed	Action static pressure range	Number of tests	Action times	Correct rate (%)
1.5 m/s	<96 kPa	500	0	0
	96–102 kPa	500	244	48.8
	>102 kPa	500	500	100
2.0 m/s	<118 kPa	500	0	0
	118–126 kPa	500	227	45.4
	>126 kPa	500	500	100
2.5 m/s	<148 kPa	500	0	0
	148–160 kPa	500	189	37.8
	>160 kPa	500	500	100

threshold of the oil flow relay is defined, which provides a criterion for the OLTC to select appropriate protective relays.

3.4 Analysis of Experimental Results

Three different types of oil flow relays from the same manufacturer with speed threshold values of 1.5 m/s, 2.0 m/s, and 2.5 m/s are used for the comparative experiment. The action pressure range and action percentage are shown in **Table 5**.

It can be seen that by increasing the applied pressure value continuously, the correct rate of oil flow relay action is gradually improved, and finally 100% correct action is achieved. Therefore, we can obtain the reliable operating pressure range of the above three oil flow relays, that is, the oil pressure range of the three oil flow relays (1.5 m/s, 2.0 m/s, and 2.5 m/s) are 96–102 kPa, 118–126 kPa, and 148–160 kPa, respectively.

Therefore, if the oil flow relay of the converter transformer OLTC is one of the above three oil flow relays, the pressure threshold of the matched oil pressure relay can be set with reference to the above results. Otherwise, a similar test method is recommended.

4 CONCLUSION

In view of the problem that the oil flow surge caused by tap switching of the OLTC may cause protection mis-operation, taking the typical double transition resistance type OLTC as an example, the simulation analysis and experimental demonstration of the flow rate and pressure of the insulating oil in the oil chamber during the action of the tap changer were carried out in this article. The conclusion is as follows:

1) The smaller the transition resistance value of the OLTC, the greater the oil flow and pressure during switching. The effect of the arcing energy on oil flow and oil pressure is basically linear. And the quantitative relationship between oil flow and oil pressure can be expressed by linear function.
2) Through the experiment, it is found that the oil pressure corresponding to the oil speed of 1.5 m/s is 96–102 kPa, the oil pressure corresponding to the oil speed of 2.0 m/s is 118–126 kPa, and the oil pressure corresponding to the oil speed of 2.5 m/s is 148–160 kPa. If the oil flow relay of the converter transformer OLTC is one of the above three oil flow relays, the pressure threshold of the matched oil pressure relay can be set with reference to the above results.

The following work of this paper will analyze more types of OLTC and summarize a unified protection configuration method.

DATA AVAILABILITY STATEMENT

The original contributions presented in the study are included in the article/Supplementary Material, further inquiries can be directed to the corresponding author.

AUTHOR CONTRIBUTIONS

HZ, ZX and JD contributed to the establishment of OLTC and analysis; XC and QZ contribute to the experiment of the OLTC; GL and XY contributed to the simulation of OLTC oil flow characteristics.

FUNDING

This work is sponsored by the National Natural Science Foundation of China (No. 52007011).

REFERENCES

Baker, A. M., and Ying, S. (1994). "A Fixed Time Performance Evaluation of Parallel CFD Applications," in *Proc. ACM/IEEE Conf. Sup.* (IEEE), 18–23. doi:10.1145/602770.602781

Castro, J. C., Lagos, G. S., and Gonzalez, O. A. (2017). Simulation and Measuring Transients in On-Load Tap Changers. *IEEE Latin Am. Trans.* 15, 1901–1907. doi:10.1109/TLA.2017.8071234

Ding, G., Zhen, C., Chen, Q., Tian, Y., Zhang, Y., and Yu, G. (2016). Experimental Study on Heavy Gas Setting Value of Domestic on Load Switch for Large Capacity Transformer. *Transformer* 3, 58–59. doi:10.19487/j.cnki.1001-8425.2016.03.015

Duan, X., Zhao, T., Li, T., Liu, J., Zou, L., and Zhang, L. (2017). Method for Diagnosis of On-load Tap Changer Based on Wavelet Theory and Support Vector Machine. *J. Eng.* 2017, 2193–2197. doi:10.1049/joe.2017.0719

Fan, R., Fu, P., Tao, J., Gao, G., Song, Z., Huang, L., et al. (2018). Strategy Design and Transient Analysis of ITER PPEN Transformer On-Load Tap Changer during Converter Operation. *J. Fusion Energ* 37, 346–353. doi:10.1007/s10894-018-0203-0

Lei, Y., Zhao, L., Peng, Z., Bao, L., Yang, J., Zhang, X., et al. (2018). Switching Process Simulation and Type-Selection Technology of On-Load Tap Changer of Converter Transformer. *Sou. Pow. Sys. Tech.* 7, 14–19. doi:10.13648/j.cnki.issn1674-0629.2018.07.003

Li, X. (2017). A New Type of on Load Tap Changer and its Analysis. *High. Vol. Elec. Appa.* 4, 197–202. doi:10.13296/j.1001-1609.hva.2017.04.031

Liang, C., Wu, H., Xia, G., and Zhou, H. (2016). Analysis of Protective Action False Case of OLTC for Converter Transformer. *Transformer* 2, 61–63. doi:10.19487/j.cnki.1001-8425.2016.02.014

Rivas-Trujillo, E., Laniado-Jácome, E., San-Román, J. L., and Díaz, V. (2010). Characterizing the Diverter Switch of a Load Tap Changer in a Transformer Using Wavelet and Modal Analysis. *Eng. Structures* 32, 3011–3017. doi:10.1016/j.engstruct.2010.05.020

Seo, J., Ma, H., and Saha, T. K. (2018). On Savitzky-Golay Filtering for Online Condition Monitoring of Transformer On-Load Tap Changer. *IEEE Trans. Power Deliv.* 33, 1689–1698. doi:10.1109/TPWRD.2017.2749374

Shen, Y., Cao, N., Yang, S., and Ma, Y. (2015). *Simulation of New Power Transformer Hybrid On-Load Tap Changer*. Harbin, china: Coal Mine Machinery

Shi, L. (2015). *Scheme and Simulation Research of a New on Load Tap Changer*. [Dissertation]. Jinan, China: Shandong University doi:10.7666/d.Y2792775

Song, D., Ding, L., Dong, B., Fan, J., and Du, H. (2019a). Experimental Analysis and Research on Arcing Process of on Load Tap Changer with Different Topology. *Adv. Tech. Elec. Eng. Ener.* 12, 55–62.

Song, D., Ma, J., Ma, Y., Lin, H., and Liu, S. (2019b). Research on the Switching Arc Loss of On-Load Tap Changer. *IEEE Access* 7, 180793–180803. doi:10.1109/ACCESS.2019.2959790

Wang, F. (2004). *Computational Fluid Dynamics Analysis - Principle and Application of CFD Software*. Beijing: Chinese Electrical Press.

Wen, D. (2010). *Engineering Fluid Mechanics (Hydraulics)*. Beijing: Tsinghua University Press.

Xu, H., Wang, J., Liao, W., Shan, H., and Wang, J. (2021). Experimental Study on Optimal Configuration of Pressure Relief Device, Pressure and Oil Flow Relay of On-Load Tap-Changer. *Transformer* 10, 48–52. doi:10.19487/j.cnki.1001-8425.2021.10.008

Xu, Y., Zhou, C., Geng, J., Gao, S., and Wang, P. (2019). A Method for Diagnosing Mechanical Faults of On-Load Tap Changer Based on Ensemble Empirical Mode Decomposition, Volterra Model and Decision Acyclic Graph Support Vector Machine. *IEEE Access* 7, 84803–84816. doi:10.1109/ACCESS.2019.2925046

Yang, S., Zhu, N., Yu, Q., and Li, H. (2014). Simulation of on Load Voltage Regulation of Power Transformer Based on PSCAD/EMTDC. *Elec. Tech.* 2, 30–32. doi:10.3969/j.issn.1673-3800.2014.02.007

Yu, B., Yang, Z., Lin, H., Jin, Y., and Yang, Y. (2020). Discussion on Multi-Dimensional Diagnostic Technology Based on Fault of On-Load Tap-Changer. *IOP Conf. Ser. Earth Environ. Sci.* 495, 012008–012012. doi:10.1088/1755-1315/495/1/012008

Zhu, Y., and Shen, D. (2012). *OLTC Electrical Mechanism*. Beijing: Chinese Electrical Press.

Zhu, Y., and Shen, D. (2016). *OLTC for Converter Transformer*. Beijing: Chinese Electrical Press.

Conflict of Interest: Authors HZ, ZX, and JD were employed by the company Extra-High Voltage Transmission Company of China Southern Power Grid. Authors XC and QG were employed by the company Shenyang Transformer Research Institute Co. Ltd.

The remaining authors declare that the research was conducted in the absence of any commercial or financial relationships that could be construed as a potential conflict of interest.

Publisher's Note: All claims expressed in this article are solely those of the authors and do not necessarily represent those of their affiliated organizations, or those of the publisher, the editors, and the reviewers. Any product that may be evaluated in this article, or claim that may be made by its manufacturer, is not guaranteed or endorsed by the publisher.

frontiers | Frontiers in Energy Research

ORIGINAL RESEARCH
published: 14 April 2022
doi: 10.3389/fenrg.2022.873262

Optimal Regulation Strategy of Electric Vehicle Charging and Discharging Based on Dynamic Regional Dispatching Price

Shaohua Yu[1], *Zhaobin Du*[1,2]* *and Lidan Chen*[3]

[1]School of Electric Power Engineering, South China University of Technology, Guangzhou, China, [2]Guangdong Province' New Energy Power System Intelligent Operation and Control Enterprise Key Laboratory, Guangzhou, China, [3]School of Electrical Engineering, Guangzhou City University of Technology, Guangzhou, China

With the continuous and rapid growth of electric vehicle (EV) ownership, a large number of disorderly charging loads accessed to the regional grid may lead to problems such as widening of the peak-to-valley load difference and deterioration of power quality. This study proposes an optimal EV charging and discharging regulation strategy based on dynamic regional dispatching price to give full play to the EV vehicle-to-grid (V2G) regulation potential and reasonably regulate EV charging and discharging behavior to ensure safe, high-quality, and economic operation of the grid. First, the EV travel chain model is constructed according to the travel behavior pattern of EV users to obtain the spatial and temporal distribution characteristics of EV charging and discharging loads. Second, considering the difference in regional grid operation states, a dynamic update strategy of regional dispatching price integrating power grid spatial and temporal information is proposed. Furthermore, considering the characteristics of EV mobile energy storage and user demand, an EV V2G optimal regulation model that takes into account the interests of distribution system operators, EV aggregators, and EV users is established to effectively guide the regulation of EV charging and discharging behavior. Finally, the simulation results show that the proposed strategy can effectively reduce the load deviation of each regional grid, operation cost of EV aggregators, and charging cost of EV users and significantly improve the safety and economy of the power system.

Keywords: electric vehicle, vehicle-to-grid (V2G), optimal regulation, dynamic dispatching price, user demand, multi-stakeholder

OPEN ACCESS

Edited by:
Dongqi Liu,
Changsha University of Science and Technology, China

Reviewed by:
Tao Chen,
Southeast University, China
Deng Youjun,
Tianjin University, China

***Correspondence:**
Zhaobin Du
epduzb@scut.edu.cn

Specialty section:
This article was submitted to Smart Grids, a section of the journal Frontiers in Energy Research

Received: *10 February 2022*
Accepted: *11 March 2022*
Published: *14 April 2022*

Citation:
Yu S, Du Z and Chen L (2022) Optimal Regulation Strategy of Electric Vehicle Charging and Discharging Based on Dynamic Regional Dispatching Price. Front. Energy Res. 10:873262. doi: 10.3389/fenrg.2022.873262

INTRODUCTION

With the continuous progress of human society and the rapid development of the world economy, the problems of energy depletion and environmental pollution caused by the continuous increase in energy demand are gradually receiving attention and importance (Schirone and Pellitteri, 2017; Fang et al., 2019). Electric vehicles (EVs) have been rapidly developed and popularized due to their significant advantages of energy efficiency, low carbon and environmental protection, and the number of ownerships continues to rise. The social, economic, and environmental benefits of transportation electrification are becoming increasingly significant (Cui et al., 2021). However, the disorderly charging behavior of a large number of EVs may bring problems to the grid such as line

and transformer overload, widening of load peak–valley difference, and deterioration of power quality, which bring great challenges to the safe, high-quality, and economic operation of the power system (Shao et al., 2017; Chen et al., 2018). In addition, in the context of the rapid development and application of vehicle-to-grid (V2G) technology, an EV has the dual attributes of source and load and has great potential to smooth out grid load fluctuations, improve grid power quality, participate in grid auxiliary services, and improve the economic efficiency of users as a highly flexible mobile energy storage unit (Chen et al., 2019; Wu et al., 2019; Lo et al., 2021). Therefore, reasonable charging and discharging regulation can effectively alleviate the negative impact of EV charging load on the grid and improve the safety and economy of power system operation (Zhang et al., 2017).

At present, in a relevant research study on the optimal regulation strategy of electric vehicle V2G, Zhou et al. (2017) classified EV V2G scheduling application scenarios into renewable energy integration, provision of auxiliary services, and demand-side active participation in the electricity market and proposed a robust energy scheduling method for electric vehicle V2G to effectively shift peak loads and reduce total system operating costs. Tabatabaee et al. (2017) aimed to minimize the grid operation cost, established a collaborative dispatch model of EV and new energy generation, and improved the grid operation economy through V2G technology. Wang et al. (2020) established an optimal market bidding model for virtual power plants considering large-scale EVs based on the EV V2G feasible domain, which significantly improved the operation economy of virtual power plants. Chandra Mouli et al. (2019) combined the characteristics of building photovoltaic (PV) power generation and EV charging/discharging behavior and proposed an EV charging and discharging energy management strategy based on the grid dynamic electricity price, which reduced the cost of EV charging and improved the system economy. Chen et al. (2020) took into account the mobility characteristics of different EV clusters and established an EV V2G scheduling strategy with the objective function of smoothing grid load fluctuations, which promoted renewable energy consumption and improved safe and economic system operation. With the goal of smoothing load fluctuations and improving EV users' revenue, Li et al. (2021) proposed an EV scheduling strategy based on user behavior to improve system operational safety and economy. However, the aforementioned research only considered the interests of one or two stakeholders among the distribution system operator (DSO), EV aggregator (EVA), and EV users. In fact, ensuring multi-stakeholder profits and win–win situation for DSO, EVA, and EV users is the premise to encourage EVs to actively participate in the optimal regulation of charge and discharge.

At the same time, in a relevant research study on EV orderly charging and discharging strategies based on the electricity price signal, Duan et al. (2020) dynamically updated the electricity price signal according to the number of EVs in the charging station and proposed an EV charging scheduling method based on a smart contract to ensure stable operation of the grid. Aiming at maximizing the revenue of charging stations, Cheng et al. (2018) proposed an orderly charging method for EVs based on a time-of-use (TOU) price signal, which significantly improved charging station revenue but had a limited effect on smoothing load fluctuations. Zhou et al. (2020) considered time sensitivity of EV users and proposed an EV charging and discharging scheduling model based on the dynamic electricity price mechanism to save users' charging costs. Based on the time-sharing tariff mechanism, Pan et al. (2019) proposed a real-time optimal scheduling strategy for EV charging that took into account the interests of the DSO, EVA, and EV users, effectively smoothed load fluctuations, reduced operating costs, and improved users' satisfaction. Based on the evaluation results of EV charging load shifting potential, Gan et al. (2020) quantified the impact of the TOU price mechanism on EV charging load transfer and realized the reasonable transfer of EV charging load based on the TOU price mechanism. However, the aforementioned research on electricity price signals mainly focuses on the time dimension, through changing the temporal distribution of EV charging power to achieve the corresponding goals. There are few EV orderly charge and discharge guidance strategies based on the electricity price signal in spatial and time dimensions. In fact, there are some differences in the grid infrastructure and operation states of each spatial region of the power system. On the one hand, the regional grid unified electricity price signal mechanism is difficult to give full play to the EV V2G regulation potential, and on the other hand it may lead to the unreasonable spatial distribution of EV charging and discharging loads and overloading of lines and transformers in local areas.

In addition, in the relevant research study based on the temporal and spatial pricing mechanism, the locational marginal pricing (LMP) can alleviate the distribution network congestion caused by EV load (Ma et al., 2016; Liu et al., 2018). Li et al. (2014) proposed an EV optimal charging strategy based on distribution LMP (DLMP), which can effectively alleviate the power grid congestion. Hu et al. (2019) proposed an optimal scheduling strategy for load aggregators based on DLMP with an iterative approach to effectively solve the bidirectional blocking problem in distribution networks. Although LMP is the most accurate pricing method, it is quite sensitive to distribution network structure, network constraints, and load level. The actual implementation is very complicated, and it is difficult to obtain the data of each node and complete the node marginal price calculation and online decision-making in the distribution system with a large number of nodes in real time, which has certain limitations (Singh and Srivastava, 2005). Therefore, the resource dispatching regional pricing mechanism as a simplified way of LMP is more in line with the needs of the engineering practice, with higher operational flexibility and easier to achieve distribution network load management.

Thus, this study proposes an optimal regulation strategy for EV V2G based on dynamic regional dispatching price. First, an EV travel behavior simulation and prediction model is constructed based on the travel chain theory to obtain the spatial and temporal distribution characteristics of EV charging and discharging loads. Second, considering the differences in regional grid operation states, a dynamic regional dispatching price update strategy integrating the

spatial and temporal information of the grid is proposed. Furthermore, an EV V2G optimal regulation model is established based on dynamic regional dispatching price taking into account the EV mobile energy storage characteristics and user demand as well as the interests of DSO, EVA, and EV users. Finally, the IEEE-33 node system is used as an example for simulation analysis to verify the effectiveness of the proposed strategy in this study. The results show that the proposed regulation strategy can effectively reduce the regional grid load deviation, the operating cost of EVA, the charging cost of EV users, and effectively improve the safety and economy of the system.

The main contributions and salient features of this study are as follows:

1) Considering the battery energy risk awareness and the uncertainty of leaving of EV users in advance, an EV-guaranteed energy adaptive adjustment method based on the regulation time is proposed to ensure the electricity demand of users and illustrate the impact of different guaranteed electricity energy on the regulation effect of EVs.
2) A dynamic update strategy of regional dispatching price based on the regional grid operation states and EV on-grid rate is proposed. Then, considering the users' features in 1), an EV V2G optimal regulation model based on regional flexible pricing is established, and the cost–benefit analysis model is used to optimize the profit of each stakeholder. The superiority of the proposed strategy is verified by comparing with the classical tariff signals in current works. Therefore, the proposed flexible dispatching price strategy has great application potential in guiding EV orderly charging and discharging behavior.

V2G REAL-TIME OPTIMIZED REGULATION ARCHITECTURE

With the development and wide application of technologies such as the Internet of Things, big data, and cloud services, the comprehensiveness and timeliness of information interaction have been greatly satisfied. In this context, the massive data between DSO, regional EVA, and EV users will interact in real time, and then the multidimensional data information of the system can be integrated to formulate the EV V2G charging and discharging regulation strategy. The electric vehicle V2G real-time optimal regulation architecture proposed in this study is shown in **Figure 1**, including the V2G real-time optimal regulation framework and energy and information flow among various stakeholders. In **Figure 1**, EV regulation cloud service (CS) is a non-profit organization to achieve the goal of optimal operation of the whole system. It is mainly responsible for the centralized interaction of various stakeholders' information, regional dispatching price update, and EV regulation strategy formulation. DSO is one of the stakeholders, aiming at minimizing the active load deviation of the grid and smoothing the active load fluctuation. It is mainly responsible for the regional base active load and EV users' supply and sales services. The regional EVA is the main executor of the V2G regulation scheme, aiming to minimize the operating cost and mainly responsible for regulating the charging and discharging behavior of regional EVs. EV users are the basis of the V2G regulation framework. It aims at minimizing the charging cost, meeting the power demand of vehicles, and realizing low charging costs.

This study adopts an incentive contract approach to regulate EVs in the system. The incentive contract approach means that the EVA and the EV user sign an incentive contract agreement in which the EV user grants the regulation right to the EVA and the EVA can freely regulate the charging and discharging behavior of authorized EVs to achieve its goal within certain restrictions, while the EVA will provide the EV user with a certain charging discount. Under the proposed regulation framework, CS communicates directly with the DSO and the regional EVA in a bidirectional manner, and based on the collected state information of DSO, EVA, and EV users, CS dynamically updates DSO's discharge incentive price and EVA's charging service fee. An EV charging and discharging regulation strategy is formulated to maximize the safety and economic benefits of the whole system considering the interests of DSO, regional EVA, and EV users. Then CS communicates the regulation scheme to DSO and regional EVA, and the regional EVA directly regulates the charging and discharging behavior of regional grid–connected EVs according to the regulation scheme. In this process, the system meets the total requirement of large-scale EV response power and realizes fast charging and discharging behavior regulation of a large number of EVs.

ELECTRIC VEHICLE CHARGING AND DISCHARGING REGULATION MODEL CONSIDERING MULTIPLE STAKEHOLDERS

Spatial and Temporal Distribution Characteristics of EV Charging Demand

Electric Vehicle Travel Chain Model

The travel chain model is an effective method to describe the travel behavior patterns of EV users (Chen et al., 2015), involving a large number of spatiotemporal characteristic variables such as travel time, travel purpose, and travel sequence. The EV travel chain model is divided into two parts: the time chain and the space chain. The time chain describes the time distribution of user travel, including time variable information such as the first travel time, travel time, arrival time, and departure time, and the space chain describes the spatial transfer of user travel, including travel purpose, travel distance, travel order, and other space information.

According to the difference in the functional properties of the block within the system area, the system area can be divided into office region (O), business region (B), and home region (H). The starting and ending locations of each EV travel chain are supposed to be home regions. Each EV can travel among different functional regions, and the travel chain structure is

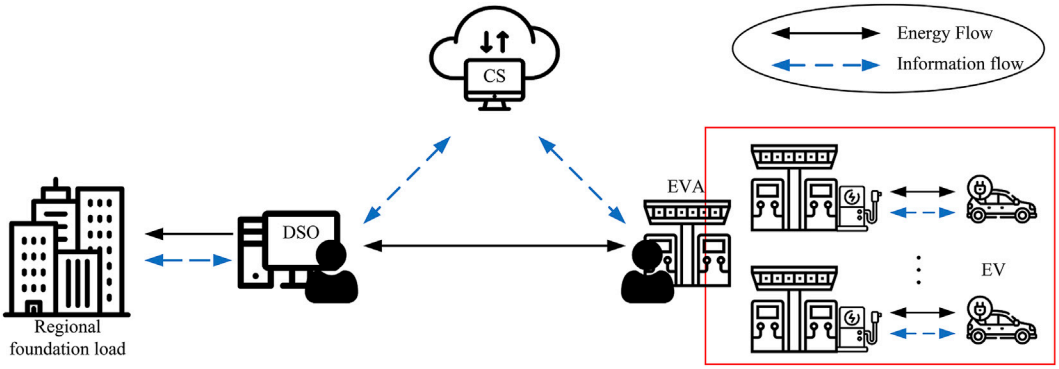

FIGURE 1 | V2G real-time optimal regulation framework.

determined based on the respective travel demand, the number of travel activities, and their travel order. The UK National Travel Survey (NTS) is a household survey of personal travel by residents of England traveling within Great Britain, from data collected *via* interviews and a 7-day travel diary, which enables analysis of patterns and trends (UK Department for Transport, 2019). Thus, based on the 2019 UK NTS database statistics and the Monte Carlo Markov chain (MCMC) method, this study generates the travel chain model for EVs, including simple and complex travel chains such as H→O→H, H→B→H, and H→O→B→H. Among them, the H→O/B→H travel chains structure represents the travel process of EV users starting from the home region to the office/business region and finally returning to the home region. The analysis of the H→O→B→H travel chain structure is the same.

According to the 2019 UK NTS database (UK Department for Transport, 2019), the probability density functions of EV arrival time, departure time, and initial state of charge (SOC) can be fitted by a normal distribution, as follows:

$$\begin{cases} f(T_{in}) = \dfrac{1}{\sqrt{2\pi}\sigma_{T_{in}}} \exp\left(-\dfrac{\left(T_{in} - \mu_{T_{in}}\right)^2}{2\sigma_{T_{in}}^2} \right); \\ f(T_{out}) = \dfrac{1}{\sqrt{2\pi}\sigma_{T_{out}}} \exp\left(-\dfrac{\left(T_{out} - \mu_{T_{out}}\right)^2}{2\sigma_{T_{out}}^2} \right); \\ f(SOC_{in}) = \dfrac{1}{\sqrt{2\pi}\sigma_{SOC_{in}}} \exp\left(-\dfrac{\left(SOC_{in} - \mu_{SOC_{in}}\right)^2}{2\sigma_{SOC_{in}}^2} \right), \end{cases} \tag{1}$$

where T_{in}, T_{out}, and SOC_{in} represent the EV arrival time, departure time, and initial SOC, respectively.

Electric Vehicle Charging Demand Model

In the process of EV charging and discharging regulation, users' behavior features will directly affect EV charging demand to an extent. That is, users have a certain risk awareness of EV battery's electricity energy and hope that EV's battery energy will be available when leaving in advance. Therefore, considering that the probability of EV leaving early gradually increases with the regulation time, the lower limit of EV SOC is adaptively adjusted according to the regulation time, as shown in **Figure 2**. Thus, the charging demand of a single EV is presented by **Eq. 2**, and the battery SOC boundaries and the regulatory region are shown in **Figure 3**.

$$\begin{cases} SOC_{n,i,t+1} = SOC_{n,i,t} + \dfrac{\left(\eta_{ch} P_{n,i,t}^{ch} - P_{n,i,t}^{disc} / \eta_{disc}\right)\Delta t}{E}, \\ SOC_{n,i,T_{n,out}} \geq SOCE_{n,i}, \\ SOC_{n,i,t}^{\min} = \left(\dfrac{t - T_{n,in}}{T_{n,out} - T_{n,in} + 1} + \lambda_n \right)^2 SOC_n^{down}, \quad t \in [T_{n,in}, T_{n,out}], \\ SOC_{n,i,t}^{\min} \leq SOC_{n,i,t} \leq SOC_{n,i,t}^{\max}, \end{cases} \tag{2}$$

where $SOC_{n,i,t}$ is the SOC of the nth EV in region i at time t; $P_{n,i,t}^{ch}$ and $P_{n,i,t}^{disc}$ are the charging and discharging power of the nth EV in region i at time t, respectively, where the home region and the office region are slow charging and slow discharging, and the business region is fast charging and fast discharging; η_{ch} and η_{disc} are the EV charging and discharging efficiencies, respectively; E is the battery capacity of a single EV; $SOCE_{n,i}$ is the off-grid minimum expected SOC of the nth EV in region i; $SOC_{n,i,t}^{\max}$ and $SOC_{n,i,t}^{\min}$ are the upper and lower SOC limits of the nth EV battery, respectively; SOC_n^{down} is the lower limit of the nth EV

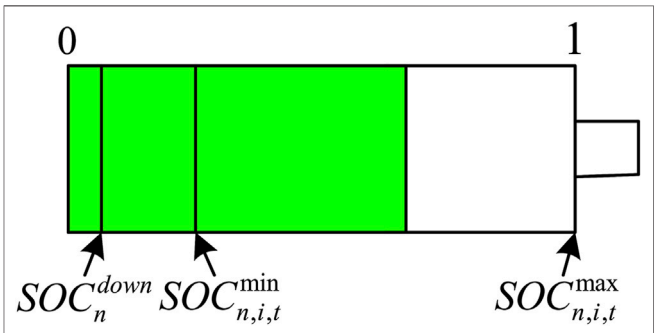

FIGURE 2 | Schematic diagram of upper and lower limits of battery SOC of EV.

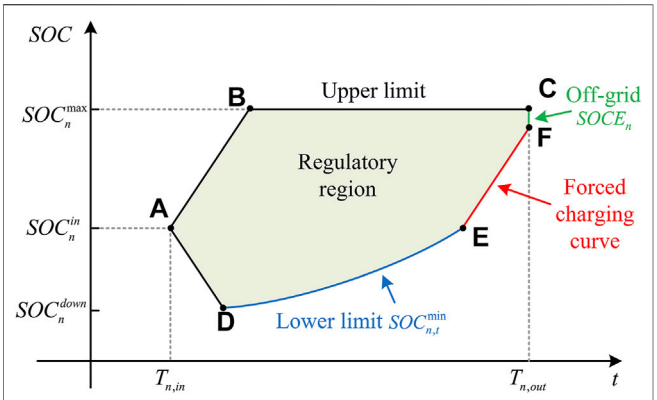

FIGURE 3 | SOC boundaries of a single EV.

battery SOC base; $T_{n,in}$ and $T_{n,out}$ are the arrival time and departure time of nth EV, respectively; λ_n is the SOC-guaranteed lower limit growth factor, which is taken as 1.5 by default; and Δt is the regulation time interval.

In **Figure 3**, the area enclosed by ABCFED represents the power and energy regulatable range of a single EV, the path ABC represents the disorderly charging curve, the slope of the straight line AB corresponds to the maximum charging rate $\eta_{ch} P_{n,i,t}^{ch,\max}/E$ of a single EV, AD represents the EV initial discharge curve, the slope corresponds to the maximum discharging rate $P_{n,i,t}^{disc,\max}/(E\eta_{disc})$ of a single EV, and the line EF represents the forced charging curve before EV leaves the grid.

Electric Vehicle Charging and Discharging Regulation Model

Based on the regional flexible dispatching electricity price signal, the EV charging and discharging regulation model takes DSO, EVA, and EV users' interests as the comprehensive optimization objective function and selects the charging and discharging power $P_{n,i,t}^{ch}$ and $P_{n,i,t}^{disc}$ of a single EV as the decision variables.

Distribution System Operator Objective

The DSO stakeholder is optimized to minimize load deviations, as follows:

$$f_1 = \sum_{t=1}^{T}\sum_{i=1}^{I}\left(P_{i,t}^{basic} + P_{i,t}^{EV} - P_i^{av}\right)^2, \tag{3}$$

where T is the regulation period; I is the number of functional regions, meaning the number of EVAs is also I; $P_{i,t}^{basic}$ is the basic active load of region i at time t; and $P_{i,t}^{EV}$ is the total EV charging and discharging power of region i at time t and P_i^{av} is the average active load in region i, expressed as follows:

$$P_{i,t}^{EV} = \sum_{n=1}^{N_{i,t}} P_{n,i,t}^{EV}; \tag{4}$$

$$P_i^{av} = \frac{1}{T}\sum_{t=1}^{T}\left(P_{i,t}^{basic} + P_{i,t}^{EV}\right), \tag{5}$$

where $P_{n,i,t}^{EV}$ is the nth EV charging and discharging power in region i at time t, with positive values indicating charging power and negative values indicating discharging power; $N_{i,t}$ is the number of EVs accessed to the grid in region i at time t.

EV Aggregator Objective

The EVA stakeholder is optimized to minimize operating costs, as follows:

$$f_2 = \sum_{t=1}^{T}\sum_{i=1}^{I}\sum_{n=1}^{N_{i,t}}\left(C_{n,i,t}^{power} + C_{n,i,t}^{incentive} - C_{n,i,t}^{reserve}\right), \tag{6}$$

where $C_{n,i,t}^{power}$, $C_{n,i,t}^{incentive}$, and $C_{n,i,t}^{reserve}$ are the EVA power purchase cost, incentive cost, and reserve revenue, respectively, expressed as follows:

$$\begin{cases} C_{n,i,t}^{power} = \left(v_{i,t}^{e} P_{n,i,t}^{ch} - v_{i,t}^{disc} P_{n,i,t}^{disc}\right)\Delta t \\ C_{n,i,t}^{incentive} = \left(\gamma_i v_{i,t}^{ch} P_{n,i,t}^{ch}\right)\Delta t \\ C_{n,i,t}^{reserve} = v_{i,t}^{re}\left(P_{n,i,t}^{up} + P_{n,i,t}^{down}\right)\Delta t \end{cases}, \tag{7}$$

where $v_{i,t}^{e}$ is the grid electricity price of region i at time t; $v_{i,t}^{ch}$ and $v_{i,t}^{disc}$ are the EV charging and discharging prices, respectively, and its development update strategy is presented in **Section 3.3.1**; γ_i is the incentive strength given by the regional EVA to EV users; $v_{i,t}^{re}$ is the electricity price for EVs to provide rotating reserve services; $P_{n,i,t}^{up}$ and $P_{n,i,t}^{down}$ are the up and down reserve power provided by the nth EV at time t, respectively, to cope with the decreasing and increasing grid frequency.

Electric Vehicle User Objective

The EV user stakeholder is optimized to minimize charging and discharging costs, including charging costs and battery degradation costs, as follows:

$$f_3 = f_{31} + f_{32}, \tag{8}$$

where f_{31} and f_{32} are the EV users charging cost and EV battery degradation cost, respectively.

1) EV users charging cost

$$f_{31} = \sum_{t=1}^{T}\sum_{i=1}^{I}\sum_{n=1}^{N_{i,t}}\left((1-\gamma_i) v_{n,i,t}^{ch} P_{n,i,t}^{ch}\right)\Delta t. \tag{9}$$

2) EV battery degradation cost

The frequent cyclic charging and discharging behavior of EV battery will bring about the problem of battery degradation, and the cost of battery degradation will directly affect the EV charging and discharging decision. Thus, it is necessary to consider the battery degradation cost in the EV charging and discharging regulation process, and the battery life is often related to factors such as the number of charge–discharge cycles and depth of discharge. Neubauer and Wood (2014) gave the relationship

between the life of lithium battery and the number of cycles, and the relevant data are provided by the battery manufacturer. The corresponding battery degradation cost based on the approximate rainflow counting method (Kazemi and Zareipour, 2018) is presented by **Eq. 10**.

$$f_{32} = \sum_{n=1}^{N_{i,t}} \frac{C^B}{L_n}, \tag{10}$$

where C^B is the battery acquisition capital cost; L_n is the lifespan of the EV battery, which is affected by the EV charging and discharging behavior, as follows:

$$\begin{cases} L_n = \dfrac{C^{F100}}{\sum_{t=1}^{T}\sum_{i=1}^{I} C_{n,i,t}^{E100}} \\ C_{n,i,t}^{E100} = \dfrac{1}{2}\left(\dfrac{D_{n,i,t}}{E}\right)^{kp} \end{cases}, \tag{11}$$

where C^{F100} is the maximum number of full cycle to failure, $C_{n,i,t}^{E100}$ is the full cycle equivalent of the partial cycle, $D_{n,i,t}$ is the partial cycle of nth EV battery of region i at time t, and kp is a constant in the range of 0.8–2.1.

Model Comprehensive Optimization Objective

In summary, the proposed model in this study is a multi-objective optimization problem. To fully reflect the importance of each objective and facilitate the solution of the model, the objectives of each stakeholder are normalized and then linearly weighted by the weighting coefficient method, and the comprehensive optimization objective function of this model is obtained, as shown in **Eq. 12**.

$$\begin{aligned} \min F = {} & \omega_1 \sum_{t=1}^{T}\sum_{i=1}^{I}\left(P_{i,t}^{basic} + P_{i,t}^{EV} - P_i^{av}\right)^2 + \\ & \omega_2 \sum_{t=1}^{T}\sum_{i=1}^{I}\sum_{n=1}^{N_{i,t}}\left(C_{n,i,t}^{power} + C_{n,i,t}^{incentive} - C_{n,i,t}^{reserve}\right) + \\ & \omega_3 \left(\sum_{t=1}^{T}\sum_{i=1}^{I}\sum_{n=1}^{N_{i,t}}\left((1-\gamma_i)v_{n,i,t}^{ch} P_{n,i,t}^{ch}\Delta t\right) + \sum_{n=1}^{N_{i,t}}\frac{C^B}{L_n}\right), \end{aligned} \tag{12}$$

where ω_1, ω_2, and ω_3 are the weight coefficients of DSO, EVA, and EV users' optimization objectives, respectively, which are flexibly determined by CS according to the importance and priority of optimization objectives. In this study, taking into account the interests of all stakeholders and based on the normalization process, ω_1, ω_2, and ω_3 are taken as 7×10^{-8}, 4.5×10^{-4}, and 5×10^{-4}, respectively.

Model Constraints

The constraints of the objective function are listed as follows.

1) EV charging and discharging constraints

$$P_{n,i,t}^{EV} = U_{n,i,t}^{ch} P_{n,i,t}^{ch} - U_{n,i,t}^{disc} P_{n,i,t}^{disc}; \tag{13}$$

$$P_{n,i,t}^{ch,\min} \le P_{n,i,t}^{ch} \le P_{n,i,t}^{ch,\max}; \tag{14}$$

$$P_{n,i,t}^{disc,\min} \le P_{n,i,t}^{disc} \le P_{n,i,t}^{disc,\max}; \tag{15}$$

$$U_{n,i,t}^{ch} + U_{n,i,t}^{disc} \le 1; \tag{16}$$

$$P_{n,i,t}^{EV} = 0, \quad t \notin \left[T_{n,in}, T_{n,out}\right], \tag{17}$$

where $P_{n,i,t}^{ch,\max}$ and $P_{n,i,t}^{ch,\min}$ are the maximum and minimum charging power of the nth EV in region i at time t, respectively; $P_{n,i,t}^{disc,\max}$ and $P_{n,i,t}^{disc,\min}$ are the maximum and minimum discharging power of the nth EV in region i at time t, respectively; and $U_{n,i,t}^{ch}$ and $U_{n,i,t}^{disc}$ are the charging and discharging marks of the nth EV, respectively, which are 0–1. $U_{n,i,t}^{ch} = 1$ means the EV is in charging state, while $U_{n,i,t}^{ch} = 0$ means the EV is not in charging state; $U_{n,i,t}^{disc}$ is similarly defined.

2) EV up and down reserve capacity constraints

$$P_{n,i,t}^{up} \le P_{n,i,t}^{EV} + P_{n,i,t}^{disc,\max}; \tag{18}$$

$$P_{n,i,t}^{down} \le P_{n,i,t}^{ch,\max} - P_{n,i,t}^{EV}, \tag{19}$$

3) Distribution transformer capacity constraints

$$P_{i,t}^{basic} + \sum_{n=1}^{N_{i,t}} P_{n,i,t}^{EV} \le P_i^{tr,\max}, \tag{20}$$

where $P_i^{tr,\max}$ is the maximum active capacity of the transformer in region i.

Dynamic Update Strategy of Regional Dispatching Price

Regional Dispatching Price Strategy

As a special commodity with dual attributes of time and space, the value of electric energy changes with different distribution of time and space, so the electricity price should also have the difference of time and space (Schweppe et al., 1988). A reasonable electricity price signal can effectively guide the regulation of EV resources charging and discharging behavior, and the dynamic update strategy of regional dispatching electricity price is the basis and key to fully play the role of electricity price signal and develop the solution of EV charging and discharging problem. Thus, in order to achieve global optimization of the system and improve participation enthusiasm of EVA and EV users, this study formulates the dynamic update strategy of regional dispatching price on the basis of peak-to-valley TOU tariff. The dynamic update strategy includes discharge incentive dispatching price and charging service fee, as follows:

1) Dynamic update strategy of EV discharge incentive dispatching price

The V2G discharge incentive dispatching price comprehensively considers the operation characteristics of the regional power grid. It is updated and formulated by the CS according to the regional DSO peak-shaving and valley-filling demand and the EV on-grid rate and communicated to the regional EVAs through the communication network. The regional EVAs respond to regulation scheme according to the

discharge incentive dispatching price level; the update strategy is as follows:

$$v_{i,t}^{comp} = k_{i,t}^{d} v^{bcomp}, \tag{21}$$

where $v_{i,t}^{comp}$ is the V2G discharge incentive dispatching price of EVs in region i at time t; v^{bcomp} is the V2G base discharge incentive dispatching price, which is taken as 0.35 Yuan/kWh in this study; and $k_{i,t}^{d}$ is the V2G discharge incentive dispatching price adjustment coefficient, which is positive when there is peak-shaving demand on the grid and zeroes otherwise, expressed as follows:

$$\begin{cases} k_{i,t}^{d} = r_i^{d} k_{i,t}^{dp} k_{i,t}^{ds} \\ k_{i,t}^{dp} = \begin{cases} 0 & P_{i,t}^{basic} < P_i^{avb} \\ \exp\left(\dfrac{P_{i,t}^{basic} - P_i^{avb}}{P_i^{avb}}\right) & P_{i,t}^{basic} \geq P_i^{avb} \end{cases} \\ k_{i,t}^{ds} = \begin{cases} k_{i,t}^{ds1} & 0 \leq \alpha_{i,t}^{s} < \alpha_{i,t}^{ds1} \\ k_{i,t}^{ds2} & \alpha_{i,t}^{ds1} \leq \alpha_{i,t}^{s} < \alpha_{i,t}^{ds2} \\ k_{i,t}^{ds3} & \alpha_{i,t}^{ds2} \leq \alpha_{i,t}^{s} \leq 100\% \end{cases} \\ \alpha_{i,t}^{s} = \dfrac{N_{i,t}}{N_i^{s}} \times 100\% \\ P_i^{avb} = \dfrac{1}{T}\sum_{t=1}^{T}\left(P_{i,t}^{basic}\right) \end{cases}, \tag{22}$$

where r_i^{d} is the discharge incentive price regulation coefficient of region i; $k_{i,t}^{dp}$ and $k_{i,t}^{ds}$ are the grid peak-shaving coefficient and EVA incentive coefficient, respectively; P_i^{avb} is the average value of the basic active load in region i; $\alpha_{i,t}^{s}$ is the EVA charging piles utilization rate, and to fully stimulate the V2G potential of EVs, more incentive subsidies should be given when the utilization rate is higher and this study sets three discount ranges; $k_{i,t}^{ds1}$, $k_{i,t}^{ds2}$, and $k_{i,t}^{ds3}$ denote the incentive strength of different ranges, respectively; $\alpha_{i,t}^{ds1}$ and $\alpha_{i,t}^{ds2}$ are the range of utilization rate, respectively; and N_i^{s} is the number of charging piles in EVA of region i, which is often one pile to one car in engineering practice.

2) Dynamic update strategy of EV charging service fee

The EV charging service fee is formulated and updated by CS and then transmitted to regional EVAs and EV users based on regional grid operation states and the EV on-grid rate. The regional EVAs and EVs respond to the regulation scheme, and the specific strategy is as follows.

$$v_{i,t}^{serv} = k_{i,t}^{c} v^{bserv}, \tag{23}$$

where $v_{i,t}^{serv}$ is the EV charging service fee of region i at time t; v^{bserv} is the basic charging service fee, which is taken as 0.6 Yuan/kWh in this study; and $k_{i,t}^{c}$ is the charging service fee adjustment coefficient, expressed as follows:

$$\begin{cases} k_{i,t}^{c} = r_i^{c} k_{i,t}^{cs} k_{i,t}^{cp} \\ k_{i,t}^{cs} = \begin{cases} k_{i,t}^{cs1} & 0 \leq \alpha_{i,t}^{s} < \alpha_{i,t}^{cs1} \\ k_{i,t}^{cs2} & \alpha_{i,t}^{cs1} \leq \alpha_{i,t}^{s} < \alpha_{i,t}^{cs2} \\ k_{i,t}^{cs3} & \alpha_{i,t}^{cs2} \leq \alpha_{i,t}^{s} \leq 100\% \end{cases} \\ k_{i,t}^{cp} = \dfrac{P_{i,t}^{basic}}{P_i^{L\max} - P_i^{L\min}} \end{cases}, \tag{24}$$

where r_i^{c} is the charging service fee regulation coefficient of region i; $k_{i,t}^{cs}$ is the EVA adjustment coefficient, and in order to reduce the charging cost of EV users, more discounts should be given when the utilization rate is higher and this study sets three discount ranges; $k_{i,t}^{cs1}$, $k_{i,t}^{cs2}$, and $k_{i,t}^{cs3}$ represent the discount coefficients in different ranges, respectively; $\alpha_{i,t}^{cs1}$ and $\alpha_{i,t}^{cs2}$ are the range of charging piles utilization rate, respectively; $k_{i,t}^{cp}$ is the peak shaving and valley filling coefficient of the power grid; and $P_i^{L\max}$ and $P_i^{L\min}$ are the maximum and minimum values of the basic active load of the power grid in region i, respectively.

3) Electricity price constraints

$$v_{i,t}^{ch} = v_{i,t}^{e} + v_{i,t}^{serv}; \tag{25}$$

$$v_{i,t}^{disc} = v_{i,t}^{e} + v_{i,t}^{comp}; \tag{26}$$

$$v_{i,t}^{ch,\min} \leq v_{i,t}^{ch} \leq v_{i,t}^{ch,\max}; \tag{27}$$

$$v_{i,t}^{disc,\min} \leq v_{i,t}^{disc} \leq v_{i,t}^{disc,\max}, \tag{28}$$

where $v_{i,t}^{ch,\max}$ and $v_{i,t}^{ch,\min}$ are the upper and lower limits of EV charging electricity price in region i at time t, respectively; $v_{i,t}^{disc,\max}$ and $v_{i,t}^{disc,\min}$ are the upper and lower limits of EV discharging electricity price in region i at time t, respectively.

Economic Cost–Benefit Analysis Model of Stakeholders

The cost–benefit analysis of stakeholders is as follows.

1) DSO economic benefit analysis

As the implementation institution of EV discharge incentive dispatching price, DSO is the main beneficiary of EV charging and discharging regulation. In the process of EV charging and discharging regulation, DSO costs mainly include the expenses of purchasing EV V2G electricity and reserve capacity, that is, the discharging cost and reserve cost paid to EVAs or EV users, and DSO benefits are mainly avoidable capacity and avoidable power benefits. The avoidable capacity benefit is the reduced investment costs for new or expanded grid construction such as transformers, transmission lines, and their supporting equipment through V2G technology, and the avoidable power benefit is the reduced cost of power purchased from generators during peak periods. The details are as follows:

$$R_g = B_g - C_g, \tag{29}$$

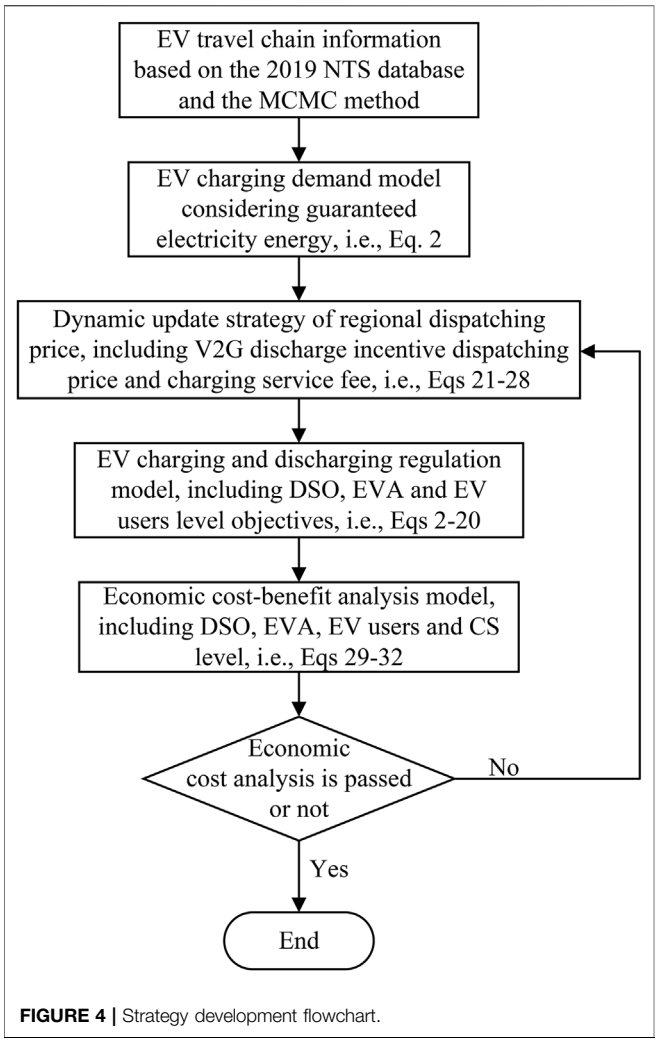

FIGURE 4 | Strategy development flowchart.

where R_g, B_g, and C_g are DSO net profit, benefit, and cost, respectively, expressed as follows:

$$\begin{cases} B_g = \sum_{k=1}^{K} \alpha_k \left(c_k \Delta V_k + \rho_k \Delta Q_k \right) \\ \quad = \sum_{k=1}^{K} \alpha_k \left(c_k \left(\sum_{t=1}^{T} \sum_{i=1}^{I} \sum_{n=1}^{N_{i,t}} P_{n,i,t}^{disc} \right) + \rho_k d_k \left(\sum_{t=1}^{T} \sum_{i=1}^{I} \sum_{n=1}^{N_{i,t}} P_{n,i,t}^{disc} \Delta t \right) \right), \\ C_g = \sum_{k=1}^{K} \alpha_k \left(d_k \sum_{t=1}^{T} \sum_{i=1}^{I} \sum_{n=1}^{N_{i,t}} \left(v_{i,t}^{disc} P_{n,i,t}^{disc} \Delta t + C_{n,i,t}^{reserve} \right) \right) \end{cases} \tag{30}$$

where ΔV_k and ΔQ_k are the avoidable capacity and avoidable power; c_k is the unit average cost of DSO transformer, transmission line, and its supporting power equipment; ρ_k is the average feed-in tariff during peak discharge periods; d_k is the total number of EV discharging days per year, which is taken as 365 days; K is the economic benefits assessment period, which is taken as 20 years; and α_k is the present value coefficient in year k, that is, $1/(1+r)^k$, and r is the discount rate, which is taken as 8%.

2) EVA economic benefit analysis

EVA is the main implementation object of dispatching price. It should ensure that EVAs' average selling price after participating in EV regulation is not less than before, as follows:

$$\frac{\sum_{t=1}^{T_i^{ls}} v_{i,t}^{comp}}{T_i^{ls}} + \frac{\sum_{t=1}^{T} v_{i,t}^{serv}}{T} \geq \frac{\sum_{t=1}^{T_i^{ls}} v^{bcomp}}{T_i^{ls}} + \frac{\sum_{t=1}^{T} v^{bserv}}{T}, \tag{31}$$

where T_i^{ls} is the total time when DSO peak-shaving demand occurs in region i.

3) Economic benefit analysis for EV users

EV users are the main implementation objects of charging service fees, and its charging cost after participating in regulation shall not be greater than that before regulation, as follows:

$$f_3 / N \leq \sum\nolimits_n C_n^0 / N, \tag{32}$$

where N is the total number of EVs in the system; C_n^0 is the charging cost before the regulation of the nth EV, that is, the disorderly charging cost of a single EV.

4) CS benefit analysis

CS leads the formulation of regional flexible dispatching price to promote optimal allocation of system EV resources. Therefore, the objective function value of model comprehensive optimization is taken as the benefit, as shown in **Eq. 12**.

Strategy Formulation Workflow

The formulation workflow of the proposed strategy is shown in **Figure 4**.

As can be seen from **Figure 4**, the regulation strategy development workflow includes the following steps. First, the EV travel chain information is obtained based on the 2019 NTS data set and the MCMC method, which reflects the travel demand of users and is the basis of EV regulation. Second, the EV charging demand model is established based on EV travel information to guarantee users' electricity energy demand. Third, the regional flexible dispatching electricity price is dynamically updated considering the regional grid operation states and EV on-grid rate. Then the EV charging and discharging regulation model based on the dynamic regional dispatching electricity price is established to achieve a win-win situation for DSO, EVA, and EV users. Finally, the economic cost–benefit model is used to analyze the profitability of different stakeholders in the proposed scheme and determine whether the profitability of multiple parties is achieved.

CASE RESULTS AND DISCUSSION

Parameter Setting

In this study, we adopted the adapted IEEE-33 node system and divided it into four functional regions according to the difference

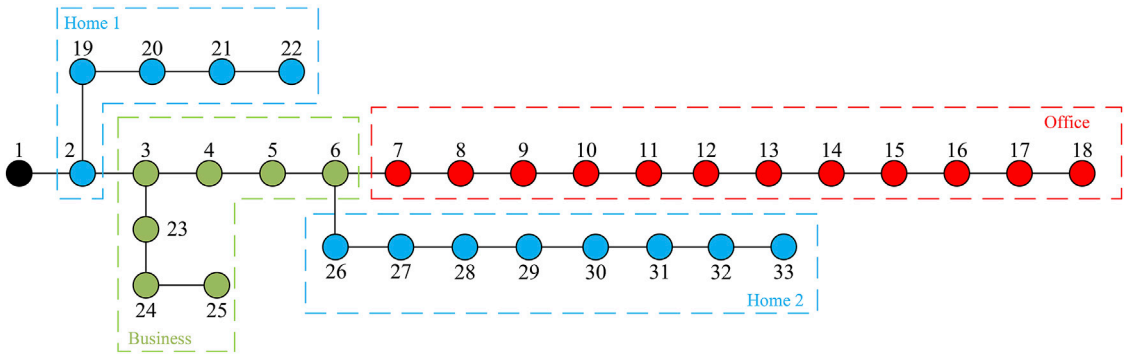

FIGURE 5 | Adapted IEEE-33 node system region division diagram.

of regional functional properties: office region, business region, home region 1, and home region 2, corresponding to four EVAs, as shown in **Figure 5**. The total basic active load of the system and the basic active load of each region are shown in **Supplementary Figure S1**. Considering that the EV charging infrastructure has been greatly developed and configured in the context of smart cities, it is assumed that each functional region has a sufficient number of charging piles, which have been properly planned and arranged. Based on the adapted IEEE-33 node system capacity size and EV penetration, it is assumed that there are 100 EVs in the system, and the parameters are shown in **Table 1**. To reflect a certain extent of uncertainty in users' charging demand, it is assumed that EV users have different expected electricity consumption in different functional regions, which follows a normal distribution of N (0.85, 0.02) in office and home regions and N (0.75, 0.02) in the business region. Based on the NTS database data and MCMC method, the number and proportion of different EV travel chains are shown in **Supplementary Table S1**, and the travel timing information of EV users is shown in **Supplementary Figure S2**. To fully utilize the EV regulation potential and users' charging demand, it is assumed that EVs are connected to the grid for regulating immediately after arriving at their destinations. EV provides reserve service at an electricity price of 0.022 Yuan/kWh (South China Energy Regulatory Administration, 2020); γ_i is taken as 0.2, the relevant price parameters are shown in **Table 2**, and the peak-to-valley TOU electricity price is shown in **Supplementary Table S2**.

The simulation period T is set from 5:00 of the previous day to 5:00 of the present day. In order to fully reflect the randomness of EV accessing and leaving the grid as well as the real-time optimal regulation effect, the simulation time interval is taken as Δt = 15 min, that is, the regulation period is 24 h, including 96 regulation periods.

The case study in this study is based on a computer with a CPU of Intel® Core™ i7-9700 @ 3.00 GHz and 16 GB of memory, modeled with MATLAB software and the YALMIP toolbox, and the CPLEX optimization solver is called to solve the optimization model. Meanwhile, the average computational cost of solving the optimization model is 8.5 min, and this computation time is considered to be very acceptable considering that the studied scenario is a 24-h (including 96 regulation periods) EV optimal regulation problem.

TABLE 1 | Simulation parameters of single EV.

Variable	Parameter value	Variable	Parameter value
E	50 kWh	$P_{n,i,t}^{ch,\max}$	7 kW/60kW
η_{ch}	0.9	$P_{n,i,t}^{disc,\max}$	7 kW/60kW
η_{disc}	0.9	C^{B}	30,000 Yuan
SOC_n^{down}	0.1	C^{F100}	3,500
$SOC_{n,i,t}^{\max}$	1.0	kp	1.0

TABLE 2 | Relevant electricity price simulation parameters.

Variable	Parameter value	Variable	Parameter value
$k_{i,t}^{ds1}$	1.00	$\alpha_{i,t}^{ds1}$	10%
$k_{i,t}^{ds2}$	1.05	$\alpha_{i,t}^{ds2}$	70%
$k_{i,t}^{ds3}$	1.10	$\alpha_{i,t}^{cs1}$	50%
$k_{i,t}^{cs1}$	1.00	$\alpha_{i,t}^{cs2}$	80%
$k_{i,t}^{cs2}$	0.98	r_i^d	1.0
$k_{i,t}^{cs3}$	0.95	r_i^c	1.0
c_k	300 Yuan/kW	ρ_k	4.23 Yuan/kWh

Electric Vehicle Real-Time Regulation Model Calculation Results

The proposed dynamic update strategy of regional dispatching price in this study is calculated and updated by CS based on the interaction information of DSO, EVA, and EV users, and the results are shown in **Figure 6**. Combined with **Figure 6** and the **Supplementary Figures S1 and S2**, it can be seen that due to the differences in the load characteristics of the regional power grids and EV travel characteristics, the EV discharge incentive dispatching prices (**Figure 6A**) and charging service fees (**Figure 6B**) in the regional grids are also quite different. The EV discharge incentive dispatching price increases with the rise of the regional grid's peak-shaving demand and EVA's charging pile utilization rate, and decreases vice versa. Also, it becomes zero

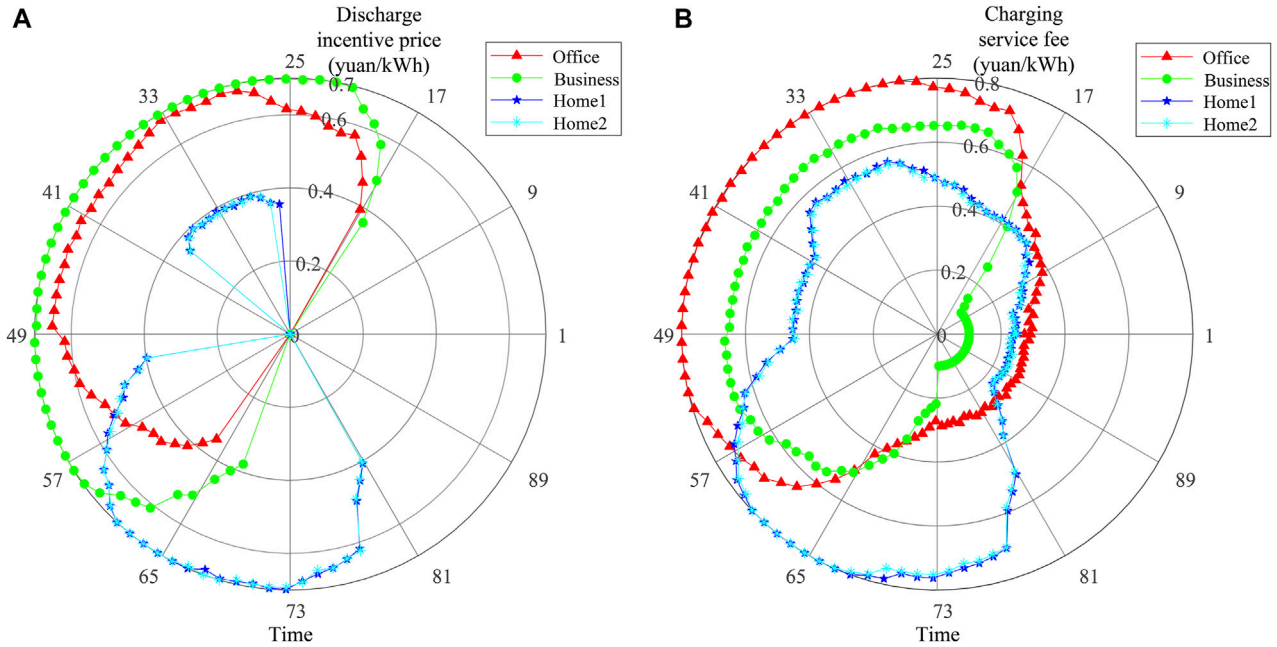

FIGURE 6 | (A) EV discharge incentive dispatching price. **(B)** EV charging service fee.

when the grid's active load is lower than the average load level, which fully reflects the active load characteristics of the regional grid and the travel characteristics of EVs. Similarly, the EV charging service fee increases with the increase of the regional grid's active load and the decrease of EVA's charging pile utilization rate. When the regional power grid's active load is at its peak, the regional charging service fee increases significantly, and decreases significantly vice versa.

The results of the EV V2G optimal regulation model are shown in **Figure 7**, which shows the base active load of each regional grid (i.e., PB, blue area in **Figure 7**), the equivalent active load variation curve of the regional grid (i.e., PEL, orange area in **Figure 7**), and the real-time regulation results of the regional EV V2G for 96 day (i.e., PEVA, green area in **Figure 7**).

As can be seen from **Figure 7**, the regional EVA guides regional on-grid EVs to reduce charging power or increase discharging power when the regional grid load peak-shaving demand is high, and when the regional grid valley-filling demand is high, regional on-grid EVs are guided to increase charging power or reduce discharging power. The effect of peak-shaving, valley-filling, and smooth load fluctuation of the power grid is significant in which the load rates of the office region, business region, home region 1, and home region 2 are increased from 63.48, 57.52, 59.56, and 59.27% of the base active load to 65.55, 58.56, 75.27, and 74.94% respectively, which is an increase of 2.07, 1.04, 15.71, and 15.67%, respectively. Due to the base active load in office and business regions being relatively stable, the effect of regional load rate improvement is limited (shown in **Figures 7A,B**). On the contrary, the base active load in home region 1 and home region 2 changes more obviously and the effect of regional load rate improvement is significant (shown in **Figures 7C,D**).

The economic benefits for DSO, EVA, and EV users are evaluated and analyzed according to **Eqs. 29–32**. From the calculation results, it can be seen that DSO regulation benefit $B_g = 4.7978\times10^7$ Yuan, regulation cost $C_g = 1.2336\times10^7$ Yuan, and net profit $R_g = 3.5642\times10^7$ Yuan when the assessment period is 20 years. So, the benefit of DSO participation in EV charging and discharging regulation is far greater than the cost, that is, DSO achieves profit. In addition, EVAs' selling price (in Yuan/kWh) for office, business, home 1, and home 2 after the regulation are 1.1240, 1.0472, 1.0361, and 1.0355, respectively, compared to 0.95 before the regulation, which increased by 18.32, 10.23, 9.06, and 9.00%, respectively, that is, the average profit on regional EVA has been improved. Furthermore, combined with **Table 4**, it can be seen that the average charging cost for EV users has been reduced from 37.2429 Yuan before regulation to 18.4832 Yuan, with a decrease of up to 50.37%. Therefore, the proposed strategy promotes the profitability of DSO, EVA, and EV users, achieving a win-win situation for all three stakeholders.

Electric Vehicle Regulation Results under Different Electricity Price Signals

The electricity price level will significantly affect the decision-making behavior of DSO, EVA, and EV users, and the guidance effect of different electricity price signals has some differences. To demonstrate the effectiveness and superiority of the regional dispatching price signals proposed in this study, the calculated results of the proposed dispatching price strategy are compared

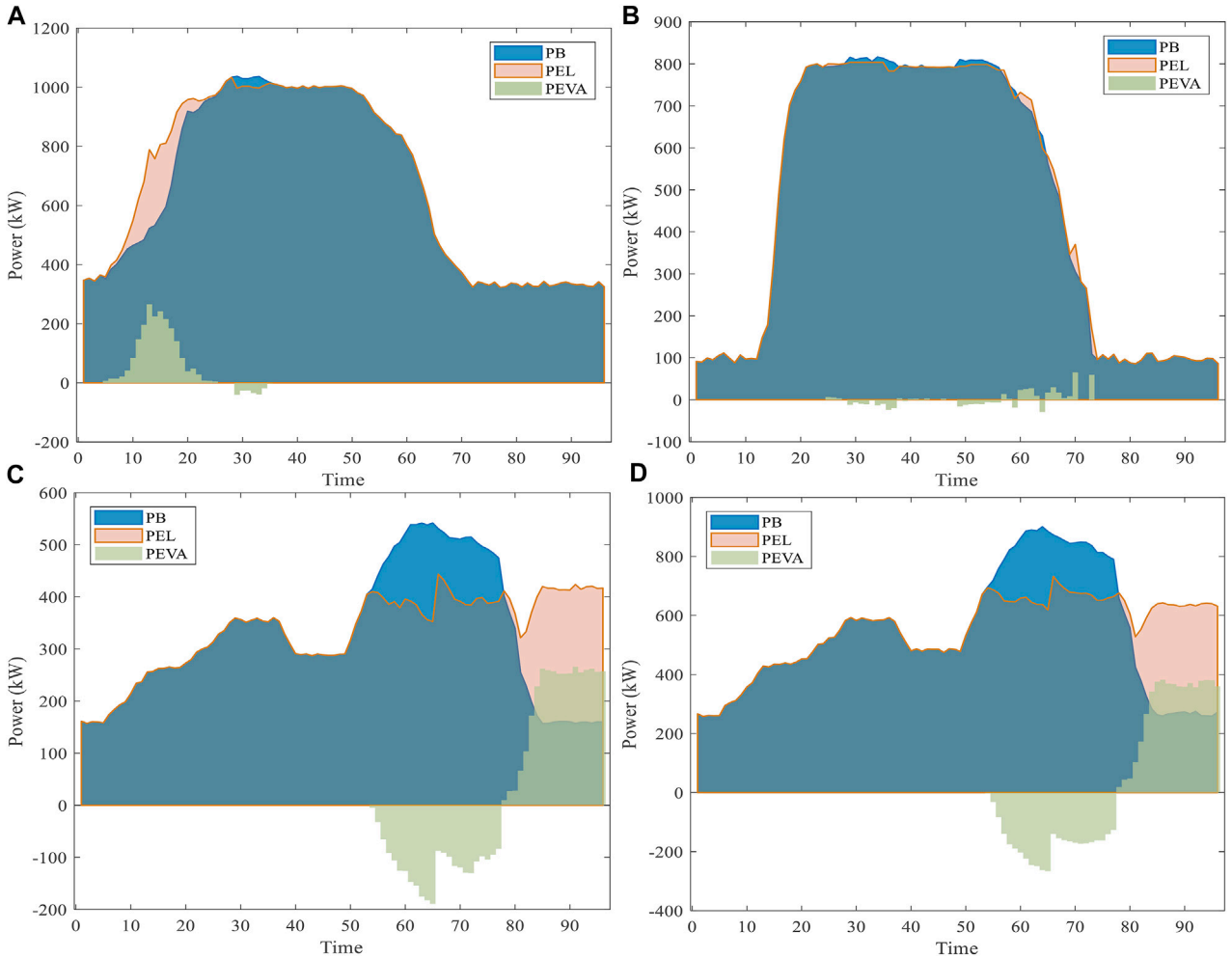

FIGURE 7 | (A) Office region calculation results. **(B)** Business region calculation results. **(C)** Home region 1 calculation results. **(D)** Home region 2 calculation results.

with three other classical electricity price scenarios in recent research.

Comparison scheme 1 (CS1): Dynamic regional dispatching price signal in this study.

Comparison scheme 2 (CS2): Disorderly charging signal, as the benchmark.

Comparison scheme 3 (CS3): Peak-to-valley TOU signal (Li et al., 2021).

Comparison scheme 4 (CS4): System dynamic electricity price signal (Zhou et al., 2020).

Combined with the EV charging and discharging regulation model established in this study, four comparison schemes of electricity price signal are used to guide the regional EV charging and discharging behavior, respectively, and the results are shown in **Figure 8** and **Table 3**.

As can be seen from **Figure 8**, under the CS2 strategy, EVs carry out disorderly charging behavior without incentive guidance. When it is given access of the power grid, it immediately charges at the maximum power, enlarging peaks or forming new load peaks on the basis of grid's base active load in each region, which further expands the load peak-valley difference. Among them, the most serious impact was on the business region grid; the load peak-valley difference increased from the original 730.44–1,099.32 kW, the growth rate was as high as 50.50%, and the active load curve of the business region grid showed obvious fluctuations, which seriously aggravated the regional grid peak regulation pressure.

Under the strategies of CS3 and CS4, EV reduces the charging power when the charging price is high and increases the charging power when the charging price is low based on meeting the charging demand. A similar analysis was carried out for discharging power. The electricity price signal plays a guiding role in EV charging and discharging behavior. Among them, under the CS3 strategy, the load rates of office region, business region, home region 1, and home region 2 increased by 9.32, 16.20, 7.63, and 5.67% compared with CS2, respectively. The EV charging and discharging regulation strategies based on the peak-valley TOU price and system dynamic price signal improved the operational security of the regional power grid to an extent. However, due to the unified electricity price signal used in the

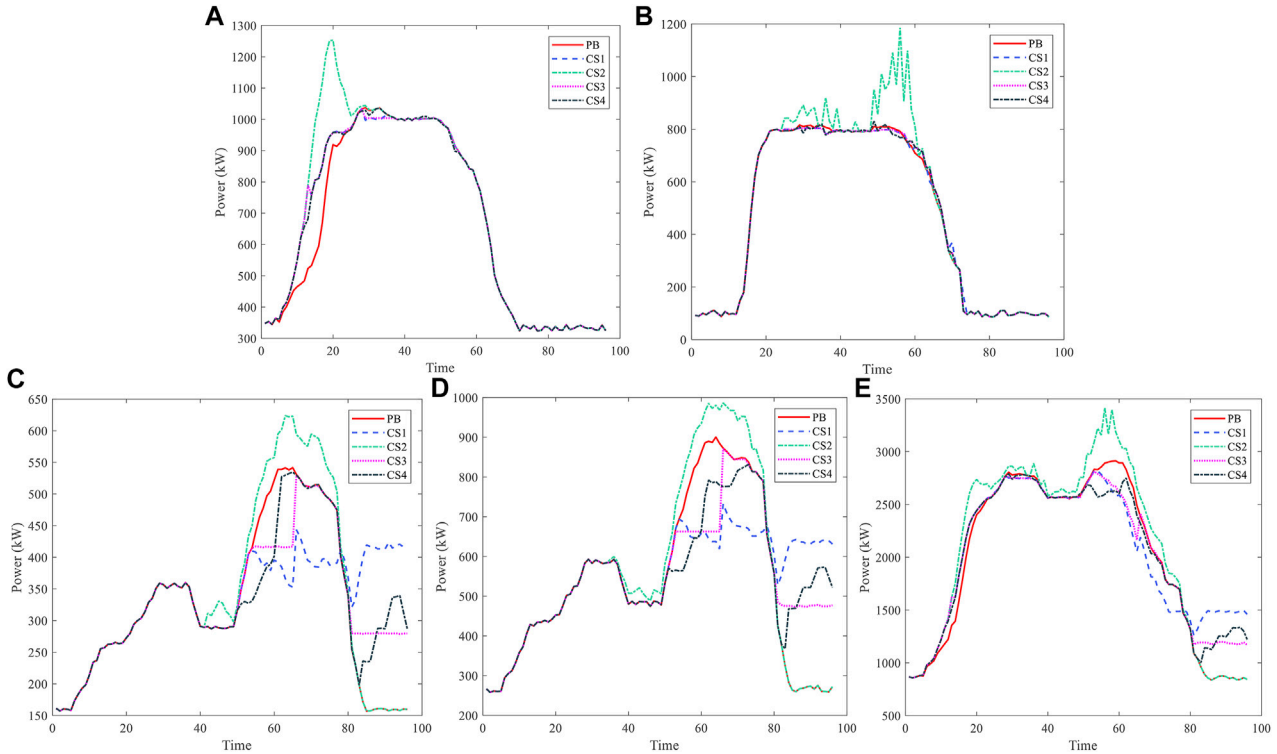

FIGURE 8 | (A) Office region calculation results. **(B)** Business region calculation results. **(C)** Home region 1 calculation results. **(D)** Home region 2 calculation results. **(E)** System load calculation results.

TABLE 3 | Results of different electricity price signals.

Electricity price signal	Load deviation (kW^2)	System total cost (Yuan)	Comprehensive objective value
CS1	1.989×10^7	−303.61	1.3483
CS2	2.969×10^7	6,472.51	5.1769
CS3	2.104×10^7	692.21	1.8634
CS4	2.119×10^7	366.48	1.6985

whole region of the system, the effect of EV charging and discharging regulation is limited, and the guiding role of the electricity price signal is not fully played, especially in home regions 1 and 2. The active load of home regions 1 and 2 is still at a high level, at times 66–77 of CS3 and 61–77 of CS4 (shown in **Figures 8C,D**).

Compared with the above schemes, the proposed flexible dispatching price strategy (CS1) considers the operational states of different regional grids, and the regional grid load rate increases significantly. Among them, the load rates of office region, business region, home region 1, and home region 2 increased by 9.32, 16.22, 20.66, and 18.13% compared with CS2, respectively, and compared with peak-to-valley TOU price and system dynamic price, it can further guide and regulate the orderly charge and discharge behavior of EVs and achieve more significant results in improving the load characteristics of the regional grid. In addition, as can be seen in **Table 3**, concerning the economics of the regulation strategy, system's total cost (the sum of EVA operating cost and users charging cost, that is, f_2+f_3) of CS2, CS3, and CS4 is 2,231.82, 327.99, and 220.71% higher than that of CS1, respectively. Thus, the proposed strategy greatly reduces the operating cost and significantly improves the operation economy of the system.

Electric Vehicle Regulation Results Under Different Optimization Objectives

EV charging and discharging regulation are jointly participated by multiple stakeholders, and the interest demands of different stakeholders will affect the formulation of optimization decision-making scheme. In order to reflect the necessity of considering the interests of multiple stakeholders, the model proposed in this

TABLE 4 | Results of different optimization objectives.

Objective	Load deviation (kW^2)	EVA operation cost (Yuan)	Users charging cost (Yuan)	Comprehensive objective value
Objective 1	1.989×10^7	−2,151.93	1848.32	1.3483
Objective 2	2.969×10^7	2,748.22	3,724.29	5.1769
Objective 3	1.938×10^7	−2,140.20	2,566.57	1.6753
Objective 4	3.243×10^7	−3,826.90	8,757.54	4.9267
Objective 5	2.353×10^7	−44.03	644.47	1.9491

study is compared with the results of the other four typical optimization objectives in the current research.

Optimization objective 1: Model of this study.

Optimization objective 2: Disorderly charging, as the benchmark.

Optimization objective 3: DSO load deviation.

Optimization objective 4: EVA operation cost.

Optimization objective 5: EV users charging cost.

The results of the models based on the above optimization objectives were calculated separately and are shown in **Table 4**. Among them, the negative value of EVA operating cost means a positive benefit.

As can be seen from **Table 4**, objective 2 performs poorly in terms of load deviation, EVA operation cost, and user charging cost. It means that it takes other interests as the cost and reduces the enthusiasm of other stakeholders to meet users' rapid charging demand, which is not conducive to the long-term operation of the whole system. Objectives 3, 4, and 5 only consider the interests of individual stakeholders of DSO, EVA, and EV users, respectively, and maximize the interests of their respective subjects. Among them, although objective 3 achieves the minimum load deviation of the DSO power grid and achieves significant peak-shaving and valley-filling effect, it comes by increasing EV users charging cost, which damages the interests of EVA and users. Objective 4 greatly reduces EVA operating cost and improves EVA revenue, but it is accompanied by a larger grid load deviation and higher charging costs of users, without considering the needs of DSO and users. Similarly, objective 5 only considers the demand of users and ignores the benefits of DSO and EVA. Although the demand of users is greatly met, the peak-shaving and valley-filling effect of the grid in general and the revenue of EVA is significantly reduced. It can be seen that the above objectives cannot promote multi-stakeholder profits and win-win results and fail to take into account the overall interests. Thus, it is difficult for the system to achieve sustainable, long-term, and mutually beneficial safe economic operation.

Compared with the aforementioned optimization objectives, the proposed model fully considers the interests of multiple stakeholders and realizes the reduction of DSO load deviation and EVA operation cost on the basis of meeting the demand of EV users. Among them, the load deviation is only 2.63% more for objective 3, but the total cost of the system is reduced by 171.21%. EVA's operating cost is 43.78% more for objective 4, but DSO load deviation and user charging cost are reduced by 38.67 and 78.89%, respectively. EV users' charging cost is 186.80% more for objective 5, but the operating cost of EVA is reduced by 4,787.42%. It can be seen that the proposed strategy maintains the global benefit of the system at a high level, which is conducive to the mutual benefit and long-term operation of all parties in the system.

Regulation Results Under Different Guaranteed Electricity Energy

EV users set different guaranteed electricity energy demands in the regulation process, which will affect the flexibility of EV regulation. Therefore, in order to consider the impact of different guaranteed electricity energy on EV regulation effects, this study sets up five comparison schemes under different EV-guaranteed electricity energy requirements.

The calculation results under different guaranteed electricity energy demands are shown in **Table 5** and **Figure 9**. As can be seen from **Table 5** and **Figure 9**, when λ_n is relatively small, the load deviation and EVA operating costs achieve good results, but the users charging cost increases, and when λ_n is large, the load deviation and EVA operating costs increase accordingly and the users charging cost decreases. In addition, with the increase of λ_n, the adjustable range of single EV battery SOC gradually

TABLE 5 | Results under different guaranteed electricity energy.

Guaranteed electricity energy	Load deviation (kW^2)	EVA operation cost (Yuan)	Users charging cost (Yuan)	Comprehensive objective value
λ_n = 2.00	2.130×10^7	−786.14	1,579.73	1.9272
λ_n = 1.75	2.011×10^7	−1731.94	1,598.27	1.4271
λ_n = 1.50	1.989×10^7	−2,151.93	1848.32	1.3483
λ_n = 1.25	1.991×10^7	−2,368.68	1977.44	1.3163
λ_n = 1.00	1.992×10^7	−2,400.80	1997.56	1.3129

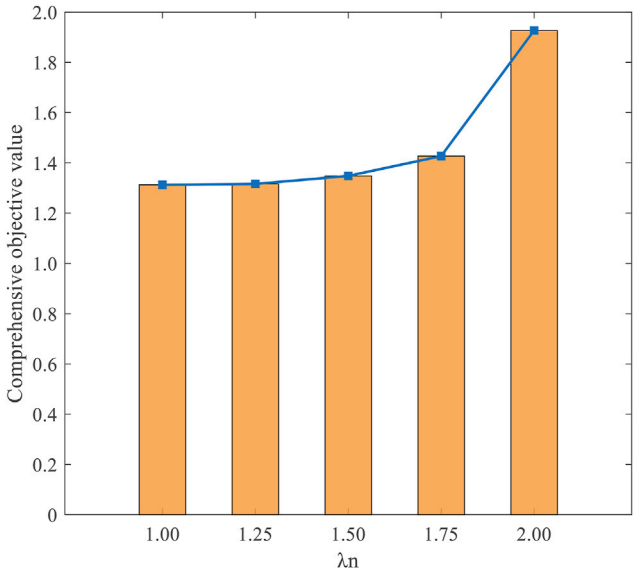

FIGURE 9 | Comprehensive objective value under different EV-guaranteed electricity energy.

decreases and the EV adjustable flexibility decreases. It makes the model comprehensive objective value to increase, but the users' battery energy demand is guaranteed when leaving early. Thus, it can be seen that different guaranteed electricity energy requirements have an impact on EV charging and discharging strategies, and it is necessary to consider them in detail in the EV charging and discharging regulation process.

CONCLUSION

In this study, an optimal regulation strategy of EV V2G based on a dynamic regional dispatching price signal is proposed, taking into account the interests of DSO, EVA, and EV users. The simulation example of a regional distribution network is analyzed, and the results show the following:

The EV orderly charging and discharging regulation strategy proposed in this study fully considers the travel demand and charging demand of EV users and effectively guide the EV charging and discharging behavior in the region. It realizes the reduction of the regional grid load deviation, EVA operation cost, and EV users' charging cost.

Under the guidance of different electricity price signals, the proposed dynamic regional dispatching price can further play the guiding role of electricity price signals by combining the regional grid operation states and EV on-grid rate, in order to increase the regional grid load rate and significantly improve the operation economy of the system.

Under solo optimization objective, it is difficult to achieve a win–win situation for multiple stakeholders by considering only DSO load deviation, EVA operation cost, or EV users' charging cost, which is not conducive to motivate DSO, EVA, and EV users to participate in the regulation process. The model proposed in this study achieves a win–win situation for all three stakeholders, which is conducive to maximize the safety and economic benefits of the system and promote the mutually beneficial and long-term operation of the system.

Under different guaranteed electricity energy, the adjustable flexibility of single EV battery SOC decreases as λ_n increases, and the model comprehensive objective value increases and overall system benefits decrease, but the users' battery energy demand is guaranteed when leaving early.

This study only regulates the V2G behavior of EVs from the perspective of the grid. In fact, EVs play an important role in coupling of the road network and power grid. The interaction between road network information and power grid information will further affect the EV charging and discharging regulation strategy. Therefore, the optimal regulation of electric vehicle V2G integrating road network information will be the next research focus.

DATA AVAILABILITY STATEMENT

The original contributions presented in the study are included in the article/**Supplementary Material**, further inquiries can be directed to the corresponding author.

AUTHOR CONTRIBUTIONS

All authors listed have made a substantial, direct, and intellectual contribution to the work and approved it for publication.

FUNDING

The research work was supported by the National Natural Science Foundation of China (Grant No. 51761145106).

SUPPLEMENTARY MATERIAL

The Supplementary Material for this article can be found online at: https://www.frontiersin.org/articles/10.3389/fenrg.2022.873262/full#supplementary-material

REFERENCES

Chandra Mouli, G. R., Kefayati, M., Baldick, R., and Bauer, P. (2019). Integrated PV Charging of EV Fleet Based on Energy Prices, V2G, and Offer of Reserves. *IEEE Trans. Smart Grid* 10, 1313–1325. doi:10.1109/TSG.2017.2763683

Chen, L., Nie, Y., and Zhong, Q. (2015). A Model for Electric Vehicle Charging Load Forecasting Based on Trip Chains. *Trans. China Electrotechnical Soc.* 30, 216–225. doi:10.19595/j.cnki.1000-6753.tces.2015.04.027

Chen, L., Zhang, Y., and Figueiredo, A. (2019). Overview of Charging and Discharging Load Forcasting for Electric Vehicles. *Automation Electric Power Syst.* 43, 177–191. doi:10.7500/AEPS20180814001

Chen, T., Zhang, B., Pourbabak, H., Kavousi-Fard, A., and Su, W. (2018). Optimal Routing and Charging of an Electric Vehicle Fleet for High-Efficiency Dynamic Transit Systems. *IEEE Trans. Smart Grid* 9, 3563–3572. doi:10.1109/TSG.2016.2635025

Chen, Z., Liu, Y., Chen, X., Zhou, T., and Xing, Q. (2020). Charging and Discharging Dispatching Strategy for Electric Vehicles Considering Characteristics of Mobile Energy Storage. *Automation Electric Power Syst.* 44, 77–85. doi:10.7500/AEPS20190114010

Cheng, S., Wang, X., and Feng, Y. (2018). Decentralized Optimization of Ordered Charging Scheduling in Electric Vehicle Charging Station. *Automation Electric Power Syst.* 42, 39–46. doi:10.7500/AEPS20170630001

Cui, Y., Hu, Z., and Duan, X. (2021). Review on the Electric Vehicles Operation Optimization Considering the Spatial Flexibility of Electric Vehicles Charging Demands. *Power Syst. Technology* 46, 1–16. doi:10.13335/j.1000-3673.pst.2021.0514

Duan, B., Xin, K., and Zhong, Y. (2020). Optimal Dispatching of Electric Vehicles Based on Smart Contract and Internet of Things. *IEEE ACCESS* 8, 9630–9639. doi:10.1109/ACCESS.2019.2961394

Fang, X., He, C., and Zhang, B. (2019). Energy Evolutional Path of the World and the Energy Structure Transformation of China. *China Rev. Polit. Economy* 10, 178–201.

Gan, L., Chen, X., Yu, K., Zheng, J., and Du, W. (2020). A Probabilistic Evaluation Method of Household EVs Dispatching Potential Considering Users' Multiple Travel Needs. *IEEE Trans. Ind. Applicat.* 56, 5858–5867. doi:10.1109/TIA.2020.2989690

Hu, J., Li, Y., Wu, J., and Ai, X. (2019). A Day-Ahead Optimization Scheduling Method for Prosumer Based on Iterative Distribution Locational Marginal Price. *Power Syst. Technology* 43, 2770–2780. doi:10.13335/j.1000-3673.pst.2019.0619

Kazemi, M., and Zareipour, H. (2018). Long-Term Scheduling of Battery Storage Systems in Energy and Regulation Markets Considering Battery's Lifespan. *IEEE Trans. Smart Grid* 9, 6840–6849. doi:10.1109/TSG.2017.2724919

Li, R., Wu, Q., and Oren, S. S. (2014). Distribution Locational Marginal Pricing for Optimal Electric Vehicle Charging Management. *IEEE Trans. Power Syst.* 29, 203–211. doi:10.1109/TPWRS.2013.2278952

Li, T., Tao, S., He, K., Lu, M., Xie, B., Yang, B., et al. (2021). V2G Multi-Objective Dispatching Optimization Strategy Based on User Behavior Model. *Front. Energ. Res.* 9. doi:10.3389/fenrg.2021.739527

Liu, Z., Wu, Q., Oren, S. S., Huang, S., Li, R., and Cheng, L. (2018). Distribution Locational Marginal Pricing for Optimal Electric Vehicle Charging through Chance Constrained Mixed-Integer Programming. *IEEE Trans. Smart Grid* 9, 644–654. doi:10.1109/TSG.2016.2559579

Lo, F., Mandrioli, R., Ricco, M., Monteiro, V., Monteiro, L. F. C., Afonso, J. L., et al. (2021). Electric Vehicles Charging Management System for Optimal Exploitation of Photovoltaic Energy Sources Considering Vehicle-To-Vehicle Mode. *Front. Energ. Res.* 9. doi:10.3389/fenrg.2021.716389

Ma, X., Wang, C., Hong, X., Li, Y., and Wang, H. (2016). A Two Layer Model for Electric Vehicle Charging Optimization Based on Location Marginal Congestion price. *Power Syst. Technology* 40, 3706–3714. doi:10.13335/j.1000-3673.pst.2016.12.011

Neubauer, J., and Wood, E. (2014). The Impact of Range Anxiety and home, Workplace, and Public Charging Infrastructure on Simulated Battery Electric Vehicle Lifetime Utility. *J. Power Sourc.* 257, 12–20. doi:10.1016/j.jpowsour.2014.01.075

Pan, Z., Yu, T., and Wang, K. (2019). Decentralized Coordinated Dispatch for Real-Time Optimization of Massive Electric Vehicles Considering Various Interests. *Proc. Chin. Soc. Electr. Eng.* 39, 3528–3540. doi:10.13334/j.0258-8013.pcsee.172688

Schirone, L., and Pellitteri, F. (2017). Energy Policies and Sustainable Management of Energy Sources. *Sustainability* 9, 2321. doi:10.3390/su9122321

Schweppe, F. C., Caramanis, M. C., Tabors, R. D., and Bohn, R. E. (1988). *Spot Pricing of Electricity*. Boston: Springer.

Shao, Y., Mu, Y., Yu, X., Dong, X., Jia, H., Wu, J., et al. (2017). A Spatial-Temporal Charging Load Forecast and Impact Analysis Method for Distribution Network Using EVs-Traffic-Distribution Model. *Proc. Chin. Soc. Electr. Eng.* 37, 5207–5219. doi:10.13334/j.0258-8013.pcsee.161470

Singh, H. K., and Srivastava, S. C. (2005). "A Reduced Network Representation Suitable for Fast Nodal price Calculations in Electricity Markets," in 2005 IEEE Power Engineering Society General Meeting.

South China Energy Regulatory Administration (2020). Implementation Rules for Auxiliary Service Management of Grid-Connected Power Plants in Southern China. Available at: http://nfj.nea.gov.cn/frontIndex/index.do (Accessed January 8, 2022).

Tabatabaee, S., Mortazavi, S. S., and Niknam, T. (2017). Stochastic Scheduling of Local Distribution Systems Considering High Penetration of Plug-In Electric Vehicles and Renewable Energy Sources. *Energy* 121, 480–490. doi:10.1016/j.energy.2016.12.115

UK Department for Transport (2019). National Travel Survey: 2019. Available at: https://www.gov.uk/government/statistics/national-travel-survey-2019 (Accessed January 7, 2022).

Wang, Z., Gao, J., Zhao, R., Wang, J., and Li, G. (2020). Optimal Bidding Strategy for Virtual Power Plants Considering the Feasible Region of Vehicle-To-Grid. *Energ. Convers. Econ.* 1, 238–250. doi:10.1049/enc2.12018

Wu, J., Xue, Y., and Xie, D. (2019). Optimization of Reserve Service Capability Made by Electric Vehicle Aggregator. *Automation Electric Power Syst.* 43, 75–81. doi:10.7500/AEPS20181204003

Zhang, H., Hu, Z., Xu, Z., and Song, Y. (2017). Evaluation of Achievable Vehicle-To-Grid Capacity Using Aggregate PEV Model. *IEEE Trans. Power Syst.* 32, 784–794. doi:10.1109/TPWRS.2016.2561296

Zhou, K., Cheng, L., Lu, X., and Wen, L. (2020). Scheduling Model of Electric Vehicles Charging Considering Inconvenience and Dynamic Electricity Prices. *Appl. Energ.* 276, 115455. doi:10.1016/j.apenergy.2020.115455

Zhou, Z., Sun, C., Shi, R., Chang, Z., Zhou, S., and Li, Y. (2017). Robust Energy Scheduling in Vehicle-To-Grid Networks. *IEEE Netw.* 31, 30–37. doi:10.1109/MNET.2017.1600220NM

Conflict of Interest: The authors declare that the research was conducted in the absence of any commercial or financial relationships that could be construed as a potential conflict of interest.

frontiers | Frontiers in Energy Research

ORIGINAL RESEARCH
published: 25 April 2022
doi: 10.3389/fenrg.2022.860461

Condition Assessment of the Cable Trench Based on an Intelligent Inspection Robot

Zhiwei Jia, Yihong Tian, Zheng Liu and Shaosheng Fan*

Hunan Province Key Laboratory of Electric Power Robot, School of Electrical and Information Engineering, Changsha University of Science and Technology, Changsha, China

Accurate evaluation of the cable trench condition is the key to realizing its intelligent operation and maintenance, and the intelligent cable trench inspection robot is a reliable information acquisition method for the condition assessment of cable trench. According to task requirements and site's environment, an intelligent inspection robot is designed. The crawler-type motion mechanism is determined based on the demand for sizes and obstacle-surmounting. Cartographer SLAM technology is used to map the underground cable trench environment, and a path planning method combined with the improved A* algorithm and dynamic window method (DWA) is presented. Multiple sensors are equipped on this robot, and various kinds of information are obtained. Based on the information obtained, a condition assessment method of an underground cable trench is proposed. An extension neural network model is constructed to assess air quality. Channel capacity and ground flatness are calculated to evaluate the internal structure of the cable trench. The water depth and water surface area are comprehensively used to evaluate the hazard of water accumulation. The evaluation results are used to realize the linkage control of the cable trench's operation and maintenance. A field test shows that the intelligent inspection robot can reliably obtain seven kinds of information from the underground cable trench, and the proposed condition evaluation method can assess the condition of the cable trench and provide four kinds of suggestions for potential hazards.

Keywords: underground cable trench, robot system, multi-sensor data fusion, condition monitoring, condition assessment

OPEN ACCESS

Edited by:
Yan Xu,
Nanyang Technological University, Singapore

Reviewed by:
Elmer Magsino,
De La Salle University, Philippines
Kai Zhao,
Shanghai Jiao Tong University, China

****Correspondence:***
Zhiwei Jia
jiayege@csust.edu.cn

Specialty section:
This article was submitted to Smart Grids, a section of the journal Frontiers in Energy Research

Received: *23 January 2022*
Accepted: *22 March 2022*
Published: *25 April 2022*

Citation:
Jia Z, Tian Y, Liu Z and Fan S (2022) Condition Assessment of the Cable Trench Based on an Intelligent Inspection Robot. Front. Energy Res. 10:860461. doi: 10.3389/fenrg.2022.860461

INTRODUCTION

The underground cable trench is a facility to accommodate multi-circuit power cables and accessories. It has the function of a power cable joint space and can provide a large amount of power to major industrial complexes and high-load urban areas. Tunnel pipelines, public pipelines, and open cable pipelines are being built (Kang et al., 2018). However, harmful gases which are easy to accumulate in the cable trench, coupled with the discharge caused by cable insulation aging, could lead to explosion and fire (Liu and Yin, 2007). Furthermore, the probability of this danger gradually increases over time. So it is very important to find and eliminate these hidden dangers as soon as possible for the safe operation of the power system (Commission of the European Communities, 2003). However, the internal environment of the underground cable trench is complex, the space is narrow, high-voltage lines on both sides are densely distributed, and the ground is usually not

hardened, which makes manual inspection extremely dangerous and difficult. Therefore, online detection of cable trench's working state plays a vital role in improving the stability and reliability of power system operation (Jongen et al., 2012; Hepburn et al., 2016).

In the early environmental safety monitoring for the underground cable trench, fixed monitoring equipment was used to measure some parameters in the trench (Siddiqui et al., 2017). Due to the large length and span of the cable trench, monitoring blind areas always existed in these situations, which could not effectively reflect the operation state of the overall cable environment. Some research works have been conducted on inspection robots for cable trenches. A remote-controlled cable trench tunnel monitoring robot designed by Sun et al. (2021) is inconvenient to operate in a narrow cable trench environment. Yijiahe Technology Co., Ltd. has developed an inspection robot for substations (Xing et al., 2018), but the volume is very large for the narrow space of the underground cable trench and is only suitable for use in a more open space. The underground cable trench robot designed by the Changsha University of Technology can realize the inspection function (Ling et al., 2020), but the designed mapping method has a poor effect in the cable trench environment, which affects the subsequent navigation work.

The diagnosis of the state of the cable trench internal environment is the ultimate requirement of an inspection robot. Wu and Zhang, (2014) used the corresponding sensors integrated into the monitoring device of low-voltage distribution equipment to measure the surface temperature of the incoming and outgoing lines of the distribution box and the water level of the cable trench and to analyze the cable trench environment and obtain the fault assessment. Acquiring and analyzing the actual values of thermal resistance and diffusion coefficient of soil around the power cable, Lyall et al. (2000) evaluated temperature distribution inside the cable trench in real time. The "hot spots" inside the cable trench are predicted and timely prevented in this manner. The BP neural network was applied to monitor the temperature and humidity of the internal environment of the underground cable trench in real time, and the internal environment assessment of the underground cable trench was realized (Song, 2015). Infrared thermal imaging data were gathered and transmitted to the adaptive neuro-fuzzy inference system (ANFIS) of the remote terminal unit, and a support vector machine (SVM) classifier was used to evaluate internal fault information of the cable trench (Pal et al., 2017). These aforementioned research studies assess the state of the underground cable trench and similar scenes in one or more aspects, and they mainly collect data through fixed monitoring equipment, as well as few sensors, which leads to incomplete signals and half results.

A substation inspection robot (Lu et al., 2017) integrates multiple sensors to perform fault monitoring, including the appearance image of cable equipment, sound of running equipment, and temperature of equipment joints, but no assessment method is mentioned. There is little research on the internal environment assessment method of the underground cable trench based on inspection robots at home and abroad. Since the robot carries multiple sensors to monitor complex environmental information inside the cable trench in the inspection process, if only relying on manual subjective evaluation of a certain amount of monitoring, this inspection is slow, has low credibility, and even ignores larger faults. Therefore, the consideration of engineering safety is far from enough (Wang et al., 2012).

During the task of automatic inspection, the inspection robot consumes a lot of memory in the fuselage computer. At the same time, in the process of moving, it will continuously collect the data from infrared cameras, high-definition cameras, and gas sensors around the cable trench and transmit the data to the remote cloud platform for data processing to obtain the evaluation results of the cable trench. However, remote sending and receiving of a large amount of data require sufficient connectivity, which is not always true in reality, and the delay and reliability of service processing are difficult to guarantee (Patel et al., 2017). Edge computing aims to provide elastic services with low latency and high bandwidth efficiency (Premsankar et al., 2018). To solve the problem of limited edge resources, models are deployed on the edge and cloud, respectively, through model segmentation technology for collaborative reasoning (Li et al., 2018). Taking the SLAM algorithm of a mobile robot as an example, the need to use edge nodes for computing offload on a remote cloud or a local robot was discussed in Dey and Mukherjee (2016). In this study, the edge server was placed at each node of the cable trench to form a distributed management system of the whole cable trench edge.

The on-site experiments performed on the edge intelligent evaluation system based on the underground cable trench inspection robot show that an inspection robot which can adapt to the environment is designed in this study. According to the characteristics of the underground cable trench environment, the condition assessment of the cable trench is performed by multi-sensor information fusion. Our contributions are as follows:

(1) An automatic navigation system was designed according to the constraints of the inspection robot in the underground cable trench environment, and the improved global path A* algorithm and the local path DWA algorithm were fused by an improved fusion scheme. Compared with the traditional fusion path algorithm, the detection speed of the improved fusion algorithm proposed in this study increased by 21%, and the total path became shorter. On-site experiments verified the superiority of the path planning method.
(2) In the process of robot inspection, we evaluated the underground cable trench using the multi-sensor fusion method comprehensively. The indexes of air quality, internal structure, and ponding hazards of the underground cable trench were calculated respectively, and the underground cable trench from these three dimensions was assessed. Furthermore, the linkage control strategy was designed according to the assessment results.

The remainder of this article is organized as follows. The structure of our robot structure is shown in *Inspection Robot*

Systems. The autonomous navigation system in the underground cable trench is described in *The Overall Scheme of the Autonomous Navigation Obstacle Avoidance System*. The condition assessment method is proposed in *Condition Assessment of the Underground Cable Trench Based on Edge Intelligence*. The experimental results and conclusion are presented in *Analysis of Actual Site Results* and *Conclusion*, respectively.

INSPECTION ROBOT SYSTEMS

To meet the strict requirements of the small and complex internal environment of the underground cable trench, such as the volume and climbing ability of the robot, the external walking mode of the cable trench inspection robot is designed as a crawler-type double drive. The crawler-type double drive has a good grasping ability and can climb the slope. The double drive mode connects the front and rear wheels for driving, which has advantages such as low power consumption, small volume, ease to control, and many more. The actual measured values of vehicle body parameters are as follows: length, width, and height: 500 × 300 × 120 mm; chassis dead weight: 8.45 kg; maximum load: 30 kg; maximum climbing angle: 35°; maximum obstacle crossing: 90 mm; and maximum span: 250 mm. The actual experiment shows that the internal environment of the underground cable trench is good.

The inspection robot needs to perform multiple tasks and assess the overall internal environment of the underground cable trench. According to the inspection task and environmental constraints, the cable trench intelligent inspection robot needs to have the following four modules:

(1) Visual module. Infrared thermal imaging and a high-definition camera are used to judge any visual anomaly inside the cable trench.
(2) Multi-sensor gas detection module. This could accurately reflect the concentration of harmful gases and combustible gases in the air of the underground cable trench.
(3) Automatic navigation module. Based on the robot operating system (ROS), the data environment of the laser radar and gyroscope is used to map and locate, and the path planning is designed to realize automatic navigation.
(4) Evaluation module. The underground cable trench diagnosis system based on edge intelligence proposed in this study is used to evaluate the internal environment of the cable trench.

Aiming at the requirements of multi-sensor information acquisition and a multitask cooperative work of the inspection robot, the system structure of the intelligent inspection robot for the underground cable trench is designed (as shown in **Figure 1**). The system uses multi-CPU collaborative work architecture to improve its data processing capability. The laser radar is chosen to provide positioning and mapping information. The core information calculation module adopts the core main control board of NVIDIA, equipped with an ROS operating system to provide the system platform to realize the autonomous navigation algorithm. The infrared imager, high-definition camera, and other visual sensors are also connected to the main control board of NVIDIA for processing to realize the information reading of infrared thermal imaging and high-definition images. The video data stream is uploaded to the operating terminal through WLAN.

In addition, two embedded sub-processor modules are designed. One embedded sub-processor realizes the motion attitude control of the robot and the platform control so that the robot can complete the multidirectional and three-dimensional visual observation of the cable trench tunnel. Another embedded sub-processor module realizes the perception of the environmental information of the cable trench tunnel, which is connected with a variety of gas sensors, water level detection sensors, and temperature and humidity sensors.

Relevant sensor information was obtained, processed, and transmitted to the operation terminal and background server through WLAN for display and data evaluation. To ensure the stability and reliability of data transmission, a combination of dual wireless network cards and high-power base stations is adapted to transfer a large amount of data, strengthen the power of wireless transmission, and ensure the stability and reliability of communication.

The operation and maintenance of the underground cable trench require long-term supervision and inspection by staff, but some human negligence will inevitably lead to accidents. To avoid this situation, this study designs an underground cable trench condition evaluation system based on edge intelligence, which mainly includes the following two steps:

The robot conducts patrol inspection in the underground cable trench through the autonomous navigation system and sends its position and sensor data to the background server in real time. The autonomous navigation algorithm consists of mapping, location, and path planning, and the involved data are huge and with high real-time ability, which could hardly be processed by an upper computer through wireless communication. Without waiting for the response of the computing center through the network, edge intelligence can process data locally, which decreases system delay, promotes the response speed significantly, and is suitable for the application of this scenario.

According to the transmitted position data, the designated robot will evaluate the overall system inside the cable trench every 50 m to realize the distributed management inside the cable trench, and according to the relevant instructions automatically generated by the evaluation results, the drainage system, exhaust system, fire extinguishing system, and other prevention systems located in the corresponding sections of the underground cable trench are started intelligently to realize the edge intelligent management of the underground cable trench.

OVERALL SCHEME OF THE AUTONOMOUS NAVIGATION OBSTACLE AVOIDANCE SYSTEM

Autonomous navigation technology of the inspection robot is mainly designed from three aspects: “Where am I?”, “Where am I going?”, and “How do I get there?”. This study solves the abovementioned three problems through the following two parts:

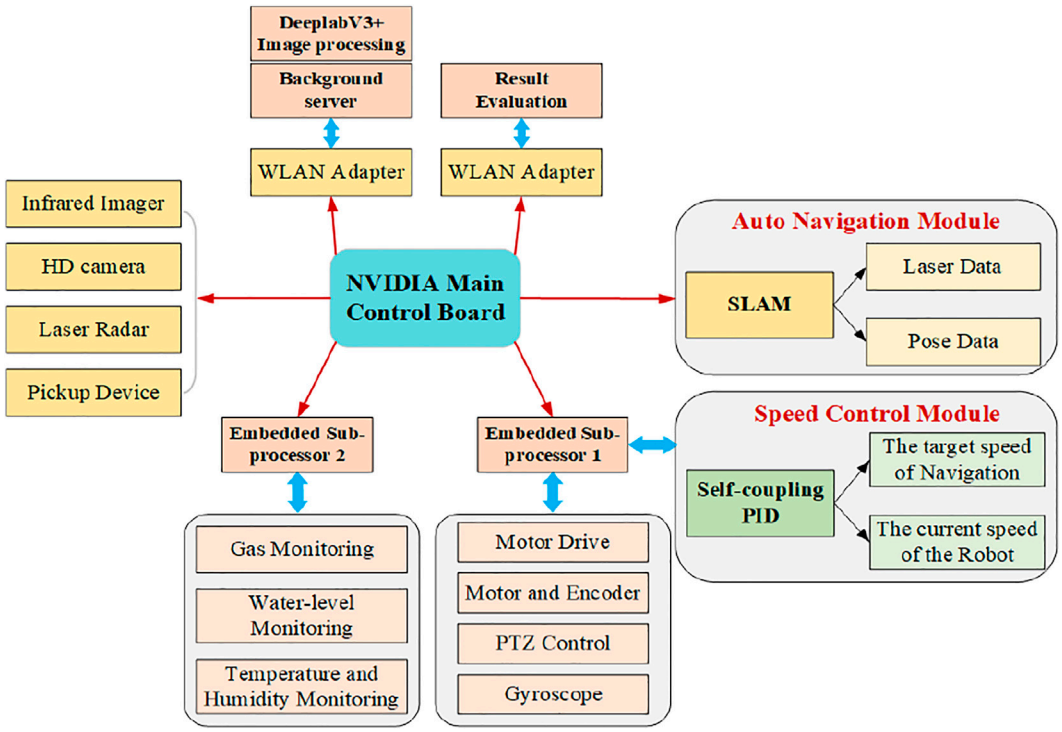

FIGURE 1 | System structure of the intelligent inspection robot for the cable trench.

the first part is the SLAM system for real-time analysis and the second part is path planning.

Simultaneous Localization and Mapping

To realize autonomous positioning and map construction, the inspection robot in this study adopts the open-source slam library cartographer SLAM (Hess et al., 2016) (released by Google in 2016). The hierarchical optimization idea is adopted in this algorithm. The front end uses the unscented Kalman filter (UKF) algorithm to fuse multi-source data (lidar, IMU, and encoder) for pose estimation, and a sub-map is constructed. The back end takes the sub-map as the basic unit to construct the loop constraint problem and proposes a branch and bound algorithm to speed up the construction of sub-map constraints. It overcomes the drawback that the filtering SLAM algorithm relies too much on the odometer and cannot build a large-scale map, and it is suitable for the scene such as the ground and the wall environment of the underground cable trench.

Path Planning

It is mainly composed of global paths and local paths. This study adopts the A * algorithm (Ammar et al., 2016) on the global path. With the combination of heuristic search and the breadth-first algorithm, the A* algorithm is the most effective direct search algorithm to solve the optimal path in a static environment.

The three improvements mentioned before are performed and compared with the original A* algorithm. **Figure 2** illustrates the difference between them. The red path in **Figure 2** is obtained by the original A* algorithm, and the yellow area is its search range. Meanwhile, the blue path is the result of the proposed improved A* algorithm, and the green area is its search range.

Local path planning used in this study is the dynamic window method (Fox et al., 1997; Seder and Petrovic, 2007; Doopalam, 2015), which is based on the forward kinematics solution of the robot. The path was simulated from the simulating space of forwarding velocity and angular velocity, and the position control of the robot was converted into a speed control. The optimal local path is obtained by scoring the trajectory to be evaluated.

The traditional global path planning and local path planning fusion scheme is shown in the document (Cao et al., 2020; Lao et al., 2021) and the ROS official navigation fusion scheme (Move base in ROS, 2021). However, in an underground cable trench, the use of traditional methods to merge the global path and the local path will cause the following problems.

(1) The dynamic window method is used too many times in the actual experiment which increases the inspection time.
(2) Due to the narrow space of the underground cable trench, the local planning will cause the robot to produce more inflection points during the forward process.
(3) If dynamic obstacles appear in the global path, the dynamic window method will linger around the obstacles appearing in the global path for a period, which will seriously affect the work efficiency of the robot.

This study proposes a fusion algorithm of global path planning and local path planning for the underground cable trench environment. The flow chart of the fusion algorithm is illustrated

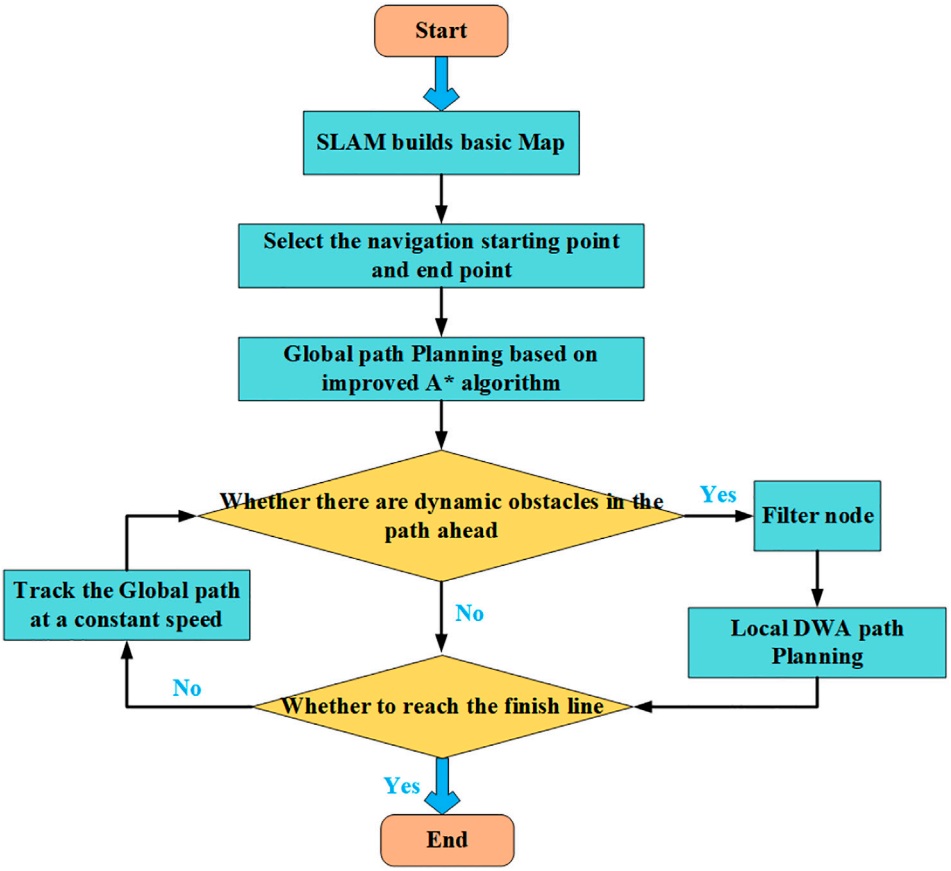

FIGURE 2 | Multiple trajectory generation graphs of the robot.

in **Figure 2**. If the current trajectory is feasible, the robot moves along with the current trajectory at a constant speed and keeps detecting the surrounding environment in real time. The measured fusion laser data are used as the center to define a circle and the length of the robot body as the radius to expand and linger around an obstacle if a new obstacle is detected in the global path planning. DWA local planning will begin, and all global path nodes included in the obstacle are discarded. The global path nodes that are out of the obstacle and close to the navigation endpoint will be used as the endpoint of DWA local planning. Three evaluation functions are used to evaluate all the paths generated from the starting point to the endpoint, and each evaluation function is accumulated to set the trajectory with the lowest cost as the best trajectory.

CONDITION ASSESSMENT OF THE UNDERGROUND CABLE TRENCH BASED ON EDGE INTELLIGENCE

Intelligent Structural Frame at the Edge of the Underground Cable Trench

The edge intelligent system of the underground cable trench is mainly analyzed and calculated by the edge computing device. First, a terminal level edge computing device is installed in the inspection robot to realize the autonomous navigation task of the robot in the internal environment of the underground cable trench. On this basis, the edge evaluation system is modeled. In this study, several fixed edge servers are installed in the internal environment of the underground cable trench. The edge server is uploaded to the cloud computing console, and the intelligent evaluation system for the underground cable trench edge is realized through the built cloud platform. The inspection robot transmits the collected sensor data to the nearest edge server during driving, realizes the distributed management of the cable trench, and visually manages the internal environment and evaluation results of the underground cable trench. Through the visual interface, the evaluation results and real-time internal environment of all sections can be displayed to the staff. The corresponding solutions are automatically generated according to the evaluation results to form a cloud edge and a collaborative underground cable trench edge intelligent evaluation system.

The network architecture of the underground cable trench edge intelligent evaluation system is shown in **Figure 4**, which is mainly divided into four layers:

(1) The sensing layer mainly completes the state perception of the inspection robot to the internal environment of the cable trench. The sensing layer includes the terminal level

autonomous navigation system and the edge level cable trench evaluation system. It is mounted on the machine Jetson Nano and carries out the terminal level autonomous navigation system through the collected lidar data. Then, the image, gas, and robot pose data are uploaded to the nearest edge server and uploaded to the cloud.

(2) The network layer mainly uses a high-power base station and power wireless private network to complete the safe and reliable transmission of data.
(3) The platform layer is mainly based on the Internet of things management platform, which systematically evaluates the underground cable trench based on multi-sensor data and manages the corresponding drainage, exhaust, and other systems of the underground cable trench.
(4) The application layer develops the upper computer based on the tablet computer, and the staff can complete the real-time monitoring of the internal environment of the underground cable trench and the independent inspection route management through the upper computer.

Underground Cable Trench Evaluation System

To achieve a comprehensive assessment of the underground cable trench condition, the following information is obtained during inspection: infrared thermal imaging images, visible-light images, depth images, angular velocity, linear acceleration output by IMU, map from lidar, temperature, humidity information of the internal environment, and water level. Based on this information, an underground cable trench condition evaluation method is proposed. It mainly consists of three aspects:

(1) Air quality assessment in the cable trench based on the data set fusion method of sulfur dioxide, ozone, carbon dioxide, carbon monoxide, and other harmful gases.
(2) Internal structure evaluation of the cable trench based on a depth camera and IMU.
(3) Hazard assessment of ponding in the cable trench based on a visible camera, IMU, encoder, and water level sensor.

Air Quality Assessment

The accumulation of methane, hydrogen sulfide gas, carbon monoxide, and other harmful combustible gases produced by microbial decomposition of some animals and plants during power transmission is the main cause of fire and explosion in the cable trench. The air quality assessment method based on the fusion of gray clustering and extension neural networks (Wang and Zhang, 2021) is adopted in this study. Representative air pollutants are selected according to the gray correlation degree, and an extension neural network is constructed to evaluate the air quality. The steps of constructing the air quality assessment model are as follows:

(1) Seven detection gas data of CO_2, TVOC, CH_4, NH_4, O_3, HS, and CO are extracted and normalized, and the correlation coefficient ε_ab is calculated between different air pollutants. The value range of the absolute correlation coefficient ε_ab is distributed in the interval of [0,1]. Generally, when the absolute correlation value is greater than 0.5, there is a positive correlation between the corresponding air pollutants. To cluster air pollutants, the first thing is to determine the value of the critical value r of the correlation degree. The value range of r is generally $0.5 < r < 1$. When $\varepsilon\_ab \geq r$, pollutants a and b are regarded as the same type.
(2) In the air quality monitoring database of the underground cable trench cloud platform, there are five air quality levels: excellent, good, light pollution, medium pollution, and heavy pollution. For each level machine, 100 measurement data at different times and different measurement positions are selected to calculate the correlation coefficient ε_ab between different pollutants. According to relevant experience, the critical value of the correlation degree $r = 0.7$ is selected here. If the accuracy of the final air quality assessment result does not meet the requirements, it will be adjusted. The seven pollutants are divided into the following three categories according to their correlation: (CO_2 and TVOC), (CH_4, NH_4, O_3, and HS), and (CO), which are selected as the indicator to represent each category.
(3) A matter-element model $M_m = (O_m, Cn, Vn)$ is constructed, with Om as the object, Cn as the object feature, and Vn as the eigenvalue, where $O_m(m = 1, 2, 3)$ represents three air quality levels; $C_n(n = 1, 2, \ldots, 7)$ represents the influencing factors of air pollution, here are the seven gases detected; and Vn (1,2,...,7) represents the value range corresponding to each air pollution influencing factor. The connection weight, feature quantity, and evaluation results of the extension neural network model could be obtained from this matter-element model of air quality evaluation. The extension neural network model is trained on the sample data set until it converges.
(4) The air quality assessment results can be calculated by inputting the detected air pollutants into the trained air quality assessment model. The overall process of the cable trench air assessment is shown in **Figure 3**.

Internal Structure Evaluation of the Cable Trench

Due to defects in the design and layout of the cable trench, cable suspensions and irregular cable stacks often exist in the interior, and construction materials and rubble cumulate on the bottom of the cable trench (as shown in **Figure 4**), which make the maintenance of the cable trench more difficult. Furthermore, the irregular layout of the cable stimulates additional eddy current on the metal sheath, leading to the operating temperature rise of the cable and local insulation aging, which affect the safe operation of the cable. Based on the information from the depth camera and IMU, the internal structure of the cable trench is evaluated from the capacity assessment of the trench and the pavement smoothness in this study.

To measure the pavement smoothness during the inspection, the IMU median integral is adopted to calculate the attitude of the robot on the ground during the inspection. The robot carrier

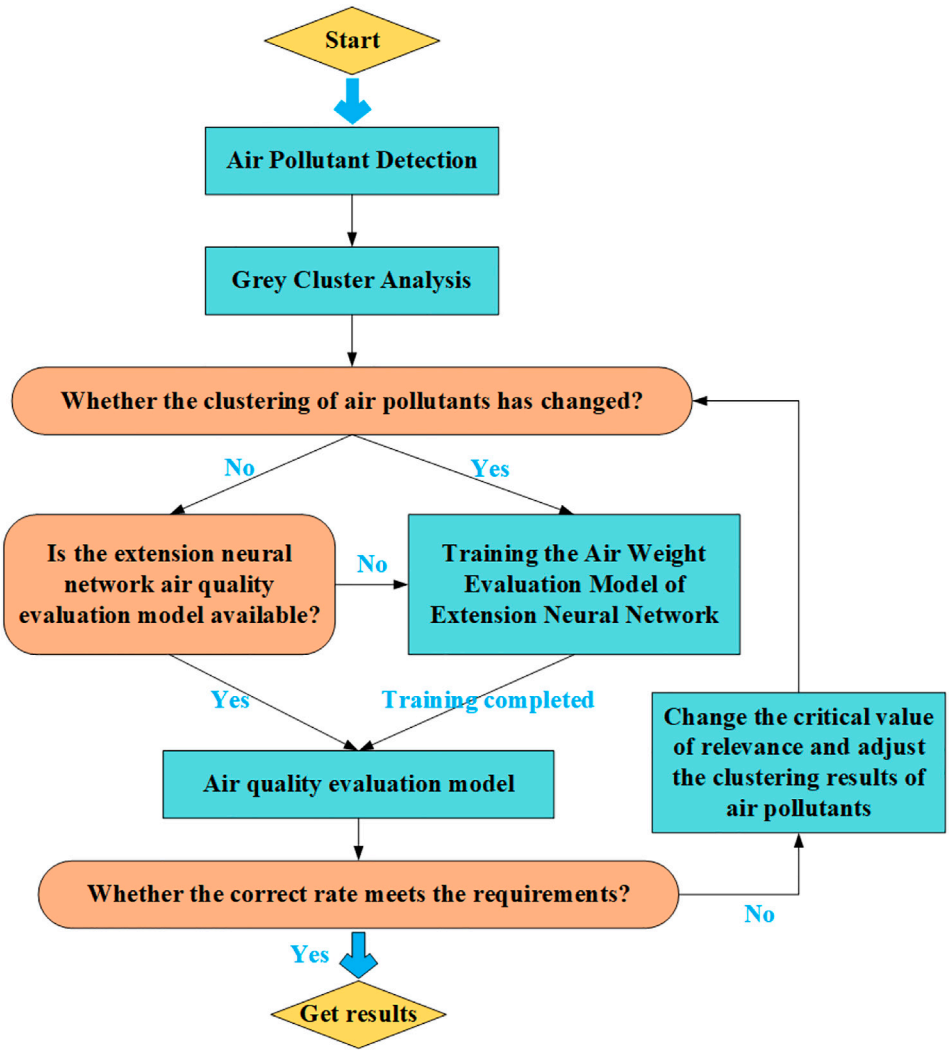

FIGURE 3 | Overall process of cable trench air assessment.

coordinate system B is consistent with the IMU coordinate system, the world coordinate system is W, the origin is the carrier center during the system initialization, and the *Z*-axis direction is aligned with the gravity direction in the world coordinate system. The attitude calculation based on the linear acceleration from IMU is as follows:

$$q_{wb_i} = \left[I + cos\frac{\phi}{2} + \frac{\Theta}{\phi} \right] q_{wb_{i-1}}, \tag{1}$$

$$\Theta = \begin{bmatrix} 0 & -\phi_x & -\phi_y & -\phi_z \\ \phi_x & 0 & \phi_z & -\phi_y \\ \phi_y & -\phi_z & 0 & \phi_x \\ \phi_z & \phi_y & -\phi_x & 0 \end{bmatrix}, \tag{2}$$

$$\phi = \frac{w_{i-1} + w_i}{2} (t_i - t_{i-1}), \tag{3}$$

where w_i is the angular velocity of IMU real-time output in the robot coordinate system in **Figure 5**; q_{wb_i} and $q_{wb_{i-1}}$ are the quaternion attitude of the robot carrier relative to the world coordinate system at the time i and $i-1$, respectively; ϕ is the rotation vector obtained by the median integral in the period from $i-1$ to i; and ϕ_x, ϕ_y, ϕ_z are the angular increment of x, y, and z axes within t_{i-1} to t_i sampling time intervals.

The unevenness of the road is mainly affected by the change rate of the pitch angle and the roll angle of the robot in the inspection process. Therefore, the variance of the pitch angle and the roll angle of the robot in the inspection process is calculated every 50 m (e.g., **Eqs 5**, **6**), where D_r and D_p are the variance of the roll angle and pitch angle of the inspection robot during driving; N is all the attitude data obtained in every 50-m section; μ_r and μ_p are the mean values of the robot roll angle and pitch angle; and q_{wb_iw}, q_{wb_ix}, q_{wb_iy}, and q_{wb_iz} are $[w, x, y, z]$ in q_{wb_i}. q_{wb_i} obtained the posture of the robot in the world coordinate system at the time t_i through **formula (1)**.

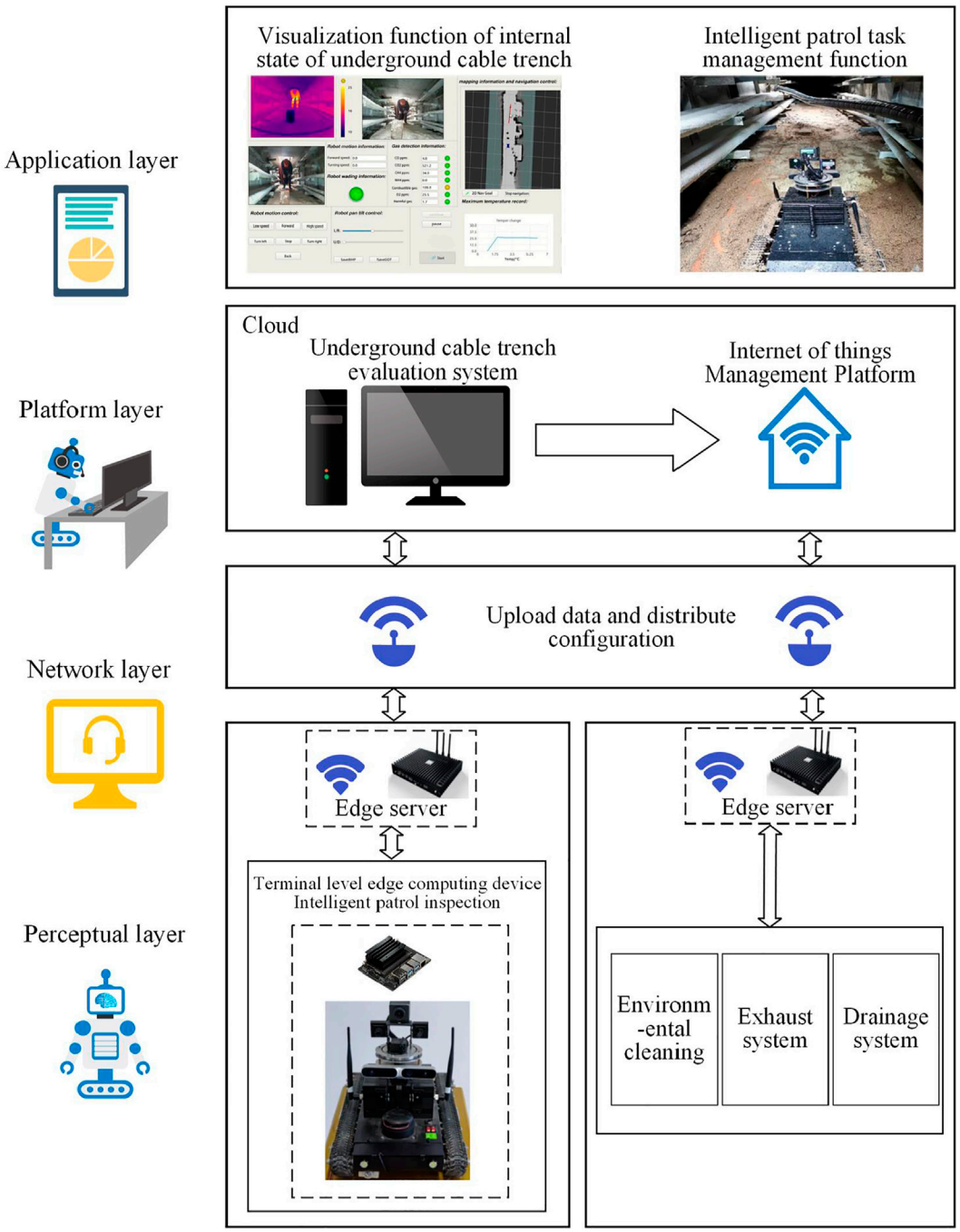

FIGURE 4 | Intelligent overall block diagram of the underground cable trench edge.

$$D_r = \sum_{i=0}^{N}\left(arctan\frac{2\left(q_{wb_{i_w}}q_{wb_{i_y}} + q_{wb_{i_y}}q_{wb_{i_z}}\right)}{1-2\left(q_{wb_{i_x}}^2 + q_{wb_{i_y}}^2\right)} - \mu_r\right), \quad (4)$$

$$D_p = \sum_{i=0}^{N}\left(\arctan\left(q_{wb_{i_w}}q_{wb_{i_y}} - q_{wb_{i_x}}q_{wb_{i_z}}\right) - \mu_p\right). \quad (5)$$

To evaluate the traffic capacity of the cable trench, a depth camera with an effective range of 20 m is placed in front of the robot to obtain 3D point cloud information. The underground cable trench in the world coordinates is a map to 3D point cloud and forms the point set P_W, and the mapping relationship could be expressed as **Eq. 7**, where $\boldsymbol{c_u}, \boldsymbol{c_v}, \boldsymbol{f_u}$, and $\boldsymbol{f_v}$ are the camera internal parameters; $Depth(u, v)$ is the depth information corresponding to the pixel point; and $[q_{wb_i}]_L$ is the quaternion left multiplier matrix obtained by IMU attitude calculation.

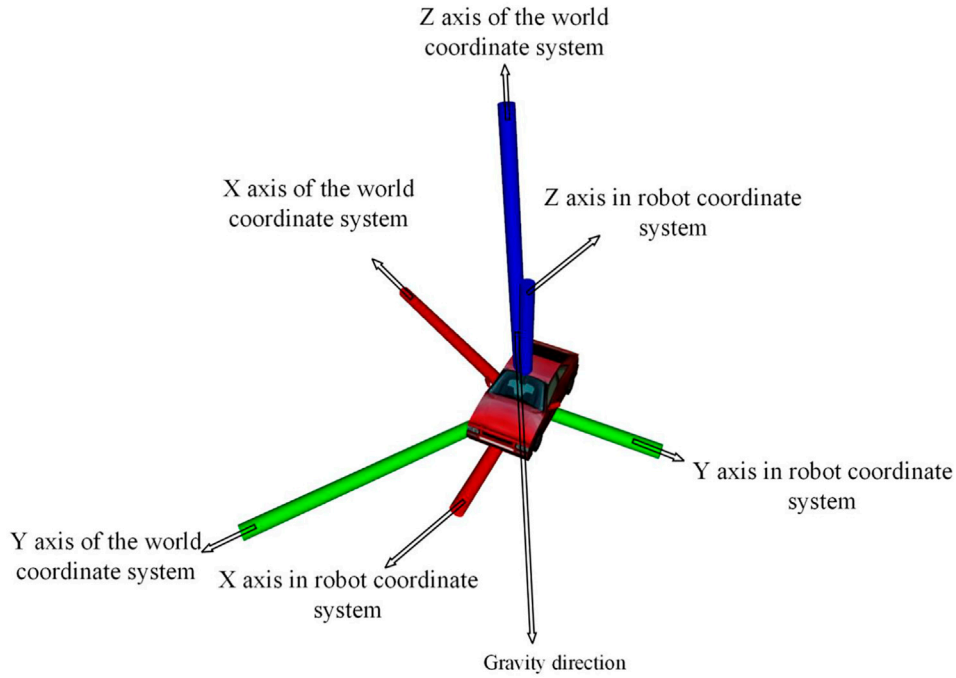

FIGURE 5 | Schematic diagram of robot and world coordinate systems.

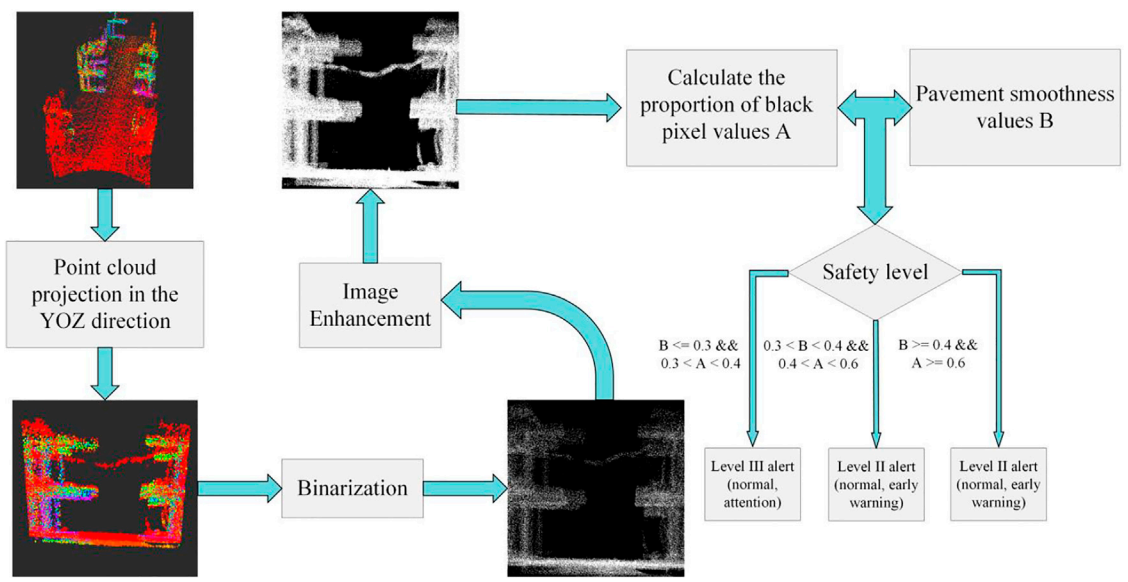

FIGURE 6 | Flow chart of cable trench trafficability evaluation.

$$P_W(X, Y, Z) = \left[q_{wb_i}\right]_L * \left(Depth(u, v), (u - c_u)\frac{Depth(u, v)}{f_u}, (v - c_v)\frac{Depth(u, v)}{f_v} \right). \quad (6)$$

All points in the set P_W are projected on the YOZ plane of the world coordinate system (as shown in **Figure 5**). A grid map is built by converting these projected points into binary images, where white pixel 1 is the obstacle and black pixel 0 is the accessible area. For any black pixel, the 5 × 5 domain around

TABLE 1 | Safety classification of the internal structure of the cable trench.

Safety level	Pavement smoothness	Traversability
Level III alert (normal and attention)	≤ 0.3	0.3–0.4
Level II alert (normal and early warning)	0.3 ~ 0.4	0.4–0.6
Level I alert (abnormal and alarm)	≥ 0.4	≥ 0.6

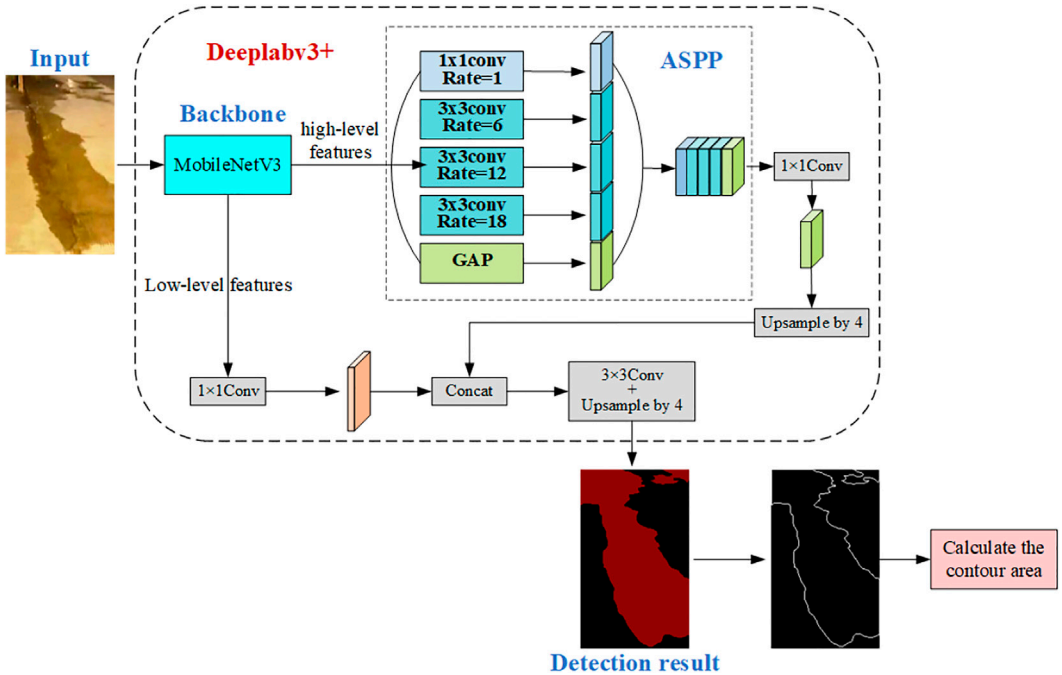

FIGURE 7 | Ponding area identification process.

FIGURE 8 | Hanging cable (left); accumulation of rubble and building materials (right).

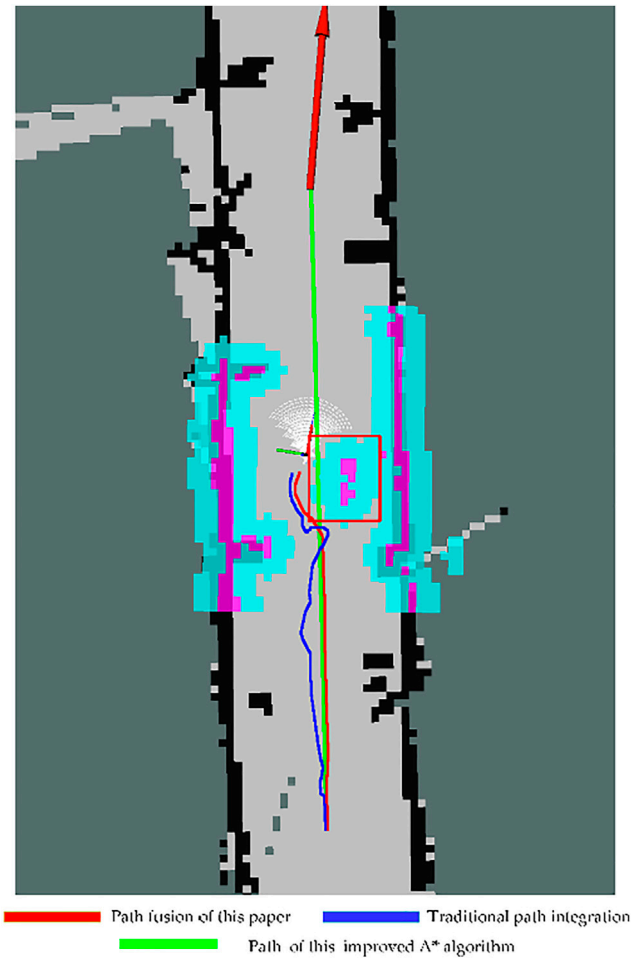

FIGURE 9 | Environmental mapping and path planning of the cable trench.

it is searched, and if there are more than three white pixels inside this domain, this black pixel will be replaced by a white one. The proportion of the remaining black pixels, at last, is calculated as the current cable trench trafficability. The overall block diagram is shown in **Figure 6**.

By performing abovementioned steps, the variance of the pitch angle and roll angle of the robot and the traffic capacity of the cable are obtained every 20 m. The sum of the variance of the pitch angle and roll angle is normalized and defined as the pavement flatness coefficient. According to the investigation results of the actual condition of the cable trench and expert analysis, the classification of the safety grade of the cable trench structure evaluation is shown in **Table 1** below.

Hazard Assessment of Water Accumulation Inside the Cable Trench

The underground cable trench easily accumulates water which makes internal moisture too high and leads to the oxidation and fracture of the metal cross arms on both sides of the cable trench. Meanwhile, heat dissipation of the cable is pretty slow in this situation, which accelerates the thermal aging of cable insulation. Therefore, water accumulation is an important factor to evaluate the condition of the cable trench. In this study, a visible-light camera, water level sensor, IMU, and encoder are integrated to evaluate the water accumulation in the cable trench.

TABLE 2 | Average value of traditional and improved fusion path algorithms.

Algorithm	Traditional fusion			Improved fusion		
Inspection channel length (m)	10	20	30	10	20	30
Average time (s)	79.4	164.3	240.7	61.2	131.6	197.8
Average total path length (m)	12.2	24.6	35.7	11.4	21.8	32.7

Considering the situation of deep ponding, a water level sensor is placed under the robot. Water hazard in the cable trench is divided into two cases. When the water level sensor under the robot is triggered, the water hazard is evaluated by the volume of ponding; otherwise, the water hazard is evaluated by the surface area of ponding. For the first case, when the robot passes through the ponding, the water level sensor is triggered, and the current travel speed of the robot v_{b_i} is read from the encoder. The current position p_{w_i} is updated from the previous position, v_{b_i} and the attitude of IMU (as shown in **Eq. 8**). The length L and the depth D of the ponding section are calculated by **Formula 9**ormula –**Formula 10**, and the volume of ponding is measured using **Formula 10**. During this process, the encoder is synchronized with IMU.

$$\boldsymbol{p}_{w_i} = \boldsymbol{p}_{w_{i-1}} + \frac{\boldsymbol{q}_{wb_i}\boldsymbol{v}_{b_i} + \boldsymbol{q}_{wb_{i-1}}\boldsymbol{v}_{b_{i-1}}}{2}(\boldsymbol{t}_i - \boldsymbol{t}_{i-1}), \tag{7}$$

$$\boldsymbol{L} = \sum_{i=1}^{N} \left\| \boldsymbol{p}_{w_i} - \boldsymbol{p}_{w_{i-1}} \right\|^2, \tag{8}$$

$$\boldsymbol{D} = \boldsymbol{max}\left(\boldsymbol{p}_{w1}^{z}, \boldsymbol{p}_{w2}^{z}, \ldots, \boldsymbol{p}_{wN}^{z}\right) - \boldsymbol{min}\left(\boldsymbol{p}_{w1}^{z}, \boldsymbol{p}_{w2}^{z}, \ldots, \boldsymbol{p}_{wN}^{z}\right), \tag{9}$$

$$\boldsymbol{V} = \mathbf{1.2} \times \boldsymbol{L} \times \boldsymbol{D}. \tag{10}$$

When the ponding is too shallow to trigger the water level sensor, the ponding area is obtained from the image data taken by the visible camera. The DeepLabV3+ neural network framework (Chen et al., 2018) is used to construct the ponding segmentation model, and MobileNetV3 (Howard et al., 2019) is selected as the backbone network for preliminary feature extraction, which not only ensures the lightweight of the network but also has good performance. The context information of the image is extracted from multiple scales, combined with the output of the low-level feature by the decoding module and the backbone network, which could significantly improve the edge detection accuracy of ponding. The visible light DeepLabV3+ identification ponding process is shown in **Figure 7**.

ANALYSIS OF ACTUAL SITE RESULTS

The field test is carried out in the cable trench environment, as shown in **Figure 8**. Jetson Nano is adopted as the core processor and is loaded with Ubuntu 18.04 and ROS. It collects data from lidar and depth cameras to build maps and navigate the route.

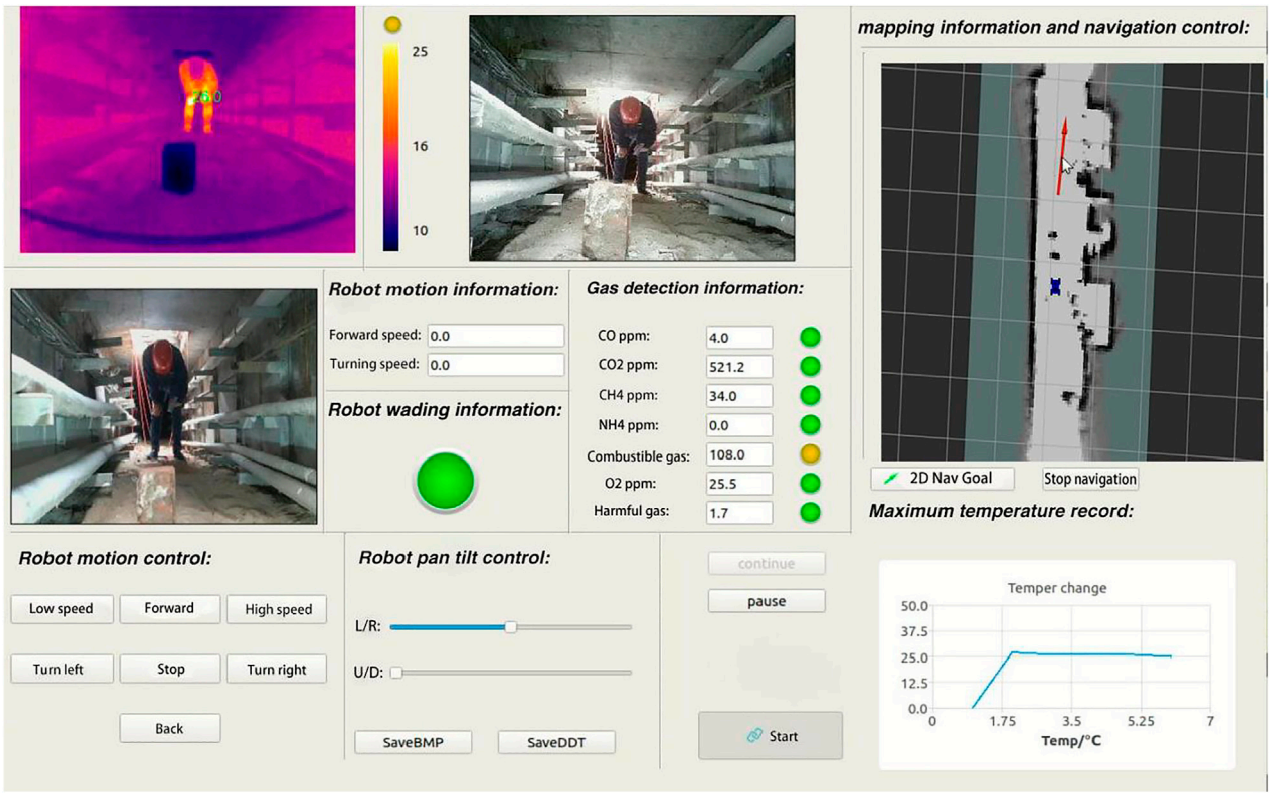

FIGURE 10 | Monitoring interface of the upper computer in the cable trench.

Two microcontrollers (STM32F103) are selected as the chip, one of which is used to receive commands from the processor and the upper computer and control the movement of the robot. The other one is equipped with methane, ozone, combustible gas, and other harmful gas detection sensors, as well as nine-axis IMU sensors and a water level sensor.

To verify the path fusion algorithm, a man-made dynamic obstacle is set in the field test (as shown in the red box of **Figure 9**). The path obtained by the traditional path fusion algorithm is shown in the blue line segment in **Figure 9**. Due to the narrow space of the cable trench and the relatively small distance between the obstacle and wall, the traditional global path planning method generates unnecessary inflection points on the path. Furthermore, when a dynamic obstacle appears on the global path, the robot will wander around the obstacle to make redundant judgments, which affects the inspection efficiency. The red line segment in **Figure 9** is the path obtained by the proposed fusion method. The robot retains the smoothness of the global path before encountering dynamic obstacles during the on-site inspection. When the dynamic obstacles appear on the global path, the global path nodes contained in the dynamic obstacles are automatically filtered, and the path avoiding the dynamic obstacles is smoother and with less judgment and higher efficiency.

To verify the effectiveness and operability further, repetitive on-site experiments were carried out using the traditional fusion path algorithm and the proposed method, respectively, with different starting points and target points. Reducing the random error caused by the operation, three cable trenches with different lengths are chosen and inspected five times each, and the average length of route and time consumption is calculated as the final results (as shown in **Table 2**). Compared with the traditional fusion path algorithm, the inspection speed of the improved fusion path algorithm proposed in this study increases by 21%, and the total path is shorter. The on-site experiments verified the advantages of the proposed path planning method.

The inspection robot completes the task of automatic navigation through the edge computing device mounted inside the fuselage. During movement, the image, gas, IMU, encoder, and robot position data are transmitted in real time to the nearest edge server, which is transmitted to the cloud computing platform through wireless transmission. In the cloud computing platform, combined with the position of the inspection robot in the underground cable trench, the underground cable trench is managed in a distributed manner. The data of every 50-m section of the underground cable trench are processed and analyzed in real time through the evaluation algorithm proposed in this study, and the corresponding solutions are given. The cloud platform is wirelessly transmitted to the edge server of the corresponding section through the Internet of things platform. Thus, the corresponding drainage system and exhaust system can be started, and the staff can monitor the real-time environment

TABLE 3 | Assessment results and countermeasures.

Patrol section (*m*)	Ponding volume (m^3) /area (m^2)	Pavement smoothness	Traversability	Air quality	Evaluation results and countermeasures
0–50	0/2.534	0.237	0.45	good	Good air, ponding hazard, and medium internal structure The hanging cable should be cleaned, and attention should be given to ponding at all times.
50–100	0.478/0	0.437	0.289	good	Air is good, ponding is harmful, and the internal structure is medium. Drainage treatment
100–150	0.63/1.79	0.626	0.36	light pollution	Air is poor, ponding is harmful, and the internal structure is serious. Ventilation should be performed, road debris should be cleaned up, and cables should be hung.
150–200	0/0.771	0.283	0.24	good	Air is good, water is harmful, and the internal structure is good.

of the underground cable trench through the flat plate. As shown in **Figure 10**, the upper computer shows the information and status of the robot working in the cable trench.

During the field test, the proposed robot can build a map in an unfamiliar environment with a positional error of less than 8 cm. Global path planning is designed based on the improved A* algorithm, and dynamic path planning is designed based on DWM. The two algorithms are integrated to navigate the route. The path is accurately tracked to avoid obstacles, and the average speed is greater than 0.4 m/s. As shown in the upper computer, the inspection robot has an infrared thermal imaging camera, high-definition camera, and depth camera to monitor the underground cable trench and can detect the concentration of seven kinds of harmful gases. Applying the underground cable trench condition assessment method based on edge intelligence presented in this study, the internal environment of the cable trench is inspected in real time, the overall evaluation of the section is carried out every 50 m, and the overall healthy environment and countermeasures are fed back to the staff. The evaluation results are illustrated in **Table 3**.

The proposed condition assessment method based on the inspected robot makes a distributed evaluation for the overall environment of the underground cable trench without manual interference. It provides a real-time condition of the cable trench from point to point and end to end. The corresponding countermeasures are given, which greatly improves the internal security of the cable trench. The feasibility and practicability of our method are verified in the field tests.

CONCLUSION

Substituting for the staff to carry out status monitoring and condition assessment in the high-risk environment of the underground cable trench, an automatic inspection robot system is proposed according to this environment, and a condition assessment method is designed based on the information collected by the robot. The designed robot has a good movement ability in the underground cable trench and can execute automatic navigation.

During the operation of the inspection robot designed in this study, all the data taken by the road section are uploaded to the background server every 50 m. Through a multi-source sensor fusion method proposed in this study, the air quality, internal structure, and ponding hazards of the underground cable trench in this road section are evaluated. At the same time, to apply the results of edge intelligent evaluation of the underground cable trench, the drainage system, exhaust system, fire extinguishing system, and alarm system of the road section can be started according to these results.

Applying the robot to an underground cable trench instead of manual inspection can reduce the inspection intensity and difficulty of staff. The stability and reliability of cable maintenance are improved significantly, and economic and social benefits are promoted a lot. The industrial application of the proposed technology in the future relies on two aspects. One is the promotion of reliability and obstacle-surmounting ability of the inspection robot platform. More field tests for the improvement of the practicality of the condition assessment method are the other aspects (Lao et al., 2021).

DATA AVAILABILITY STATEMENT

The raw data supporting the conclusions of this article will be made available by the authors, without undue reservation.

AUTHOR CONTRIBUTIONS

ZJ, ZL and SF contributed to the concept and design of the study. ZJ and ZL realized the robot. YT performed the field tests. ZJ wrote the first draft of the manuscript. YT and ZL wrote sections of the manuscript. All authors contributed to manuscript revision, read, and approved the submitted version.

FUNDING

This work was supported in part by the Research Foundation of Education Bureau of Hunan Province, China (Grant Nos. 19B016 and 20A028), in part by the Open Research Foundation of Hunan Province Key Laboratory of Electric Power Robot, China (Grant Nos. PROF1905 and PROF1901), and in part by the Changsha Municipal Natural Science Foundation, (Grant No. kq2014105).

REFERENCES

Ammar, A., Bennaceur, H., Châari, I., Koubâa, A., and Alajlan, M. (2016). Relaxed Dijkstra and A* with Linear Complexity for Robot Path Planning Problems in Large-Scale Grid Environments[J]. *Methodologies Appl.* 20, 4149–4171. doi:10.1007/s00500-015-1750-1

Cao, Y., Zhou, Y., and Zhang, Y. (2020). Obstacle Avoidance Path Planning of mobile Robot Based on Optimized A* and DWA Algorithm [J]. *Machine tools and hydraulics* 48 (24), 246–252. doi:10.3969/j.issn.1001-3881.2020.24.034

Chen, L. C., Zhu, Y., Papandreou, G., Schroff, F., and Adam, H. (2018). *Encoder-Decoder with Atrous Separable Convolution for Semantic Image Segmentation [J]*. Cham: Springer.

Commission of the European Communities (2003). *Background Paper Undergrounding of Electricity Line in Europe[R]*. Brussels: Commission of the European Communities.

Dey, S., and Mukherjee, A. (2016).Robotic SLAM: a Review from Fog Computing and Mobile Edge Computing Perspective[C], Proceeding of the the 13th International Conference. New York, NY: ACM.

Doopalam, T. (2015). Hybrid Motion Planning Method for Autonomous Robots Using Kinect-Based Sensor Fusion and Virtual Plane Approach in Dynamic Environments[J]. *J. Sensors* 2015 (5), 1–13. doi:10.1155/2015/471052

Fox, D., Burgard, W., and Thrun, S. (1997). The Dynamic Window Approach to Collision Avoidance. *IEEE Robotics Automation Mag.* 4 (1), 23–33. doi:10.1109/100.580977

Hepburn, D. M., Zhou, C., Song, X., Zhang, G., and Michel, M. (2016).Analysis of On-Line Power cable Signals[C], Proceeding of the International Conference on Condition Monitoring & Diagnosis, April 2008, Beijing, China. IEEE.

Hess, W., Kohler, D., Rapp, H., and Andor, D. (2016).Real-time Loop Closure in 2D LIDAR SLAM, Proceedings of the 2016 IEEE International Conference on Robotics and Automation (ICRA). Stockholm, Sweden: IEEE, 1271–1278. doi:10.1109/icra.2016.7487258

Howard, A., Sandler, M., Chu, G., Chen, L. C., Chen, B., Tan, M., et al. (2019). "Searching for Mobilenetv3," in *Proceedings of the IEEE International Conference on Computer Vision*, 1314–1324. doi:10.1109/iccv.2019.00140

Jongen, R., Quak, B., Tenbohlen, S., and Gulski, E. (2012).New Developments in On-Site Testing of Long Lengths of (E)HV Power Cable[C], Proceeding of the International Conference on Condition Monitoring & Diagnosis, Sept. 2012, Bali, Indonesia. IEEE.

Lyall, J. S., Nourbakhsh, G., and Zhao, H. C., "Underground Power cable Environment On-Line Monitoring and Analysis," Proceeding of the 2000 Power Engineering Society Summer Meeting (Cat. No.00CH37134), 2000, July 2000. Seattle, WA, USA, 457–462. vol. 1, doi:10.1109/PESS.2000.867629

Kang, K. J., Lee, J. W., Lee, E. D., and Kim, M-D. (2018).Intelligent Autonomous Driving Condition Monitoring and Diagnosis Robot-System of Underground Electric Power Conduit Pipe[C], Proceeding of the 2018 Condition Monitoring and Diagnosis (CMD), Sept. 2018, Perth, WA, Australia. IEEE, 1–5.

Lao, C., Peng, L., and Yu, F. (2021). Greenhouse Robot Path Planning Based on the Fusion of Improved A* and DWA Algorithm [J]. *J. Agric. machinery* 52 (01), 14–22. (in Chinese). doi:10.6041/j.issn.1000-1298.2021.01.002

Li, E., Zhou, Z., and Chen, X. (2018). *Edge Intelligence: On-Demand Deep Learning Model Co-inference with Device-Edge Synergy[J]*.

Ling, Z., Tang, M., Zhang, K., fan, S., and Jia, Z. (2020). Design of cable Trench Inspection Robot System Based on Improved D * Lite Algorithm [J]. *Comp. Meas. Control* 28 (09), 187–190+201. (In Chinese). doi:10.16526/j.cnki.11-4762/tp.2020.09.037

Liu, K., and Yin, Y. (2007). Technical and Economic Analysis of Overhead Lines and Underground Cables in Urban Power Grid [J]. *Guangdong electric power* 20 (05), 25–27. (in Chinese). doi:10.3969/j.issn.1007-290X.2007.05.007

Lu, S., Zhang, Y., and Su, J. (2017). Mobile Robot for Power Substation Inspection: a Survey. *Ieee/caa J. Autom. Sinica* 4 (4), 830–847. doi:10.1109/JAS.2017.7510364

Move base in Ros *Move Base in ROS*. Available online: http://wiki.ros.org/move_base/(accessed on 3 20, 2021).

Pal, D., Meyur, R., Menon, S., Reddy, M. J. B., and Mohanta, D. K. (2017). Real-Time Condition Monitoring of Substation Equipment Using Thermal Cameras [J]. *Iet Generation Transm. Distribution* 12 (4), 895–902. doi:10.1049/iet-gtd.2017.0096

Patel, P., Ali, M. I., and Sheth, A. (2017). On Using the Intelligent Edge for IoT Analytics[J]. *IEEE Intell. Syst.* 32, 64–69. doi:10.1109/mis.2017.3711653

Premsankar, G., Di Francesco, M., and Taleb, T. (2018). Edge Computing for the Internet of Things: A Case Study [J]. *IEEE Internet Things J.* 5, 1275–1284. doi:10.1109/jiot.2018.2805263

Seder, M., and Petrovic, I. (2007).Dynamic Window Based Approach to mobile Robot Motion Control in the Presence of Moving Obstacles [C], Proceedings of the IEEE International Conference on Robotics and Automation, April 2007, Rome, Italy. IEEE.

Siddiqui, B. A., Pakonen, P., and Verho, P. (2017). Novel Inductive Sensor Solutions for On-Line Partial Discharge and Power Quality Monitoring. *IEEE Trans. Dielect. Electr. Insul.* 24 (1), 209–216. doi:10.1109/tdei.2016.005908

Song, W. (2015). *Research on Wireless Sensing and Safety Status Evaluation of Underground cable Channel [D]*. Kunming, China: Kunming University of Technology. (In Chinese).

Sun, T., Ye, L., Xie, J., Zhang, J., Fan, M., and Fan, H. (2021). Research and Application of Substation cable Trench Inspection Robot Communication System. *J. Phys. Conf. Ser.* 2031 (1), 012025. doi:10.1088/1742-6596/2031/1/012025

Wang, B., Guo, R., Li, B., Han, L., Sun, Y., and Wang, M. (2012). SmartGuard: an Autonomous Robotic System for Inspecting Substation Equipment. *J. Field Robotics* 29 (1), 123–137. doi:10.1002/rob.20423

Wang, T., and Zhang, X. (2021). Research on Air Quality Evaluation Method of Civil Air Defense Engineering Based on Improved Extension Neural Network [J]. *Mech. Des. manufacturing* 2021 (01), 286–291. (in Chinese). doi:10.19356/j.cnki.1001-3997.2021.01.066

Wu, Y-H., and Zhang, J. S. (2014). System of Fault Diagnosis and Operation Monitoring for Low-Voltage Distribution Equipment[J]. *J. Mech. Electr. Eng.* 31, 795–799. doi:10.3969/j.issn.1001-4551.2014.06.026

Xing, Y., Jin, L., and Yang, Z. (2018). Development and Application of Substation Inspection Robot Control System Based on DSP [J]. *Electrotechnical* (03), 44–46. (In Chinese). doi:10.3969/j.issn.1002-1388.2018.03.015

Conflict of Interest: The authors declare that the research was conducted in the absence of any commercial or financial relationships that could be construed as a potential conflict of interest.

frontiers | Frontiers in Energy Research

ORIGINAL RESEARCH
published: 26 April 2022
doi: 10.3389/fenrg.2022.880825

Voltage Optimization Control Strategy for Islanded Microgrid Source-Grid-Load Active-Reactive Power Coordination Based on Collaborative Di-MPC

Xiaojie Liu[1], *Zhaobin Du*[1,2]*, *Yefa Tan*[1] *and Yao Liu*[1]

[1]School of Electric Power Engineering, South China University of Technology, Guangzhou, China, [2]Guangdong Province' New Energy Power System Intelligent Operation and Control Enterprise Key Laboratory, Guangzhou, China

To cope with the volatility and randomness of wind power, photovoltaic (PV) power, and load demands in the islanded microgrid, and also to ensure the safety and economic operation of the islanded microgrid system. A collaborative Distributed model predictive control (Di-MPC) based voltage optimization control strategy is proposed, which considers the strong coupling characteristic of active and reactive power due to the impedance ratio of islanded microgrid, and the requirements of real-time and robustness in the optimization as well. By coordinating the controllable devices in the source-grid-load side of the islanded microgrid, the proposed strategy aims to make full use of the voltage regulation capability of each controllable device. Firstly, by considering the different operating characteristics of the controllable devices, a multi-time scale distributed voltage optimal control model is established. It divides the optimal control process into long-time scale and short-time scale and optimizes for respective objective functions and control variables in different time scales. Secondly, a collaborative Di-MPC-based voltage optimal control strategy is proposed. With the proposed collaboration mechanism, the power output increments of the distributed generators (DGs) are solved in the short-time scale, and the errors in the long-time scale control are also fixed. Finally, the simulation results show that compared with a traditional optimal control method and a centralized model predictive control (CMPC) method, the proposed voltage optimization control strategy can effectively reduce the voltage deviation and fluctuation at each node while ensuring the economic operation of the islanded microgrid system.

Keywords: distributed model predictive control, coordinated optimization of active-reactive power, optimal control of voltage, islanded microgrid, collaborative method

OPEN ACCESS

Edited by:
Yan Xu,
Nanyang Technological University, Singapore

Reviewed by:
Yushuai Li,
University of Oslo, Norway
Yunhe Hou,
The University of Hong Kong, Hong Kong, SAR China
Wenjie Zhang,
National University of Singapore, Singapore

***Correspondence:**
Zhaobin Du
epduzb@scut.edu.cn

Specialty section:
This article was submitted to Smart Grids, a section of the journal Frontiers in Energy Research

Received: *21 February 2022*
Accepted: *31 March 2022*
Published: *26 April 2022*

Citation:
Liu X, Du Z, Tan Y and Liu Y (2022) Voltage Optimization Control Strategy for Islanded Microgrid Source-Grid-Load Active-Reactive Power Coordination Based on Collaborative Di-MPC. Front. Energy Res. 10:880825. doi: 10.3389/fenrg.2022.880825

1 INTRODUCTION

With the growing demand for clean energy in recent years, microgrids, as a limited integration of multiple renewable power generation technologies, have the characteristic of flexibility, scalability, and ease of establishment. It has helped to decentralize and decarbonize energy (Katiraei et al., 2008; Morstyn et al., 2018) and was widely used in many countries (Jiayi et al., 2008), effectively increasing the utilization of renewable energy. Microgrids are usually operated in two modes: grid-connected

mode and islanded mode. Due to the small size of islanded microgrids, their dynamic regulation capability is greatly limited by the uncertainty of DGs, such as wind turbine (WT) and PV stations. Moreover, the lack of reactive power support from the external grid makes them more vulnerable to voltage control problems compare to grid-connected microgrids (Han et al., 2016; Mehmood et al., 2021).

At present, the main DGs in the islanded microgrid are WT and PV. Both sources and the load demands have strong randomness and volatility, which brings great uncertainty to the islanded microgrid system. Due to the prediction error of the day beforehand, the system uncertainty will gradually increase as the prediction time moves forward, which makes it difficult to control the islanded microgrid system optimally. To cope with the growing pressure of optimal control for the islanded microgrid system, many works have been done and reported. In contrast to the traditional single-time scale open-loop optimal control method, model predictive control (MPC), as a model-based finite-time rolling optimal closed-loop control method (Ferrari-Trecate et al., 2004; Kouro et al., 2009; Villalon et al., 2020; Hu et al., 2021), can better resist the impact of system uncertainty and show good robustness, and its application in the study of optimal control of power systems has received wide attention. (Liu And Kong, 2013; Wang et al., 2015). In (Raimondi Cominesi et al., 2018), the authors presented a two-layer algorithm for the optimal energy management in MGs, and combined the high-level off-line economic optimization with the low-level online stochastic MPC. In (Xia et al., 2019), to solve the problem of rapid and frequent voltage fluctuations caused by the high proportion of wind power connected to the grid, the authors introduced the multi-time scale optimal control method based on MPC into the reactive voltage control process, which enabled the system to respond to the predictable changes in advance and track the fluctuation of the grid voltage in time. Authors in (Xu et al., 2015) proposed an MPC-based automatic wind farm voltage control method to coordinate the WT and static var generators (SVG). It solved the problems of the time lag and equipment incoordination brought by the traditional reactive power optimization method based on the current time sections for decision-making. In (Yan et al., 2019), the authors proposed a multi-time scale reactive power voltage control method. To fully exploit the dynamic reactive power voltage regulation capability of renewable energy, a multi-time scale reactive power optimization model based on MPC was established, and the voltage overrun caused by the uncertainty factor was well suppressed. However, because of the strong coupling characteristic of active and reactive power caused by the high impedance ratio of islanded microgrid, it is not comprehensive to implement the optimal voltage control while only standing on the perspective of reactive power control. Such an approach ignores the influence of the active power during the voltage control process and limits the optimization space for optimal voltage control in islanded microgrids.

In addition, unlike the main grids, the spacing between source and load in the microgrids is shorter, which causes a strong coupling between active and reactive power. It makes the node voltage not only being affected by reactive power but also closely related to the active power. Therefore, the unilateral analysis of active or reactive power optimization in microgrids based on the traditional active and reactive decoupling method is inadequate and inaccurate. In (Zhang and Wang, 2016), the authors proposed an MPC-based coordinated optimization method of active and reactive power dispatching for microgrid, considering voltage constraints. Then a real-time rolling optimization was used to optimize the power outputs of microsource and energy storage system (ESS), which achieved the purpose of economic and stable operation of the microgrid and reduced the voltage deviation of nodes within the system. Authors in (Gao et al., 2018) used the branch flow model-based relaxed optimal power flow to optimize the robust coordinated optimization of active and reactive powers, which is described as a mixed-integer second-order cone programming problem. In order to address the uncertainty of renewable energy and load demand, a two-stage robust optimization model was proposed. In (Zhang et al., 2017), the authors proposed an MPC-based active-reactive power coordination control method for distribution networks with distributed photovoltaic stations, which performed separate MPC at different time scales for respective control objectives and control variable, then the established non-convex and non-linear model was solved by using the second-order cone programming in a relaxed manner. However, with the growing number of controllable DGs and devices within the microgrid, centralized method like CMPC approach used in the above-mentioned research will face great challenges. The traditional centralized control method relies on global information, and when the number of controllable devices increases, the pressure on computation and communication will become intense. Moreover, the original model has to be readjusted once there are any devices withdrawn from failure, which makes the method less robust and scalable, and cannot adapt to the requirements of microgrid operation and control in the context of increasing penetration of DGs.

Furthermore, in order to achieve the real-time and robust requirements of voltage optimization control in the microgrids, distributed control method like Di-MPC has been approached for its advantages of high reliability, flexibility, and fast solution, and it also overcomes the shortcomings of the traditional CMPC. In (Zheng et al., 2018), authors combined the Di-MPC method to transform the microgrid energy dispatching problem into several interconnected non-linear and integer planning problems, which simplifies the plug-and-play feature. The proposed method reduces the computation of the problem to a large extent and improves the solution efficiency. Authors in (Guo et al., 2019) combined with the consistency-based distributed information synchronization and estimation to coordinate and optimize the control of the active and reactive power outputs of the wind farm, which ensures that the WT tracks the reference frequency while reducing its fatigue load through active power control, and reduces the deviation of the node voltage through reactive power/voltage control. In (Zhao et al., 2020), the authors proposed a control strategy based on Di-MPC to optimize the economic scheduling of multi-microgrids on island groups. The proposed strategy designed a trading mechanism by using dynamic non-cooperative game theory to regulate trading behavior between microgrids with different owners. Authors in (F. et al., 2021) proposed a distributed model predictive control strategy for the operation of isolated microgrids based on a consensus strategy, which can tackle both the economic dispatch and frequency restoration over the same time scale. It is also robust to load variations and communication issues. Authors in (Fan et al.,

2021) presented a distributed discrete-time control scheme for the DC microgrids, and it had achieved the optimal coordination of CGs and RGs, where the generation cost of the CGs is minimized, and the energy utilization of RGs is maximized. In (Yang et al., 2021), the authors proposed a novel distributed model predictive control (DMPC) strategy for a DC microgrid based on voltage observers for multiple energy storage systems (ESs) to achieve a tradeoff between voltage regulation and power-sharing. In order to reduce the impact of communication delay on voltage observers, an improved DMPC consensus algorithm is proposed, which effectively improves the robustness of the system to the delay.

Meanwhile, for multi-energy systems such as microgrids, many works have also been done and reported (Li et al., 2021). The authors in (Liu and Yang, 2022) established a multi-objective optimization model with operating costs and gas emissions as the competing objective functions, simultaneously. To achieve the purpose of optimal energy dispatching with reasonable operating costs and gas emissions, a distributed algorithm with dynamic weights based on initial values was proposed, where participants only need to share information with neighboring controllers to achieve energy management. In (Li et al., 2020), the authors established a double-mode energy management model for the multi-energy system, which modeled the islanded and network-connected modes into a unified and distributed form. Then, a novel distributed dynamic event-triggered Newton-Raphson algorithm is proposed to solve the double-mode energy management problem in a fully distributed fashion, in which the adaptability and flexibility of the multi-energy system can be enhanced. Therefore, distributed control methods are more in line with the needs of the engineering practice for their real-time and robust performance, which can better coordinate the controllable devices within the multi-energy system.

Thus based on the collaborative Di-MPC, this paper proposes a method for optimizing the active-reactive power coordinated voltage control of islanded microgrid by considering multiple controllable devices on the source-grid-load subsystems, which divides the whole optimization control process into long-time scale and short-time scale according to the different action speeds and limits of the controllable devices. In different time scales, different control objectives and control variables are optimized. For long-time scale, based on the WT power, PV power, and load demands day-ahead forecast data, the active and reactive power outputs of each DG, the gear of on-load tap changer (OLTC), and the number of capacitor banks (CB) are optimally solved to minimize the system network losses. For short-time scale, the results of the long-time scale optimization are used as the initial values, and the voltage/reactive power sensitivity model is used as the voltage prediction model, based on the real-time WT power, PV power, and load demand forecast values. By calculating the active and reactive power output increments of the micro gas turbine (MT) and ESSs, as well as the reactive increments of WT and PV stations, it aims to minimize the voltage deviation and fluctuation so that the islanded microgrid system can run in a safe and economical way.

The main contributions and salient features of this paper are as follows:

1. Considering the strong coupling characteristic of active and reactive power that caused by the high impedance ratio of islanded microgrid, also the uncertainty of renewable energy and load. A multi-time scale source-grid-load active-reactive coordinated voltage optimization control strategy is proposed, which expands the optimization space of the traditional active-reactive decoupling method. The proposed strategy also enhances the ability of the islanded microgrid to cope with the uncertainty through the collaborative regulation mechanism of controllable devices in different time scales.

2. Considering the requirements of real-time and robustness of the regulation method in short time scale optimization stage. A source-load collaboration mechanism based on Di-MPC was proposed. In the proposed mechanism, the coordination problem between the agents is reduced to a cooperative game where they have to choose one out of the three strategies, and only two rounds of information interactions are required to reach an agreement. Therefore, it has a good performance of real-time and robustness.

2 ACTIVE-REACTIVE POWER COORDINATED OPTIMAL CONTROL STRATEGY BASED ON DISTRIBUTED MODEL PREDICTIVE CONTROL

2.1 Collaborative Distributed Model Predictive Control Theory

MPC is a model-based finite-time domain closed-loop optimization control algorithm, which is a process control method with easy modeling, good applicability, and high robustness. Based on this feature, MPC is widely used in the field of optimal control of power systems as a control algorithm with both applicability and robustness, and its basic framework consists of three major parts: predictive model, cost function, and solving algorithm (Villalon et al., 2020; Hu et al., 2021). The first element of the control sequence is applied to the controlled object, and at the next sampling moment, the optimal control problem is reconstructed based on the system state and the new measurement values after the control execution in the previous moment, and the above process is repeated (Rawlings and Mayne, 2009).

Traditional CMPC has a simple structure, and it is easy to implement because only one centralized controller needs to be designed to control the whole interconnected system. However, on the one hand, with the increasing number of distributed devices in the interconnection system, the computation burden of the centralized controller increases significantly, which has a significant impact on performing the real-time online rolling optimization. On the other hand, it lacks robustness since when one of the subsystems fails and withdraws from the interconnection system, the CMPC needs to correct the model in time to avoid wrong control command, which will cause the crash of the system. The correction is very time-consuming and complicated. Considering the shortcomings of CMPC, this paper adopts the collaborative Di-MPC to solve the voltage optimization problem. Di-MPC firstly decomposes the interconnected system into several subsystems with coupling

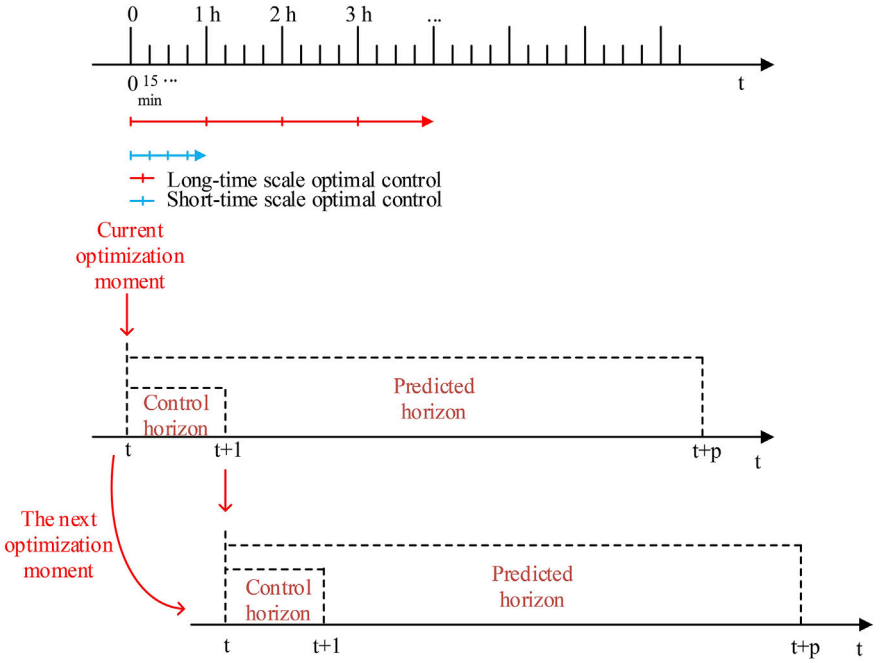

FIGURE 1 | Multi-time scale optimal control schematic.

relationships, and each subsystem can obtain the global information of the interconnected system through communication. Compared with CMPC, Di-MPC decouples a large online optimization problem and distributes them to each subsystem for a solution. Each sub-optimization problem is not only independent but also coupled, and each sub-optimization problem can be independently and parallelly solved, thus it greatly reducing the scale and complexity of solving the online optimization problems and improving the solution efficiency while ensuring the control performance (Le et al., 2020).

2.2 Multi-Time Scale Source-Grid-Load Active-Reactive Power Coordination and Optimal Control Strategy Based on Collaborative Distributed Model Predictive Control

In addition, the network-side devices have a slow response time when participating in the voltage regulation, so they should not be operated frequently. On the contrary, each DG in the source side is connected to the islanded microgrid through the inverter, and the fast response characteristics of the inverter itself enable the DGs to operate in a short time during the voltage regulation process. So the proposed collaborative Di-MPC carefully considers the operating characteristics of the above devices and comprehensively utilizes the regulatory potentials in the source-grid-load side. Based on the collaborative Di-MPC, a multi-time scale distributed voltage optimal control model is established in this paper proposes. The long-time scale optimal control model ensures the safety and the economic operation of the system, and the short-time scale optimal control further optimizes the voltage control effect. Thus each DG can ensure the economical and safe operation of the system while making full use to the voltage regulation capability of each controllable device in the source-grid-load side. The schematic diagram of the multi-time scale optimal control is shown in **Figure 1**.

3 MULTI-TIME SCALE OPTIMAL MODEL OF ACTIVE-REACTIVE POWER COORDINATED VOLTAGE OPTIMIZATION CONTROL

3.1 Long-Time Scale Optimal Control Model

The long-time scale optimal control model takes the active and reactive power outputs of ESS and MT, the reactive power outputs of WT and PV stations, as well as the gear of the OLTC and the number of the CB as control variables, and the predicted data of wind power, photovoltaic power and load demands as input variables. Then by using 1 h as the optimization time window to optimally solve the above control variables.

3.1.1 Optimization Objective

The optimization objective of the long-time scale optimal control is to ensure the economical operation of the islanded microgrid system and reduce the network losses, so the objective function is designed to minimize the system network losses, described as:

$$\min f_1 = \min \sum_{t=1}^{N_{C,1h}} \sum_{j=1}^{N} P_{j,t}^{loss} \tag{1}$$

where $N_{C,1h}$ is the optimization cycle of the long-time scale optimal control model; N is the total number of nodes; $P_{j,t}^{loss}$ is the active loss in node j at time t.

3.1.2 Constraints

1) Power flow constraints

The used LinDistflow model (Baran and Wu, 1989; Šulc et al., 2014) can linearize the original non-linear and non-convex power flow constraint, as well as the on-load tap changer constraint, which allows it to solve the original optimal control problem in a more efficient manner without affecting the precision, described as:

$$\begin{cases} \sum\limits_{k:\ (j,k)} P_{jk,t} = P_{ij,t} - p_{j,t} \\ \sum\limits_{k:\ (j,k)} Q_{jk,t} = Q_{ij,t} - q_{j,t} \\ V_{j,t} = V_1 - \sum\limits_{i\in[2,j]} \left(r_{ij}P_{ij,t} + x_{ij}Q_{ij,t}\right)\Big/V_1 \\ p_{j,t} = p_{j,t}^{c} - p_{j,t}^{g} \\ q_{j,t} = q_{j,t}^{c} - q_{j,t}^{g} \end{cases} \tag{2}$$

where k: (j,k) denotes the set of all line end nodes with node j as the start node; $P_{ij,t}, Q_{ij,t}$ are the active and reactive power flowing through branch ij at time t, respectively; $p_{j,t}, q_{j,t}$ are the active and reactive power injected in node j at time t, respectively; $p_{j,t}^{c}$, $q_{j,t}^{c}$ are the active and reactive power demanded in node j at time t, respectively; $p_{j,t}^{g}$, $q_{j,t}^{g}$ are the microsource active and reactive power outputs in node j at time t, respectively; $V_{j,t}$ is the voltage magnitude in node j at time t; r_{ij} and x_{ij} are the resistance and the reactance of branch ij, respectively; V_1 is the voltage reference values, $V_1 = 1.0p.u.$

2) Voltage constraints

$$V_j^{\min} \le V_{j,t} \le V_j^{\max} \tag{3}$$

where $V_j^{\min}$, $V_j^{\max}$ are the lower and upper limits of the voltage amplitude in node j, respectively.

3) DGs and other devices operating constraints

1) WT operation constraints

$$\begin{cases} P_{j,t}^{WT} = P_{j,t}^{WT\mathrm{pre}} \\ \left(P_{j,t}^{WT}\right)^2 + \left(Q_{j,t}^{WT}\right)^2 \le \left(S_j^{WT\max}\right)^2 \end{cases} \tag{4}$$

where $P_{j,t}^{WT}$, $Q_{j,t}^{WT}$ are the active and reactive power outputs of the WT in node j at time t, respectively; $S_j^{WT\max}$ is the inverter capacity of the WT in node j; $P_{j,t}^{WTpre}$ is the predicted active power outputs of the WT in node j at time t.

2) PV stations operation constraints

$$\begin{cases} P_{j,t}^{PV} = P_{j,t}^{PVpre} \\ \left(P_{j,t}^{PV}\right)^2 + \left(Q_{j,t}^{PV}\right)^2 \le \left(S_j^{PV\max}\right)^2 \end{cases} \tag{5}$$

where $P_{j,t}^{PV}$, $Q_{j,t}^{PV}$ are the active and reactive power outputs of the PV station in node j at time t, respectively; $S_j^{PV\max}$ is the inverter capacity of the PV station in node j; $P_{j,t}^{PVpre}$ is the predicted active power outputs of the PV station in node j at time t.

3) MT operation constraints

$$\begin{cases} \left(P_{j,t}^{MT}\right)^2 + \left(Q_{j,t}^{MT}\right)^2 \le \left(S_j^{MT\max}\right)^2 \\ 0 \le P_{j,t}^{MT} \le P_j^{MT\max} \\ P_{j,t}^{MT} - P_{j,t-1}^{MT} \le \delta_j^{MT\ up} \\ P_{j,t-1}^{MT} - P_{j,t}^{MT} \le \delta_j^{MT\ down} \end{cases} \tag{6}$$

where $P_{j,t}^{MT}$, $Q_{j,t}^{MT}$ are the active and reactive power outputs of the MT in node j at time t, respectively; $S_j^{MT\max}$ is the capacity of the MT in node j; $P_j^{MT\max}$ is the maximum active power outputs of the MT in node j; $\delta_j^{MT\ up}$, $\delta_j^{MT\ down}$ are the upper and lower limits of the ramping rate of the MT, respectively.

4) ESS operation constraints

$$\begin{cases} 0 \le P_{j,t}^{ESScha} \le \delta_{cha,t}^{ESS} P_{cha\max}^{ESS} \\ 0 \le P_{j,t}^{ESSdis} \le \delta_{dis,t}^{ESS} P_{dis\max}^{ESS} \\ \delta_{cha,t}^{ESS} + \delta_{dis,t}^{ESS} \le 1 \\ \left(P_{j,t}^{ESScha}\right)^2 + \left(Q_{j,t}^{ESS}\right)^2 \leqslant \left(S_j^{ESS\max}\right)^2 \\ \left(P_{j,t}^{ESSdis}\right)^2 + \left(Q_{j,t}^{ESS}\right)^2 \leqslant \left(S_j^{ESS\max}\right)^2 \end{cases} \tag{7}$$

$$\begin{cases} E_{soc,t} = E_{soc,t-1} + \eta_{cha} P_{j,t}^{ESScha} \Delta t/E \\ \qquad - \dfrac{P_{j,t}^{ESSdis}}{\eta_{dis} E} \Delta t \\ \qquad E_{soc\min} \le E_{soc,t} \le E_{soc\max} \end{cases} \tag{8}$$

where $P_{j,t}^{ESScha}$ is the charging power of the ESS in node j at time t; $P_{j,t}^{ESSdis}$ is the discharging power of the ESS in node j at time t; $\delta_{cha,t}^{ESS}$, $\delta_{dis,t}^{ESS}$ are the charging and discharging status flags of the ESS at time t, respectively, and are 0–1 variables; P_{chamax}^{ESS}, P_{dismax}^{ESS} are the maximum charging and discharging power of the ESS, respectively; $Q_{j,t}^{ESS}$ is the reactive power outputs of the ESS in node j at time t; $S_j^{ESS\max}$ is the inverter capacity of ESS in node j; $E_{soc,t}$ is the stored power of the ESS at time t; η_{cha}, η_{dis} are the charging and the discharging efficiencies of the ESS, respectively; $E_{soc\max}$, $E_{soc\min}$ are the upper and lower limits of stored power of the ESS, respectively; Δt is the amount of change in time. E is the battery capacity of the ESS.

5) OLTC operation constraints

$$\begin{cases} k_{ij,t} = k_{ij,0} + T_{ij,t}\Delta k_{ij} \\ T_{ij}^{\min} \le T_{ij,t} \le T_{ij}^{\max} \\ \left|T_{ij,t} - T_{ij,t-1}\right| \le T_{ij}^{ones\max} \end{cases} \tag{9}$$

where $k_{ij,t}$ is the ratio of the OLTC at branch ij at time t; Δk_{ij} is the adjustment step length of the OLTC ratio; $k_{ij,0}$ is the initial value of the OLTC ratio at branch ij; $T_{ij,t}$ is the OLTC step at branch ij at time t; $T_{ij}^{\max}$, $T_{ij}^{\min}$ are the upper and lower limits of the adjustable step of the OLTC at branch ij, respectively; $T_{ij}^{ones\max}$ is the limit value of the single adjustment step of the OLTC.

For the branch containing the OLTC, the voltage constraint is modified as

$$V_{j,t} = k_{ij,t}V_1 - \left(r_{ij}P_{ij,t} + x_{ij}Q_{ij,t}\right)/V_1 \tag{10}$$

6) CB operation constraints

$$\begin{cases} Q_{j,t} = m_{j,t}\Delta Q_j \\ m_j^{\min} \le m_{j,t} \le m_j^{\max}, m_{j,t} \in Z \\ \left|m_{j,t} - m_{j,t-1}\right| \le M_j^{ones\max} \end{cases} \tag{11}$$

where $Q_{j,t}$ is the amount of reactive power compensation of the CB in node j at time t; ΔQ_j is the amount of reactive power compensation of a single group of the CB; $m_{j,t}$ is the number of groups of CB being put into operation or removed in node j at time t; $m_j^{\max}$, $m_j^{\min}$ are the upper and lower limits of the number of groups that can be put into operation or removed of the CB, respectively; $M_j^{ones\max}$ is the limit value of the number of groups that can be put into operation or removed in a single adjustment of the CB group.

3.2 Short-Time Scale Optimal Control Model

The short-time scale optimal control model takes the active and reactive power output increments of MT and ESS, the reactive power output increments of WT and PV station as the control variables. It also takes the power outputs and actions of each DG and controllable device, and the voltage of each node solved by the long-time scale optimal control as the input variables. Then by using 15 min as the optimization time window in this stage to optimally solve the above control variables.

3.2.1 Optimization Objective

The optimization objective of the short-time scale optimal control aims at further reducing the voltage fluctuations based on the long-time scale optimal control regulation, which are due to the fluctuations of the wind power, photovoltaic power, and load demands. The optimization objective function is described as:

$$\begin{cases} \min f_3 = \min \sum_{t=1}^{N_{C,15\min}} \sum_{j=1}^{N} \left|V_{j,t}^{pre} - \Delta V_{j,t} - V_{j,t}^{ref}\right| \\ \min f_4 = \min \sum_{t=1}^{N_{C,15\min}} \sum_{j=1}^{N} \left|V_{j,t}^{pre} - \Delta V_{j,t} - V_{j,t-1}\right| \end{cases} \tag{12}$$

where $N_{C,15\min}$ is the optimization cycle of the short-time scale optimal control; $V_{j,t}^{pre}$ is the predicted voltage value in node j at time t, which is calculated based on the steady-state node voltage and voltage/power sensitivity solved on a long-time scale; $\Delta V_{j,t}$ is the voltage variation in node j at time t due to the variation of the injected active-reactive power; $V_{j,t}^{ref}$ is the reference voltage in node j at time t obtained after the optimal control calculation on the long-time scale; $V_{j,t-1}$ is the actual voltage value in node j at time t-1.

3.2.2 Constraints

The constraints in short-time scale contain the operation constraints of DGs and ESS as shown in **Eq. 13**, **Eq. 14**, respectively.

$$\begin{cases} \left(P_{j,t}^{WT}\right)^2 + \left(Q_{T1j,t}^{WT} + \Delta Q_{j,t}^{WT}\right)^2 \le \left(S_j^{WT\max}\right)^2 \\ P_{j,t}^{WT} = P_{j,t}^{WTpre} \\ \left(P_{j,t}^{PV}\right)^2 + \left(Q_{T1,j,t}^{PV} + \Delta Q_{j,t}^{PV}\right)^2 \le \left(S_j^{PV\max}\right)^2 \\ P_{j,t}^{PV} = P_{j,t}^{PVpre} \\ \left(P_{T1j,t}^{MT} + \Delta P_{j,t}^{MT}\right)^2 + \left(Q_{T1j,t}^{MT} + \Delta Q_{j,t}^{MT}\right)^2 \le \left(S_j^{MT\max}\right)^2 \\ 0 \le P_{T1j,t}^{MT} + \Delta P_{j,t}^{MT} \le P_j^{MT\max} \\ \left(P_{T1j,t}^{MT} + \Delta P_{j,t}^{MT}\right) - \left(P_{T1j,t-1}^{MT} + \Delta P_{j,-1}^{MT}\right) \le \delta_j^{MTup} \\ \left(P_{T1j,t-1}^{MT} + \Delta P_{j,t}^{MT}\right) - \left(P_{T1j,t}^{MT} + \Delta P_{j,-1}^{MT}\right) \le \delta_j^{MTdown} \end{cases} \tag{13}$$

$$\begin{cases} 0 \le P_{T1j,t}^{ESScha} + \Delta P_{j,t}^{ESScha} \le \delta_{cha,t}^{ESS} P_{cha,\max}^{ESS} \\ 0 \le P_{j,t}^{ESSdis} + \Delta P_{j,t}^{ESSdis} \le \delta_{dis,t}^{ESS} P_{dis,\max}^{ESS} \\ \delta_{cha,t}^{ESS} + \delta_{dis,t}^{ESS} \le 1 \\ \left(P_{T1j,t}^{ESScha} + \Delta P_{j,t}^{ESScha}\right)^2 + \left(Q_{T1j,t}^{ESS} + \Delta Q_{j,t}^{ESS}\right)^2 \le \left(S_j^{ESS\max}\right)^2 \\ \left(P_{T1j,t}^{ESSdis} + \Delta P_{j,t}^{ESSdis}\right)^2 + \left(Q_{T1j,t}^{ESS} + \Delta Q_{j,t}^{ESS}\right)^2 \le \left(S_j^{ESS\max}\right)^2 \\ E_{soc,t} = E_{soc,t-1} + \eta_{cha}\left(P_{T1j,t}^{ESScha} + \Delta P_{j,t}^{ESScha}\right)\Delta t/E - \dfrac{P_{T1j,t}^{ESSdis} + \Delta P_{j,t}^{ESSdis}}{\eta_{dis}E}\Delta t \\ E_{soc\min} \le E_{soc,t} \le E_{soc\max} \end{cases} \tag{14}$$

where $Q_{T1j,t}^{WT}$, $Q_{T1,j,t}^{PV}$ are the long-time scale reactive power output results of the WT and PV station in node j at time t, respectively; $\Delta Q_{j,t}^{WT}$, $\Delta Q_{j,t}^{PV}$ are the reactive power output increments of WT and PV station in short-time scale optimal control in node j at time t, respectively; $P_{T1j,t}^{MT}$ is the long-time scale active power output results of MT in node j at time t; $\Delta P_{j,t}^{MT}$ is the active power output increments of MT in node j at time t; $Q_{T1j,t}^{MT}$ is the long-time scale reactive power output results of MT in node j at time t; $\Delta Q_{j,t}^{MT}$ is the reactive power output increments of MT in node j at time t; $P_{T1j,t}^{ESScha}$, $P_{T1j,t}^{ESSdis}$ are the long-time scale charging and discharging power results of the ESS in node j at time t, respectively; $\Delta P_{j,t}^{ESScha}$, $\Delta P_{j,t}^{ESSdis}$ are the charging and discharging power of the ESS in node j at time t, respectively; $Q_{T1j,t}^{ESS}$ is the long-time scale reactive power output results of the ESS in node j at time t; $\Delta Q_{j,t}^{ESS}$ is the reactive power output increments of the ESS in node j at time t.

3.2.3 Voltage Prediction Model Based on Voltage/Power Sensitivity

Islanded microgrids are mainly powered by renewable energy sources such as wind power and photovoltaic power, which are subjected to environmental uncertainties. Combined with the characteristics of the islanded microgrid transmission lines, the voltage of each node will be affected when the output of WT and PV stations fluctuates due to environmental impacts. In order to control the DGs in time to achieve the purpose of voltage regulation, it is necessary to predict the node voltage fluctuations caused by the fluctuation of wind power, photovoltaic power, and load demands. Then reasonably arrange the power outputs of each DG to reduce the voltage deviation and

fluctuation. In this paper, from the perspective of active-reactive power coordination control, in order to regulate the system voltage, the active and reactive power outputs of DGs inside the islanded microgrid is regulated under different stages. Based on the conventional AC power flow equation, the non-linear power flow is linearized at the steady-state solution of the power flow, and the following matrix can be obtained (Wang et al., 2005):

$$\begin{bmatrix} \Delta P \\ \Delta Q \end{bmatrix} = \begin{bmatrix} \frac{\partial P}{\partial \theta} & \frac{\partial P}{\partial V} \\ \frac{\partial Q}{\partial \theta} & \frac{\partial Q}{\partial V} \end{bmatrix} \begin{bmatrix} \Delta \theta \\ \Delta V \end{bmatrix} = J \begin{bmatrix} \Delta \theta \\ \Delta V \end{bmatrix} \tag{15}$$

where ΔP, ΔQ are the node active and reactive power injection variation matrix, respectively; $\Delta\theta$ is the node voltage phase angle variation matrix; ΔV is the node voltage magnitude variation matrix; J is the Jacobi matrix.

The inverse of this matrix expression yields:

$$\begin{aligned} \begin{bmatrix} \Delta \theta \\ \Delta V \end{bmatrix} &= J^{-1} \begin{bmatrix} \Delta P \\ \Delta Q \end{bmatrix} = S \begin{bmatrix} \Delta P \\ \Delta Q \end{bmatrix} \\ &= \begin{bmatrix} S_{P\theta} & S_{Q\theta} \\ S_{PV} & S_{QV} \end{bmatrix} \begin{bmatrix} \Delta P \\ \Delta Q \end{bmatrix} \end{aligned} \tag{16}$$

where S_{PV}, S_{QV} are the voltage-active and voltage-reactive sensitivity factors, respectively, indicating the degree of voltage variation at each node when the node is injected with unit active and reactive power; $S_{P\theta}$, $S_{Q\theta}$ are the phase-angle-active and phase-angle-reactive sensitivity factors, respectively, indicating the degree of voltage phase angle change at each node when the node is injected with unit active power and reactive power. Based on these matrixes, the relationship between the voltage variation at each node and the matrix of the change in active and reactive power injected into the node can be expressed by the following equation:

$$\Delta V = S_{PV} \Delta P + S_{QV} \Delta Q \tag{17}$$

Then the voltage in node j at time t can be expressed as

$$V_{j,t}^{pre} = V_{j,t}^{0} + \sum_{j=1}^{N} S_{PV} \Delta P_{j,t} + \sum_{j=1}^{N} S_{QV} \Delta Q_{j,t} \tag{18}$$

Equation 18 will be used as the predictive model in the short-time scale optimal control process, which can forecast the node voltage under fluctuating wind power and photovoltaic output as well as load demand.

4 ACTIVE-REACTIVE POWER COORDINATED VOLTAGE OPTIMIZATION CONTROL BASED ON COLLABORATIVE DISTRIBUTED MODEL PREDICTIVE CONTROL

4.1 Problem Description of The Optimal Control Model

The islanded microgrid source-grid-load active-reactive power coordinated voltage optimization control problem studied in this paper contains continuous control variables, which are the power output of DGs and ESS. The problem also contains discrete control variables, which are the gear of OLTC, the switching group of CB, and the charging and discharging states flags of ESS. All the above variables form a multi-variable mixed integer programming problem with multiple constraints. According to the operating characteristic of the devices placed in the source, network, and load side, the problem is divided into long-time scale and short-time scale and solved.

4.2 Collaborative Control Mechanism

4.2.1 Long-Time Scale Optimal Control

The main optimization objectives in the long-time scale optimal control is to minimize the active network losses of the day-ahead islanded microgrid system, ensure the safety and economic operation of the islanded microgrid, and provide the initial reference voltage and the initial values of the active and reactive power outputs of each DG for the intra-day rolling voltage optimization. Among them, ESS is considered as the load-side device in this paper due to its charging and discharging power characteristics. The main control member in the long-time scale optimal control are WT, PV stations, and MT, which are considered as source-side devices. The on-load tap changer and capacitor banks are as considered as network-side devices.

4.2.2 Short-Time Scale Optimal Control

In the short-time scale optimal control, since it is not suitable for network-side devices such as OLTC and CB to operate in a short time period, only the source-side and load-side devices are optimized and controlled. The source-side devices and load-side devices of the islanded microgrid system are regarded as two interconnected subsystems, and corresponding agents under the structure of DI-MPC are set in each subsystem to carry out the coordinated control of active and reactive power. After receiving the optimization results of the long-time optimal control, the first communication between the agents of each subsystem is carried out. The source and load-side agents calculate their own selfish solutions and altruistic solutions through information interaction and then carry out the second communication. Each agent generates a 3 × 3 strategy table according to the obtained conservative solutions, selfish solutions, and altruistic solutions. Since both agents contain the same information of the system at this time, both agents finally choose the same control strategy in the strategy table that makes the global objective function optimal.

To better describe the proposed mechanism, the following definitions are introduced (Maestre et al., 2011):

U_i: is the input sequence of agent i at future moments, and the elements in the sequence represent the decision variables in the online optimization problem solved by each agent.

$$U_A = \begin{bmatrix} u_{A,1} \\ u_{A,2} \\ \vdots \\ u_{A,N_P} \end{bmatrix}, U_B = \begin{bmatrix} u_{B,1} \\ u_{B,2} \\ \vdots \\ u_{B,N_P} \end{bmatrix} \tag{19}$$

J_i: is the global objective function.

$U_i^d(t)$: is the optimal input sequence for agent i at time t. The defined equation is as follows:

$$U_A^d(t) = \begin{bmatrix} u_{A,1}^d \\ u_{A,2}^d \\ \vdots \\ u_{A,N_P}^d \end{bmatrix}, U_B^d(t) = \begin{bmatrix} u_{B,1}^d \\ u_{B,2}^d \\ \vdots \\ u_{B,N_P}^d \end{bmatrix} \tag{20}$$

$U_i^S(t)$: is the conservative solution sequence of agent i at time t, and is the remaining sequence of the optimal control sequence excluding the first element at time t-1

$$U_A^S(t) = \begin{bmatrix} u_{A,2}^d \\ \vdots \\ u_{A,N_p-1}^d \\ u_{A,N_p}^d \end{bmatrix}, U_B^S(t) = \begin{bmatrix} u_{B,2}^d \\ \vdots \\ u_{B,N_p-1}^d \\ u_{B,N_p}^d \end{bmatrix} \tag{21}$$

$U_i^*(t)$: is the sequence of selfish solutions for agent i at time t. It is the sequence of solutions obtained by solving the following problem under the assumption that the neighboring agents use the conservative solution control sequence.

$$\begin{cases} U_A^*(t) = \arg\min_{U_A} J_{A^*}\left(x_A(t), U_A, U_B^s(t)\right) \\ U_B^*(t) = \arg\min_{U_B} J_{B^*}\left(x_B(t), U_B, U_A^s(t)\right) \end{cases} \tag{22}$$

$U_i^\omega(t)$: is the sequence of altruistic solutions for agent i at time t. It is the sequence of solutions obtained by solving the following problem under the assumption that the local agent uses a selfish solution sequence.

$$\begin{cases} U_{B|A^*}^\omega(t) = \arg\min_{U_B} J_{A^\omega}\left(x_A(t), U_A^*(t), U_B\right) \\ U_{A|B^*}^\omega(t) = \arg\min_{U_A} J_{B^\omega}\left(x_B(t), U_B^*(t), U_A\right) \end{cases} \tag{23}$$

To discuss the designed inter-agent collaboration mechanism in terms of the game theory. At each time step of the collaborative Di-MPC, both source and load agents can be regarded as participating in a mutual cooperation game, each subsystem agent interacts with each other in two rounds of computation, the source agent sends the selfish solution $U_A^*(t)$, the altruistic solution $U_{A|B^*}^\omega(t)$ to the load agent and receives the selfish solution $U_B^*(t)$ and the altruistic solution $U_{B|A^*}^\omega(t)$ from the load agent, then both the source and load agents contain three different control sequences:

$$\begin{aligned} U_A &= \left\{U_A^S(t), U_A^*(t), U_{A|B^*}^\omega(t)\right\} \\ U_B &= \left\{U_B^S(t), U_B^*(t), U_{B|A^*}^\omega(t)\right\} \end{aligned} \tag{24}$$

The cooperative game can be represented by a 3 × 3 strategy table. Each row of the table represents one of the three possible strategies of the source agent, and each column represents one of the three possible strategies of the load agent, and each cell contains the sum of the respective objective functions of each agent for the specified future input control sequence. That is, at each time step, each agent selects the control sequence combination that minimizes the sum of the objective functions. Because both agents share the same information with each other, in the end, they will choose the same combination of control sequences, and this combination of control sequences is the optimal strategy at the current moment. The 3 × 3 strategy table is shown in **Table 1**.

TABLE 1 | Objective function-based strategy table.

Variables	U_B^s	U_B^*	U_{B/A^*}^W
U_A^s	J_1	J_2	J_3
U_A^*	J_4	J_5	J_6
U_{A/B^*}^W	J_7	J_8	J_9

The nine strategies in the table are expanded and as shown in the following equation

$$\begin{cases} J_1 = J_A\left(x_A(t), U_A^s, U_B^s\right) + J_B\left(x_B(t), U_B^s, U_A^s\right) \\ J_2 = J_A\left(x_A(t), U_A^s, U_B^*\right) + J_B\left(x_B(t), U_B^*, U_A^s\right) \\ J_3 = J_A\left(x_A(t), U_A^S, U_{B/A^*}^W\right) + J_B\left(x_B(t), U_{B/A^*}^W, U_A^S\right) \\ J_4 = J_A\left(x_A(t), U_A^*, U_B^s\right) + J_B\left(x_B(t), U_B^s, U_A^*\right) \\ J_5 = J_A\left(x_A(t), U_A^*, U_B^*\right) + J_B\left(x_B(t), U_B^*, U_A^*\right) \\ J_6 = J_A\left(x_A(t), U_A^*, U_{B/A^*}^W\right) + J_B\left(x_B(t), U_{B/A^*}^W, U_A^*\right) \\ J_7 = J_A\left(x_A(t), U_{A/B^*}^W, U_B^s\right) + J_B\left(x_B(t), U_B^s, U_{A/B^*}^W\right) \\ J_8 = J_A\left(x_A(t), U_{A/B^*}^W, U_B^*\right) + J_B\left(x_B(t), U_B^*, U_{A/B^*}^W\right) \\ J_9 = J_A\left(x_A(t), U_{A/B^*}^W, U_{B/A^*}^W\right) + J_B\left(x_B(t), U_{B/A^*}^W, U_{A/B^*}^W\right) \end{cases} \tag{25}$$

The algorithm flowchart of the collaborative Di-MPC-based islanded microgrid source-grid-load active-reactive power coordinated voltage optimization control strategy is shown in **Figure 2**. T1, T2 are the optimal time cycles of long-time scale optimal control and short-time scale optimal control, respectively.

5 CASE RESULTS AND DISCUSSION

5.1 Parameter Setting

In this paper, we adopt the adapted IEEE 33-BUS system, which is used for simulation analysis and as shown in **Figure 3**. The reference value of the microgrid is set to: S_B = 1 MVA, U_B = 12.66 kV, and the access location of each DG and other controllable devices are shown in **Table 2**. More simulation parameters can be seen in **Table 3**. The day-ahead forecast and real-time active power outputs of PV stations and WT are given in **Figure 4**, and the day-ahead and ultra-short-term active/reactive load demands forecast are given in **Figure 5**. The case study in this paper is based on a computer with a central processing unit of Intel(R) Core (TM) i7-9700 @ 3.00 GHz and 16 GB of RAM, modelled with MATLAB software and YALMIP toolbox, and the CPLEX optimization solver is used to solve the optimization model.

In order to verify the effectiveness of the proposed strategy, two other active-reactive coordinated voltage optimization strategies are compared to solve the same study case.

Strategy 1: Single-time scale conventional optimal control.

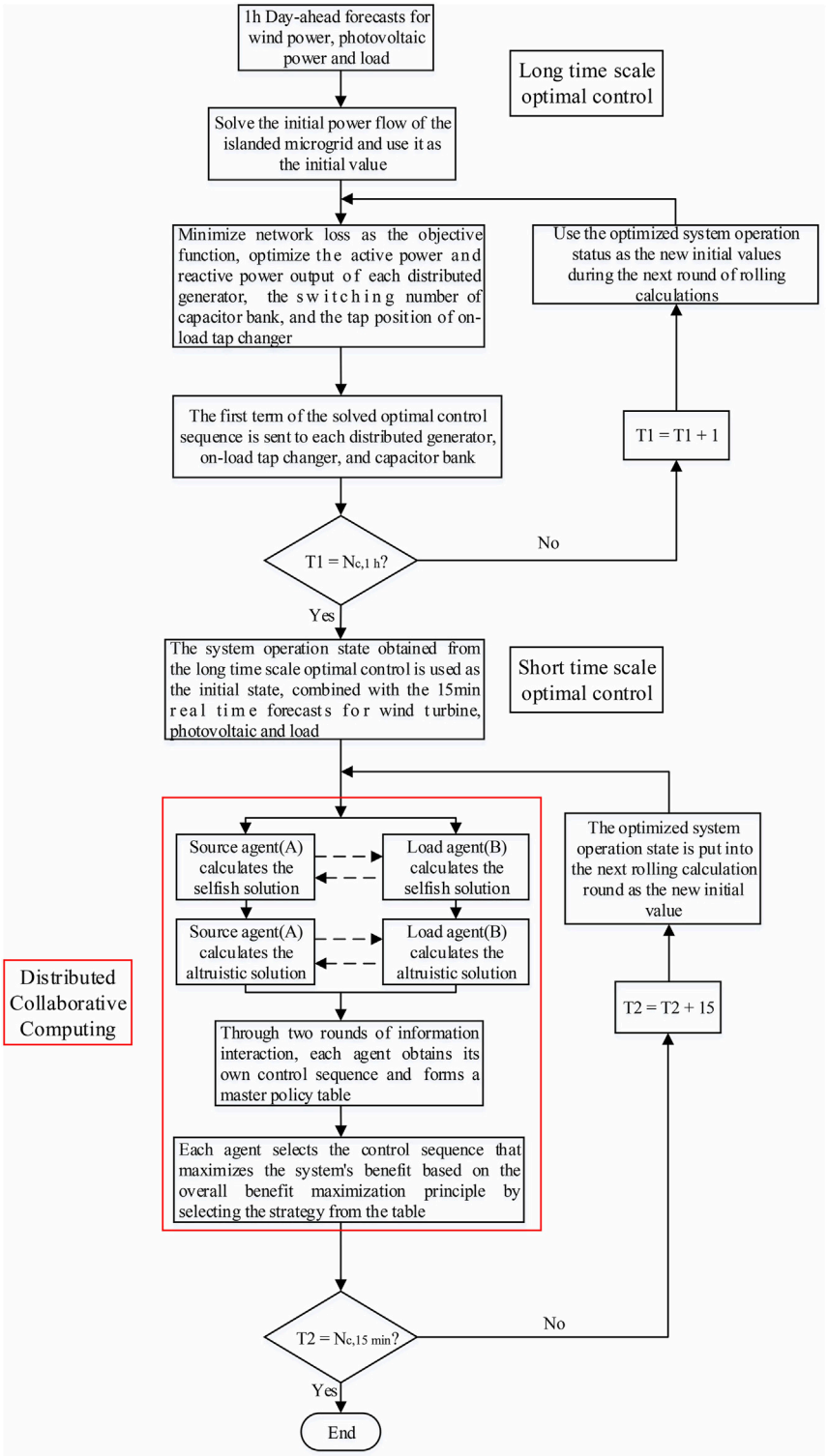

FIGURE 2 | Algorithm flowchart of the collaborative Di-MPC for islanded microgrid source-grid-load active-reactive power coordinated voltage optimization control strategy.

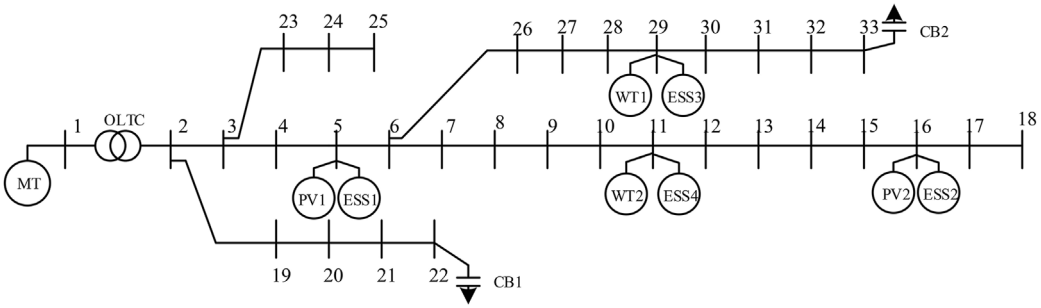

FIGURE 3 | Adapted IEEE 33-BUS system.

TABLE 2 | Place location of DGs and other devices.

Device	Node	Device	Node
MT	1	OLTC	Between 1 and 2
PV	5, 16	CB	22, 33
WT	11, 29	ESS	5, 11, 16, 29

With the objectives of minimizing the active network losses, as well as the total voltage deviation of each node and the minimum voltage fluctuation in adjacent time periods, a traditional optimal control strategy with a single-time scale is used to optimally control all the devices involved in the voltage regulation within the islanded microgrid.

Strategy2: Multi-time scale CMPC.

With the objective of minimizing active network losses, the OLTC and CB switching schedule (24×1 h) and the active and reactive power outputs of DG are uniformly optimized before the day. During the day, the active and reactive power output increments of each DG are optimized on a rolling basis (96 × 15 min) using CMPC with the objective of minimizing the total voltage deviation of each node, as well as the

TABLE 3 | Simulation parameters.

Variables	Parameter value	Variables	Parameter value	Variables	Parameter value	Variables	Parameter value
$S_j^{WT\,max}$	0.5 MVA	P_{chamax}^{ESS}	0.05 MW	$E_{soc\,max}$	0.9	$T_{ij}^{ones\,max}$	1
$S_j^{PV\,max}$	0.2 MVA	P_{dismax}^{ESS}	0.05 MW	$E_{soc\,min}$	0.4	ΔQ_j	0.005 Mvar
$P_j^{MT\,max}$	0.3 MW	$S_j^{ESS\,max}$	0.1 MVA	$k_{ij,0}$	1	m_j^{max}	6
$S_j^{MT\,max}$	0.45 MVA	E	0.3 MWh	Δk_{ij}	0.0025 p.u.	m_j^{min}	0
$\delta_j^{MT\,up}$	0.03 MW/min	η_{cha}	0.9	T_{ij}^{max}	20	$M_j^{ones\,max}$	1
$\delta_j^{MT\,down}$	0.03 MW/min	η_{dis}	0.8	T_{ij}^{min}	−20	—	—

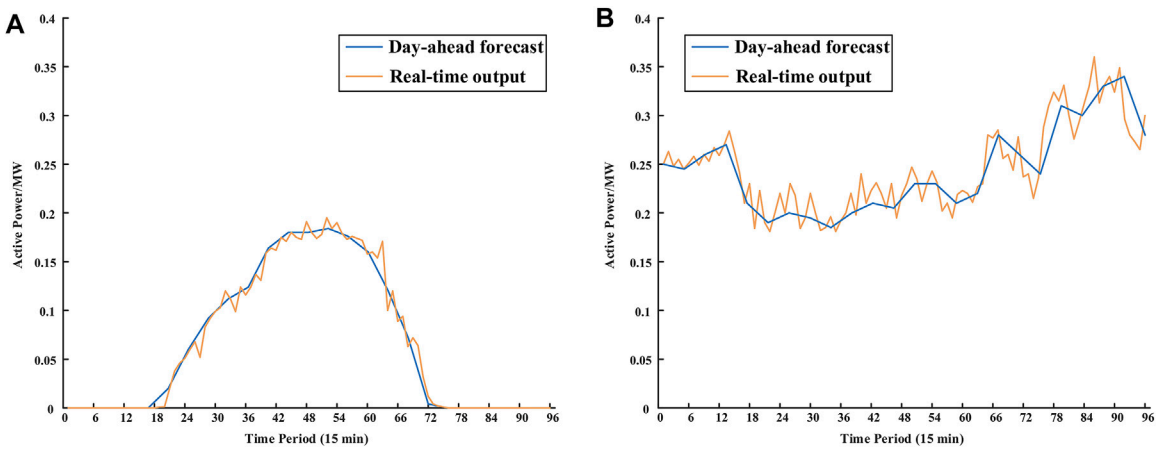

FIGURE 4 | (A) Day-ahead forecast and real-time active power outputs of PV stations. **(B)** Day-ahead forecast and real-time active power outputs of WT.

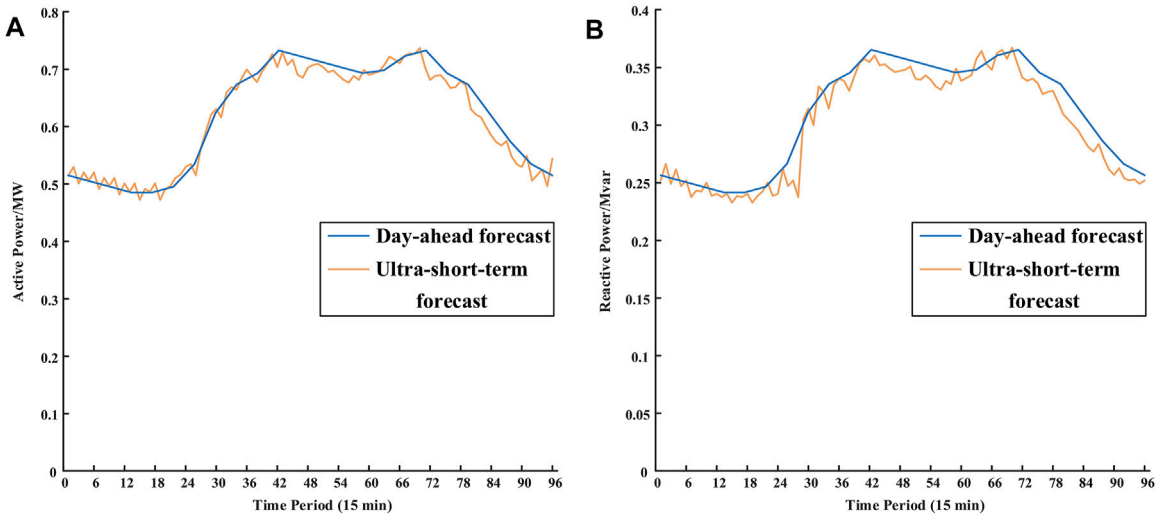

FIGURE 5 | (A) Day-ahead and ultra-short-term active load damands forecast. **(B)** Day-ahead and ultra-short-term reactive demands load forecast.

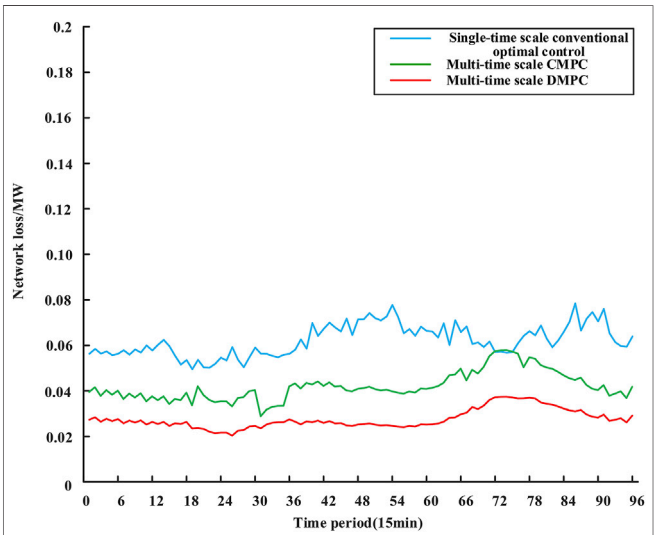

FIGURE 6 | System network losses under three different strategies.

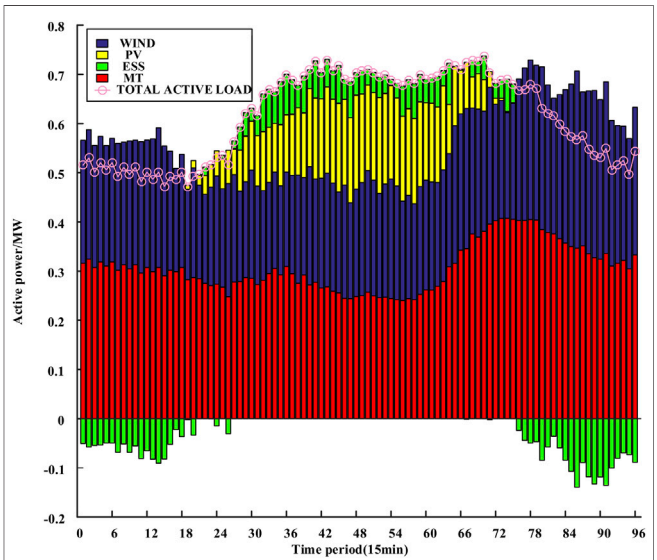

FIGURE 7 | DGs active power output results in the islanded microgrid.

voltage fluctuation in adjacent time periods (Liu et al., 2016). All the control instructions are performed through one centralized controller in this strategy.

Strategy 3: Multi-time scale collaborative Di-MPC.

With the objective of minimizing active network losses, the OLTC and CB switching schedule (24×1 h) and the active and reactive power outputs of DG are uniformly optimized before the day. During the day, the active and reactive power output increments of each DG are optimized on a rolling basis (96 × 15 min) using collaborative Di-MPC with the objective of minimizing the total voltage deviation of each node, as well as the voltage fluctuation in adjacent time periods. The final control instruction is generated and performed after the interaction between the two agents is complete.

5.2 Optimal Control Results Under Normal System State

1) Network losses result analysis

The system network losses result after applying three different optimal control strategies is shown in **Figure 6**. It can be seen that the network losses change under the multi-time scale optimal control strategy and all have the same trend. When the PV power decreases and the load demands increase in the evening hours, the network losses increase. Then by adjusting the DGs in the system, their output increases, and the network losses decrease. Through the vertical comparison, the proposed strategy can significantly reduce the network losses, and the maximum

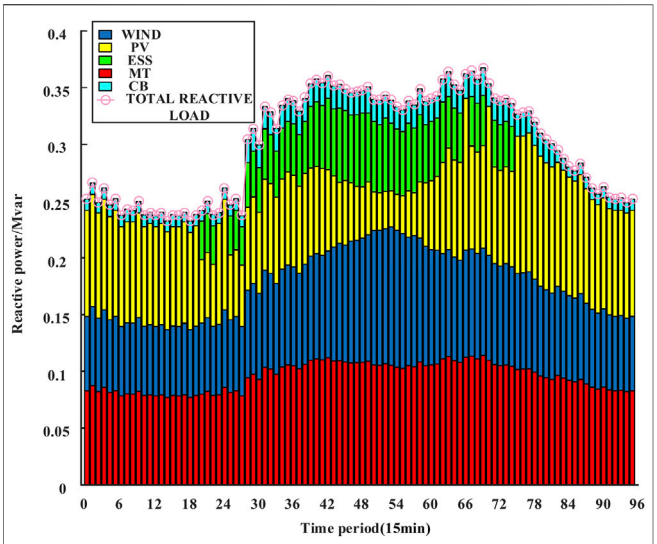

FIGURE 8 | DGs reactive power output results in the islanded microgrid.

intra-day reduction is 65.38% compared with the conventional optimal control method, which can ensure the safe and cost-effective operation of the islanded microgrid system.

2) DGs output results analysis

The active power outputs of each DG in the islanded microgrid are shown in **Figure 7**. From the figure, we can see that wind power and PV power undertake the majority of the active load demands, which significantly reduce the phenomenon of wind and light abandonment and improves the effective utilization rate of DGs. The surplus power that occurs is stored by ESS. **Figure 8** shows the reactive power outputs of each DG and CB. The results demonstrate that, although the frequency and amplitude fluctuations of each DG are large, the total reactive power outputs still match the trend of reactive load demands. The reactive power regulation limit of each DG depends on its active power outputs and rated capacity. The anti-peak regulation characteristic of WT is conducive to the expansion of its reactive power regulation space during the daytime, so that PV has sufficient reactive power margin when it is not generating

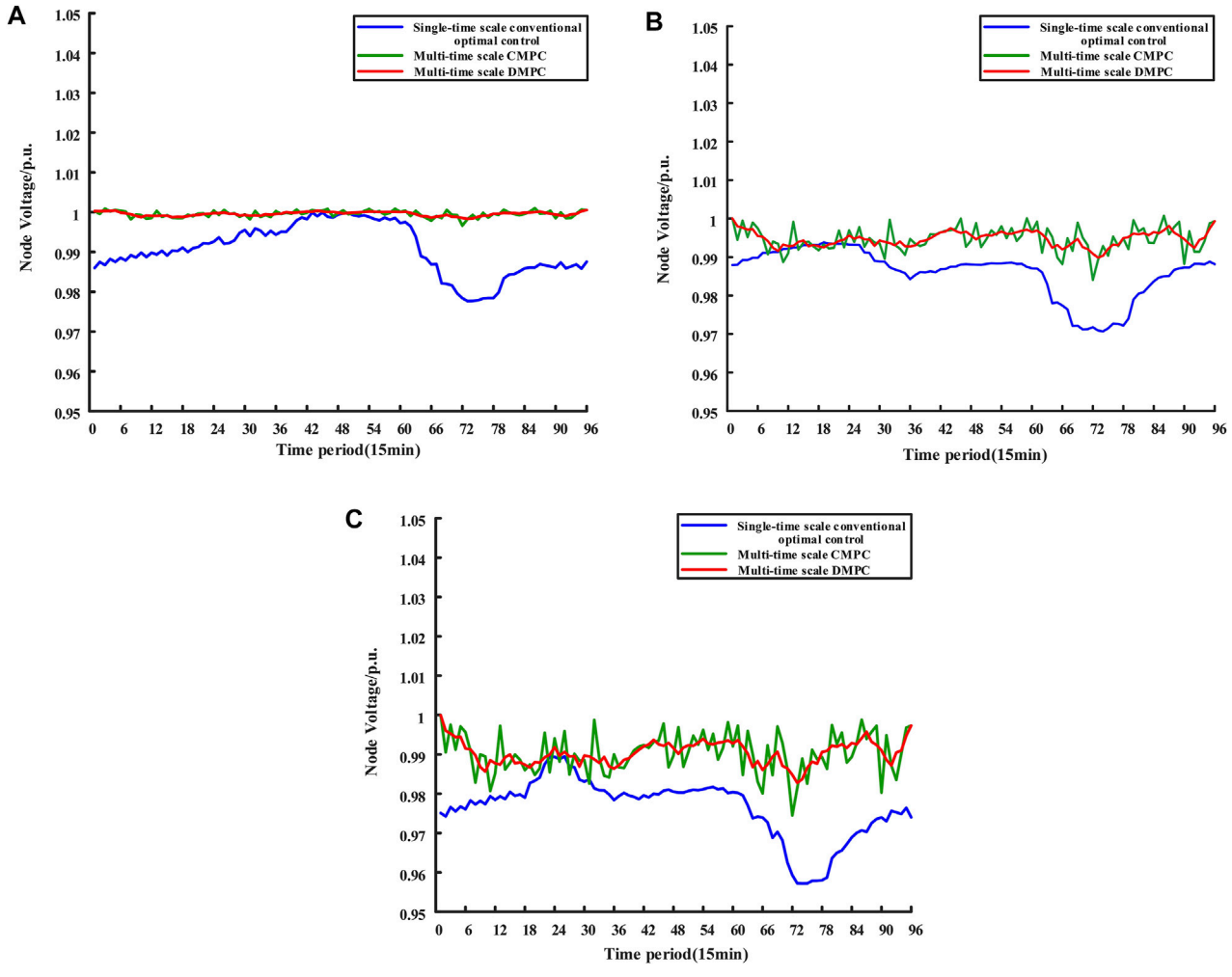

FIGURE 9 | (A) Voltage control result of node 5. **(B)** Voltage control result of node 11. **(C)** Voltage control result of node 18.

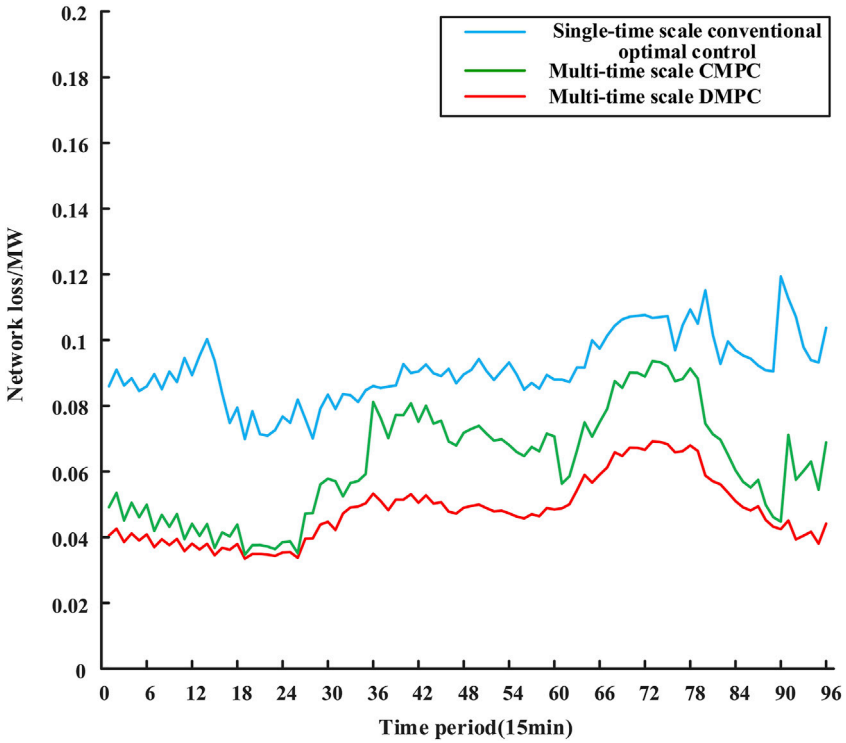

FIGURE 10 | System network losses under three different strategies.

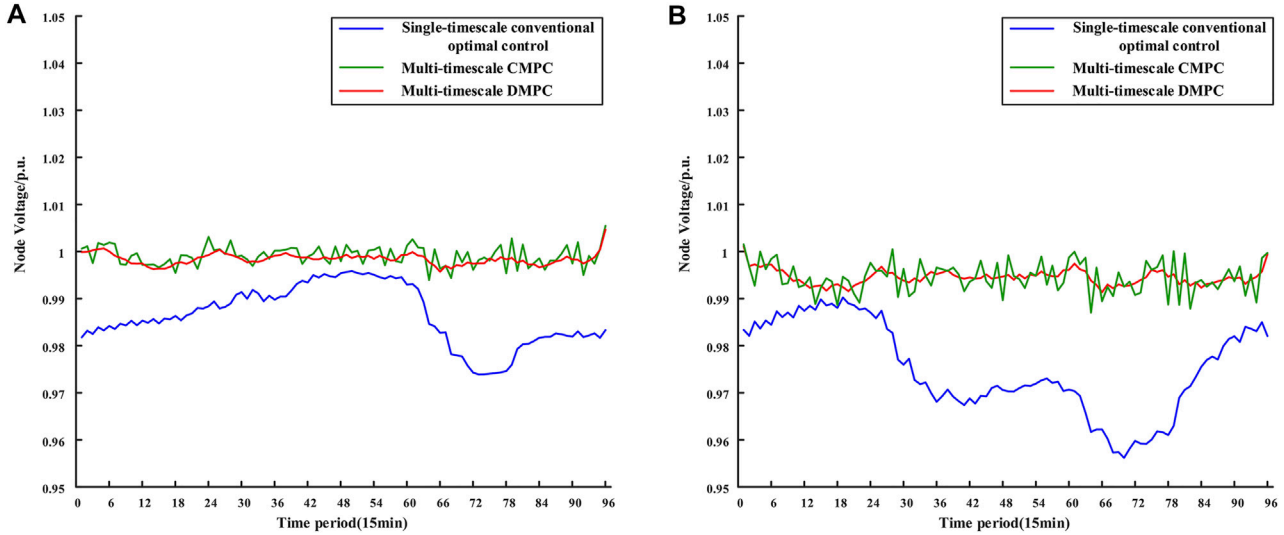

FIGURE 11 | (A) Voltage control result of node 5. **(B)** Voltage control result of node 18.

at night, and the reactive power compensation is limited by the centralized power outputs during the daytime, forming a complementary trend with wind power.

3) Voltage control results analysis

The voltage control results of nodes 5, 11, and 18 under three optimal strategies are shown in **Figure 9**.

As shown in **Figure 9**, although the three strategies used in the study case can control the voltage of the three typical nodes within the safe limits, the voltage fluctuations of nodes 5, 11, and 18 are greater under the conventional optimal control method with a single time scale. In contrast, while under the multi-time scale optimization control method, the overall voltage fluctuation trend of node 5 at the beginning of the transmission line is gentle, and the voltage fluctuation increases as the position moves back,

but the voltage fluctuation of each node is the smallest with the third strategy compared to other strategies, which demonstrate the best voltage control effect.

5.3 Optimal Control Results Under Faulty System State

In order to reflect the applicability and robustness of the proposed strategy, it is assumed that the PV station originally placed at the No. 16 node is out of operation due to a failure, which is a large system state changing for the island microgrid system with weak adjustment capability. At this time, it is necessary to appropriately optimize and control the controllable devices in the system to deal with the failure and avoid larger problems. The applicability and robustness of the proposed strategy are reflected by comparing the network losses and voltage fluctuation of the key nodes under the three different strategies.

1) Network losses results analysis

As can be seen from **Figure 10**, compared with the system under normal state, both the amplitude and fluctuation range of the network losses have increased, indicating that the self-regulation ability of the islanded microgrid system will be weakened when facing the generator failure. It is more necessary to reasonably coordinate the controllable devices to make up for the lack of regulation ability. In addition, we can see that among the three optimal control strategies adopted, the strategy proposed in this paper significantly reduces the network losses by 76% at the moment of the maximum network losses in the daily time. Therefore, the proposed strategy can still effectively reduce network losses when dealing with system failures and shows certain applicability and robustness.

2) Voltage control results analysis

From **Figure 11A**, we can see that compared to the normal system state, due to the connection of PV station and ESS at node-5, although the voltage fluctuation at node-5 has increased, the overall trend remains consistent with the level before the fault. However, node 18 is at the end of the transmission line, which has a large voltage fluctuation. Node 16, which is related to node-18, was in the middle section of the transmission line, and it is connected with a PV station as well as an ESS. When the PV station and the ESS were out of operation, node-18 needs to deal with its own load fluctuations while facing a longer power transmission distance, which will make the voltage regulation of the node more difficult. As can be seen from **Figure 11B**, the proposed strategy primely solved the voltage fluctuation problem faced by node-18 and reflects a better voltage control effect as well as robustness compared to the other two strategies.

6 CONCLUSION

In this paper, a collaborative Di-MPC-based source-grid-load active-reactive power coordinated voltage optimization control strategy is proposed. It considers the strong coupling characteristic of active and reactive power caused by the high R/X ratio of the islanded microgrid, as well as the difficulty of real-time online optimization and low robustness of the centralized method. The simulation case of a modified islanded microgrid is analyzed, and the results show that:

The proposed active-reactive power coordinated optimal control strategy can significantly reduce the system network losses. Furthermore, it gives priority to the consumption of wind power and photovoltaic when the load fluctuates, which reduces the wind power and photovoltaic curtailment and ensures the safe and economic operation of the islanded microgrid system.

The proposed collaborative Di-MPC-based voltage optimization control strategy can fully mobilize the voltage regulation potential of the source-grid-load triad, and it effectively suppresses the voltage deviation and fluctuations caused by the uncertainty of DGs and load demand.

From the perspective of modeling, this paper only considered the participation of conventional DGs in voltage regulation. In fact, multiple types of DG and other controllable device have already connected to the multi-energy system like microgrids, such as intelligent terminals, and electric vehicles, which are challenging to be considered in the optimization model. Therefore, more coordination possibilities by considering more DGs and controllable devices will be the research focus in our future work.

From the perspective of the collaboration mechanism, the proposed mechanism still needs some information interaction during the optimization process. This means that if there is any interaction failure appears or information losses, the real-time and robustness of the mechanism will be affected. Therefore, how to better deal with the failure and information losses during the interaction will be the research focus in our future work.

DATA AVAILABILITY STATEMENT

The original contributions presented in the study are included in the article/Supplementary Material, further inquiries can be directed to the corresponding author.

AUTHOR CONTRIBUTIONS

All authors listed have made a substantial, direct, and intellectual contribution to the research work and approved it for publication.

FUNDING

This research was funded by the Key-Area Research and Development Program of Guangdong Province (2019B111109001) and the National Natural Science Foundation of China (Grant No. 51761145106).

REFERENCES

Baran, M. E., and Wu, F. F. (1989). Network Reconfiguration in Distribution Systems for Loss Reduction and Load Balancing. *IEEE Trans. Power Deliv.* 4, 1401–1407. doi:10.1109/61.25627

Fan, Z., Fan, B., and Liu, W. (2021). Distributed Control of DC Microgrids for Optimal Coordination of Conventional and Renewable Generators. *IEEE Trans. Smart Grid* 12, 4607–4615. doi:10.1109/TSG.2021.3094878

Ferrari-Trecate, G., Gallestey, E., Letizia, P., Spedicato, M., Morari, M., and Antoine, M. (2004). Modeling and Control of Co-generation Power Plants: a Hybrid System Approach. *IEEE Trans. Contr. Syst. Technol.* 12, 694–705. doi:10.1109/TCST.2004.826958

Gao, H., Liu, J., and Wang, L. (2018). Robust Coordinated Optimization of Active and Reactive Power in Active Distribution Systems. *IEEE Trans. Smart Grid* 9, 4436–4447. doi:10.1109/TSG.2017.2657782

Gómez, J. S., Llanos, J., Rute, E., Sáez, D., and Sumner, M. (2021). Distributed Predictive Control Strategy for Frequency Restoration of Microgrids Considering Optimal Dispatch. *IEEE Trans. Smart Grid* 12, 2748–2759. doi:10.1109/TSG.2021.3053092

Guo, Y., Gao, H., Wu, Q., Østergaard, J., Yu, D., and Shahidehpour, M. (2019). Distributed Coordinated Active and Reactive Power Control of Wind Farms Based on Model Predictive Control. *Int. J. Electr. Power Energ. Syst.* 104, 78–88. doi:10.1016/j.ijepes.2018.06.043

Han, H., Hou, X., Yang, J., Wu, J., Su, M., and Guerrero, J. M. (2016). Review of Power Sharing Control Strategies for Islanding Operation of AC Microgrids. *IEEE Trans. Smart Grid* 7, 200–215. doi:10.1109/TSG.2015.2434849

Hu, J., Shan, Y., Guerrero, J. M., Ioinovici, A., Chan, K. W., and Rodriguez, J. (2021). Model Predictive Control of Microgrids - an Overview. *Renew. Sust. Energ. Rev.* 136, 110422. doi:10.1016/j.rser.2020.110422

Jiayi, H., Chuanwen, J., and Rong, X. (2008). A Review on Distributed Energy Resources and MicroGrid. *Renew. Sust. Energ. Rev.* 12, 2472–2483. doi:10.1016/j.rser.2007.06.004

Katiraei, F., Iravani, R., Hatziargyriou, N., and Dimeas, A. (2008). Microgrids Management. *IEEE Power Energ. Mag.* 6, 54–65. doi:10.1109/MPE.2008.918702

Kouro, S., Cortes, P., Vargas, R., Ammann, U., and Rodriguez, J. (2009). Model Predictive Control-A Simple and Powerful Method to Control Power Converters. *IEEE Trans. Ind. Electron.* 56, 1826–1838. doi:10.1109/TIE.2008.2008349

Le, J., Liao, X., Zhang, Y., Chang, J., and Lu, J. (2020). Review and Prospect on Distributed Model Predictive Control Method for Power System. *Automation Electric Power Syst.* 44, 179–193.

Li, Y., Gao, D. W., Gao, W., Zhang, H., and Zhou, J. (2020). Double-Mode Energy Management for Multi-Energy System via Distributed Dynamic Event-Triggered Newton-Raphson Algorithm. *IEEE Trans. Smart Grid* 11, 5339–5356. doi:10.1109/TSG.2020.3005179

Li, Y., Wang, J., Wang, R., Gao, D. W., Sun, Q., and Zhang, H. (2021). A Switched Newton-Raphson-Based Distributed Energy Management Algorithm for Multienergy System under Persistent DoS Attacks. *IEEE Trans. Automat. Sci. Eng.*, 1–13. doi:10.1109/TASE.2021.3104393

Liu, L., and Yang, G.-H. (2022). Distributed Optimal Energy Management for Integrated Energy Systems. *IEEE Trans. Ind. Inf.* 1, 1. doi:10.1109/TII.2022.3146165

Liu, W., Guo, P., Dan, Y., Cai, W., Wen, J., Xie, C., et al. (2016). Double -time Scale Reactive Power Control with Large-Scale Wind Power Integrated into Grid. *Renew. Energ. Resour.* 34, 1811–1818.

Liu, X., and Kong, X. (2013). Present Situation and Prospect of Model Predictive Control Application in Complex Power Industrial Process. *Proc. CSEE* 33, 79–85+14.

Maestre, J. M., Muñoz de la Peña, D., and Camacho, E. F. (2011). Distributed Model Predictive Control Based on a Cooperative Game. *Optim. Control. Appl. Meth.* 32, 153–176. doi:10.1002/oca.940

Mehmood, F., Khan, B., Ali, S. M., and Rossiter, J. A. (2021). Distributed MPC for Economic Dispatch and Intermittence Control of Renewable Based Autonomous Microgrid. *Electric Power Syst. Res.* 195, 107131. doi:10.1016/j.epsr.2021.107131

Morstyn, T., Hredzak, B., Aguilera, R. P., and Agelidis, V. G. (2018). Model Predictive Control for Distributed Microgrid Battery Energy Storage Systems. *IEEE Trans. Contr. Syst. Technol.* 26, 1107–1114. doi:10.1109/TCST.2017.2699159

Raimondi Cominesi, S., Farina, M., Giulioni, L., Picasso, B., and Scattolini, R. (2018). A Two-Layer Stochastic Model Predictive Control Scheme for Microgrids. *IEEE Trans. Contr. Syst. Technol.* 26, 1–13. doi:10.1109/TCST.2017.2657606

Rawlings, J., and Mayne, D. Q. (2009). *Model Predictive Control: Theory and Design*.

Sulc, P., Backhaus, S., and Chertkov, M. (2014). Optimal Distributed Control of Reactive Power via the Alternating Direction Method of Multipliers. *IEEE Trans. Energ. Convers.* 29, 968–977. doi:10.1109/TEC.2014.2363196

Villalón, A., Rivera, M., Salgueiro, Y., Muñoz, J., Dragičević, T., and Blaabjerg, F. (2020). Predictive Control for Microgrid Applications: A Review Study. *Energies* 13, 2454. doi:10.3390/en13102454

Wang, J., Zhang, Y., Wang, C., Xun, J., Jin, Z., Xu, F., et al. (2005). Power System Reactive Power/Voltage Assessment Based on Sensitivity Analysis and Optimal Power Flow. *Power Syst. Tech.*, 65–69.

Wang, T., O'Neill, D., and Kamath, H. (2015). Dynamic Control and Optimization of Distributed Energy Resources in a Microgrid. *IEEE Trans. Smart Grid* 6, 2884–2894. doi:10.1109/TSG.2015.2430286

Xia, P., Liu, W., Zhu, D., Wang, N., and Hua, X. (2019). Multi-time Scale Optimal Control Method of Reactive Power and Voltage Based on Model Predictive Control. *Electric Power Automation Equipment* 39, 64–70.

Xu, F., Guo, Q., Sun, H., Lan, H., and Liu, X. (2015). Automatic Voltage Control of Wind Farms Based on Model Predictive Control Theory. *Automation Electric Power Syst.* 39, 59–67.

Yan, X., Xu, Y., Li, R., Jin, Y., and Li, T. (2019). Multi-Time Scale Reactive Power Optimization of Distribution Grid Based on Model Predictive Control and Including RDG Regulation. *TRANSACTIONS CHINA ELECTROTECHNICAL SOCIETY* 34, 2022–2037.

Yang, Q., Zhou, J., Chen, X., and Wen, J. (2021). Distributed MPC-Based Secondary Control for Energy Storage Systems in a DC Microgrid. *IEEE Trans. Power Syst.* 36, 5633–5644. doi:10.1109/TPWRS.2021.3078852

Zhang, Y., Ji, Y., and Tang, Y. (2017). Coordinated Control of Active and Reactive Power for Distribution Network with Distributed Photovoltaic Based on Model Predictive Control. *Automation Electric Power Syst.* 41, 140–146.

Zhang, Z., and Wang, J. (2016). An Active and Reactive Power Joint Real-Time Dispatch Approach for Microgrid Using Model Predictive Control. *Proc. CSEE* 36, 6743–6750+6928.

Zhao, Z., Guo, J., Lai, C. S., Xiao, H., Zhou, K., and Lai, L. L. (2021). Distributed Model Predictive Control Strategy for Islands Multimicrogrids Based on Noncooperative Game. *IEEE Trans. Ind. Inf.* 17, 3803–3814. doi:10.1109/TII.2020.3013102

Zheng, Y., Li, S., and Tan, R. (2018). Distributed Model Predictive Control for On-Connected Microgrid Power Management. *IEEE Trans. Contr. Syst. Technol.* 26, 1028–1039. doi:10.1109/TCST.2017.2692739

Conflict of Interest: The authors declare that the research was conducted in the absence of any commercial or financial relationships that could be construed as a potential conflict of interest.

frontiers | Frontiers in Energy Research

POLICY AND PRACTICE REVIEWS
published: 12 May 2022
doi: 10.3389/fenrg.2022.880444

Discussion on the Reconstruction of Electrical Engineering Undergraduate Teaching Scheme Facing the New Generation Power System

Wangyang Gong[1], Feng Deng[2], Xuhong Wang[2] and Fangfang Chen[2]*

[1]Department of Management Science, Hunan University, Changsha, China, [2]Department of Electric Power Engineering, Changsha University of Science and Technology, Changsha, China

With the construction of a new generation of electric power systems with new energy as the main body, there are major changes in the traditional electrical engineering undergraduate teaching system. On the one hand, the dynamic operating characteristics of the power system dominated by new energy sources and dominated by power electronic equipment will be significantly different from the traditional power system dominated by synchronous generators. Therefore, there is an urgent need to reform the curriculum system to train electrical engineering professionals who can adapt to the future development trend of the power system. On the other hand, with the rapid advancement of advanced information technology in recent years, the application of cutting-edge technologies such as cloud computing, big data, and artificial intelligence in the field of electrical engineering has become more and more in-depth. Therefore, there is an urgent need to cultivate advanced technical experts who possess more advanced information theory and cybernetics knowledge and master the application of cutting-edge information technology in the field of electrical engineering. From the perspective of student training and professional construction needs, this paper systematically analyzes the lag of the traditional electrical engineering curriculum system, and analyzes the knowledge needs of electrical engineering students adapting to the development of the new generation of power systems. From the perspective of teaching schemes, curriculum systems, and evaluation systems, a plan for restructuring the teaching system was proposed. The work in this article can provide a reference for the training of college students majoring in electrical engineering, and it can also provide a more feasible improvement idea for the training of college students in other majors.

Keywords: electrical engineering teaching scheme, reform in education, curriculum system, undergraduate education, new generation of power system

OPEN ACCESS

Edited by:
Yan Xu,
Nanyang Technological University, Singapore

Reviewed by:
Xiaoyu Ji,
Zhejiang University, China
Tiancong Shao,
Beijing Jiaotong University, China

****Correspondence:***
Wangyang Gong
gongwangyang@hnu.edu.cn

Specialty section:
This article was submitted to Smart Grids, a section of the journal Frontiers in Energy Research

Received: *21 February 2022*
Accepted: *15 April 2022*
Published: *12 May 2022*

Citation:
Gong W, Deng F, Wang X and Chen F (2022) Discussion on the Reconstruction of Electrical Engineering Undergraduate Teaching Scheme Facing the New Generation Power System. Front. Energy Res. 10:880444. doi: 10.3389/fenrg.2022.880444

1 INTRODUCTION

The Paris Agreement on climate change (Preston, 2021) charts the course for the world to transition to green and low-carbon development. On 22 September 2020, Chinese President Xi Jinping delivered an important speech at the 75th United Nations General Assembly, stating: China aim to have CO_2 emissions peak before 2030 and achieve carbon neutrality before 2060 (The Xinhua News

Agency, 2020). Driven by the goal of "green and low-carbon development," it will promote the transformation of renewable energy to the main energy source (Shu, 2021). According to statistics, China's total electricity consumption is expected to increase from 7.5 trillion kWh in 2020 to 15–17 trillion kWh in 2060 (Global Energy Internet Development Cooperation Organization, 2021). Renewable energy will become the main force in the supply of electric power. It is estimated that by 2030, the installed capacity of wind power and photovoltaics will exceed 1.6 billion kilowatts, and the power generation of renewable energy will be about 3.5 trillion kilowatt-hours (China Energy Research Association, 2020). After 2030, traditional non-fossil energies such as hydropower and nuclear power are constrained by resources and sites, and construction will gradually slow down, and the development of renewable energy will further accelerate. It is estimated that by 2060, the installed capacity of wind power and photovoltaics will exceed five billion kilowatts, accounting for more than 80% of the installed capacity, and the power generation of renewable energy will exceed 9.6 trillion kWh, accounting for more than 60%, becoming an important support for the power system (Peng, 2021). Obviously, the new power system with a high proportion of renewable energy will be the core development direction of the future energy system, which will bring great challenges to the traditional power system:

1) The ultra-high proportion of renewable energy is connected, the uncertainty faced by the system is further increased, and the balance of power and electricity is under great pressure (Hou et al., 2019; Impram et al., 2020). Renewable energy has strong uncertainty, and the randomness and volatility of its output will bring huge pressure to the power and power balance of the power system (Niu et al., 2022). Especially in extreme conditions such as earthquakes, bad weather, and sudden disasters, it is difficult to ensure Stable supply of electricity.
2) With a large number of power electronic devices connected to the power grid, the inertia of the power system is greatly reduced, and safe and stable operation faces great challenges (Muzhikyan et al., 2017; Peng et al., 2018). With the orderly withdrawal of conventional thermal power units and the grid connection of large-scale renewable energy sources, as well as the commissioning of a large number of transmission equipment containing a high proportion of power electronic components, the inertia of the future power system will inevitably be greatly reduced (Fernández-Guillamón et al., 2019). The system frequency regulation capability will be significantly reduced, which will subvert the existing system control operation mode and threaten the safe and stable operation of the power system.
3) It is difficult for traditional large power grids to meet future power transmission needs. For a long time, China's wind power and photovoltaic resources and loads have been distributed inversely. The northwest region is rich in wind power and photovoltaic resources, but has a sparse population and low power consumption; while the eastern region has few wind power and photovoltaic resources, but is densely populated and has a high level of power consumption. China connects resource areas such as northwest China with load areas in central and eastern China through the construction of UHV transmission channels (Zhang and Li, 2009). With the increasing demand for electricity in the eastern region, the scale of power transmission in the future will reach the level of trillions of kilowatt-hours, a large number of UHV power transmission channels are required to be constructed, which will result in huge costs.

It can be seen that in order to truly implement China's national "green and low-carbon development" strategy and to utilize renewable energy such as wind power and photovoltaics on a large scale, there are still many practical difficulties to overcome. How to solve these difficulties? State Grid Corporation of China (Xin, 2021) and China Southern Power Grid Corporation (Rao, 2021) have, respectively put forward action plans for building new generation of power system after research. Among them, the main points include the following:

1) Empowerment of digital technology to form an energy Internet that integrates multiple energy sources (Wu et al., 2020). With the prominent features of distributed production and distributed utilization of energy (Yan and Hu, 2018), by deepening the integration and application of advanced information and communication technology, control technology and energy technology (Zhang, 2021), driven by digital technologies such as cloud computing, big data, and the Internet of Things, the smart grid will evolve into a self-balancing, self-running and self-processing smart energy system integrating source, network and load.
2) Promote the collaborative interaction of source, network, load and storage, and develop microgrid technology (Wu and Jiang, 2019; Fan et al., 2021). With the development of artificial intelligence, big data and other technologies, users can use information technology to intelligently adjust their energy consumption characteristics to participate in the interaction of supply and demand for the power grid. Through extensive user participation and complete information support, microgrid can promote more effective supply and demand interaction, thereby breaking the operation limit of traditional power system "power output follow with load."
3) Establish scientific and reasonable electricity price mechanism and economic policy (Davison et al., 2002; de Menezes et al., 2016). Deepen the reform of the electricity market, guide and regulate the production and consumption of electricity in the market through electricity prices, and encourage users to conduct electricity spot transactions through supply and demand interaction, electricity sales through partition walls, etc., to form a prosperous electricity market, stimulate economic vitality, and promote the sustainable and efficient development of the power system.

It can be seen that the construction of the new power system conforms to the development trend of the new generation of energy technology in the world, and is also the demand for the development of international power science and technology. In

order to build and maintain a new type of power system with a high proportion of renewable energy, there will be a continuous strong demand for relevant professionals, and power grid companies will need to recruit a large number of people with knowledge in electrical, information, control, computer, business management and other fields. The professionals trained by any of the existing traditional disciplines do not have such a comprehensive knowledge base (Zhu et al., 2020). Therefore, it is urgent to develop the training concept and training path of the electrical engineering major, break the existing disciplinary boundaries, strengthen the interdisciplinary, and establish a new professional personnel training scheme and training model to cultivate professionals with low-carbon, environmental protection, innovation, and open value concepts as well as a broad basic knowledge of complex subjects and the ability to solve interdisciplinary problems.

Based on the exploration and practice of undergraduate teaching in the electrical engineering and automation major of Changsha University of Science and Technology in the past 5 years, this paper systematically expounds some thoughts, understandings and practices of the authors on the training of new generation power system professionals based on the electrical engineering discipline. The second chapter takes Changsha University of Science and Technology as an example to introduce the current educational scheme of electrical engineering undergraduate teaching; The third chapter analyzes the knowledge structure that undergraduate graduates should have to meet the needs of building new generation power systems from the perspective of industry development needs, and points out the shortcomings of using the existing electrical engineering knowledge structure to deal with the development of new generation power systems. The fourth chapter puts forward the reform plan of electrical engineering undergraduate education from two aspects of teaching scheme reform and industry-university-research linkage. Finally a conclusion.

2 THE CURRENT UNDERGRADUATE TEACHING SCHEME OF ELECTRICAL ENGINEERING——TAKING CHANGSHA UNIVERSITY OF SCIENCE AND TECHNOLOGY AS AN EXAMPLE

2.1 Introduction to Electrical Engineering Major of Changsha University of Science and Technology

Changsha University of Science and Technology is a multi-disciplinary university focusing on engineering, with coordinated development of engineering, management, management, economics, literature, and law, with undergraduate education as the main body, with post-doctoral research stations and the right to confer doctoral degrees. It is a national university of "Basic Capacity Building Project of Universities in the Central and Western Regions of China." One of the predecessors of Changsha University of Science and Technology was Changsha Electric Power College, which was founded in 1957 and was directly affiliated to the Ministry of Electric Power Industry of the People's Republic of China. Therefore, the electrical engineering major of Changsha University of Science and Technology is the main major and advantageous major of the school, which has remarkable characteristics of the power industry, and has a history of running education for more than 60 years. Now it is a national characteristic major and has been selected into the "Excellent Engineer Education and Training Program" of the Ministry of Education of China.

2.2 Professional Training Goals

The personnel training objectives of the electrical engineering major of Changsha University of Science and Technology are:

This major cultivates Senior engineering and technical personnel engaged in system operation, engineering design, manufacturing, research and development and engineering management in power systems, electrical equipment manufacturing and scientific research institutes with a sense of social responsibility, good professional ethics and comprehensive quality, strong adaptability and innovative awareness, a knowledge structure combining strong and weak electricity, a forward-looking professional vision, and engineering practice ability, self-learning ability and innovation ability. Therefore, according to the training objectives, the graduation requirements for the quality of personnel training are formulated, including 12 aspects–professional norms, engineering knowledge, problem analysis, design/development solutions, research, use of modern tools, engineering and society, environment and sustainable development, individuals and teams, communication, project management, lifelong learning:

1) Professional norms: establish a scientific worldview, have humanities and social science literacy, be able to understand and abide by engineering professional ethics and norms in electrical engineering practice, and fulfill responsibilities.
2) Engineering Knowledge: Ability to apply mathematics, natural sciences, engineering fundamentals and expertise to solve complex electrical engineering problems.
3) Problem Analysis: Be able to apply fundamental principles of mathematics, natural sciences, and engineering sciences, and through literature research, to identify, express, and analyze complex electrical engineering problems to obtain valid conclusions.
4) Design/Develop Solutions: Be able to design solutions to complex electrical engineering problems, design electrical systems, units (components) or control devices to meet specific needs, and be able to reflect innovation in the design process, taking into account social, health, safety, Legal, cultural and environmental factors.
5) Research: Be able to conduct research on complex electrical engineering problems based on scientific principles and using scientific methods, including designing experiments, analyzing and interpreting data,

and obtaining reasonable and effective conclusions through information synthesis.

6) Use of modern tools: The ability to develop, select and use appropriate techniques, resources, modern engineering tools and information technology tools for complex electrical engineering problems in order to predict and simulate complex electrical engineering problems and understand their limitations.
7) Engineering and Society: Be able to conduct rational analysis based on engineering-related background knowledge, evaluate the impact of professional electrical engineering practice and solutions to complex electrical engineering problems on society, health, safety, law and culture, and understand responsibilities.
8) Environment and Sustainability: Be able to understand and evaluate the impact of practices addressing complex electrical engineering issues on environmental and social sustainability.
9) Individuals and Teams: Ability to work as a team and function in a multidisciplinary context, taking on the roles of individuals, team members and leaders.
10) Communication: Be able to effectively communicate and communicate with industry peers and the public on complex electrical engineering issues, including writing reports and design manuscripts, making presentations, expressing clearly or responding to instructions, etc. And have a certain international perspective, able to communicate, exchange and cooperate in a cross-cultural context.
11) Project management: understand and master the basic knowledge of engineering management principles and economic decision-making methods, and be able to apply them to engineering practice in a multidisciplinary environment.
12) Lifelong learning: have the awareness of independent learning and lifelong learning, and have the ability to continuously learn and adapt to development.

2.3 Professional Curriculum System

According to the normative guidance on the training objectives and knowledge structure of electrical engineering students in the 2012 Chinese Ministry of Education's "General Colleges and Universities Subject Catalog and Major Introduction (2012)," Through the visits and seminars of employers, alumni symposiums, and fresh graduates symposiums, etc., the training objectives and graduation requirements are determined in combination with social needs, and then the knowledge, ability requirements and training methods are determined according to the graduation requirements, and finally the curriculum system is set up and formed.

2.3.1 Mathematics and Natural Science Courses

In terms of the setting of mathematics and natural science courses, the principle of combining advanced mathematics and engineering mathematics is comprehensively considered, and in conjunction with the establishment of the follow-up engineering basic courses, professional basic courses and professional courses of this major, the mathematics courses are opened: 1) Basic Advanced Mathematics: Advanced Mathematics, Linear Algebra, Probability Theory and Mathematical Statistics; 2) Engineering Mathematics: Complex Variable Function and Integral Transformation. In terms of natural science courses, combined with the graduation requirements of this major and the needs of practical engineering, the university physics course and supporting experimental courses have been opened.

The credits of mathematics courses are set at 18.5 credits, and the credits of natural science courses are set at 7 credits, all of which are required courses, accounting for 15.2% of the total credits. The compulsory courses of mathematics and natural science courses are organized by the school's Academic Affairs Office to organize professional teachers from relevant colleges to teach, and unified examinations at the end of the semester to establish unified assessment standards to ensure the teaching quality of mathematics and natural science courses and meet the graduation requirements The curriculum setting of mathematics and natural science courses is shown in **Table 1**.

2.3.2 Engineering Basic Courses, Professional Basic Courses and Professional Core Courses

In the training plan, the engineering basic courses are 24 credits, the professional basic courses are 17 credits, the professional core courses are 24 credits, and the three types of courses are 65 credits in total, accounting for 38.7% of the total credits. Engineering basic courses include "Engineering Drawing," "Circuit Theory," "Analog Electronic Technology," "Digital Electronic Technology," "Electromagnetic Field," "Computer and Programming Fundamentals" and other courses. Professional basic courses include "Electrical Machinery," "Power Electronics" Technology," "Steady-State Analysis of Power System" and other core compulsory courses, professional core courses set up "Power Plant Electrical Part," "Power System Transient Analysis," "Relay Protection Principle," "High Voltage Technology" according to the characteristics of running a school and other professional core courses and professional elective courses closely related to power system. The setting of each course is shown in **Table 2**.

2.3.3 Engineering Practice and Graduation Design

In order to cultivate professional talents with solid theoretical foundation, outstanding practical ability, strong innovation consciousness and ability, the content of practical teaching has been greatly strengthened in recent years, and the coordination and integration of curriculum teaching and practical teaching has been promoted. The teaching concept of continuously strengthening practical teaching during the 4-year study, thereby driving students' practical ability and practical ability to be greatly improved.

The practical teaching system includes three parts: Course design, internship and graduation design.

2.3.3.1 Course Design

The course design of this major is arranged to start in the same semester or the next semester after the end of the theoretical course, so that students have sufficient time and energy to

TABLE 1 | Curriculum setting of mathematics and natural science courses.

Course title	Category	Credit	Hours	Academic year
Advanced Mathematics (I)	Required	5	80	1 (Autumn)
University Physics (I)	Required	3	48	1 (spring)
Linear Algebra	Required	2	32	1 (spring)
Complex function and integral transformation	Required	3	48	1 (spring)
Advanced Mathematics (II)	Required	6	96	1 (spring)
University Physics (II)	Required	3	48	2 (Autumn)
University Physics Experiment	Required	1	30	2 (Autumn)
Probability Theory and Mathematical Statistics	Required	2.5	40	2 (Autumn)

TABLE 2 | Curriculum Setting of Engineering basic courses, professional basic courses and professional core courses.

Engineering fundamentals courses				
Course title	**Category**	**Credit**	**Hours**	**Academic year**
Computer and Programming Fundamentals	Required	2.5	40	1 (Autumn)
Introduction to Electrical Engineering	Elective	0.5	8	1 (Autumn)
Engineering Drawing	Required	2	32	1 (Autumn)
Fundamentals of programming applications	Required	2	32	1 (spring)
Circuit theory (I)	Required	3	48	1 (spring)
Circuit theory (II)	Required	3.5	56	2 (Autumn)
Electromagnetic Field	Required	2	32	2 (Autumn)
Simulation software and its application	Elective	2.5	40	2 (Spring)
Analog Electronic Technology	Required	3	48	2 (Spring)
Digital Electronic Technology	Required	3	48	2 (Spring)
Total Engineering Fundamentals	Compulsory 21 credits, elective 3 credits			
Professional Basic Courses				
Course Title	Category	Credit	Hours	Academic year
Electrical Machinery (I)	Required	3.5	56	2 (Autumn)
Electrical Machinery (II)	Required	3	48	2 (Spring)
Automatic Control Theory	Required	3.5	56	3 (Autumn)
Principle and Application of Microcomputer	Required	3	48	3 (Autumn)
Power Electronics Technology	Required	2	32	3 (Autumn)
Steady-state Analysis of Power System	Required	3.5	56	3 (Autumn)
Total professional basis	Compulsory 18.5 credits			
Professional Core Courses				
Course Title	Category	Credit	Hours	Academic year
Electrical Part of Power Plant	Required	3.5	56	3 (spring)
Transient Analysis of Power System	Required	3.5	56	3 (spring)
Relay Protection Principle	Required	4	64	3 (spring)
High Voltage Technology	Required	3	48	3 (spring)
Automatic Control Technology of Power System	Required	3	48	3 (spring)
Microcomputer protection	Elective	2	32	4 (Autumn)
Emerging Technologies of Electrical Engineering	Elective	2	32	4 (Autumn)
Relay Protection of Large Generator and Transformer	Elective	2	32	4 (Autumn)
Automatic Scheduling of Power System	Elective	2	32	4 (Autumn)
Power System Planning	Elective	2	32	4 (Autumn)
Total professional cores	Compulsory 17 credits			

complete the relevant content. The course design that each student must complete before graduation includes the course design of power grid, the course design of power plant and the course design of relay protection. The three compulsory course design links all require students to work as a team of about 4–6 people to complete the prescribed tasks through teamwork around a selected topic. Please refer to **Table 3** for relevant course information.

2.3.3.2 Internship

Arrange students to visit and learn about power plants, substations and electrical equipment manufacturing enterprises, and experience the production processes of power plants and substations, such as operation, maintenance, scheduling, and overhaul, at close range. Visit and understand the production process and production process of transformers, relay protection devices and other equipment, and complete the

TABLE 3 | Course design list.

Course design name	Design content and design requirements	Credit
Course Design—Power Grid	Main content 1. Determine the power supply voltage level. According to the size of the power supply load, the transmission distance and the existing voltage level of the power grid, the power supply voltage level is determined 2. Preliminarily formulate a number of power grid wiring schemes to be selected. According to the distribution of power points and load points, and the requirements for power supply reliability, a number of power grid wiring schemes to be selected are initially drawn up 3. Selection of main transformers in power plants and substations. The main transformers of power plants and substations are determined according to the capacity, wiring method, and role and status of power plants and substations in the power grid 4. Technical and economic comparison of power flow calculation and power grid wiring scheme. Carry out power flow calculation for the proposed power grid wiring scheme, and make technical and economic comparisons 5. Selection of conductor cross section of transmission line. For newly-built transmission lines, use the economical current density method to select the conductor cross-section 6. Voltage regulation calculation. According to the voltage regulation requirements, select and check the main transformer taps of power plants and substations Time required to complete: in 3 weeks	3
Course Design—Electrical Part of Power Plant	Main content 1. Learn the basic method and basic process of electrical primary system design in power plants, and master the general rules of electrical primary system design in power plants and substations 2. Training of basic skills of electrical primary system design: such as calculation, drawing, consulting materials and manuals, using standards and specifications, and training in computer-aided design and drawing 3. Be able to formulate and analyze the design scheme based on the function and work flow requirements of the electrical primary system of the power plant and substation, reasonably select the main wiring and the electrical wiring form used in the plant, and correctly configure the main electrical equipment 4. Be able to analyze and calculate the load and long-term heat generation according to the normal working conditions of the electrical primary system of the power plant and substation, reasonably select the number, capacity and type of transformers, and preliminarily select the main rated electrical parameters and dimensions of other major electrical equipment 5. Analyze and calculate the short-circuit current, short-term heat generation and electric power according to the short-circuit working conditions of the electrical primary system of the power plant and substation, check the short-circuit operation capability of the primary electrical equipment, and determine the electrical parameters and dimensions of the electrical equipment 6. Be able to draw electrical system diagrams, the drawings conform to the drawing standards, the dimensions and symbols are correctly marked, and the technical requirements are complete and reasonable Time required to complete: in 3 weeks	3
Course Design—Power System Relay Protection	Main content Protection configuration and setting calculation design of electrical equipment in power plants (type 1 topic) 1. Calculation of short-circuit current of a typical power network (it is recommended to use a short-circuit current calculation program to calculate) 2. Relay protection configuration scheme for electrical equipment in typical power plants or substations 3. Setting calculation of electrical equipment relay protection (can be respectively for transmission lines, transformers and other electrical equipment) 4. Design of electrical secondary circuit and selection of secondary equipment Circuit Design and Simulation of Complete Protection Devices (Type 2 topic) 1. Functional design of integrated circuit protection devices for typical electrical equipment (such as line distance protection, transformer differential protection) 2. Internal circuit design of integrated circuit protection device 3. Simulation analysis and parameter determination of the internal circuit of the integrated circuit protection device 4. Action test and simulation of integrated circuit protection device Time required to complete: in 3 weeks	3

course tasks of production practice. Each student should participate in the cognition internship and graduation internship, which content and requirements are shown in **Table 4**.

For a long time, this major has cooperated with Datang Xiangtan Power Generation Company, Datang Huayin Power Leiyang Power Plant, Hunan Ziguang Measurement and Control Co., Ltd., Huazi Technology Co., Ltd., State Grid Hunan Electric Power Company Maintenance Company Xingsha Training Branch, Hunan Dewopu Electric Co., Ltd. and other companies jointly build a practical education base, which provides a good platform for students' practical activities. In addition, students can also choose a suitable electric power company or electric company as their

TABLE 4 | The cognition internship and graduation internship.

Category	Content requirements and teaching methods	Credit
Cognition Internship	Main content 1. Understand the main equipment and production management of the internship site unit and its status in the power system 2. Carefully study and be familiar with on-site safety technical regulations and pass the safety examination 3. Understand the power plant equipment and production process, and establish the initial concept of power production 4. Further understanding of the power production process and main equipment of the power plant (for thermal power plants, understand the combustion system, soda-water system and electrical system of the power plant; for hydropower plants, learn about the hydraulic structure, water machine system and electrical system of the power plant) Internship duration: 2 weeks	2
Graduation Internship	Main content 1. Understand the work characteristics and work nature of the power production site 2. Familiar with the primary electrical wiring of the power plant (or substation), the wiring of the factory electricity (station electricity) and the corresponding operating characteristics 3. Master the configuration, working principle, setting principle, debugging method and debugging process of electrical secondary equipment such as power system relay protection and automatic device 4. Understand the characteristics and operation of new technologies and new equipment at the power production site 5. Understand on-site technical management and production command system and related issues of safe and economical operation Internship duration: 4 weeks	4

practice base according to their own situation. These bases are important places for student employment and school-enterprise industry-university-research cooperation.

3.3.3.3 Graduation Project

The graduation project (thesis) is divided into basic research papers and engineering practical papers according to the content. Basic research papers are for in-depth systematic analysis and discussion of one or some specific problems and phenomena to obtain meaningful conclusions or algorithms; engineering practical papers are based on industrial or engineering practical problems to solve the system design of practical engineering and some practical problems in engineering practice.

The undergraduate graduation project (thesis) of the electrical engineering major makes full use of the actual industrial engineering projects undertaken and participated by the teachers of this major to realize "one student, one project," so that senior students can directly contact the practical problems in the engineering field of this major. More than 70% of the graduation project (thesis) are practical engineering design problems, which can enable students to truly feel the practical application of the knowledge they have learned. In the process of completing the graduation project (thesis), train students to master design standards and specifications, face practical engineering problems, and comprehensively use the knowledge to improve their ability to analyze and solve problems.

2.3.4 The Support Relationship of the Training Scheme to the Graduation Requirements

The contents of various courses and their assessment methods included in the professional training plan can effectively support the achievement of graduation requirements, which are: 1) professional norms (PN), 2) engineering knowledge (EK), 3) problem analysis (PA), 4) design/development solutions (DS), 5) research (RE), 6) use of modern tools (UT), 7) engineering and society (ES), 8) environment and sustainable development (ED), 9) individuals and teams (IT), 10) communication (CM), 11) project management (PM), 12) lifelong learning (LL) respectively. The correspondence matrix between the curriculum system and graduation requirements of this major is shown in **Table 5**. The degree of correlation between courses and graduation requirements is represented by "H (high)," "M (medium)," "L (low)," and H represents the course covers at least 80% of the graduation requirements, M means that the course covers at least 50% of the graduation requirements, and L means that the course covers at least 30% of the graduation requirements.

3 NEW REQUIREMENTS OF NEW GENERATION POWER SYSTEM FOR ELECTRICAL ENGINEERING STUDENTS' KNOWLEDGE STRUCTURE

3.1 Demand for New Technology Fusion of Cyber-Physical Systems With Advanced Information Technology as the Core

The new power system will present the characteristics of deep integration of digital information and the physical system of the power grid. Using advanced information and control technology, the traditional power system can be transformed and upgraded. Using information technology in power system planning and design, scheduling optimization, safety and stability, protection and control, etc., can achieve "comprehensive, accurate measurable and highly controllable" on the power generation side; on the power grid side, a cloud-edge fusion control system can be formed; Effectively aggregate massive adjustable resources on the

TABLE 5 | Correspondence matrix of courses and graduation requirements.

Course title	Graduation requirements											
	1 PN	2 EK	3 PA	4 DS	5 RE	6 UT	7 ES	8 ED	9 IT	10 CM	11 PM	12 LL
University English										H		
Advanced Mathematics		M	H									
Engineering Drawing	H	H	M	H		H						
Linear Algebra		M	H									
Ideological and Moral Cultivation and Legal Basis	H			L			L					
Fundamentals of Computer and Programming						H						
Introduction to Electrical Engineering	H					L	L			L		
Complex function and integral transformation		M	H									
University Physics		M	H		H							
Circuit Theory		H	H	M	M							H
Outline of Modern Chinese History	H											
Electromagnetic Field			H	L			M					
Electrical Machinery		H	H	L			L	H				
Probability Theory and Mathematical Statistics		M	H		H							
Analog Electronic Technology			H	M								
Digital Electronic Technology			H	M								
Simulation software and its application		M				H						
Thermal part of power plant		H		L		L	M	L				
Steady-state Analysis of Power System			H	M	M							
Automatic Control Theory			M	H	M							
Principle and Application of Microcomputer				H		M						
Cognition Internship				M	L			M	H	M		M
Course Design—Power Grid	H	H	L	H	H	L		H	H	H	H	H
Power Electronics Technology			H	M	M					H		
Electrical Part of Power Plant		M	H	H	L			L				
Transient Analysis of Power System			H	H	M							
Relay Protection Principle			M	H	M							
High Voltage Technology			L	H	H		H	H				
Automatic Control Technology of Power System			H	M								
Course Design—Electrical Part of Power Plant	H	H	H	H	H	H		H	H	H	H	H
Course Design—Power System Relay Protection	H	H	L	H	H	H		H	H	H	H	H
Microcomputer protection		M		L		L	L	L				
Professional English	M					L	L	L		M		L
Emerging Technologies of Electrical Engineering			H	M	M							
Relay Protection of Large Generator and Transformer			H	M	M							
Automatic Scheduling of Power System			H	M	M							
Power System Planning			H	M	M							
Graduation Internship	L	L					H	M	H	H		H
Graduation Project	L	M	H	H	H	H	H	H	L	H	H	H

power consumption side to support real-time dynamic response. Through massive information data analysis and high-performance computing technology, the power grid has super sensing ability, intelligent decision-making ability and rapid execution ability.

At present, in the State Grid Corporation of China and China Southern Power Grid Corporation, new technologies such as digital twins, big data, cloud computing, Internet of Things, and artificial intelligence have begun to be popularized and applied in the industry, but the courses taught in colleges and universities are generally based on traditional circuits—motor—power system model-based theory and control technology, lack of data-centric, data-driven, model and parameter adaptive system modeling theory and methods, Students do not know how to use digital tools to model through data. Therefore, cultivating compound professionals who can adapt to the development needs of the times and can skillfully use information tools to solve practical problems in the power system is a shortcoming that must be filled in the process of building a new generation power system.

3.2 Students Need to Understand the New Mode of Power System Operation and New Control Objects With Deep Interaction Between Source, Grid, Load and Storage

The large-scale development of renewable energy places higher requirements on the flexibility of the power system. Traditionally, the demand for flexibility of the power system comes from adjusting the power supply to balance the changes and fluctuations of the load in real time, while the output of non-water renewable energy is volatile. In the scenario of power decarbonization, the power system must face the dual volatility of the load side and the power supply side caused by flexible loads and large-scale renewable energy. On the one hand, the challenges brought by this flexibility demand will be

reflected in the urgent need for more effective energy storage materials and devices. On the other hand, due to carbon reduction requirements, fossil energy cannot fully undertake the task of flexible demand response. Therefore, the traditional power system must be further developed in the direction of deep interaction between source, network, load and storage.

The flexible and sufficiently elastic microgrid operation mode will become an important operation mode in the distribution network, which puts forward higher requirements for the peak regulation, frequency regulation and voltage regulation capabilities of the microgrid with a high proportion of renewable energy generation. However, in the current teaching system of electrical engineering, the proportion of professional courses closely related to the above new objects and new models is not high, and the system is not strong. For example, knowledge of energy storage materials and devices, knowledge of wind power and other renewable energy power generation principles, knowledge of microgrid operation and control, and knowledge of demand response, these professional courses closely related to the operation and control of new power systems are generally missing.

3.3 Build a New Mechanism for mid- and Long-Term, Spot and Ancillary Services Transactions in Electricity With Market Participation

The high degree of digitalization of the new power system will accelerate the development of the power market. With the deep integration of the digital economy and the traditional power industry, the power market transactions continue to enrich, including medium and long-term power transactions, spot power transactions, and auxiliary grid service transactions. These trading mechanisms will promote the transformation of energy consumption from a single, passive, generalized utilization mode to an efficient utilization mode that integrates multiple needs, active participation, and customization.

On 28 January 2022, China's National Development and Reform Commission and China's National Energy Administration issued the "Guiding Opinions on Accelerating the Construction of a National Unified Electricity Market System," which repeatedly emphasized the requirements for nearby consumption and trading of distributed energy: Encourage renewable energy power projects to supply power to nearby industrial parks or enterprises through innovative power transmission and operation methods; Promote the market-oriented transaction of distributed power generation, and support distributed power generation (including electric energy storage, electric vehicles and ships, etc.) and electricity users in the same distribution network to conduct transactions nearby through the power trading platform; In rural areas support the development of renewable energy electricity trading nearby. At present, the Guangdong electric power spot market and the regional frequency regulation auxiliary service market have carried out the settlement trial operation. The above business model is not available in the existing electricity market. Therefore, it is urgent to strengthen the economic literacy of students, so that students can understand the important role of market tools in the operation of the power system and be able to innovate the power trading mechanism.

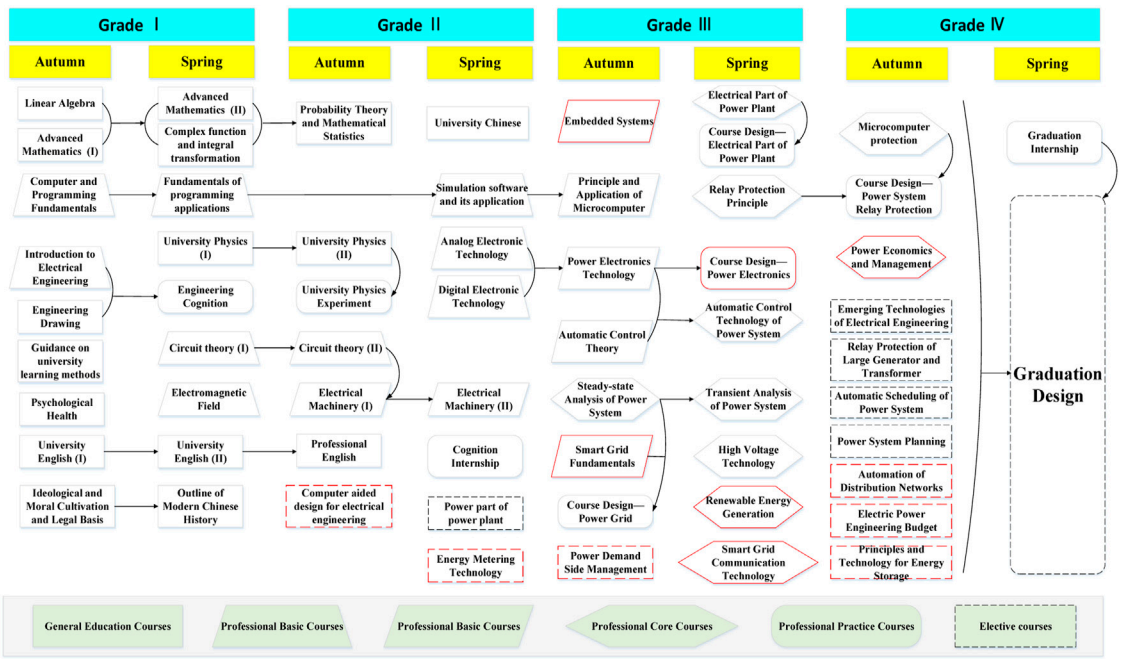

FIGURE 1 | The overall curriculum system for concentration in Smart grid Information Engineering.

4 EXPLORATION ON THE REFORM OF ELECTRICAL ENGINEERING UNDERGRADUATES TEACHING SCHEME TO MEET THE NEEDS OF NEW POWER SYSTEM CONSTRUCTION

4.1 Build a New Professional Concentration and Corresponding Training Scheme

In order to cultivate specialized talents with good basic theoretical knowledge of electrical engineering and information engineering and strong engineering practice ability to meet the needs of new power system construction and economic and social development, after long-term thinking, the authors have made in-depth adjustments to the training scheme of electrical engineering major. On this basis, a new training scheme was formulated, and a new professional concentration was developed accordingly–Concentration in Smart grid Information Engineering.

The curriculum of concentration in Smart grid Information Engineering integrates the relevant courses of "electrical engineering" and "electronic information engineering." Specialized courses are set up such as "Demand side management of power grid," "Energy Metering technology," "Automation of distribution networks," "Renewable energy generation," "Smart grid communication technology," "Power economics and management," etc., so that students not only master the production and operation rules of traditional power systems but also familiar with the development trends of smart grid as well as knowledge of technics, ethics, regulations and industry standards related to distributed power generation, microgrid control and smart grid information engineering. The overall curriculum system of the concentration in Smart grid Information Engineering is shown in **Figure 1**.

The curriculum system shown in **Figure 1** well responds to the new requirements for students' knowledge and ability proposed in **Section 3**. As for "demand for new technology fusion of cyber-physical systems with advanced information technology," through the course "Smart Grid Fundamentals," students can develop a conceptual and macro understanding of cyber-physical system of power grid; Through the course "Smart Grid Communication Technology," students are trained to understand and master various wired and wireless communication modes and principles widely used in Smart Grid; Through the course "Energy Metering Technology," students are trained to master the means of advanced metering infrastructure and understand the use of which in management of loads and distributed renewables. As for "demand for understand the new mode of power system operation and new control objects with deep interaction between source, grid, load and storage," through the course "Renewable Energy Generation," students are trained to understand the principle of renewable energy generation; Through the course "Principle and Technology for Energy Storage," students are trained to understand the application prospect and development trend of energy storage technology in power system; Through the course "Power Demand Side Management," students are introduced to the role of electric vehicles, flexible loads and other controllable loads in the regulation of Power system; Through the course "Automation of Distribution Networks," we discussed with students the principle and method of automatic control of distribution network with a large amount of distributed power generations and controllable loads. As for "demand for new mechanism for transactions in electricity with market participation," through the course "Power Economics and Management," students are trained to understand the concept of electricity market and Electric spot trading, and through the course "Electric Power Engineering Budget," students are trained to understand the concept of project cost and project budget.

Compared with the curriculum system introduced in the second part, the curriculum system highlights the characteristics of the combination of strong and weak electricity and the intersection of disciplines, and offers the following characteristic courses:

- "Smart Grid Communication Technology." Based on communication systems and principles and information communication technology, this course systematically introduces the key technologies of smart grid communication and the current situation and development of China's power communication network, including information coupling technology, cloud computing, information security and other smart grid information technologies, power communication Network system and traditional power business and new business of smart grid, new generation power communication technology and key technology of power backbone transmission network in the era of 5G and Internet of Things, intelligent power distribution communication technology and application, power data network structure and related technologies, Internet of Things Technology and research and application in smart grid, etc.
- "Automation of Distribution Networks." This course introduces the basic concepts of distribution network automation, distribution network primary equipment, distribution network automation data communication, distribution network feeder monitoring terminal, power user power information collection terminal, distribution network feeder automation, power user power consumption information Acquisition system, distribution network automation master station system, distribution network advanced application software, build the knowledge structure necessary for electrical engineering automation students, and lay the necessary foundation for engineering practical application and subsequent theoretical research.
- "Energy Metering Technology." This course includes overview of electric energy measurement technology, inductive electric energy meter, electronic electric energy meter and special electric energy meter, measuring transformer, electric energy measurement method, wiring inspection of electric energy measurement device, electric

energy measurement inspection device and inspection method, smart electric meter, automation Meter reading, remote meter reading technology, etc., enable students to have the theoretical knowledge and practical operation skills of conventional electric energy measurement technology necessary for power system and automation majors.

- "Renewable Energy Generation." This course introduces the working principles and characteristics of wind, solar, hydro, ocean, biomass, geothermal and other power generation forms, as well as power conversion technology in renewable energy power generation.
- "Principles and Technology for Energy Storage." This course introduces the basic knowledge, basic processes and some application examples of energy storage principles and technologies. Including the development history, working principle, characteristics, classification, materials, design and manufacture, testing technology, safety, etc., of energy storage batteries. At the same time, the pumped storage technology, superconducting energy storage technology, compressed air energy storage technology, metal-air battery, supercapacitor, etc., are briefly introduced.
- "Power Demand Side Management." This course introduces the importance, basic knowledge and development of DSM at home and abroad, and introduces the cost-effectiveness of orderly electricity consumption, energy-saving services, energy substitution, multi-coordinated control of source, network, and load, demand-side response, and demand-side management., demand side management under the smart grid mode and other practical technologies for power demand side management.
- "Power Economics and Management". This course includes time value of capital and equivalent calculation, basic data of power technical and economic evaluation, economic evaluation methods (deterministic evaluation method and uncertainty evaluation method), feasibility study of power construction projects, equipment renewal and leasing decision-making, etc., so that students can analyze, evaluate and make decisions on power technology and economic issues from the aspects of power technology advancement, power economic rationality, social justice and ecological adaptability, so as to choose projects and schemes with the best comprehensive benefits.

A large number of power electronic devices are indispensable in the new power system with new energy source as the main body. In fact, whether wind power, photovoltaic, charging piles, energy storage devices, are connected to the power grid through power electronic devices as the interface of the grid. Microgrid, which is developing rapidly at present, is also built with new energy source as the main body, and inevitably contains a large number of power electronic devices. Therefore, the power electronics course design is set up to design the corresponding power electronics circuit and controller centering on the application of renewable energies in microgrid, so as to improve students' ability to master power electronics technology Design content and requirements for power electronics course design is shown in **Table 6**.

The correspondence matrix between the new opened courses and graduation requirements of this major is shown in **Table 7**. The graduation requirements are: 1) professional norms (PN), 2) engineering knowledge (EK), 3) problem analysis (PA), 4) design/development solutions (DS), 5) research (RE), 6) use of modern tools (UT), 7) engineering and society (ES), 8) environment and sustainable development (ED), 9) individuals and teams (IT), 10) communication (CM), 11) project management (PM), 12) lifelong learning (LL), respectively.

4.2 Construct a Student Training Mechanism With Industry-University-Research Collaboration

In order to better integrate the technical achievements and business requirements of the new power system industry into the whole process of electrical engineering talent training and meet the needs of industrial development, the electrical engineering major of Changsha University of Science and Technology follows the concept of open cooperation, complementary advantages, and mutual benefit and win-win results, carried out school-enterprise collaborative education, through customized practical courses, compiling a series of practical teaching materials, revising practical teaching plans, adding engineering practice content on the basis of the original professional practice, incorporating social practice into the scope of professional practice, and implementing school-enterprise joint management; Professional teachers, corporate mentors, and counselors" are jointly responsible for professional guidance, job guidance and psychological counseling.

For a long time, Changsha University of Science and Technology has continuously innovated the practice of industry-university-research cooperation education based on the major strategic needs of the country and the power industry, and strived to create an engineering practice platform for school-enterprise collaboration. We have built experimental teaching bases such as the National Virtual Simulation Experiment Teaching Center for "Power Production and Control," and the National Practice Teaching Demonstration Center for "Energy System and Power Engineering," and cooperated with Hunan Provincial Power Grid Corporation to build a "Power Grid Transmission and Transformation" project. "Electrical Equipment Disaster Prevention and Mitigation" State Key Laboratory Branch, cooperated with Hunan Huazi Technology Co., Ltd. to build a national engineering practice education center, and cooperated with Hunan Electric Power Maintenance Company to build a national undergraduate teaching engineering college students off-campus practice education base, relying on these engineering practice platforms to create a new model of innovative talent training that meets the development needs of new generation power systems.

TABLE 6 | New course design—Power electronics.

Course design name	Design content and design requirements	Credit
Course design—Power electronics	Main content Students choose to complete 2 of the following 8 projects 1. Three-phase thyristor rectifier DC motor reversible drive power supply. Design main circuit, control, drive, protection circuit schematic diagram, design thyristor, rectifier transformer, DC flat wave reactance and other components rated parameters, controller parameters 2. LCC-HVDC converter for HVDC transmission. Design the main circuit, control, drive, protection circuit schematic diagram of the feeder converter, receiver converter, design thyristor, converter transformer, DC flat wave reactance, DC filter and other components rated parameters, controller parametersetc. 3. Flyback DC power supply. Design the main circuit, control, drive, protection circuit schematic diagram, design MOSFET, diode, flyback transformer and other components of the rated parameters, controller parameters 4. TCR + TSC static reactive power compensation device (SVC). Design main circuit, control, drive, protection circuit schematic diagram, design thyristor, capacitance, inductance and other components rated parameters, controller parametersetc. 5. Three-phase bridge PWM rectifier. Design main circuit, control, drive, protection circuit schematic diagram, design power devices, DC capacitor, AC filter inductor (capacitor), rectifier transformer and other components of the rated parameters, controller parameters 6. Three phase photovoltaic grid-connected inverter device. Design main circuit, control, drive, protection circuit schematic diagram, design power devices, DC capacity, energy storage inductor, AC filter inductor (capacitor), grid-connected transformer and other components rated parameters, controller parametersetc. 7. Three-phase PWM energy storage converter (PCS). Design the main circuit, control, drive, protection circuit schematic diagram, design power devices, DC capacitor, AC filter inductor (capacitor), grid-connected transformer and other components rated parameters, controller parametersetc. 8. On-line uninterruptible power supply (UPS). Design rated parameters and controller parameters of power devices, DC capacitor, AC filter inductor (capacitor), grid-connected transformer, energy storage battery and other components **Time required to complete: in 3 weeks**	3

TABLE 7 | Correspondence matrix of the new opened courses.

Course title	Graduation requirements											
	1 PN	2 EK	3 PA	4 DS	5 RE	6 UT	7 ES	8 ED	9 IT	10 CM	11 PM	12 LL
Computer aided design for electrical engineering		M		**H**		H			L	L	L	
Embedded Systems			M	H	M	M						
Smart Grid Fundamentals	M	H	H		H		H	H			M	H
Smart Grid Communication Technology		H	M	M		H						
Automation of Distribution Networks		H	M	M		H	M	M			M	
Energy Metering Technology		H	M	M		H						
Renewable Energy Generation		H	H	H	M	M	H	H				
Principles and Technology for Energy Storage		H	H	H			H	H				
Power Demand Side Management		H			H	L	L	L	L			
Power Economics and Management		L				M	H	H			H	
Electric Power Engineering Budget	H	M					M	M		H	H	
Course Design—Power Electronics		H	H	H	L	H	M	M	H	H	H	H

We have constructed a five-step progressive undergraduates training model for college students of "course teaching→enterprise practice→scientific research and development→innovative application→entrepreneurship and employment, as **Figure 2** shown:

1) Course teaching stage. This stage is mainly through classroom teaching, so that students can understand and master the basic knowledge of the major. In order to meet the development needs of the industry and meet the transformation of the energy industry, we propose to reform and reconstruct the training plan for electrical engineering professionals, upgrade and update multiple courses, and increase the proportion of information technology content;
2) Enterprise practice stage. This stage mainly organizes college students to go deep into the grass-roots power enterprises to carry out professional study, independently explore solutions to the scientific and technological problems of enterprises, and conduct problem-oriented research and study;
3) Research and development stage. At this stage, professional teachers lead the student team to carry out scientific research and project cooperation. By participating in the scientific research projects of the

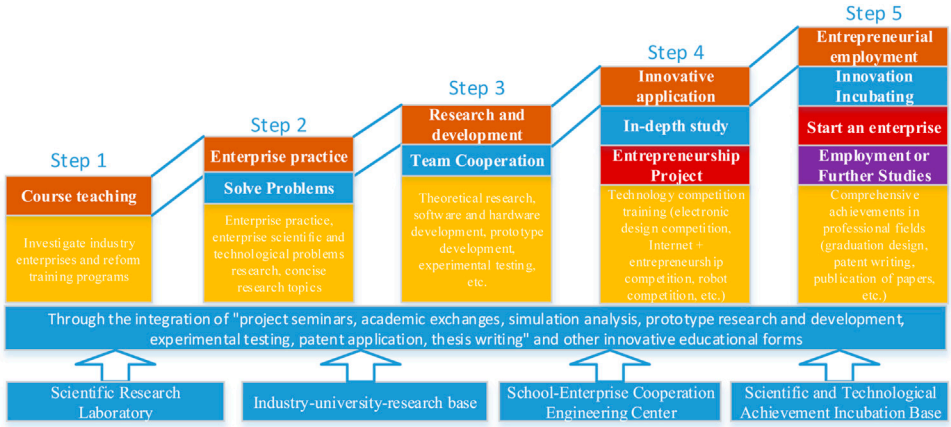

FIGURE 2 | School-enterprise collaboration five-level progressive undergraduates training model.

TABLE 8 | Calculation of grading value of graduation requirement 'EK'.

Course title	Evaluation of graduation requirement item "engineering knowledge (EK)"					
	Weight	$W_{PN,i}$	$A_{EK,i}$	$T_{EK,i}$	$A_{EK,i}/T_{EK,i}$	$G_{EK,i}$
Advanced Mathematics	M(0.5)	0.0318	10.5	15	0.7	0.02226
Engineering Drawing	H (0.7)	0.0446	22.5	30	0.75	0.03345
Linear Algebra	M(0.5)	0.0318	10.5	15	0.7	0.02226
Complex function and integral transformation	M(0.5)	0.0318	7	10	0.7	0.02226
University Physics	M(0.5)	0.0318	23	30	0.77	0.02449
Circuit Theory	H (0.7)	0.0446	22.5	30	0.75	0.03345
Electrical Machinery	H (0.7)	0.0446	28	40	0.7	0.03122
Probability Theory and Mathematical Statistics	M(0.5)	0.0318	8.8	10	0.88	0.02798
Simulation software and its application	M(0.5)	0.0318	13.5	20	0.68	0.02162
Thermal part of power plant	H (0.7)	0.0446	43.5	50	0.87	0.0388
Course Design—Power Grid	H (0.7)	0.0446	51	60	0.85	0.03791
Electrical Part of Power Plant	M(0.5)	0.0318	24.5	30	0.82	0.02608
Course Design—Electrical Part of Power Plant	H (0.7)	0.0446	43.5	60	0.73	0.03256
Course Design—Power System Relay Protection	H (0.7)	0.0446	47.5	60	0.79	0.03523
Computer aided design for electrical engineering	M(0.5)	0.0318	28	40	0.7	0.02226
Smart Grid Fundamentals	H (0.7)	0.0446	21.5	30	0.72	0.03211
Smart Grid Communication Technology	H (0.7)	0.0446	23.5	30	0.78	0.03479
Automation of Distribution Networks	H (0.7)	0.0446	15	20	0.75	0.03345
Computer aided design for electrical engineering	M(0.5)	0.0318	36	50	0.72	0.0229
Renewable Energy Generation	H (0.7)	0.0446	18.5	25	0.74	0.033
Principles and Technology for Energy Storage	H (0.7)	0.0446	19	25	0.76	0.0339
Power Demand Side Management	H (0.7)	0.0446	18	25	0.72	0.03211
Power Economics and Management	L (0.2)	0.0127	7	10	0.7	0.00889
Electric Power Engineering Budget	M(0.5)	0.0318	15	20	0.75	0.02385
Course Design—Power Electronics	H (0.7)	0.0446	44	60	0.73	0.03256
Graduation Internship	L (0.2)	0.0127	8	10	0.8	0.01016
Graduation Project	M (0.5)	0.0318	15	20	0.75	0.02385
Grading Value of Graduation Requirement G_{EK}				0.7534		

tutor, the student team conducts software and hardware development, prototype research and development, experimental testing and other scientific research work to improve their mastery of professional knowledge and temper their work ability;

4) Innovative application stage. This stage undertakes the scientific research projects or cooperative projects of the third stage of research, extracts students' innovative projects from them, and conducts relevant training for science and technology competitions under the guidance of the project team and enterprise teachers;
5) Entrepreneurial employment stage. This stage summarizes scientific research achievements, condenses dissertations, applies for patents and transforms achievements, and conducts targeted employment and entrepreneurship based on research foundations and achievements.

4.3 Build an Evaluation Mechanism to Help Improve the Quality of Education Continuously

In order to evaluate the degree of achievement of graduation requirements of this major and to test the degree of support of graduation requirements to training objectives, this paper designed the evaluation mechanism and algorithm of achievement of graduation requirements, which are described as follows.

For courses using standardized tests, The degree of course evaluation value C_{value} is calculated as follows. Where T_{value} is examination evaluation value and F_{value} is feedback evaluation value.

$$C_{value} = T_{value} \times 80\% + F_{value} \times 20\% \tag{1}$$

Where F_{value} is the weighted sum of student evaluation S_{eva} and peer evaluation P_{eva}:

$$F_{value} = (S_{eva} \times 60\% + P_{eva} \times 40\%)/100 \tag{2}$$

The examination evaluation value T_{value} is calculated as follow:

$$T_{value} = Min\left(\frac{A_{PN}}{T_{PN}}, \frac{A_{EK}}{T_{EK}}, \frac{A_{PA}}{T_{PA}}, \frac{A_{DS}}{T_{DS}}, \frac{A_{RE}}{T_{RE}}, \frac{A_{UT}}{T_{UT}}, \frac{A_{ES}}{T_{ES}}, \frac{A_{ED}}{T_{ED}}, \frac{A_{IT}}{T_{IT}}, \frac{A_{CM}}{T_{CM}}, \frac{A_{PM}}{T_{PM}}, \frac{A_{LL}}{T_{LL}}\right) \times W_1 + \frac{U_{score}}{100} \times W_2 \tag{3}$$

Where A_* are the average scores of the examination questions corresponding to each graduation requirements 1–12 shown in **Tables 5**, **7**, and T_* are the total scores of the examination questions corresponding to each graduation requirements 1–12. U_{score} is the average score of usual performance scores of students. W_1 and W_2 are the weighted value.

For the evaluation of the curriculum system, the grading value of the curriculum system G_{cum} is calculated as follows.

$$G_{cum} = Min(G_{PN}, G_{EK}, G_{PA}, G_{DS}, G_{RE}, G_{UT}, G_{ES}, G_{ED}, G_{IT}, G_{CM}, G_{PM}, G_{LL}) \tag{4}$$

Where G_* are the grading value of each graduation requirements 1–12 shown in **Tables 5**, **7**. Take G_{PN} as an example, its calculation rules are as follows.

$$G_{PN} = \sum_{i=1}^{k}\left(W_{PN,i} \times \frac{A_{PN,i}}{T_{PN,i}}\right) \tag{5}$$

Where k denotes the number of courses within sub-item professional norms (PN). $W_{PN,i}$ is the normalized course weight value for sub-item PN. According to **Tables 5**, **7**, H represents the course covers at least 80% of the graduation requirements, M means that the course covers at least 50% of the graduation requirements, and L means that the course covers at least 30% of the graduation requirements. Therefore, corresponding to graduation requirements, the initial weight of courses in each sub-item $IW_{PN,i}$ is:

$$IW_{PN,i} = \begin{cases} 0.7 & where\ PN = H \\ 0.5 & where\ PN = M \\ 0.2 & where\ PN = L \end{cases} \tag{6}$$

$$W_{PN,i} = IW_{PN,i} \Big/ \sum_{i=1}^{k} IW_{PN,i} \tag{7}$$

For G_{PN}, G_{EK}, G_{PA}, G_{DS}, G_{RE}, G_{UT}, G_{ES}, G_{ED}, G_{IT}, G_{CM}, G_{PM}, G_{LL}, the calculation is the same as for $G_{PN.}$ the grading value of the curriculum system G_{cum} curriculum. When the grading value of the curriculum system G_{cum} is obtained, observe its value. The closer its value is to 1, the more responsive it is to graduation requirements. Generally speaking, when G_{cum} is greater than 0.7, it is considered that the curriculum scheme has basically reached the training goal.

The following takes engineering knowledge (EK) as an example to calculate the degree of achievement of this item. The courses, course weights, total score of course examination involved in item EK (T_{EK}), average score of students (A_{EK}), degree of achievement of each courses for item EK (A_{EK}/T_{EK}), and the final grading value of graduation requirement 'EK' (G_{EK}) are shown in **Table 8**.

The calculation methods for the remaining 11 graduation requirements are similar and will not be described here. The minimum value of the degree value of all graduation requirements is taken as the index to evaluate the degree of the curriculum system. The closer this value is to 1, the closer the student is to the desired goal of the preset graduation requirements.

5 CONCLUSION

With the construction and development of new power systems, the existing teaching schemes and personnel training systems for electrical engineering and automation can not fully meet the talent needs of new power system construction. Therefore, it is urgent to jump out of the original framework and build a new undergraduates training scheme through the intersection of disciplines. The author introduces the current undergraduate teaching scheme of electrical engineering in Changsha University of Science and Technology, And from the perspective of industry development needs, it analyzes the knowledge structure that undergraduate graduates should have to meet the needs of building new power systems, and points out the lack of current training scheme. Based on the exploration and practice of undergraduate teaching in the electrical engineering and automation major of Changsha University of Science and Technology, the author proposes a reform plan for undergraduate education in electrical engineering that meets the needs of the construction of new power systems from three aspects: reform of the teaching scheme, educate students through industry-university-research practice, and establish an evaluation mechanism for the entire teaching process. It provides a valuable reference for relevant teaching institutions engaged in electrical engineering education.

AUTHOR CONTRIBUTIONS

WG wrote the manuscript; FD contributed to the structure and outlines of the manuscript; XW provide useful comments on the overall structure and content of the manuscript; FC helped improve the language of the manucript.

FUNDING

This work was supported by the Changsha University of Science and Technology Teaching Reform Research Project (Grant No. XJG21-095). This work was supported in part by the Hunan Provincial Graduate Research and Innovation Project (No. CX2017B152).

REFERENCES

China Energy Research Association (2020). *China Energy Outlook 2030[M]*. (Beijing: Economy & Management Publishing House).

Davison, M., Anderson, C. L., Marcus, B., and Anderson, K. (2002). Development of a Hybrid Model for Electrical Power Spot Prices. *IEEE Trans. Power Syst.* 17 (2), 257–264. doi:10.1109/tpwrs.2002.1007890

de Menezes, L. M., Houllier, M. A., and Tamvakis, M. (2016). Time-Varying Convergence in European Electricity Spot Markets and Their Association with Carbon and Fuel Prices. *Energy Policy* 88, 613–627. doi:10.1016/j.enpol.2015.09.008

Fan, H., Yu, Z., Xia, S., and Li, X. (2021). Review on Coordinated Planning of Source-Network-Load-Storage for Integrated Energy Systems. *Front. Energy Res.* 9, 641158. doi:10.3389/fenrg.2021.641158

Fernández-Guillamón, A., Gómez-Lázaro, E., and Muljadi, E. (2019). Power Systems with High Renewable Energy Sources: A Review of Inertia and Frequency Control Strategies over Time. *Renew. Sustain. Energy Rev.* 115, 109369. doi:10.1016/j.rser.2019.109369

Global Energy Internet Development Cooperation Organization (2021). Research on China's Energy and Power Development Planning in 2030 and Prospect in 2060. Available at: http://www.sxepa.org/?m=home&c=View&a=index&aid=647 (Accessed March 19, 2021).

Hou, Q., Du, E., Zhang, N., and Kang, C. (2019). Impact of High Renewable Penetration on the Power System Operation Mode: A Data-Driven Approach [J]. *IEEE Trans. Power Syst.* 35 (1), 731–741. doi:10.1109/TPWRS.2019.2929276

Impram, S., Nese, S. V., and Oral, B. (2020). Challenges of Renewable Energy Penetration on Power System Flexibility: A Survey. *Energy Strategy Rev.* 31, 100539. doi:10.1016/j.esr.2020.100539

Muzhikyan, A., Mezher, T., and Farid, A. M. (2017). Power System Enterprise Control with Inertial Response Procurement[J]. *IEEE Trans. Power Syst.* 33 (4), 3735–3744. doi:10.1109/TPWRS.2017.2782085

Niu, S., Zhang, Z., Ke, X., Zhang, G., Huo, C., and Qin, B. (2022). Impact of Renewable Energy Penetration Rate on Power System Transient Voltage Stability. *Energy Rep.* 8, 487–492. doi:10.1016/j.egyr.2021.11.160

Peng, L. (2021). Thoughts and Suggestions on Building a New Power System[J]. *Electr. Power Equip. Manag.* (15), 32–33,38.

Peng, Q., Yang, Y., Wang, H., and Blaabjerg, F. (2018). "On Power Electronized Power Systems: Challenges and Solutions," in 2018 IEEE Industry Applications Society Annual Meeting (IAS), Portland, OR, USA, 23-27 Sept. 2018 (IEEE), 1–9. Available at: https://d.wanfangdata.com.cn/periodical/dlsbgl202115006.

Preston, B. J. (2021). The Influence of the Paris Agreement on Climate Litigation: Causation, Corporate Governance and Catalyst (Part II). *J. Environ. Law* 33 (2), 227–256. doi:10.1093/jel/eqaa021

Rao, H. (2021). Digital Grid to Promote the Construction of New Energy-Based Power System[J]. *Electr. Power Equip. Manag.* (08), 21–22.

Shu, Y. (2021). Building a New Electric Power System Based on New Energy Sources[J]. *Strategic Study CAE* 23 (6), 9. doi:10.15302/j-sscae-2021.06.003

The Xinhua News Agency (2020). Xi Jinping Delivered an Important Speech at the General Debate of the Seventy-Fifth United Nations General Assembly. Available at: http://www.gov.cn/xinwen/2020-09/22/content_5546168.htm (Accessed March 19, 2021).

Wu, X., and Jiang, Y. (2019). Source-Network-Storage Joint Planning Considering Energy Storage Systems and Wind Power Integration. *IEEE Access* 7, 137330–137343. doi:10.1109/access.2019.2942134

Wu, Y., Wu, Y., Guerrero, J. M., Vasquez, J. C., Palacios-Garcia, E. J., and Li, J. (2020). Convergence and Interoperability for the Energy Internet: From Ubiquitous Connection to Distributed Automation. *EEE Ind. Electron. Mag.* 14 (4), 91–105. doi:10.1109/mie.2020.3020786

Xin, B. (2021). Accelerate the Construction of A New Power System to Help Achieve the"Double Carbon"Target[J]. *Electr. Power Equip. Manag.* (11), 23–24.

Yan, Z., and Hu, J. (2018). Energy Internet in the Yangtze River Delta: Opportunities, Challenges, and Suggestions. *Front. Energy* 12 (4), 484–492. doi:10.1007/s11708-018-0600-0

Zhang, J. (2021). Distributed Network Security Framework of Energy Internet Based on Internet of Things. *Sustain. Energy Technol. Assessments* 44, 101051. doi:10.1016/j.seta.2021.101051

Zhang, Y-Z., and Li, H. (2009). Analysis on the Development Strategies of the UHV Grid in China[J]. *Proc. CSEE* 29 (22), 1–7. doi:10.3321/j.issn:0258-8013.2009.22.001

Zhu, G., Lin, J., Sun, H., Kang, C., Yu, X., and Zeng, R. (2020). Reform Practice of Electrical Engineering Undergraduate Teaching System for Energy Internet[J]. *Proc. CSEE* 40 (13), 4063–4072. doi:10.13334/j.0258-8013.pcsee.200461

Conflict of Interest: The authors declare that the research was conducted in the absence of any commercial or financial relationships that could be construed as a potential conflict of interest.

frontiers | Frontiers in Energy Research

ORIGINAL RESEARCH
published: 09 June 2022
doi: 10.3389/fenrg.2022.879869

A Dissolved Gas Assessment Model for Power Transformers According to Weighted Association Rule Mining

Chenhao Sun[1], Zhuoyu Zhou[2], Yongxi Zhang[2], Zhiwei Jia[2], Jingjie Huang[2] and Chenyang Huang[3]*

[1]Key Laboratory of Renewable Energy Electric-Technology of Hunan Province, Changsha University of Science and Technology, Changsha, China, [2]School of Electrical and Information Engineering, Changsha University of Science and Technology, Changsha, China, [3]Northeast Branch of State Grid Corporation of China, Shenyang, China

As one indispensable part of power systems, the reliable-operated power transformers are vital for energy transmission, whereas they are remarkably threatened by potential fault events. To achieve the satisfying and valid operation of power transformers, any fault events that may impact their health ought to be evaluated and early warned. With such motivations, this paper presents original insights on the assessment of power transmission health states via their internal dissolved gas, and an enhanced Association Rule Mining (ARM) model incorporating the analysis of High-Impact-Low-Probability (HILP) components, as well as a dynamic fault event risk evaluation approach, is proposed. The first step is to differentiate the risky components. Unlike the standard ARM, the rarely occurred components in each feature can also be assessed explicitly as the common components to explore the underlying HILP components in the proposed model, rather than just being viewed as trivial data and directly omitted. The second step is to rate the risk level of each risky component. A component importance measure-based evaluation approach is deployed to assess the corresponding risk weights of distinguished risky components. In this approach, the risk weight is determined straightforwardly via the impacts of each component on the variation level of total risks in the system, rather than simply by its frequency of occurrence or data share. Finally, the parameters of the risk weight evaluation approach can be dynamically adapted in an adjustment framework as well. This model is testified through an empirical case study, and the leading results can demonstrate its flexibility and robustness during real applications.

Keywords: transformer diagnosis, dissolved gas analysis (DGA), weighted association rule mining, HILP component, component importance measure (CIM)

OPEN ACCESS

Edited by:
Yan Xu,
Nanyang Technological University, Singapore

Reviewed by:
Narottam Das,
Central Queensland University, Australia
Hao Ming,
Southeast University, China
Xin Wang,
Shanghai Jiao Tong University, China

****Correspondence:***
Chenhao Sun
chenhaosun@csust.edu.cn

Specialty section:
This article was submitted to Smart Grids, a section of the journal Frontiers in Energy Research

Received: *20 February 2022*
Accepted: *16 May 2022*
Published: *09 June 2022*

Citation:
Sun C, Zhou Z, Zhang Y, Jia Z, Huang J and Huang C (2022) A Dissolved Gas Assessment Model for Power Transformers According to Weighted Association Rule Mining. Front. Energy Res. 10:879869. doi: 10.3389/fenrg.2022.879869

INTRODUCTION

As one core part of power systems, power transformers are one key primary equipment, since their failure may cause power supply interruption and even blackouts which will result in significant economic losses. Ergo, it is vital to ensure the safe operation of power transformers. Any transformer failure may lead to the interruption of power supplies, which will consequently cause great losses (Cui et al., 2021; Zhang et al., 2021). Power transformers are usually affected by several inner factors such as thermal stress, overload, and aging of insulating materials. Therefore, the timely and effective fault diagnosis based on these internal characteristics of transformers will be salutary for the subsequent

maintenance. Once the countermeasures are implemented, the potential risks of failure can thus be greatly reduced (Lijun et al., 2021; Meira et al., 2021).

Unlike the electrical signal parameters which are largely affected by the electromagnetic environment within the transformer, there is also a strong correlation between the fault event and the gas composition in transformer oil. Therefore, dissolved gas analysis (DGA) is commonly utilized for transformer fault diagnoses (Cui et al., 2020; Meira et al., 2021).

At present, many researchers have proposed a large number of research ideas on the DGA (Bakar et al., 2014), and considerable progress has been achieved. In the traditional methods, the three-ratio method, the Rogers ratio method, and the Duval triangle method based on the DGA have played an important role, but there are still some drawbacks such as the incomplete state coding and the absolutely coding boundaries. They might limit the practical application of these approaches (Malik and Mishra, 2016; Shi et al., 2016).

In recent years, many scholars have applied machine learning theories to transformer fault diagnosis modeling, and have achieved satisfying results. The first one is the DGA method based on the optimization algorithm (Asafuddoula et al., 2018). To improve the accuracy and reliability of oil-immersed transformer fault diagnosis, References (Youwen et al., 2021; Wu et al., 2021) studied a transformer fault diagnosis method based on genetic algorithm optimization of extreme gradient lifting, and Siada *et al.* employed fuzzy logic models to assess the concentration of each sort of the dissolved gas in (Abu Bakar and Abu- Siada, 2017), or to reduce the dependency for standardizing the DGA interpretation techniques by (Abu- Siada et al., 2013). In (Huanpeng et al., 2017), the Least Squares Dual Support Vector Machine (LS-TSVM) model was deployed. Based on the genetic algorithm, and Genetic Algorithm Support Vector Machine (GA-SVM) along with the crisscross optimization method for the DGA feature was realized in (Anbo et al., 2016; Jing et al., 2020). These DGA methods based on the optimization algorithm can often obtain the intuitive fault probability, but it is necessary to count the large-capacity data for a long period, which requires a larger size of input data.

The second type is the DGA method using the neural network (Jan and Verma, 2021). In (Yingjie and Tienan, 2021), a diagnosis method based on the improved Elman neural network was proposed. In order to improve the accuracy and performance under small sample data scenarios, a method based on the residual BP neural network was established in reference (Wenqing et al., 2020). In (Yan and Taihua, 2020), an optimized probabilistic neural network fault diagnosis method based on digital twinning technology was proposed. A transformer condition assessment method based on fuzzy neural network and local statistics was built in reference (Rigatos and Siano, 2016). The DGA method based on neural networks generally has strong stability and fault tolerance, but they also require large-capacity input data generally.

The third one is the DGA method based on the vector machine (Moazami et al., 2016). Reference (Yiyi et al., 2018) proposed a transformer fault diagnosis model based on the support vector machine (SVM) which was optimized by the imperial colonial competition algorithm, and Rao *et al.* selected non-linear SVM to classify diverse types of power transformer faults by (Rao et al., 2021). In (Jun et al., 2017), the AdaBoost algorithm was combined with the quadratic mapping support vector machine to find a transformer fault diagnosis model. References (Bacha et al., 2012; Xinbo et al., 2020) applied the support vector machine to realize the classification and discrimination of transformer faults. Although the results of the DGA method based on the vector machine are generally or close to the global optimization, it is difficult to solve the multi-classification problems.

To handle these, association rule mining (ARM) (Nahar et al., 2013) is often exploited in the DGA method because it can select input features or states according to requirements. In (Li et al., 2015), the diagnosis model is further optimized based on the grid search (GS) algorithm. An integrated algorithm combining the set pair analysis and the ARM was created by (Sheng et al., 2018). In (Tian -en et al., 2019), the probabilistic image model was applied in the ARM to further improve the efficiency. Remarkable achievements have been made in the literature, whereas there are still some improvable aspects. Firstly, the standard ARM algorithms usually deploy a fixed and uniform importance measure criterion, thus some components with a lower frequency of occurrence will be directly screened out without any assessment. However, there might also be some high-impact (HI) components that can cause failures in these low-probability components, hence these high-risk- low-probability (HILP) components should be extracted and analyzed; Secondly, the risk weight of the selected HI components ought to be determined directly by the risks they generate, rather than simply via their frequency of occurrence; Finally, the predefined parameters in the ARM need to be adjusted or modified during the diagnosis to further enhance the performance.

To realize these, this paper proposes a DGA method based on an improved Weighted Association Rule Mining (WARM) model. In the preprocessing step, the assessment mapping space is established for collecting and integrating all the input data. In this model, the first step is to explore the risky components from the whole input components. The calculation methods of several significance selecting criteria are modified to pick out the HILP components, so that the HILP data can be extracted from the rare data for further analysis along with the HI components which are chosen from the common components. The second step is to evaluate the risk level of the distinguished risky components from the first step, and a risk weight evaluation approach is proposed in light of the component importance measure (CIM). In this model, the influence degree of the HI and the HILP components themselves on the variation level of total reliability of a transformer, rather than the proportion in a database or the frequency of appearance, is incorporated to measure the risk weights. At last, a dynamic adjustment framework is established where the parameters in the risk weight evaluation approach can be periodically adapted and amended in line with the previous diagnosis performance. An empirical case study is conducted, and the results demonstrate that the proposed method can improve diagnostic accuracy, operational efficiency, and reliability during real-world applications.

DATA PREPROCESSING

In order to construct a unified processing space for subsequent analysis, the whole collected fault event records, as well as the relevant features and including components need to be integrated.

Suppose $\{t_A, t_1, t_2, \ldots t_i, \ldots, t_m\}$ is a vector contains the labels of totally m fault records, where t_i is one fault event while t_A is the label number. Assuming that $A = \{a_1, a_2, \ldots, a_j, \ldots, a_n, a_T\}$ is a vector containing all n features in the database, where a_j (j = 1, 2, …, n) is one feature, and a_T is the target feature. For a feature a_j, supposing $a_j = \{e_{j,1}, e_{j,2}, \ldots, e_{j,k}, \ldots, e_{j,l}\}$ is a vector of all the l elements contained, where $e_{j,k}$ (k = 1, 2, …, l) is one element of the feature a_j. This paper selects $X = \{x_{i1}, x_{i2}, \ldots, x_{ij}, \ldots, x_{in}\}$ as the whole relevant factors in a fault event t_i, where $x_{i,j}$ can be any one component of the feature a_j. Seven commonly applied types of dissolved gases in transformer oil as inputs, including the contents of hydrogen (H_2), methane (CH_4), acetylene (C_2H_2), ethylene (C_2H_4), ethane (C_2H_6), the relative gas production rates of carbon monoxide (CO) and carbon dioxide (CO_2) (Rezaie et al., 2022) are considered in this paper as the input features.

As for the target feature a_T, the states of a transformer are selected as the components of the target, and assumes $T = \{T_1, T_2, \ldots, T_o, \ldots, T_m\}$ is a vector that includes the target features in all fault event records. In this paper, seven states of one transformer are taken into account: normal operation, low temperature overheating, medium temperature overheating, high temperature overheating, low energy discharge, high energy discharge, and partial discharge. Hence, T_o may belong to any one of all the seven states, that is $T_o = T(\beta) \in \{T(g_1), T(g_2), \ldots, T(g_7)\}$. Combined with the supposition of the factor set X, an association rule or more specifically, the component-risk patterns can be delineated as $X \rightarrow T$

Based on the above assumptions, the assessment mapping space can be constructed as a matrix form $\boldsymbol{H}$:

$$\boldsymbol{H} = \begin{bmatrix} t_A & a_1 & \ldots & a_j & \ldots & a_n & a_T \\ t_1 & x_{11} & \ldots & x_{1j} & \ldots & x_{1n} & T_1 \\ \vdots & \vdots & \ddots & \vdots & \ddots & \vdots & \vdots \\ t_i & x_{i1} & \ldots & x_{ij} & \ldots & x_{in} & T_i \\ \vdots & \vdots & \ddots & \vdots & \ddots & \vdots & \vdots \\ t_m & x_{m1} & \ldots & x_{mj} & \ldots & x_{mn} & T_m \end{bmatrix} \quad (1)$$

where each row (except the first row) indicates one record of a fault event, x_{ij} is an entry in the i -th fault record, that is, any one element $e_{j,k}$ corresponding to feature a_j. Thus, in an event t_i, $x_{i,1}, x_{i,2}, \ldots, x_{i,j}, \ldots, x_{i,n}$ are the corresponding components in each feature, T_i is the result.

WARM MODEL

Background of ARM

Assuming that there is a set I containing all items, a subset X of I is called the item set. Supposing the database $D = \{t_1, t_2, \ldots, t_m\}$ contains all the fault records. An association rule can be expressed as $X \rightarrow T$, which means that if the item set X appears, the target T will also occur.

The establishment of association rules generally depends on the discovery of the large item sets as well as the frequent rules, and the selection criteria for them are called the significance selecting criteria. The most commonly-used significance selecting criterion is called the support ($supp(X)$), which describes the proportion of X in D (Hipp et al., 2000). In addition, there are some evaluation criteria focusing on the selection of frequent rules. The confidence ($conf(X \rightarrow T)$) refers to the proportion of X that contains T simultaneously (Doostan and Chowdhury, 2017); The rule power factor ($rbf(X \rightarrow T)$) measures the weight of confidence by $X \rightarrow T$ (Hipp et al., 2000); The certainty factor ($cf(X \rightarrow T)$) measures the change degree of the probability of T appearing simultaneously in the rules containing X (Ochin et al., 2016). Based on the aforementioned criteria, if the score of the item sets or rules can meet or above the corresponding thresholds, these item sets and rules will be considered as the large item sets and frequent rules.

Refinement of Significance Selecting Criteria

Among the input components, there are often some that occur less frequently. However, a part of these rare feature quantity values will also lead to transformer failures, then cause serious losses. Therefore, those HILP components cannot be simply ignored. The standard ARM algorithm employs the same and fixed score calculation methods of significance selecting criteria, which makes the rare variables be discarded directly without any analyses. Therefore, based on the standard significance selecting criteria, this paper designs the weighted significance selecting criteria that consider the rare variables.

In the ARM, large item sets and frequent rules are filtered by a uniform calculation approach which results in the dominance of common components that account for a large proportion of the database. In other words, rare components along with the HILP components will be screened out. In order to properly handle these rare data, this paper establishes four weighted significance selecting criteria.

Firstly, an association rule can be redefined as:

$$X^{\mathrm{f}} + X^{\mathrm{r}} \rightarrow T \quad (2)$$

where X^{f} and X^{r} represent the item sets containing common components and rare components, respectively.

If the association rule contains at least one rare element in a feature a_j, the weighted significance selecting criteria can be built as:

$$supp_j = \frac{\left|t_i \in \boldsymbol{H}(i,1); X^{\mathrm{f}} \subseteq \boldsymbol{G} \neq 0; \boldsymbol{H}(i,j) \in X^{\mathrm{r}} \neq \phi\right|}{\left|t_i \in \boldsymbol{H}(i,1); \boldsymbol{H}(i,j) \in X^{\mathrm{r}} \neq \phi\right|} \times 100\% \quad (3)$$

$$conf_{j,\beta} = \frac{\left|t_i \in \boldsymbol{H}(i,1); X^{\mathrm{f}} \subseteq \boldsymbol{G} \neq 0; \boldsymbol{H}(i,j) \in X^{\mathrm{r}} \neq \phi; \boldsymbol{H}(i,n+1) = T(\beta)\right|}{\left|t_i \in \boldsymbol{H}(i,1); \boldsymbol{H}(i,j) \in X^{\mathrm{r}} \neq \phi\right|} \times 100\% \quad (4)$$

$$rpf_{j,\beta} = \frac{\left|t_i \in \boldsymbol{H}(i,1); X^{\mathrm{f}} \subseteq \boldsymbol{G} \neq 0; \boldsymbol{H}(i,j) \in X^{\mathrm{r}} \neq \phi; \boldsymbol{H}(i,n+1) = T(\beta)\right|}{\left|t_i \in \boldsymbol{H}(i,1); \boldsymbol{H}(i,j) \in X^{\mathrm{r}} \neq \phi\right|} \cdot conf_{j,\beta} \times 100\% \tag{5}$$

$$cf_{j,\beta} = \frac{\left(conf_{j,\beta} - \frac{\left|t_i \in \boldsymbol{H}(i,1); \boldsymbol{H}(i,j) \in X^{\mathrm{r}} \neq \phi; \boldsymbol{H}(i,n+1) = T(\beta)\right|}{\left|t_i \in \boldsymbol{H}(i,1); \boldsymbol{H}(i,j) \in X^{r} \neq \phi\right|}\right)}{\left(\frac{\left|t_i \in \boldsymbol{H}(i,1); \boldsymbol{H}(i,j) \in X^{r} \neq \phi; \boldsymbol{H}(i,n+1) \neq T(\beta)\right|}{\left|t_i \in \boldsymbol{H}(i,1); \boldsymbol{H}(i,j) \in X^{r} \neq \phi\right|}\right)} \times 100\% \tag{6}$$

where $\mathbf{G}^{1\times n} = \boldsymbol{H}(i, 2 \sim (n+1))$; $|\cdot|$ represents the cardinality of the fault event records that meet all the inside conditions; $T(\beta)$ denotes the states under study. For the confidence, rule power factor, and certainty factor, the superscript β shows that there are seven different forms of these criteria corresponding to seven different transformer states.

Establishment of Risk Weight Evaluation Model

Since different components in each feature have different impacts on the states of a transformer, further investigation of the relative magnitude of the risk weight of each component is indispensable. In most current studies, the evaluation of risk weights relies on the proportion in a database or the frequency of occurrence. However, they are not equal to the influence of a component on the state of the entire transformer. Therefore, the relative risk weights of each component are determined based on the degree of influence on the transformer itself in this paper.

This paper describes the overall fault risk of a transformer based on the system risk structure theory, and the principle of the CIM is utilized to describe the impact of different components, so as to design the risk weight evaluation model. For the purpose of distinguishing the relative risk weights of rare components, this paper forms two independent processing subspaces of $\boldsymbol{H}$: S^{f} contains all the records, while S_j^{r} only includes the records of either rare component in a certain feature a_j. In addition, a_j^{f} and a_j^{r} represent all the common and rare components in that feature, respectively.

The CIM can measure the impact of each component on the overall risks. In this paper, the risk of a component, that is, the risk of an element $e_{j,k}$, means that a fault event is related to that element $e_{j,k}$ in a feature a_j. The overall risk of a transformer indicates the comprehensive likelihood of a failure in that transformer. This paper deploys two CIM indicators. The risk achievement worth (RAW) (Vesely et al., 1983) describes the relative rise in the overall risk due to the presence of elements $e_{j,k}$, and its mathematical expression is:

$$I^{\mathrm{RAW}}\left(e_{j,k}\right) = \frac{1 - R(0_k, \mathrm{p})}{1 - R(\mathrm{p})} \tag{7}$$

where $1 - R(0_k, \mathrm{p})$ denotes the overall risk when the element $e_{j,k}$ is confirmed to be related; $1 - R(\mathrm{p})$ represents the overall risk.

Similarly, the risk reduction worth (RRW) (Vesely et al., 1983) represents the relative decline in the overall risk if the element $e_{j,k}$ does not appear, and its mathematical expression is:

$$I^{\mathrm{RRW}}\left(e_{j,k}\right) = \frac{1 - R(\mathrm{p})}{1 - R(1_k, \mathrm{p})} \tag{8}$$

where $1 - R(1_k, \mathrm{p})$ denotes the overall risk when the element $e_{j,k}$ is ensured to be irrelevant.

In a fault record, even if a component changes, this fault may no longer occur. Ergo, the occurrence of the fault requires that all the corresponding elements of each feature in this record are confirmed to be relevant. Based on this, the mathematical form of the overall risk can be written as:

$$1 - R(\mathrm{p}) = 1 - \prod_{j=2}^{n+1} R(1_k, \mathrm{p}) = 1 - \prod_{j=2}^{n+1}\left(\sum_{i=2}^{\left|t_i \in S_j^{\mathrm{r}}\right|} \frac{\left|t_i \in \boldsymbol{H}(i,1); \boldsymbol{H}(i,j) = e_{j,k}; \boldsymbol{H}(i,j) \in X^{\mathrm{r}}\right|}{\left|t_i \in \boldsymbol{H}(i,1); \boldsymbol{H}(i,j) \in a_j\right|}\right) \tag{9}$$

In this paper, the relative risk weight of an element $e_{j,k}$ is composed of two parts, which can be expressed as:

$$\omega_{e_{j,k}} = \omega_{j,k}^{\mathrm{f}} + \omega_{j,k}^{\mathrm{r}} \tag{10}$$

where $\omega_{j,k}^{\mathrm{f}}$ represents the risk caused by common elements, $\omega_{\mathrm{j,k}}^{\mathrm{r}}$ represents the risk from rare elements.

The mathematical expression of $\omega_{j,k}^{\mathrm{f}}$ is:

$$\omega_{j,k}^{\mathrm{f}} = \begin{cases} 0, & \text{if } e_{j,k} \in a_j^{\mathrm{f}} \\ \sum_{i=2}^{\left|t_i \in S^{\mathrm{f}}\right|} \frac{\left|\boldsymbol{H}(i,j) = e_{j,k}\right|}{|m|}, & \text{if } e_{j,k} \in a_j^{\mathrm{r}} \end{cases} \tag{11}$$

This paper selects the mean value of the impact of formula (**7**-**8**) to measure the risk from rare elements, so $\omega_{j,k}^{\mathrm{r}}$ can be expressed as:

$$\omega_{j,k}^{\mathrm{r}} = \begin{cases} (A_{\mathrm{RAW}} + A_{\mathrm{RRW}})/2, & \text{if } e_{j,k} \in a_j^{\mathrm{r}} \\ 0, & \text{if } e_{j,k} \in a_j^{\mathrm{f}} \end{cases} \tag{12}$$

where A_{RAW} and A_{RRW} illustrates the risks from the risk increase and the risk decrease, respectively, and namely:

$$A_{\mathrm{RAW}} = \frac{1 - \prod_{k=1}^{l}\left(\sum_{i=2}^{\left|t_i \in S_j^{\mathrm{r}}\right|} \frac{\left|t_i \in \boldsymbol{H}(i,1); \boldsymbol{H}(i,j) = e_{j-k}; \boldsymbol{H}(i,j) \in X^{\mathrm{r}}\right|}{\left|t_i \in \boldsymbol{H}(i,1); \boldsymbol{H}(i,j) \in a_j\right|}\right)}{1 - \prod_{j=2}^{n+1}\left(\sum_{i=2}^{\left|t_i \in S_j^{\mathrm{r}}\right|} \frac{\left|t_i \in \boldsymbol{H}(i,1); \boldsymbol{H}(i,j) = e_{j-k}; \boldsymbol{H}(i,j) \in X^{\mathrm{r}}\right|}{\left|t_i \in \boldsymbol{H}(i,1); \boldsymbol{H}(i,j) \in a_j\right|}\right)}$$

$$A_{\mathrm{RRW}} = \frac{1 - \prod_{j=2}^{n+1}\left(\sum_{i=2}^{\left|t_i \in S_j^{\mathrm{r}}\right|} \frac{\left|t_i \in \boldsymbol{H}(i,1); \boldsymbol{H}(i,j) = e_{j-k}; \boldsymbol{H}(i,j) \in X^{\mathrm{r}}\right|}{\left|t_i \in \boldsymbol{H}(i,1); \boldsymbol{H}(i,j) \in a_j\right|}\right)}{1 - \prod_{k=1}^{l}\left(\sum_{i=2}^{\left|t_i \in S_j^{\mathrm{r}}\right|} \frac{\left|t_i \in \boldsymbol{H}(i,1); \boldsymbol{H}(i,j) \neq e_{j-k}; \boldsymbol{H}(i,j) \in X^{\mathrm{r}}\right|}{\left|t_i \in \boldsymbol{H}(i,1); \boldsymbol{H}(i,j) \in a_j\right|}\right)} \tag{13}$$

Formation of Adjustment Framework

During the application of the diagnosis method, the occurrence of failures varies in different periods. Moreover, with the increase in application time, the parameters ought to be adjusted according to the previous performance to further improve the accuracy of weight evaluations.

In this paper, 1 year is supposed as a research cycle. Therefore, let $D_y \in D = \{D_1, D_2, \cdots, D_y, \cdots, D_Z\}$ denote the records of 1 year in the database D, that is, the records of all faults

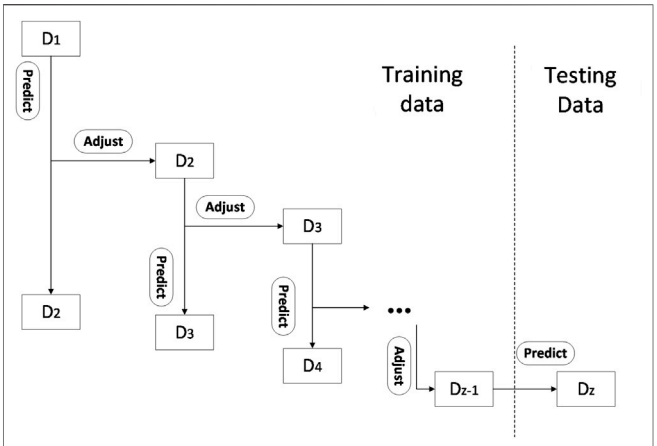

FIGURE 1 | An illustration of dynamic parameter adjustment framework.

within that year. Thus, the parameters in the model will be dynamically modified per year, which is shown in **Figure 1**.

To start with, the initial parameters can be determined from the previous knowledge or engineering experiences. Next, the parameters will be amended in line with the diagnosis performance of the previous cycle. If the actual number of faults in the investigated system is higher than the predicted number of faults according to the comparison between the predicted results and the actual consequences at the end of a year y. In this case, the model needs to "identify" more faults in the next period $y+1$, i.e., the thresholds of significance selecting criteria should be reduced. Therefore, the threshold needs to be adjusted downward compared to their foregoing values in y. On the contrary, when the actual number of faults is less than the predicted numbers, the thresholds need to be updated upward. In summary, the dynamic adjustment of the method is achieved by resetting the threshold of the significance selecting criteria. Also, the importance scores solved by the weighted criteria calculation method are updated directly in accordance with the new annual database D_{y+1}. By combining these two, the proposed approach can be updated based on the rules via the different years of input data.

EMPIRICAL CASE STUDY

Database

In this case study, the transformer maintenance records from a high-voltage transmission system in a central province of China are selected as input data. The total number of sample records is 1,564 which covers the contents of five gases (H_2, CH_4, C_2H_2, C_2H_4, C_2H_6) and relative gas production rates of two (CO, CO_2). Seven states of a transformer (normal operation, low temperature overheating, medium temperature overheating, high temperature overheating, low energy discharge, high energy discharge, and partial discharge) are incorporated as the target.

Validation Tools

In this paper, two 10-fold cross-validation test cases are generated: the general case which is conducted separately according to all states of a transformer; the state case that studies the individual influence of the events by each kind of the state.

When comparing the diagnosis results with the test data, the receiver operating characteristic (ROC) and the precision-recall (PR) curves are deployed to validate the performance (Ziege, 2012). On the basis of these two curves, the area under the curve (AUC) (Swets, 2016) is implemented as the performance indicator, and the higher the AUC value is, the more accurate the diagnosis will be.

General Case

In the very beginning, this paper takes all types of transformer faults as a whole, and applies the WARM-based DGA method to diagnose whether the transformer is faulty or not, i.e., the transformer has only two states: faulty and normal operation.

To verify the effectiveness of both the significance selecting and risk weight evaluation enhancements in the proposed WARM model, two standard ARM algorithms are taken for comparison: the Relim and the Apriori methods. These two algorithms are different in item searching, recording, and sorting, whereas sharing similar procedures in significance selecting and weight evaluation steps. In that case, two DGA techniques (WARM(Relim), WARM(Apriori)) that adopt the improved significance selecting criteria and risk weight evaluation model but apply the Relim and the Apriori algorithms, respectively, will be compared with the two standard forms (WARM(Relim), ARM(Apriori)). The comparison of the ROC and PR curves of these DGA methods are shown in **Figure 2**.

It can be concluded from **Figure 2** that the WARM method which is based on the refined significance selecting criteria and risk weight evaluation model can achieve more accurate transformer fault diagnoses than the ARM model. It can be concluded that the accuracy of the results obtained by the Relim and the Apriori algorithms is relatively close. That is, these two algorithms cannot notably improve the diagnosis precision compared with each other. However, compared with the DGA method based on the ARM, the AUC of the ROC and PR curves of both two algorithms with the WARM model is raised by 19.6 and 14.1% on average. This indicates that the proposed WARM model can successfully enhance the diagnostic performance for either one of the two algorithms.

State Case

Next, the separate diagnoses of all the seven states are carried out, and the comparison is illustrated in **Figure 3**, where NO-normal operation, LTO-low temperature overheating, MTO-medium temperature overheating, HTO-high temperature overheating, LED-low energy discharge, HED-high energy discharge, and PD-partial discharge are applied.

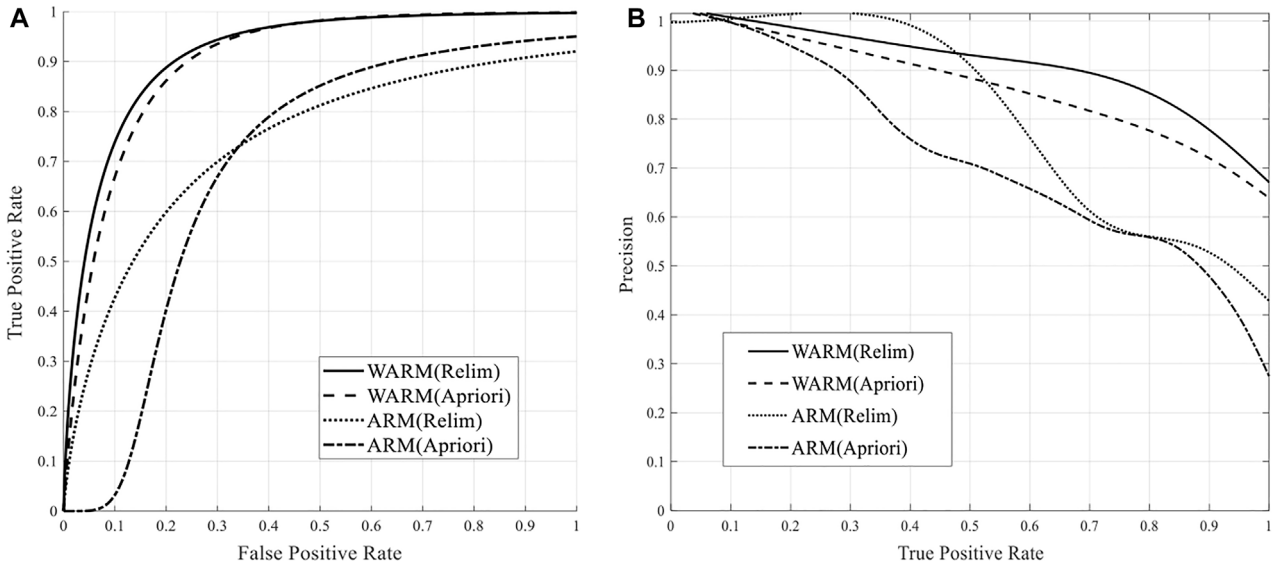

FIGURE 2 | Performance comparison of general case: **(A)** ROC, **(B)** PR.

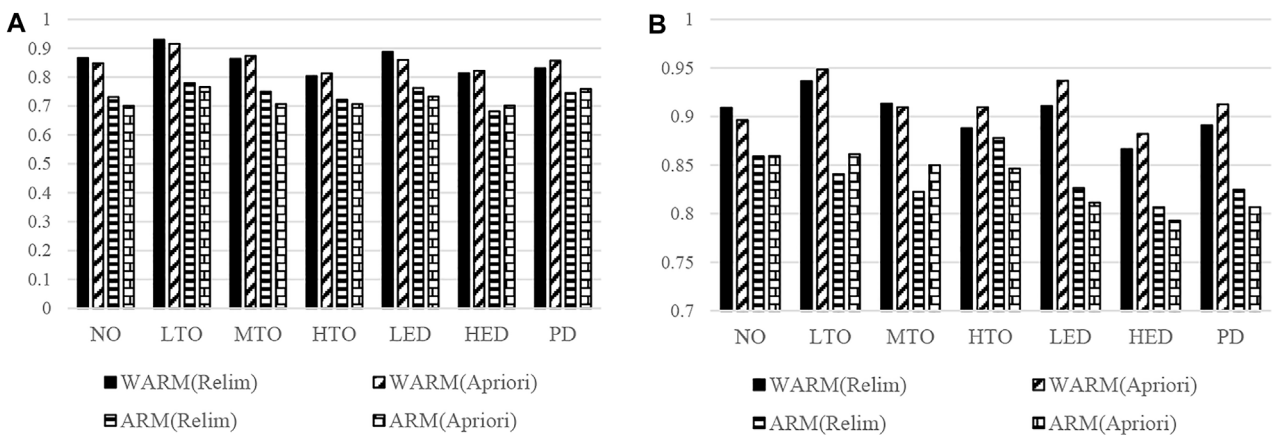

FIGURE 3 | Performance comparison of state case by AUC statistics: **(A)** ROC, **(B)** PR.

From **Figure 3**, the enhancements in diagnoses performance can be achieved via the significance selecting and risk weight evaluation in the WARM model for all the seven transformer conditions. Among them, the diagnosis of the LTO is the most precise one whereas the HED gets the lowest scores in both two evaluations. According to the input database, the HED events seldom happen in recent years while the LTO is one most frequent events. This is in line with the different data volumes of each transformer state, so as the performance. Nevertheless, the significant enhancement of the HED is conducted through the WARM model. Ergo, the benefits of the WARM can be verified especially when the input data is limited. Furthermore, the WARM-based method is also able to operate during some extreme scenarios.

CONCLUSION

For the purpose of handling some limitations in the standard ARM-based DGA method, such as ignorance of the HILP data, the simple evaluation of risk, and the static parameters during applications, this paper proposes an enhanced WARM-based DGA technique. The main works can be summarized as:

1) In the first step, the risky components ought to be distinguished from the whole input data. Unlike the common components, the rarely distributed components are generally viewed as trivial components and simply discarded. Nonetheless, some HILP components which may also cause fault events should be extracted from the rare components. To this end, the calculation approach of four

significance selecting criteria is rebuilt, and the records with any rare component of each feature will be explored once again to decide the HILP components according to the different distributions of rare components in every feature. This can improve the diagnostic accuracy and cover some potential extreme situations during applications;

2) In the second step, the risk level of each risky component will be assessed. In real scenarios, the correlation between a component and the fault event risk is not simply equal to its percentage in the database or frequency of occurrence. That is, a frequent component may not be a risky one whereas a rare component might be a risky one. Ergo, based on CIM, the risk weight of each extracted HI or HILP component can be measured straightforwardly according to the corresponding impact on the variation direction and amounts of the overall risks of a transformer, rather than simply by the frequency of appearance or the data share;
3) During applications, the predefined default parameters might not be suitable or optimal within different scenes or periods. In this paper, these parameters will be modified or adapted in accordance with the previous diagnostic performance, and can thus further improve the accuracy, especially within dissimilar conditions in future periods.

The results of an empirical study validate that the proposed DGA method can ameliorate the precision, practicability, and efficiency within real scenarios.

DATA AVAILABILITY STATEMENT

The datasets presented in this article are not readily available because secrecy agreement. Requests to access the datasets should be directed to State Grid of China.

AUTHOR CONTRIBUTIONS

CS: Conceptualization, Methodology, Software, Writing; ZZ: Data curation; YZ: Investigation; ZJ: Supervision; JH: Validation; CH: Reviewing.

FUNDING

This work is financially supported by Key Laboratory of Renewable Energy Electric-Technology of Hunan Province, Grant No: 2020ZNDL006.

REFERENCES

Abu Bakar, N., and Abu-Siada, A. (2017). A New Method to Detect Dissolved Gases in Transformer Oil Using NIR-IR Spectroscopy. *IEEE Trans. Dielect. Electr. Insul.* 24 (1), 409–419. doi:10.1109/tdei.2016.006025

Abu-Siada, A., Hmood, S., and Islam, S. (2013). A New Fuzzy Logic Approach for Consistent Interpretation of Dissolved Gas-In-Oil Analysis. *IEEE Trans. Dielect. Electr. Insul.* 20 (6), 2343–2349. doi:10.1109/tdei.2013.6678888

Anbo, M., Haiming, L., and Zhuangzhi, G. (2016). Fault Diagnosis Method of Transformer Based on Crisscross Optimization Algorithm and Fuzzy Clustering[J]. *Electr. Meas. Instrum.* 53 (13), 25–29. doi:10.3969/j.issn.1001-1390.2016.13.006

Asafuddoula, M., Verma, B., and Zhang, M. (2018). A Divide-and-Conquer-Based Ensemble Classifier Learning by Means of Many-Objective Optimization. *IEEE Trans. Evol. Comput.* 22 (5), 762–777. doi:10.1109/tevc.2017.2782826

Bacha, K., Souahlia, S., and Gossa, M. (2012). Power Transformer Fault Diagnosis Based on Dissolved Gas Analysis by Support Vector Machine. *Electr. Power Syst. Res.* 83 (1), 73–79. doi:10.1016/j.epsr.2011.09.012

Bakar, N., Abu-Siada, A., and Islam, S. (2014). A Review of Dissolved Gas Analysis Measurement and Interpretation Techniques. *IEEE Electr. Insul. Mag.* 30 (3), 39–49. doi:10.1109/mei.2014.6804740

Cui, H., Yang, L., Zhu, Y., Li, S., Abu-Siada, A., and Islam, S. (2020). A Comprehensive Analyses of Aging Characteristics of Oil-Paper Insulation System in HVDC Converter Transformers. *IEEE Trans. Dielect. Electr. Insul.* 27 (5), 1707–1714. doi:10.1109/tdei.2020.008788

Cui, H., Yang, L., Zhu, Y., Li, S., Abu-Siada, A., and Islam, S. (2021). Dissolved Gas Analysis for Power Transformers within Distributed Renewable Generation-Based Systems. *IEEE Trans. Dielect. Electr. Insul.* 28 (4), 1349–1356. doi:10.1109/tdei.2021.009490

Doostan, M., and Chowdhury, B. H. (2017). Power Distribution System Fault Cause Analysis by Using Association Rule Mining. *Electr. Power Syst. Res.* 152 (1), 140–147. doi:10.1016/j.epsr.2017.07.005

Hipp, J., Güntzer, U., and Nakhaeizadeh, G. (2000). Algorithms for Association Rule Mining - a General Survey and Comparison. *SIGKDD Explor. Newsl.* 2 (1), 58–64. doi:10.1145/360402.360421

Huanpeng, C., Shu, H., and Qiuli, N. (2017). Fault Diagnosis of Power Transformer Based on RELS-TSVM and DGA[J]. *Power Syst. Prot. Control* 45 (21), 134–139. doi:10.7667/PSPC161753

Jan, Z., and Verma, B. (2021). Multicluster Class-Balanced Ensemble. *IEEE Trans. Neural Netw. Learn. Syst.* 32 (3), 1014–1025. doi:10.1109/tnnls.2020.2979839

Jing, W., Su-an, X., Kai-xing, H., Ce, W., Yong, L., Xing, C., et al. (2020). Transformer Based on DGA Feature Quantity Optimization and GA-SVM Fault Diagnosis Model[J]. *Transformer* 57 (12), 36–46.

Jun, L., Lijin, Z., Liang, H., Hua-rong, Z., Xun, H., Huan, C., et al. (2017). Fault Diagnosis Method for Power Transformer Based on Adaboost.MK and SM-SVDD [J]. *J. Electr. Power Sci. Technol.* 32 (03), 139. doi:10.3969/j.issn.1673-9140.2017.03.022

Li, L., Yong, C., Jun, X., Li-Qiu, J., Ning, M., Ming, L., et al. (2015). An Integrated Method of Set Pair Analysis and Association Rule for Fault Diagnosis of Power Transformers[J]. *IEEE Trans. Dielectr. Electr. Insulation* 22 (04), 2368–2378. doi:10.1109/tdei.2015.004855

Lijun, Z., Xiangyu, Z., Zhenyu, W., Tong, L., Xiaowei, X., Chenqingyu, Z., et al. (2021). Oscillation Wave Modeling and Axial Shift Fault Analysis of Transformer Winding[J]. *Electr. Power Autom. Equip.* 41 (3), 157–163. doi:10.16081/j.epae.202101029

Malik, H., and Mishra, S. (2016). Application of Gene Expression Programming (GEP) in Power Transformers Fault Diagnosis Using DGA. *IEEE Trans. Ind. Appl.* 52 (6), 4556–4565. doi:10.1109/tia.2016.2598677

Meira, M., Verucchi, C., Alvarez, R., and Catalano, L. (2021). Dissolved Gas Analysis in Mineral Oil and Natural Ester Liquids from Thermal Faults. *IEEE Trans. Dielect. Electr. Insul.* 28 (4), 1317–1325. doi:10.1109/tdei.2021.009334

Moazami, S., Noori, R., Amiri, B. J., Yeganeh, B., Partani, S., and Safavi, S. (2016). Reliable Prediction of Carbon Monoxide Using Developed Support Vector Machine. *Atmos. Pollut. Res.* 7 (3), 412–418. doi:10.1016/j.apr.2015.10.022

Nahar, J., Imam, T., Tickle, K. S., and Chen, Y.-P. P. (2013). Association Rule Mining to Detect Factors Which Contribute to Heart Disease in Males and Females. *Expert Syst. Appl.* 40 (4), 1086–1093. doi:10.1016/j.eswa.2012.08.028

Ochin, W., Kumar, S., and Joshi, N. (2016). Rule Power Factor: A New Interest Measure in Associative Classification. *Procedia Comput. Sci.* 93 (1), 12–18. doi:10.1016/j.procs.2016.07.175

Rao, U. M., Fofana, I., Rajesh, K. N., and Picher, P. (2021). Identification and Application of Machine Learning Algorithms for Transformer Dissolved Gas

Analysis. *IEEE Trans. Dielect. Electr. Insul.* 28 (5), 1828–1835. doi:10.1109/tdei.2021.009770

Rezaie, S., Bafghi, Z. G., Manavizadeh, N., and Kordmahale, S. B. (2022). Highly Sensitive Detection of Dissolved Gases in Transformer Oil with Carbon-Doped ZnO Nanotube: A DFT Study. *IEEE Sensors J.* 22 (1), 82–89. doi:10.1109/jsen.2021.3126654

Rigatos, G., and Siano, P. (2016). Power Transformers' Condition Monitoring Using Neural Modeling and the Local Statistical Approach to Fault Diagnosis. *Int. J. Electr. Power & Energy Syst.* 80 (1), 150–159. doi:10.1016/j.ijepes.2016.01.019

Sheng, G., Hou, H., Jiang, X., and Chen, Y. (2018). A Novel Association Rule Mining Method of Big Data for Power Transformers State Parameters Based on Probabilistic Graph Model[J]. *IEEE Trans. Smart Grid* 9 (02), 695–702. doi:10.1109/tsg.2016.2562123

Swets, A. (2016). *Signal Detection Theory and ROC Analysis in Psychology and Diagnostics: Collected Papers [M]*. USA: Lawrence Erlbaum Associates.

Tian-en, H., Qinglai, G., and Hongbin, S. (2019). A Deep Spatial-Temporal Data-Driven Approach Considering Microclimates for Power System Security Assessment[J]. *Appl. Energy* 237 (1), 36–48. doi:10.1016/j.apenergy.2019.01.013

Vesely, W. E., and Davis, T. C. (1983). Two Measures of Risk Importance and Their Application[J]. *Nucl. Technol.* 68 (2), 226–234.

Wenqing, Z., Hai, Y., Zhendong, Z., and Xuqiang, S. (2020). Fault Diagnosis of Transformer Based on Residual BP Neural Network[J]. *Electr. Power Autom. Equip.* 40 (2), 143–148. doi:10.16081/j.epae.201912021

Shi, X., Zhu, Y., Ning, X., Wang, L., Sun, G., and Chen, G. (2016). Transformer Fault Diagnosis Based on Deep Auto-Encoder Network[J]. *Electr. Power Autom. Equip.* 36 (5), 122–126. doi:10.16081/j.issn.1006-6047.2016.05.021

Xinbo, H., Weitao, J., Yongcan, Z., and Yi, T. (2020). Transformer Fault Prediction Based on Time Series and Support Vector Machine[J]. *High. Volt. Eng.* 46 (7), 2530–2538. doi:10.13336/j.1003-6520.hve.20191344

Yan, W., and Taihua, Z. (2020). Fault Diagnosis of Transformers Based on Optimal Probabilistic Neural Network Based on Digital Twin[J]. *Modul. Mach. Tool Automatic Manuf. Tech.* 11 (1), 20–23. doi:10.13462/j.cnki.mmtamt.2020.11.005

Yingjie, W., and Tienan, C. (2021). Transformer Fault Diagnosis Method Based on Improved Elman Neural Network[J]. *J. Shenyang Univ. Technol.* 43 (3), 254–258. doi:10.7688/j.issn.1000-1646.2021.03.03

Yiyi, Z., Jian, J., Ke, W., Hanbo, Z., Jiake, F., Hao, Z., et al. (2018). Power Transformer Fault Diagnosis Model Based on Support Vector Machine Optimized by Imperialist Competitive Algorithm[J]. *Electr. Power Autom. Equip.* 38 (1), 99–104. doi:10.16081/j.issn.1006-6047.2018.01.014

Youwen, Z., Bin, F., Ye, C., Weihan, L., Chuangxin, G., et al. (2021). Fault Diagnosis Method for Oil-Immersed Transformer Based on XGBoost Optimized by Genetic Algorithm[J]. *Electr. Power Autom. Equip.* 41 (2), 200–206. doi:10.16081/j.epae.202012021

Zhang, J., Zhang, H., Ding, S., and Zhang, X. (2021). Power Consumption Predicting and Anomaly Detection Based on Transformer and K-Means[J]. *Front. Energy Res.* 9 (1), 113–122. doi:10.3389/fenrg.2021.779587

Wu, Z., Zhou, M., Lin, Z., Chen, X., and Huang, Y. (2021). Improved Genetic Algorithm and XGBoost Classifier for Power Transformer Fault Diagnosis[J]. *Front. Energy Res.* 9 (1), 65–76. doi:10.3389/fenrg.2021.745744

Ziege, E. (2012). System Reliability Theory: Models, Statistical Methods, and Applications[J]. *Technometrics* 46 (4), 495–496. doi:10.1002/9780470316900

Conflict of Interest: Author CH is employed by the Northeast Branch of State Grid Corporation.

The remaining authors declare that the research was conducted in the absence of any commercial or financial relationships that could be construed as a potential conflict of interest.

frontiers | Frontiers in Energy Research

METHODS
published: 04 July 2022
doi: 10.3389/fenrg.2022.842938

Cyber Security Protection of Power System Equipment Based on Chip-Level Trusted Computing

Wei Xi, Xiaobo Li, Qihui Feng, Hao Yao, Tiantian Cai and Yang Yu*

Digital Grid Research Institute, China Southern Power Grid, Guangzhou, China

This article proposes a network security protection scheme for power system embedded devices based on chip-level trusted computing, gives the overall architecture of power equipment chip-level trusted computing, introduces the principle of trust chain transfer within power terminals, and proposes the method of using the on-chip SRAM inside the main control chip of power system embedded devices as the PUF to construct the trusted root. Furthermore, we propose a complete trust transfer mechanism from booting trust to the loading that trust on operating system and application, and give the corresponding program design framework and program logic. The chip-level trusted computing program designed in this article was applied in a distribution automation DTU device equipped with the FUXI chip that is developed by the China Southern Power Grid and the Sylix OS operating system. Finally, we carry out the security protection test. The validity of the designed program is verified by running malicious programs to attack the power equipment. The results show that the designed program can effectively detect and intercept illegal programs, and provide an effective solution for the security protection of power equipment in the open network environment.

Keywords: power equipment, cyber security, trusted computing, embedded system, on-chip security

OPEN ACCESS

Edited by:
Xiangjun Zeng,
Changsha University of Science and Technology, China

Reviewed by:
Sheng Su,
Changsha University of Science and Technology, China
Xuan Liu,
Hunan University, China

****Correspondence:***
Wei Xi
csgxiwei@foxmail.com

Specialty section:
This article was submitted to Smart Grids, a section of the journal Frontiers in Energy Research

Received: *24 December 2021*
Accepted: *09 May 2022*
Published: *04 July 2022*

Citation:
Xi W, Li X, Feng Q, Yao H, Cai T and Yu Y (2022) Cyber Security Protection of Power System Equipment Based on Chip-Level Trusted Computing. Front. Energy Res. 10:842938. doi: 10.3389/fenrg.2022.842938

1 INTRODUCTION

With the development of smart grids, digitization, openness, and interconnection have become the future trend of power grids (Srinivas et al., 2021; Ciavarella et al., 2016; Liu R. et al., 2015). It is foreseeable that a large number of terminal devices and multiple users will be connected to the power grid in the future (Bedi et al., 2018; Park et al., 2019), gradually forming an open and interactive network environment, and the information security of power system terminals, such as electric energy meters, concentrators, and protective measurement and control devices, will face unprecedented challenges. "Stuxnet virus attack" (Li, 2019), "Ukraine blackout" (Guo et al., 2016), "U.S. oil pipeline WannaCry blackmail attack" (Yu and Guan, 2021), and other incidents show that the energy system has always been the key target and object of various malicious attacks. At the same time, the bottom layer of the power system terminal is chip processor, which may also be maliciously exploited because of the vulnerability. In 2018, two vulnerabilities of Meltdown and Spectre were discovered (Efe and Güngör, 2019), which threaten hundreds of millions of PCs, smartphones, and other devices worldwide, as well as a large number of users' privacy data are at the risk of leakage (Kolias et al., 2017).

The abovementioned threats are mainly attacked by exploiting the security vulnerabilities on the computing platform, and the root cause is the lack of the active defense mechanism on the computing platform itself. In order to protect the industrial control terminals of the power system from

cyberattacks, the China power grid has established a comprehensive network security in-depth protection system based on network isolation and border protection (National Development and Reform Commission of China, 2014). In 2015, the National Energy Administration of China issued the "Overall Security Protection Plan for Power Monitoring System," requiring to "gradually promote the application of trusted computing technology," to realize the transformation of power terminals from passive defense to active immunity (Zhang, 2019).

Trusted computing is an active defense technology. It uses hardware attributes as the root of trust and measures layer by layer when the system starts to establish an isolated execution operating environment, and guarantees the security of sensitive operations on the computing platform, thus achieving the protection of a trusted code (Avizienis et al., 2004). Trusted computing establishes trust anchors by integrating dedicated hardware modules in the computing platform and uses cryptographic mechanisms to establish a trust chain, to build a trustworthy computing environment, making it possible to fundamentally solve the security problem of the computing platform (Feng et al., 2011).

Beginning late 1990s, IBM, HP, and other computer companies began to propose trusted computing technology solutions and cosponsored the establishment of the Trusted Computing Group (TCG) (Trusted Computing Group, 2003), whose purpose and goal is to ensure computing security through the development and opening of trusted computing industry standards. The TCG has published a series of specifications such as trusted platform module (TPM) (Trusted Computing Group, 2017a), trusted software stack (TSS) (Trusted Computing Group, 2017b), trusted network connection (TNC) (Trusted Computing Group, 2017c), and mobile trusted module (MTM) (Kylanpaa and Ekberg, 2007). The Institute of Software Research of the Chinese Academy of Sciences has proposed a trusted computing architecture based on the trusted cryptography module (TCM) (Feng et al., 2020) and researched the application of this system for security protection of computer systems, mobile communication terminals, and the Internet of Things, which can promote the active immunity function of the power terminal part.

Although some achievements have been made in the field of Trusted Computing, the current achievements are mainly applied to personal computers and servers. For the realization of Trusted Computing of power grid terminals, related scholars have made some explorations such as these literatures works. Zhang et al. (2017), Wang (2018), and Zheng (2019) carried out research on information security of power consumption information collection terminals based on trusted computing. Xu (2014) carried out the research and implementation of embedded power distribution terminals based on trusted computing. Sun et al. (2014) designed a trusted authentication mechanism based on trusted computing theory and trusted security chip technology, and the literature. Zhang and Zhao (2019) made a research on the trusted computing technology in power collection terminals. To sum up, in the field of power systems, the application of trusted computing technology has sprouted, but it is far from mature, and the research on the security protection of power system terminals based on trusted computing is still in the exploratory stage.

In this article, we are trying to meet the requirement; that is, the power terminals realize active security defense in the open environment, and we design a chip-level trusted computing architecture for power embedded terminals. On this basis, based on the TCM trusted computing architecture, we use the hardware properties of the chips of power system devices to build a root of trust, and establish a trusted execution environment free from malicious code attacks to ensure system entities behave as expected. The structure of this article is as follows.

2 OVERALL ARCHITECTURE OF CHIP-LEVEL TRUSTED COMPUTING FOR POWER EQUIPMENT

Damaging critical components of the computer, tampering with the running code of the system, and modifying the configuration of the system are important means of hacker attacks. These attacks actually tamper with the trusted execution environment of the original system by modifying the correct running code of the system and changing the important configuration files of the system, and then use this untrusted execution environment to achieve their own attack goals. Therefore, building a trusted computing environment for computer systems has become an urgent problem in the field of computer security.

The TCG defines trust as follows: if an entity's behavior always moves toward an expected goal in an expected manner, then the entity is credible. Based on its definition of trust, the TCG gives a way to build a trusted execution environment for computer systems: trust chain. Through the layer-by-layer measurement and trust chain transfer of the computer system, the trust from the lowest level of trusted hardware to the target application is established. Then by using the security chip that is implanted in the hardware platform to protect the measurement data, the credibility of the computer system execution environment is established.

Based on the trust chain construction technology, this article describes an embedded trusted computing security protection architecture for power industrial control terminals that includes trusted boot, operating system measurement, and application program measurement, as shown in **Figure 1**. The architecture is a set of security systems that run through the hardware layer, kernel layer, and application layer. In the system, the hardware layer uses hardware cryptographic algorithm modules and secure boot modules to enhance the computer system security; the kernel layer includes measurement modules, management modules, integrity management modules, and management and control modules, and it provides core trusted computing functions; and the application layer contains the measurement agent, kernel interface library, trusted software library, and client interface GUI, and it provides operable, manageable, and visual user application support.

The power equipment trusted computing system is responsible for collecting data and information on the

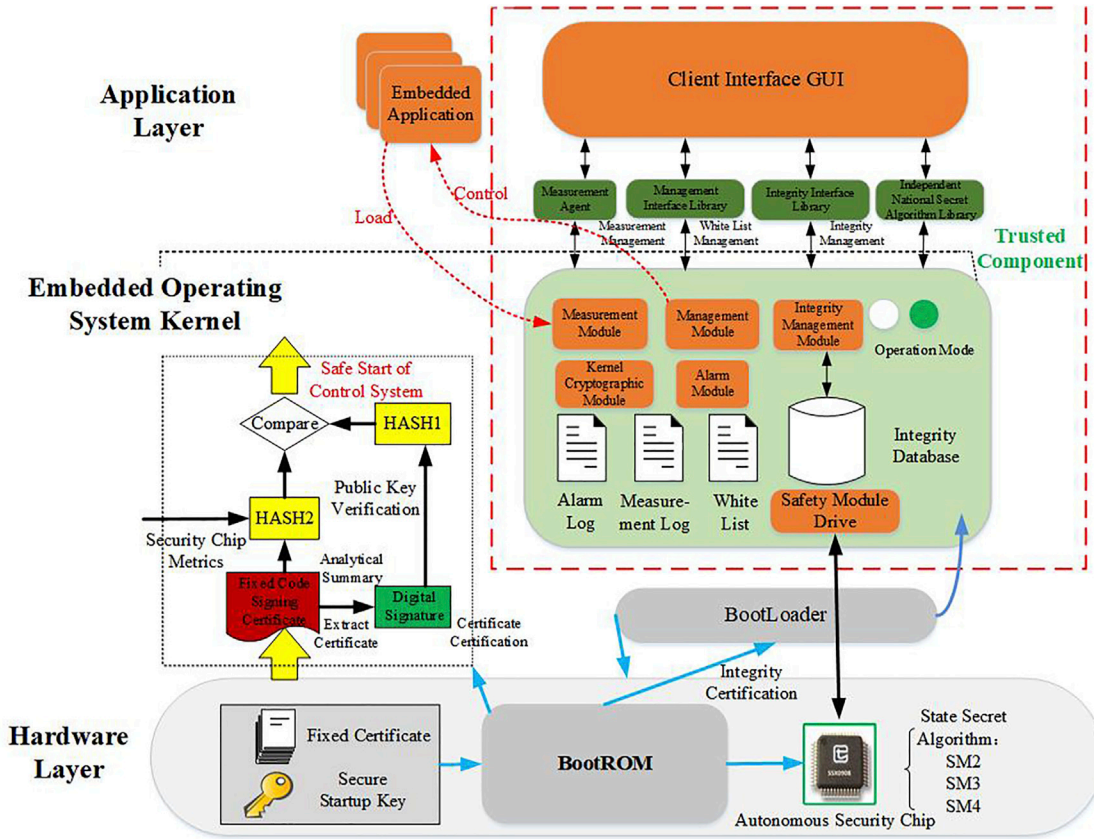

FIGURE 1 | Embedded trusted computing security protection system architecture for power industrial control terminals.

environmental integrity of the power equipment, comparing the integrity information of the equipment with the whitelist deployed on the equipment, and displaying the verification results. The administrator can make a whitelist for different devices according to specific needs. The system executes a mandatory protection function, the host enters the control state, and processes that are not on the whitelist are prohibited from running. The hardware layer of the power equipment adopts a security chip that implements a cryptographic algorithm to form the secure hardware root of a trusted computing environment.

3 THE PRINCIPLE OF TRUST CHAIN TRANSFER

The chain of trust technology starts from the root of trust, establishing a chain of trust from the underlying hardware to the application layer through gradual measurement and verification. It transfers trust from the root of trust to the uppermost application code to ensure the credibility of the entire system platform. When the system is powered on and started, each entity that obtains system control must be measured before it is allowed to run on the system. A typical trust chain construction needs to solve two problems: (1) select the entity that can be the starting point of the trust chain as the root of trust. The root of trust is the first entity in the chain of trust and the anchor of trust for the entire device, which must be safe and reliable, and (2) choose an algorithm that measures system entities to transfer trust.

This article designs a chip-level complete chain for the power system terminal equipment. The trust chain requires the hardware layer to provide components, including secure boot BootROM, secure boot keys, firmware certificates, and hardware security module.

(1) Secure boot BootROM: it is equipped with the boot code with secure boot and is solidified on the device. It is responsible for implementing security functions such as metrics and authentication firmware.
(2) Secure boot key: an asymmetric key used to sign the firmware of the device, and the public key part is solidified on the device during production.
(3) Firmware certificate: the certificate issued by the device vendor for the device firmware using the private key of the secure boot key, which can prove the legitimacy of the firmware.
(4) Hardware security module: it should provide SM2, SM3, SM4, and other independent domestic cryptographic algorithm systems, and key storage functions to provide

high-speed and secure cryptographic services for the upper-level software (Office of State Commercial Cipher Administration, 2006; Office of State Commercial Cipher Administration, 2010; Office of State Commercial Cipher Administration, 2012).

Among them, the hardware security module equipped with national cryptographic algorithm is the root of trust of the system. After booting up, the root of trust measures the boot code stored in the Bootloader, and then the system performs hash integrity calculation for each component (hardware and software module) that will be loaded during the boot process, such as OS loader, OS kernel, device driver module, initialization process, application, and network service, to obtain its metric value before it is loaded and run. The system determines the transmission of the trust chain according to the measurement value, and records the whole trust chain delivery through the measurement value, preventing the firmware loaded by the device from being tampered with, and ensuring the credibility of the operating environment when the system starts (Feng et al., 2015).

The process of trust chain execution is as follows:

(1) After the device is powered on, BootROM loads and measures the operating system loader BootLoader to obtain the measured value.
(2) Using the secure boot key on the device to verify the firmware certificate of the BootLoader firmware and verifying whether the measurement value is consistent with the standard integrity value in the firmware certificate. Only when they are consistent, the boot is allowed.
(3) BootLoader loads and metrics the OS image after booting by using the secure boot key to verify the operating system image certificate. Meanwhile, matching the measured value with the standard value in the certificate only starts the operating system kernel when it matches. The trust established by the autonomous security chip is passed to the operating system itself when the operating system is started.
(4) The operating system kernel-level extended measurement module measures all the applications loaded in the system, and guarantees the degree of trust chain with the help of independent security chips.

At each link of the trust chain transfer, the corresponding subsystems will be built, such as the trusted boot system (TCWG GRUB), the operating system measurement architecture (TCWG OSMA), the TCWG dynamic measurement, and the component measurement system. During the initialization phase of the operating system, the kernel measurement module supporting the SM3 algorithm will be automatically loaded to measure the executable program during the operating system boot process. The images of all the executable programs are first loaded into the system memory, and the measurement module analyzes the images loaded in the memory and calculates the integrity hash function, and expands the calculation results to the internal storage of the autonomous security chip for safe storage.

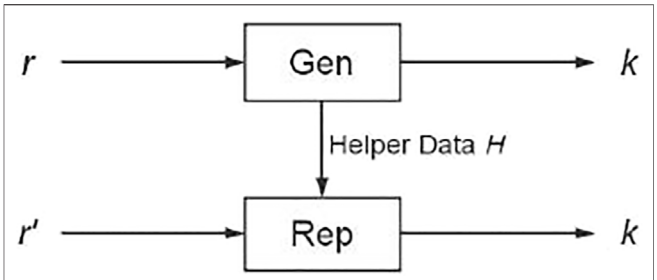

FIGURE 2 | Logic realization of the PUF.

4 REALIZATION OF CHIP-LEVEL TRUSTED COMPUTING

4.1 Construction of the Root of Trust

The physical unclonable function (PUF) (Liu Z. L. et al., 2015) refers to the use of random process deviations of integrated circuit chips in the manufacturing process to cause differences in the device size or electrical characteristics between chips, and using the readout circuits to sample the random characteristics to obtain a unique and unclonable data.

The PUF circuit is derived from the random deviation process of the analog circuit structure, and since the process deviation of each circuit is different, the difference is completely random. The PUF circuit is unique and cannot be cloned. The PUF value is output by the PUF circuit when it is powered on, and the value does not exist in non-volatile memory such as EEPROM or FLASH. It has the characteristics of being lost when power is off and cannot be read, which greatly improves the non-clonable characteristics of the PUF value (Mispan et al., 2015; Song, 2019).

The realization of the PUF includes two parts, namely, production (Gen) and reconstruction (Rep). The Gen algorithm extracts key k from PUF response r, and generates auxiliary data H, which does not include confidential data and does not require secure storage. The Rep algorithm takes H as a parameter to regenerate key k from PUF's noisy response r'. Key k is generated by the PUF owner or issuer in the Gen algorithm, so it is easy to bind new key k' to the PUF by re-running the Gen algorithm and obtaining new auxiliary data H' (3rd Generation Partnership Project (3GPP), 2018a; 3rd Generation Partnership Project (3GPP), 2018b).

This feature enables the implementation of the key update mechanism to become possible. The logic realization of the PUF is shown in **Figure 2**.

This article uses the on-chip SRAM that is inside the main control chip of the power system embedded device as the PUF to construct the root of trust for the device. It mainly includes two stages, including the production process and the reconstruction process. The manufacturer issues the key for the device during the production process, and the device is reconstructed. The process uses its own SRAM PUF to calculate the key issued by the manufacturer in real time. The specific process is shown in **Figure 3**.

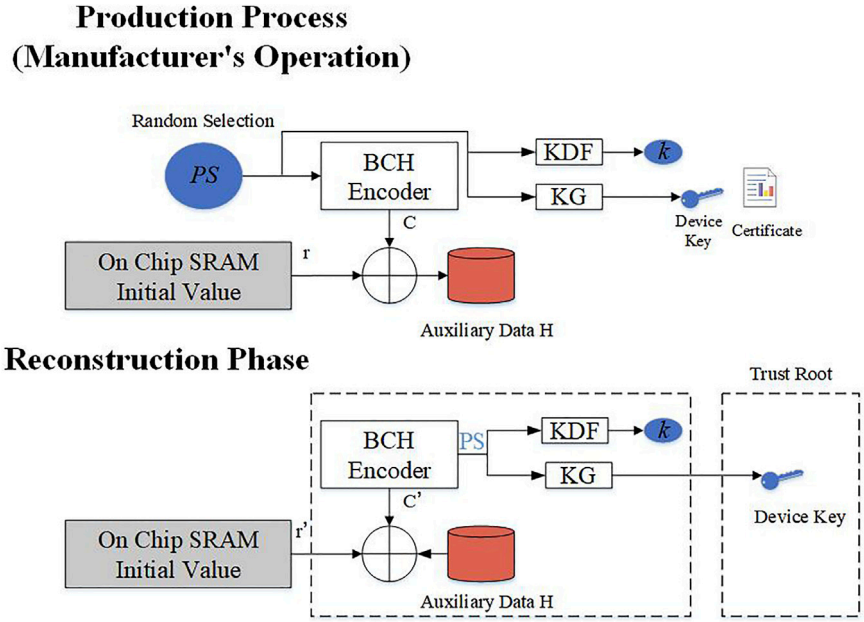

FIGURE 3 | Specific process of production and reconstruction.

4.1.1 Production Process

The production process is invoked by the vendor when the device is shipped, and it receives as input the power-up initial value of the on-chip SRAM (a binary string consisting of the initial values of the SRAM cells), and then performs the following steps.

(1) The receiving vendor randomly generates a random value *PS*, and then encodes the *PS* using a BCH error correction code to obtain a code word $C = \mathrm{BCH}_{\mathrm{Enc}}(PS)$.
(2) XOR the code word C and r, and the resulting value is recorded as auxiliary data H. H does not need to be stored safely, as long as it is stored on the persistent storage device of the device. H will help BB to regenerate *PS* during the reconstruction phase.
(3) Input a key derivation function KDF and a deterministic key generation algorithm KG to *PS*, respectively, and then generate symmetric key k and a public–private key pair (pk, sk). The manufacturer uses its signature key to issue a certificate $Cert_{pk}$ to pk. The certificate contains the standard integrity values of the embedded firmware, and these integrity values can be used to establish a chain of trust for this device.
(4) Finally, the manufacturer stores auxiliary data H and certificates $Cert_{pk}$ persistently on the device.

The main task of this stage is that the manufacturer implicitly binds the master seed *PS* to the device and issues a certificate for the device key exported by the *PS*. Here, "implicit" means *PS* that is not physically stored on the device but is calculated at run-time.

4.1.2 The Reconstruction Process of Building Blocks

After the embedded device is powered on, it first runs the code stored on BootROM, which is responsible for measuring the initial value r' of the on-chip SRAM and passing r r' to BB. SRAM is a kind of PUF, and its initial value after power-on has a certain amount of error with the manufacturer's metric value r in the production stage, which is also the reason for using error correction codes. The reconstruction process receives r' as an input, performs an XOR operation with auxiliary data H, and obtains a BCH code word with a certain error, and then the BCH decoder eliminates the error of C to obtain main seed *PS* that is bound to the device, during the production process. Finally, *PS* is used to generate symmetric key k and the asymmetric key pair of the device (pk, sk).

4.2 Transmission of Trust

The trust chain technology starts from the static trust metric root and establishes a trust chain from the underlying hardware to the application layer through step-by-step measurement and verification, passing trust from the trust metric root to the uppermost application codes to guarantee the trust of the whole system platform. The establishment of a static trust chain mainly includes two aspects: integrity measurement and trust transfer.

Trusted computing technology refers to the measurement process of a trusted entity to another entity as a measurement event. The measurement events involve two types of data: 1) the measured data, which is the expression of the code or data being measured, and 2) the measurement summary, which is the hash value of the measured data. The entity responsible for the measurement obtains the measurement summary by hashing the measured data. The measurement summary is equivalent to a snapshot of the measured data and is the integrity mark of the measured data. The measurement summary marks the integrity information of the measured data, and the integrity report needs

to use the measurement summary. Therefore, the measurement summary needs to be protected, and it is usually protected by the trusted storage root of the security chip. The measured data do not need to be protected by a trusted chip, but they need to be re-measured during the integrity verification process, so the computing platform needs to save these data.

In the system designed in this article, the SM3 algorithm is designed as an algorithm for the encrypted hash calculation. For a message m with a length of l (l < 264) bits, the SM3 hash algorithm is filled and iteratively compressed to generate a hash value. The length of the hash value is 256 bits:

(1) Filling: Assume that the length of the message m is l bits. First, add bit "1" to the end of the message, and then add k "0"s, where k is the smallest non-negative integer that satisfies l+1 + k ≡ 448mod512. Then add a 64-bit bit string, which is a binary representation of length l. The bit length of the padded message m' is a multiple of 512.

(2) Iteration: Group the padded message m′ according to 512 bits

$$m' = B^{(0)}B^{(1)} \ldots B^{(n-1)} \tag{1}$$

$$n = (l + k + 65)/512 \tag{2}$$

(3) Expand: Expand the message group $B^{(i)}$ to 132 words [W_0 , W_1,..., W_{67}],[w_0, w_1,..., w_{63}]:

- Divide the message group Bi into 16 words;
- FOR j = 16 To j = 67:

$$W_j \leftarrow P_1\left(W_{j-16} \oplus W_{j-9} \oplus \left(W_{j-3} \lll 15\right) \oplus \left(W_{j-13} \lll 7\right)\right) \oplus W_{j-6}. \tag{3}$$

$$w_j \leftarrow W_j \oplus W_{j+4}. \tag{4}$$

(4) Compression. Let A, B, C, D, E, F, G, and H be word registers. SS1, SS2, TT1, and TT2 are intermediate variables; then the compression function $V^{i+1} = CF(V^i, B^i)$ is calculated as follows:

$$ABCDEFGH \leftarrow V^i. \tag{5}$$

FOR j = 0 To 63:

$$SS_1 \leftarrow \left((A \lll 12) + E + \left(T_j \lll j\right)\right) \tag{6}$$

$$SS_2 \leftarrow SS_1 \oplus (A \lll 12) \tag{7}$$

$$TT_1 \leftarrow FF_j(A, B, C) + D + SS_2 + w_j \tag{8}$$

$$TT_2 \leftarrow GG_j(E, F, G) + H + SS_1 + W_j \tag{9}$$

$$D \leftarrow C \tag{10}$$

$$C \leftarrow B \lll 9 \tag{11}$$

$$B \leftarrow A \tag{12}$$

$$A \leftarrow TT_1 \tag{13}$$

$$H \leftarrow G \tag{14}$$

$$G \leftarrow F \lll 9 \tag{15}$$

$$F \leftarrow E \tag{16}$$

$$E \leftarrow P_0(TT_2) \tag{17}$$

END FOR

$$V^{i+1} \leftarrow ABCDEFGH \oplus V^i. \tag{18}$$

(5) Iteration: Iterate on m′ according to the following calculation steps:

FOR i = 0 to n-1,

$$V^{i+1} = CF\left(V^i, B^i\right). \tag{19}$$

END FOR

Among them, CF is the compression function, V^0 is the initial value of 256 bits, B^i is the packed group, and the compressed result of n iterations is V^n.

$$V^0 = 7380166f\ 4914b2b9\ 172442d7\ da8a0600\ a96f30bc\ 163138aa\ e38dee4d\ b0fb0e4e \tag{20}$$

Trust transfer follows the following idea: first measure, then verify, and finally jump. Starting from the root of trust, each currently running component first measures the next-level component to be run next, and then verifies its security according to the metric value. If its integrity meets the requirements, then the current-level component can jump to the lower-level component after running. Otherwise, it means that the lower-level components are unexpected, and the establishment of the trust chain is suspended.

4.3 Running Mode of the Embedded Trusted Computing

Based on the abovementioned static measurement technology, trust can be transferred from the root of trust to the uppermost application layer software to establish a complete static trust chain system. The construction of the static trust chain of the computer system is mainly divided into hardware startup code (BootROM or BIOS), Bootloader, and operating system. The idea of establishing the trust chain in each stage is as follows: after gaining control, measuring the code that will be run at the next level, and then extending it to the corresponding secure storage on the secure chip. The static chain of the trust system is generally divided into two stages: the first stage is trusted boot, which is responsible for safely booting the system to the operating system kernel, and the second stage is operating system integrity measurement, which is responsible for measuring the executables of the operating system kernel and application layer components.

4.3.1 Trusted Boot

Trusted boot uses a static metric mechanism to check the trustworthiness of each stage of the OS booter, configuration, OS kernel image, *etc*., and stores the metric results in the security chip in order, thus ensuring the security of the OS pre-boot environment. Taking Linux Grub as an example, the main steps of a general trusted boot are as follows:

(1) When the system is powered on, the hardware startup code (BootROM or BIOS) measures the first stage code of the

platform Bootloader, that is, the Grub Stage1 code, and the measurement results are saved to the integrity storage of the security chip, and then loaded into Stage1 and executed.
(2) Grub Stage1 loads and measures the first sector in Grub Stage1.5 and expands to the integrity storage of the security chip, and then executes Stage1.5.
(3) After Grub Stage1.5 gains control, it loads and measures Grub Stage2, and expands to the integrity storage of the security chip, and then transfers control to Grub Stage2. At this point, the Bootloader grub has been fully started and can perform operating system-related loading tasks.
(4) Grub measures its configuration file grub.conf and extends it to the integrity storage of the security chip, and then measures the operating system kernel that needs to be loaded, which finally verifies the overall integrity of the kernel file.

The trusted boot system ensures the security of the OS loader itself and prevents attackers from injecting the malicious code before the OS boots. All of these lay a secure foundation for the OS boot. The trust chain construction method of the trusted boot system is similar, and its main goal is to ensure the integrity of the Bootloader's own code, the Bootloader configuration file, and the OS kernel image.

4.3.2 Chain of Trust at the Operating System Layer

The operating system trust chain construction system is used to transfer the trust established by the trusted boot to the operating system and even the application program. To ensure the security of the trust chain construction, the measurement agent of the operating system trust chain is generally implemented in the OS kernel. The operating system kernel is executed from the decompressed image, and the OS measurement agent calls the TPM to measure the kernel modules, kernel service programs, *etc*., in turn when various modules of the OS are loaded according to the execution process of the operating system, thereby completing the construction of the operating system trust chain. After the operating system is started, in order to ensure the safety of running applications, the simplest idea is that each program can be executed after being measured by the OS measurement agent when it is loaded. This trust chain construction method can also cooperate with the program's black and white list mechanism to further enhance the security of system operation.

4.4 Logic of the Designed Trusted Computing Program

The core function of the trusted computing program is measurement and management. In the normal mode, the trusted computing program only measures executable programs. In the management and control mode, the trusted computing program simultaneously measures and controls executable programs. The overall program logic of these two modes is described in the following text.

4.4.1 Normal Mode Program Operation Logic

In the normal mode, when the actual power application is running on the power device, the program operation logic of the trusted computing program is shown in **Figure 4**, which is summarized as follows:

(1) The executable program of the power application is loaded and run by the system.
(2) The kernel module captures the loading behavior of the executable program by implanting HOOK functions.
(3) Before the specific operation, the captured executable program image is delivered to the trusted computing program measurement module.
(4) The trusted computing program measurement module invokes the function of the cryptographic module and uses the SM3 algorithm to measure the executable program image.
(5) The measurement results are added to the measurement log, and all the power applications that have been run by the system are recorded in the measurement log to form a snapshot of the current operating status of the power installation system.
(6) The kernel transmits the measurement log to the application layer measurement agent through the pipeline.
(7) The measurement agent further transmits the measurement log to the GUI interface through a communication mechanism (such as socket) for the administrator to observe the measurement log in real time and grasp the current operating status of the power device.

4.4.2 Operation Logic of Control Mode Program

In the management and control mode, the program operation logic of the trusted computing program is more complicated, as shown in **Figure 5**, which can be divided into two stages: the strategy generation stage and the specific operation stage.

4.4.2.1 Strategy Generation Stage

In the strategy generation stage (the lower part of **Figure 6**), the power device is initially installed and in an initial credible state. The administrator uses the knowledge base collection tool of the trusted computing program to formulate the whitelist. The program logic of the strategy generation stage is summarized as follows:

(a) The initial installation of the power device is completed, and the expected operating power application is deployed to the device according to the application scenario requirements of the device.
(b) The administrator enters the path where the expected power application is located and calls the trusted computing program knowledge base collection tool.
(c) The knowledge base collection tool will recursively search for executable programs in the specified path, call the SM3 measurement algorithm of the cryptographic module to hash all the executable programs, and add all the generated measurement results to the knowledge base to generate "expected executable programs knowledge base."
(d) The administrator operates the knowledge base by adding, deleting, modifying, checking, *etc*., and it sets the executable programs that are allowed to run on the power device to be

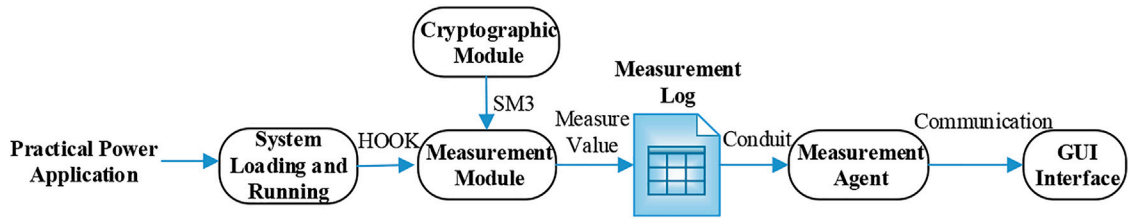

FIGURE 4 | Program running logic of the trusted computing program in the normal mode.

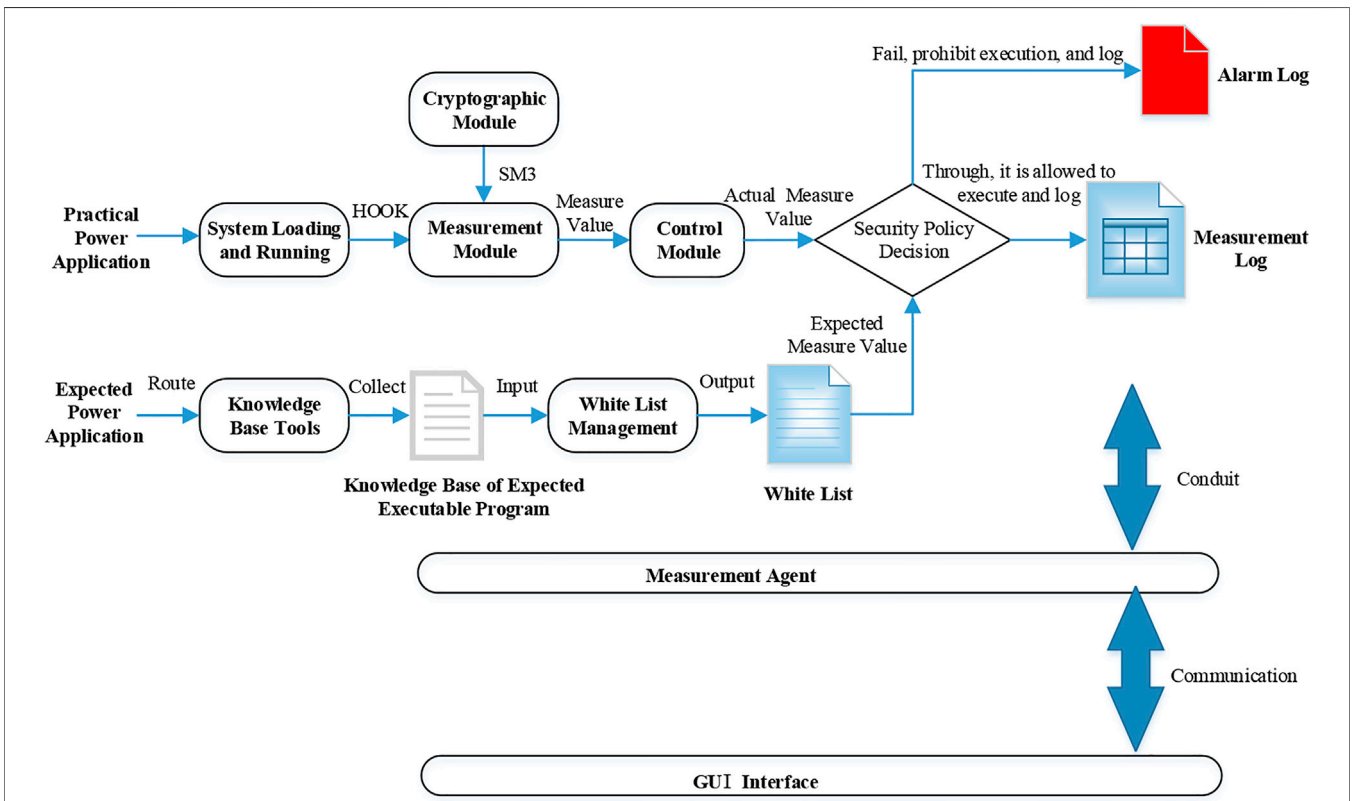

FIGURE 5 | Program operation logic of the trusted computing program in the control mode.

trusted, and the programs that are not allowed to run on the power device to be untrusted. The whitelist of the execution program is used by the kernel management and control module to execute the security policy.

4.4.2.2 Specific Operating Stage

In the specific operation stage (as shown in the upper part of **Figure 5**), the power device is already in the daily operation stage, and may be infected with viruses or be implanted with the malicious code. At this time, the trusted computing program will play a safe role in the control mode. The specific program logic at this stage is summarized as follows:

(a) The executable program of the actual power application is loaded and run by the system.

(b) The kernel module captures the loading behavior of the executable program by implanting HOOK hooks.

(c) Before the specific operation, the captured executable program image is handed over to the trusted computing program measurement module.

(d) The trusted computing program measurement module calls the function of the cryptographic module and uses the SM3 algorithm to measure the executable program image.

(e) The trusted computing program measurement module transmits the real-time measurement value to the trusted computing program management and control module.

(f) The trusted computing program management and control module enters the integrity verification program. The main logic is to match the actual measurement value of the measurement module with the expected measurement

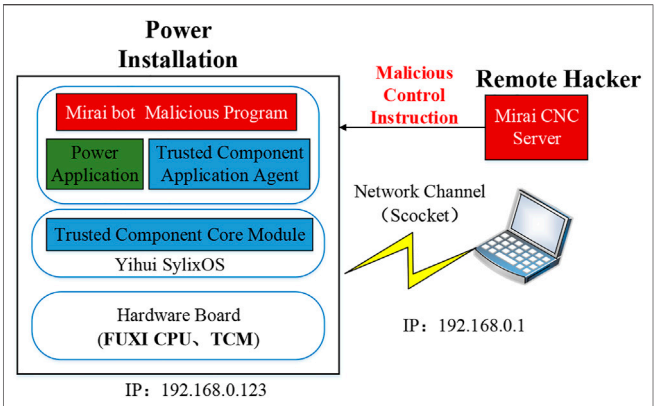

FIGURE 6 | Test environment.

value in the whitelist and give a security judgment based on the matching result. Those that meet the whitelist policy are considered acceptable and credible, and those that do not meet the whitelist strategy are considered untrustworthy.

(g) If it is judged to be credible, it means that the actual power application executable program has passed the security policy, and the management and control module will execute it to allow it to execute, restore its loading and operation to the normal system process, and record the measurement value in the measurement log.

(h) If it is judged to be untrustworthy, it means that the actual power application executable program has not passed the security policy. The control module will take over the normal system operation process, prohibit the program execution, and treat the attempted execution of the program as a malicious event, and the relevant information is recorded in the alarm log.

(i) Data generated by the trusted computing program such as whitelist, measurement log, and alarm log will be passed to the application layer measurement agent through the pipeline. The measurement agent further transmits the whitelist and log information to the GUI interface for display through other communication mechanisms (such as socket) for the administrator to view.

(j) At the same time, the GUI interface can receive the control instructions of the administrator and pass them to the measurement agent through the communication mechanism. The measurement agent is further passed to the trusted computing program of the kernel layer through the pipeline. The trusted computing program can complete the desired operation according to the control instruction, such as setting whitelist, set control mode, and clear blank list.

5 EXPERIMENTAL VERIFICATION

The experimental environment is shown in **Figure 6**. It consists of four parts: power terminal, remote hacker, management and control terminal, and debugging terminal. The four parts are interconnected through switch networking.

The power terminal used in the experiment is a distribution terminal unit (DTU) device, which is composed of hardware plug-ins, operating system, and application programs. It is developed based on the FUXI chip that is reached and developed by the China Southern Power Grid Digital Grid Research Institute, and the SylixOS operating system. The device is embedded with the built-in credibility component core module and trusted computing component application agent. In this experiment, Mirai CNC server simulates the remote attack hackers who access the network. The control terminal is used to enable control of the trusted computing components and display the measurement value of the measured program in the measurement log and alarm log.

The test environment is shown in the following text:

The trusted computing component is installed in the operating system kernel, as shown in **Figure 7**.

The authors have selected a dataset consisting of multiple executable programs. Some programs in this dataset are commonly used as power applications, some programs are third-party software libraries (such as OPENSSL), and some programs are simulated as malicious codes. For this dataset, a stress test script TCC_CompressionTest.sh is written, which selects programs from the dataset to trigger running every 10 s, and runs the script for a period of time to test the detection rate of illegal programs by the trusted computing program.

$$\text{Illegal program detection rate} = \frac{\text{the actual number of illegal programs detected n}}{\text{the test number of illegal programs injectedN}} \times 100\%$$

A sample set includes legal programs, illegal programs, and unknown programs, which is constructed on the actual power device. Through the brute force cycle test, the program is randomly selected from the sample set to trigger and run every 10 s, and it runs continuously, and then the effect of the trusted computing program on illegal programs is checked.

The components are tested by brute force injection of illegal programs. The test methods are as follows:

First, testing the real-time measurement function of the trusted computing component by running the env program that displays the operating environment of the system, which is shown on the QE interface. As we can see in **Figure 8**, the measurement value of the env program and the measurement value of the dependent library file libvpmpdm.so are all captured in real time.

Next, testing the security protection capabilities of the tested DTU device under malicious program operation. The implementation process is as follows:

Implanting a malicious program “portmap.cid” disguised as a configuration file through the MMS protocol to demonstrate the isolation function of the power terminal against malicious programs. The power terminal is interconnected with the monitoring system through the MMS protocol, and through the file service function provided by the MMS protocol, the

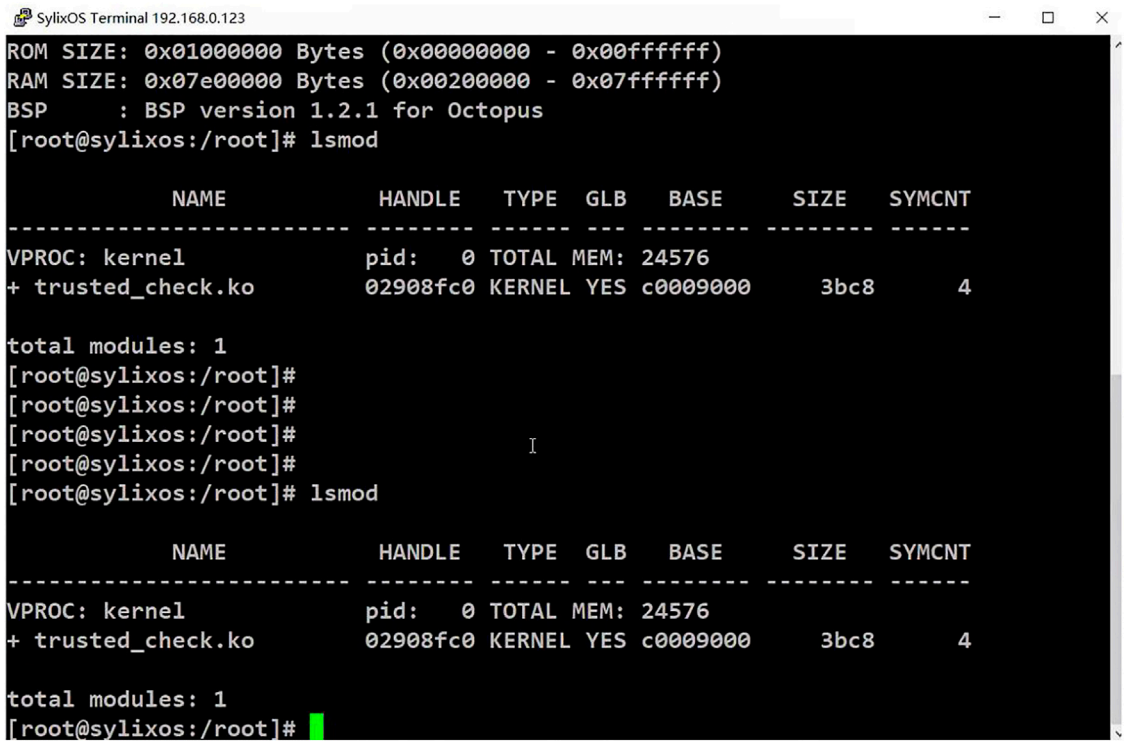

FIGURE 7 | Trusted_check.ko.

FIGURE 8 | Measurement value of the env program and the library file libvpmpdm.so.

malicious program disguised as a normal file "portmap.cid" is implanted in the device and called for operation.

It can be seen from **Figure 9** that "portmap.cid" is identified as an illegal program since there exists difference between the measurement value of "portmap.cid" disguised as a normal file and the measurement value of the real portmap.cid in the whitelist. The trusted computing component isolates the malicious program, and the malicious program cannot run.

In order to evaluate the impact of integrity measurement on the operating system loading and application loading of relay protection devices, the time performance of using the SM3 algorithm to obtain encrypted summary information is tested. In order to standardize test indicators, the integrity of 10KB data is measured uniformly, and the measurement time is recorded. **Figure 10** shows the results of 100 tests.

It can be seen from **Figure 10** that in 100 tests, the highest value is 0.719 ms/10KB and the lowest value is 0.586 ms/10KB, both less than 1 ms, indicating that the integrity measurement will not have a great impact on the system startup time and application loading time.

According to the test process described previously, an illegal virus implanted program disguised as a configuration file is transmitted to the DTU device through the MMS

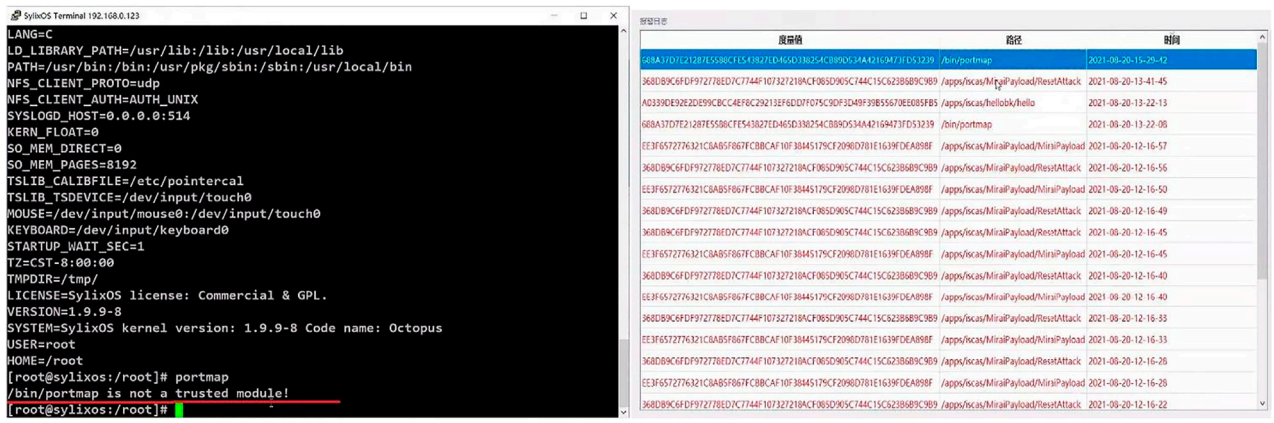

FIGURE 9 | A malicious program "portmap.cid" is identified as an illegal program.

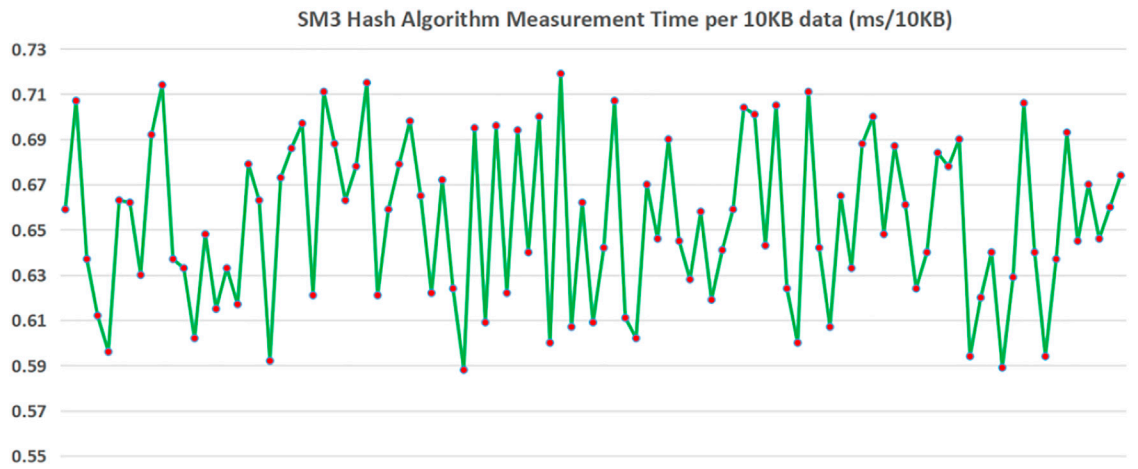

FIGURE 10 | A malicious program "portmap.cid" is identified as an illegal program.

protocol and loaded. In 300 repeated tests, the illegal program is detected 300 times, indicating that the detection rate of illegal programs by a test is 100%. Actually, on the premise that the physical security of the static root of trust is guaranteed, the trust chain is trusted to execute in the expected order of bootloader, OS, and APP, and all illegal programs can be detected.

6 CONCLUSION

With the advancement of the construction of the Energy Internet, a large number of terminal devices and multiple users have been connected to the power grid, gradually forming an open and interactive network environment, which has greatly changed the existing state grid's hierarchical and partitioned information security protection pattern with the vertical encryption and horizontal isolation. Once a threat invades, is adsorbed to the terminal equipment, or breakthrough the boundary protection, it will be unimpeded, and it is easy to cause major power grid safety accidents. In summary, this article proposes a network security protection scheme for power system embedded devices based on chip-level trusted computing. The main technical contributions are as follows:

(1) Designing the overall architecture of the chip-level trusted computing for power equipment.
(2) Proposing a method of using the on-chip SRAM of the main control chip as the PUF to construct the root of trust.
(3) Designing the program logic of the trusted computing component.
(4) Transplanting and applying the self-developed FUXI chip of the China Southern Power Grid and Sylix OS operating system in a distribution automation DTU device, and conduct the performance tests and safety protection tests.

The power system terminal chip-level trusted computing security protection solution developed in this article is suitable for the management needs of the future smart grid information security, and provides technology assurance for the construction of an open power business ecosystem with Chinese domestic chips as the core and the implementation of power Internet of Things technology.

DATA AVAILABILITY STATEMENT

The original contributions presented in the study are included in the article/Supplementary Material. Further inquiries can be directed to the corresponding author.

AUTHOR CONTRIBUTIONS

WX contributed to the conception of the study, YY performed the experiment, QF and HY contributed significantly to analysis and manuscript preparation, WX and XL wrote the manuscript, and TC helped perform the analysis with constructive discussions.

FUNDING

This work was supported by the Science and Technology Project of China Southern Power Grid Digital Power Grid Research Institute (Grant No. 670000KK52200002).

REFERENCES

3rd Generation Partnership Project(3GPP) (2018b). *3GPP TS 33. 163 Battery Efficient Security for Very Low Throughput Machine Type Communication (MTC) Devices (BEST) V16. 0.0*. http://www.3gpp.org/ftp/Specs/archive/33-series/33.163/33163-g00.

3rd Generation Partnership Project(3GPP) (2018a). *3GPP TS 33. 220 Generic Authentication Architecture (GAA):generic Bootstrapping Architecture (GBA) V15.3.0*. http://www.3gpp.org/ftp/Specs/archive/33-series/33.220/33220-f30.

Avizienis, A., Laprie, J.-C., Randell, B., and Landwehr, C. (2004). Basic Concepts and Taxonomy of Dependable and Secure Computing. *IEEE Trans.Dependable Secure Comput.* 1, 11–33. doi:10.1109/tdsc.2004.2

Bedi, G., Venayagamoorthy, G. K., Singh, R., Brooks, R. R., and Wang, K.-C. (2018). Review of Internet of Things (IoT) in Electric Power and Energy Systems. *IEEE Internet Things J.* 5 (2), 847–870. doi:10.1109/JIOT.2018.2802704

Ciavarella, S., Joo, J.-Y., and Silvestri, S. (2016). Managing Contingencies in Smart Grids via the Internet of Things. *IEEE Trans. Smart Grid* 7 (4), 2134–2141. doi:10.1109/TSG.2016.2529579

Efe, A., and Güngör, M. O. (2019). The Impact of Meltdown and Spectre Attacks. *Int. J. Multidiscip. Stud. Innovative Technol.* 01, 38–43.

Feng, D. G., Liu, J. B., Qin, Y., and Feng, W. (2020). Trusted Computing Theory and Technology in Innovation-Driven Development. *Sci. Sin.* 50 (08), 1127–1147. doi:10.1360/ssi-2020-0096

Feng, D. G., Qin, Y., Wang, D., et al. (2011). Research on Trusted Computing Technology. *J. Comput. Res. Dev. Chin.* 48 (8), 1332–1349.

Feng, W., Qin, Y., Feng, D. G., Yang, B., and Zhang, Y. J. (2015). Design and Implementation of Secure Windows Platform Based on TCM. *J. Commun.* 36 (8), 91–103.

Guo, Q. L., Xin, S. J., and Sun, H. B. (2016). Comprehensive Security Assessment for a Cyber Physical Energy System:a Lesson from Ukraine Blackout. *Automation Electr. Power Syst. Chin.* 40 (5), 145–147.

Kolias, C., Kambourakis, G., Stavrou, A., and Voas, J. (2017). DDoS in the IoT: Mirai and Other Botnets. *Computer* 50 (7), 80–84. doi:10.1109/mc.2017.201

Kylanpaa, M., and Ekberg, J.-E. (2007). *Mobile Trusted Module (MTM)-an Introduction*. Ecoli http://research.nokia.com/files/NRCTR2007015.pdf.

Li, D. (2019). Analysis of Stuxnet Virus Incident and Enlightenment of Improving Industrial Control Security Protection Ability. *Netw. Secur. Technol. Appl.* 01, 9–10+24. (in Chinese).

Liu, R., Vellaithurai, C., Biswas, S. S., Gamage, T. T., and Srivastava, A. K. (2015). Analyzing the Cyber-Physical Impact of Cyber Events on the Power Grid. *IEEE Trans. Smart Grid* 6 (5), 2444–2453. doi:10.1109/tsg.2015.2432013

Liu, Z. L., Liu, B. J., Lu, Z. J., and Tong, Q. L. (2015). FPGA Design of Low Resource Consumed Arbiter PUF. *J. Huazhong Univ. Sci. Technol. Sci. Ed.* 44 (02), 5–8+14. (in Chinese).

Mispan, M. S., Halak, B., Chen, Z., et al. (2015). "TCO-PUF: a Subthreshold Physical Unclonable function[Conference Presentation]," in 2015 11th Conference on Ph.D. Research in Microelectronics and Electronics (PRIME) (Glasgow, UK.

National Development and Reform Commission of China (2014). *Development and Reform Commission Order No. 14 Electric Power Monitoring System Safety Protection Regulations*. [Standard].

Office of State Commercial Cipher Administration (2006). *Block Cipher for WLAN Products-SMS4*. http://www. oscca.gov.cn/Up File/200602101642319790. pdf.

Office of State Commercial Cipher Administration (2012). *SM2 Elliptic Curve Public Key Cryptography Algorithm*. http://www. oscca.gov.cn/Up File/20101222148226 92.pdf.

Office of State Commercial Cipher Administration (2010). *SM3 Hash Cipher Algorithm*. http://www.oscca.gov.cn/index.htm.

Park, L., Lee, C., Kim, J., Mohaisen, A., and Cho, S. (2019). Two-Stage IoT Device Scheduling with Dynamic Programming for Energy Internet Systems. *IEEE Internet Things J.* 6 (5), 8782–8791. doi:10.1109/JIOT.2019.2923432

Song, J. (2019). "Level-shifter Current Influence to Power Loss of Gate Driver IC [Conference Presentation]," in International Exhibition and Conference for Power Electronics, Intelligent Motion, Nuremberg, Germany (Renewable Energy and Energy Management).

Srinivas, J., Das, A. K., Li, X., Khan, M. K., and Jo, M. (2021). Designing Anonymous Signature-Based Authenticated Key Exchange Scheme for Internet of Things-Enabled Smart Grid Systems. *IEEE Trans. Ind. Inf.* 17 (7), 4425–4436. doi:10.1109/TII.2020.3011849

Sun, C., Liu, D., Ling, W. S., and Lu, Y. M. (2014). Research on Trustiness of Remote Terminal Units in Distribution Automation. *Power Syst. Technol.* 38 (3), 736–743.

Trusted Computing Group (2017b). *TCG Software stack(TSS) Specification. Version 1.10*. Ecoli http://www.trustedcomputinggroup org/developers/software_stack.

Trusted Computing Group (2017a). *TCG Specification Architecture Overview. Version 1. 2*. E.coil. https://www trustedcomputinggroup.org.

Trusted Computing Group (2017c). *TNC Architecture for Interoperability*. E coli http://www trusted-computing group org/resources/tnc_architecture_for_interoperability_specification.

Wang, Z. N. (2018). *Research on Information Security of Electric Energy Data Acquirsition Terminals Based on Trusted Computing*. Beijing, China: North China Electric power university.

Xu, R. H. (2014). *The Research and Implementation of Embedded Power Distribution Terminal Based on Trusted Computing*. Beijing, China: North China Electric power university.

Yu, H. Y., and Guan, C. L. (2021). The Cronier Security Incident in the U.S. A Warning to My Country's Energy Security Resilience. *Energy(in Chin.* 6, 26–29.

Zhang, L. (2019). Research on Trusted Computing Technology for Collection Terminal under Power IoT. *Electron. Components Inf. Technol.* 3 (12), 113–116.

Zhang, S. M., Wang, Z. N., and Wang, B. Y. (2017). Terminal Integrity Detection Scheme of Electricity Information Acquisition System Based on Trusted Computing. *Electr. Power Autom. Equip.* 37 (12), 60–66.

Zhang, T., Zhao, D. Y., Xue, F., et al. (2019). Research Framework of Information Security Protection Technology for Intelligent Terminals in Power System. *Automation Electr. Power Syst. Chin.* 43 (19), 1–8.

Zheng, T. F. (2019). *Research on Information Security of Smart Meter Based on Trusted Computing*. Beijing, China: North China Electric power university.

Conflict of Interest: The authors declare that the research was conducted in the absence of any commercial or financial relationships that could be construed as a potential conflict of interest.

Publisher's Note: All claims expressed in this article are solely those of the authors and do not necessarily represent those of their affiliated organizations, or those of the publisher, the editors, and the reviewers. Any product that may be evaluated in this article, or claim that may be made by its manufacturer, is not guaranteed or endorsed by the publisher.

frontiers | Frontiers in Energy Research

TYPE Original Research
PUBLISHED 08 August 2022
DOI 10.3389/fenrg.2022.865060

OPEN ACCESS

EDITED BY
Yan Xu,
Nanyang Technological University, Singapore

REVIEWED BY
Wei Liu,
Chengdu University of Technology, China
Xue (Elsa) Feng, Singapore Institute of Technology, Singapore

*CORRESPONDENCE
Liang Liu,
liu_0826@126.com

SPECIALTY SECTION
This article was submitted to Smart Grids, a section of the journal Frontiers in Energy Research

RECEIVED 29 January 2022
ACCEPTED 05 July 2022
PUBLISHED 08 August 2022

CITATION
Liu C, Wang W, Wang Z, Chen S, Su P, Gao H, Xu C, Ge B, Ding H and Liu L (2022), Optimal operation and locating method of new energy building with shared charging service. *Front. Energy Res.* 10:865060. doi: 10.3389/fenrg.2022.865060

Optimal operation and locating method of new energy building with shared charging service

Chang Liu[1], Wei Wang[1], Zhixun Wang[2], Shangfa Chen[1], Peifang Su[1], Hongyuan Gao[1], Chao Xu[1], Biyuan Ge[3], Hongfa Ding[4] and Liang Liu[5]*

[1]Changjiang Institute of Survey, Planning, Design and Research, Wuhan, China, [2]State Grid Hubei Economic Research Institute, Wuhan, China, [3]Department of Architecture, Technical University of Darmstadt, Darmstadt, Germany, [4]School of Electrical and Electronic Engineering, Huazhong University of Science and Technology, Wuhan, China, [5]College of Energy and Power Engineering, Changsha University of Science and Technology, Changsha, China

In order to cope with global climate change, an electric vehicle (EV) and new energy building are constantly being innovated and improved. With the popularity and application of big data and Internet of Things, the new energy building with available charging piles may also become a charging station, which can solve the problem of difficult charging of EVs and promote the local energy consumption of the building. Therefore, this study proposes a shared charging concept for buildings, that is, shared photovoltaic, charging, and energy storage building (sPCEB). First, based on the analysis results of big data in cities or settlements of people, a locating method of the sPCEB system is introduced, and further proposes an optimal operating strategy that maximizes the combined benefit of the building. The efficiency and effectiveness of the proposed methods are verified by simulation.

KEYWORDS

location problem, data analysis, new energy building, analytic hierarchy process, electric vehicle, optimal operating strategy, mixed-integer linear programming

1 Introduction

On 12 December 2015, nearly 200 parties of the *United Nations Framework Convention on Climate Change* reached the *Paris Agreement* at the *21st United Nations Climate Change Conference*. This is the second legally binding climate agreement after the *Kyoto Protocol*, setting out arrangements for global action to address climate change after 2020. According to the US Environmental Protection Agency, buildings are one of several major sources of global greenhouse gas emissions.

In 2020, China proposed a major strategy to achieve "peak carbon dioxide emissions" by 2030 and "carbon neutrality" by 2060, and the key to carbon reduction lies in replacing the massive use of non-renewable fossil fuels with electrification of production and living. Actually, buildings should also move from being energy consumers to being contributors that support large-scale clean energy access, and integrating energy use, capacity, and storage into one (Feng et al., 2019; Huanan and Quande, 2019; Heinstein et al., 2013).

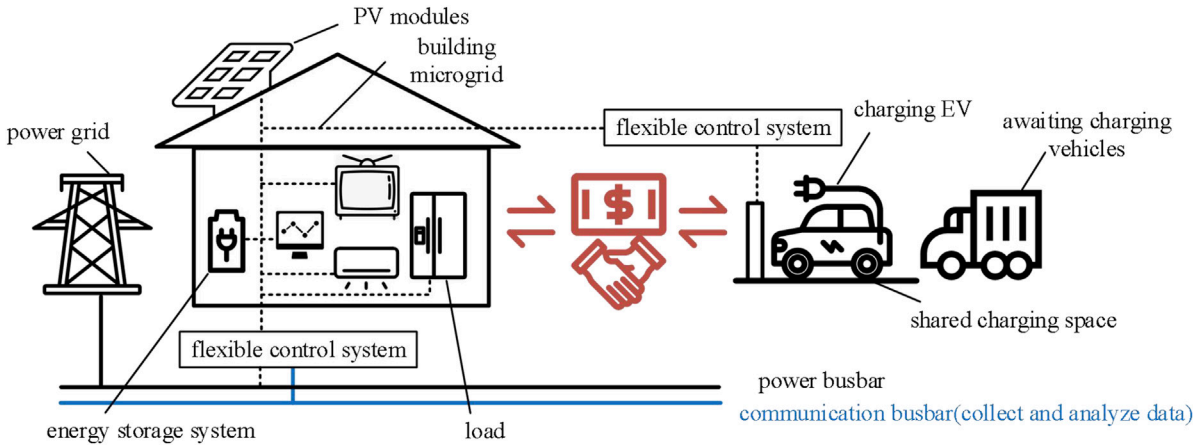

FIGURE 1
Schematic diagram and operation of an sPCEB system.

Therefore, the concept of a new energy building is created, which is realized through the following ways: first, the way of building electricity consumption is changed to "supply-oriented, demand responsive", that is, the electrical device flexibly adjusts the use time according to the actual photovoltaic (PV) power generation status and consumes the power in time when the power capacity is sufficient or suspends/reduces the power consumption; second, the internal storage system is developed to cover the shortage of electricity dynamically; third, the storage and consumption capacity of the electric vehicle is dynamically used to flexibly meet the building power demand (Igor et al., 2012; Kapsalaki et al., 2012).

At present, the percentage of electric vehicles (EVs) in the global automotive market is further expanding, but the charging problem becomes an obstacle to increasing the penetration of EV. With the popularization and application of big data and Internet of Things, the new energy building system may also become a charging station, which is an effective way to solve the charging problem. Therefore, this study proposes a concept of shared photovoltaic, charging, and energy storage building (sPCEB), that is, the sPCEB system uses the analysis results of big data to provide short-term charging services for public EV users by the surplus PV power or storage energy on the basis of satisfying its own electricity consumption.

In order to successfully implement the shared charging service in a building system, it is necessary to solve the location problem of the sPCEB system at first. A proper location can provide favorable prerequisites for the effective operation of the sPCEB system. Then, the optimal operation of the shared charging strategy should be further combined with the energy use of the sPCEB system itself. Therefore, this article first proposes a sPCEB system locating method based on an improved analytic hierarchy process (AHP), on the basis of determining the location, an optimal operation of the sPCEB system is further proposed, which can maximize the combined benefits of society, environment, the building, and the EV users.

2 Shared operation mode of shared photovoltaic, charging, and energy storage building system

Figures 1 shows the schematic diagram of sPCEB system operation. The main connection line is the power busbar, the PV modules, energy storage system, and loads in the building are connected together in the building microgrid, and the communication between the modules is connected by applying the communication busbar. The energy generated from the PV module is first consumed in the building itself, and then the sPCEB system is connected to the external power grid based on signals from the flexible control system. Unlike ordinary buildings, the sPCEB system needs to selectively provide charging services to public EV users at specific time on the basis of its current power supply and consumption. The public EV users are required to pay for the charging service according to payment rules, which is also one of the revenue sources of the sPCEB system.

3 Locating method for shared photovoltaic, charging, and energy storage building system

As mentioned earlier, the sPCEB system has two functions: providing daily energy for the building and providing shared EV

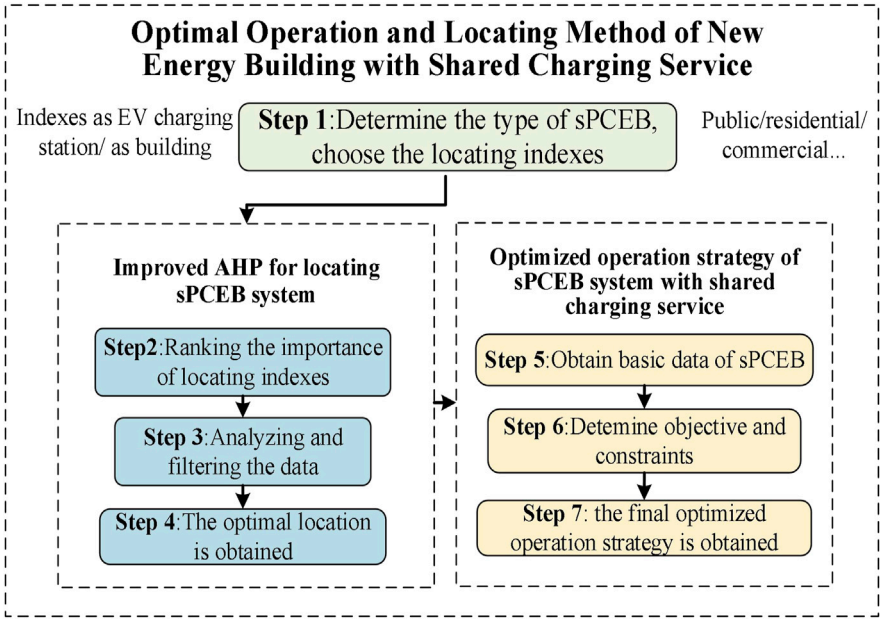

FIGURE 2
Flow chart of the proposed method.

charging service. Therefore, it is not only necessary to select the location of the building according to the general planning of the region but also to establish a locating model based on the spatial distribution of the EV users' charging demand in the region. The locating method in this article requires a thorough consideration of multiple aspects from the perspective of both the EV charging station and the building.

3.1 Indexes as electric vehicle charging station

3.1.1 Traffic flow

On the one hand, the traffic flow reflects the development, on the other hand, the charging demand becomes higher when the EV penetration rate is higher (Bheema and June, 2017; Michael et al., 2021; Sayali et al., 2021). The traffic data in the analyzed region should be collected, and some typical days are selected as the samples. The data mainly include the traffic flow of EVs and traditional petrol vehicles, represented as M and N, respectively. The index of traffic flow is defined as:

$$L = \omega_1 M + \omega_2 N, \tag{1}$$

where ω_1 and ω_2 are the weights of M and N, respectively.

3.1.2 Public transport accessibility

The concept of accessibility was first introduced by Hansen, an American scholar (Hansen, 1959). It indicates the opportunities for the transportation network to interact with each other and is mainly used in the study of urban land use (Muhammad et al., 2018; Albacete et al., 2017). It is necessary to consider how convenient it is for public EV users to reach the sPCEB system once charging is complete.

$$y = \frac{1}{1 + \left(\frac{d}{D}\right)^3} \tag{2}$$

$$y_{final} = \sum_{i=1}^{n} \omega_n y_n. \tag{3}$$

The distance y for public transport accessibility is defined as shown in Eq. 2. d is the straight-line distance (Euclidean distance) from the location to the nearest traffic node and D is the average walking distance based on the type of traffic node. The average walking distance to the bus station is defined as 150 m and the average walking distance to the subway station is 450 m (Olszewski and Wibowo, 2005). Different weights ω are given to bus stations and subway stations respectively, and the maximum value of each public transport accessibility is multiplied by the corresponding weight as the final value, as shown in Eq. 3.

3.1.3 Population density

Population density distribution reflects the dynamics of economic activity and is therefore an important determinant in sPCEB system's location selection. Larger population density represents larger passenger flow and better advertising effect. The population density γ is calculated as:

$$\gamma = \frac{p}{q}, \tag{4}$$

where p is the number of people in the analyzed region and q is the area of the region, usually expressed in square kilometers.

3.2 Indexes as building

The types of building are classified as residential buildings, public buildings, industrial buildings, and agricultural buildings. The industrial and agricultural buildings are generally far away from the busy area, and the demand for EV charging is comparably low, so the main building types are residential buildings and public buildings in this article. The indexes of locating residential buildings include traffic flow, public transport accessibility, regional population density, green space accessibility, and housing price. For locating public buildings, green space accessibility is not a key factor, but the building attractiveness needs to be considered.

3.2.1 Green space accessibility

Green space has become an important place for urban residents to interact and organize various activities; it plays an irreplaceable role during the development of the human living environment. The green coverage has become an important factor for discussing the ecological livability of a region, and the green space accessibility is also an important element in the locating method (Schirmer et al., 2014). Green space accessibility needs to consider the distance from the location to the green space and the area of the green space; therefore, the green space accessibility index P_i is defined as:

$$PP_i = \frac{1}{1 + \left(\frac{f_i}{150}\right)^3}, \tag{5}$$

$$PA_i = \frac{1}{1 + e^{\frac{250000 - g_i}{62500}}}, \tag{6}$$

$$P_i = \frac{PP_i}{2} + \frac{PA_i}{2}. \tag{7}$$

The distance from the location to the nearest green space is f_i, and the area of the nearest green space from the location is g_i. PP_i is the normalized value of the distance to the nearest green space, and PA_i is the normalized value of the area of the green space.

3.2.2 Housing price

High economic growth is often closely related to the increase in housing price; housing price also reflects the degree of economic development of the analyzed region. Housing price can be obtained by collecting published data using web crawler.

3.2.3 Building attractiveness

The Huff model is one of the most commonly used models in building locating; it explains the attractiveness of public buildings to users and various resistance factors for users to make decisions (Huff, 1964). Based on the Huff model, the attractiveness of building j to point i is defined as:

$$U_{ij} = S_j^{\alpha} d_{ij}^{\lambda}, \tag{8}$$

where U_{ij} is the attractiveness to users, S_j is the area of building j, and d_{ij} is the traffic cost parameter that reflects the users go from the activity point i to the building j. α and λ are sensitive parameters for S_j and d_{ij}, respectively. The value of α is 0.82 and the value of λ is -1.16 (Yandong et al., 2018).

3.2.4 Construction cost

In the engineering project, the construction and installation cost of public buildings mainly includes the installation works, outdoor, and supporting works. The main building installation work mainly includes civil engineering, water supply and drainage engineering, and electric engineering. The overall construction cost is calculated based on the construction area and is proportional to the area. Therefore, in the locating of public buildings, this article uses the floor area of public buildings to express the construction cost.

3.3 Improved analytic hierarchy process for locating shared photovoltaic, charging, and energy storage building system

Based on the process of the aforementioned data, each sPCEB system corresponds to multiple indexes. How to deal with these indexes requires further analysis and judgment. AHP is a hierarchical analysis method that combines qualitative and quantitative approaches (Muhammad 2014). The basic steps of AHP are divided into four main steps: first, the recursive hierarchy model is established; second, the judgment matrix is constructed; third, consistency test; and at last, all the options are compared and decisions are made.

In fact, the most important step of AHP is the construction of the judgment matrix; however, the traditional method has some inherent drawbacks. If there are too many elements, the statistics are large, the judgment matrix is hard to pass the consistency test, and repeatedly modifying the judgment matrix may be contrary to the original intention of the decision. Therefore, this section proposes some improvements for the traditional AHP.

TABLE 1 Improved scales in criteria.

Intensity of importance	Definition
3	Strong importance
2	Moderate importance
1	Equal importance
Reciprocals of above	If activity i has one of the aforementioned non-zero numbers assigned to it when compared with activity j, then, it has the reciprocal value when compared with i

TABLE 2 Improved scales in alternatives.

Intensity of importance	Definition
1	$\delta < 1.5$, equal importance
2	$1.5 \leq \delta < 2.5$, the importance increases
3	$2.5 \leq \delta < 3.5$, as above
4	$3.5 \leq \delta < 4.5$, as above
5	$4.5 \leq \delta < 5.5$, as above
6	$5.5 \leq \delta < 6.5$, as above
7	$6.5 \leq \delta < 7.5$, as above
8	$7.5 \leq \delta < 8.5$, as above
9	$8.5 \leq \delta < 10$, strong importance
Reciprocals of above	If activity i has one of the aforementioned non-zero numbers assigned to it when compared with activity j, then, it has the reciprocal value when compared with i

3.3.1 The construction of judgment matrix in criteria

If there are n different elements in criteria, n (n-1)/2 comparisons are required to judge the order of importance of multiple elements by using the traditional AHP. The steps of comparison will be very tedious if there are too many elements. In addition, it may also cause illogical results.

A method for constructing the judgment matrix of the criterion level based on the importance ranking is proposed. Three importance indicators of adjacent elements are defined as: strong importance, moderate importance, and equal importance. Importance indicators of non-adjacent elements can be obtained by superimposing the importance of adjacent elements. The scales of importance indicators of adjacent elements are defined as 3, 2, and 1, respectively. The improved scales are shown in Table 1.

3.3.2 The construction of judgment matrix in alternatives

Each alternative has specific values, the order of importance should be judged objectively based on the specific values. Therefore, the construction method of the judgment matrix of the alternatives based on quantitative data is further proposed. First, the data need to be normalized to range 1–10, and the scales of alternatives δ are defined as the differences between two elements. According to the definition of the scales of alternatives in Table 2, the judgment matrix in alternatives can be constructed.

According to the aforementioned improvements, the optimal location can be directly selected by applying the AHP with simply giving an order of importance to the elements in alternatives and criteria.

4 Optimized operation strategy of shared photovoltaic, charging, and energy storage building system with shared charging service

After determining the location of the building, a strategy for optimizing the operation of the sPCEB system with shared charging services is further proposed. The optimization objective is to maximize the combined benefits created by the building, and the main constraint is that the building's annual purchase of non-renewable energy from the power grid cannot be greater than the amount of the electricity sold to the power grid in the context of market-based electricity trading. Based on the floor area of the building, the area where PV modules can be installed, and the different photoelectric conversion efficiencies of the roof/wall, the required PV capacity, energy storage device capacity, charging and discharging power of energy storage system, and the purchased and sold electricity to the power grid are solved. It belongs to the field of mixed-integer linear programming (MILP), thus an optimization model is needed (Danhong et al., 2021; Qiwei et al., 2021).

4.1 Objective function

As a low-carbon and energy-efficient building system, the optimization objective of the sPCEB system is defined as the maximization of the combined benefits that the building brings to the overall society, that is, the difference between the incremental benefit S and the incremental cost C.

4.1.1 Incremental benefit S

Incremental benefits include three elements: incremental economic benefits S_{ec}, incremental environmental benefits S_{en}, and incremental social benefits S_{so}. Incremental economic benefits S_{ec} are defined as economic benefits S_{ec1} obtained by owners from the sPCEB system and economic benefits S_{ec2} gained by shared charging services.

$$S_{ec} = S_{ec1} + S_{ec2}, \tag{9}$$

$$Q_{pv} = \left(\lambda_1 P_{pv} s_1 + \lambda_2 P_{pv} s_2\right) \frac{H}{G_{st}}, \tag{10}$$

$$S_{ec1} = \left(\sum_{i=1}^{n} Q(i)_{pv} I(i)_{pur}\right)(s_1 + s_2), \tag{11}$$

$$S_{ec2} = \sum_{i=1}^{n} Q(i)_{\text{share}} I(i)_{\text{share}}, \tag{12}$$

where Q_{pv} is the annual power generation capacity of the building through its PV modules. P_{pv} is the power generated by the PV modules, λ_1 and λ_2 are the power generation coefficients of the top surface and sunny side of the building, respectively, G_{st} is the reference value of solar irradiance, and H is the actual value. I_{pur} is the saved electricity cost, s_1 is the area of PV modules installed on the top surface, and s_2 is the area of PV modules installed on the sunny side. n is the number of hours in a year. Q_{share} is the amount of charging power provided to public EV users, and I_{share} is the revenue from charging.

4.1.2 Incremental cost *C*

The incremental cost mainly include the device cost C_{pv}, C_{store}, the electricity cost/revenue C_{grid}, and the operation and maintenance cost C_{op}.

$$C_{pv} = (s_1 + s_2) I_{pv}, \tag{13}$$

$$C_{store} = CA_{store} I_{store}, \tag{14}$$

$$C_{grid} = \sum_{i \neq j}^{n} P(i)_{buy} C(i)_{buy} - P(j)_{sell} C(j)_{sell}, \tag{15}$$

$$C_{op} = a \cdot (s_1 + s_2) + b \cdot CA_{store}, \tag{16}$$

where C_{pv} is the total cost of PV modules, and I_{pv} is the cost of PV modules per square meter. C_{store} is the cost of energy storage system. CA_{store} is the capacity of the energy storage, and I_{store} is the unit cost. P_{buy} is the electricity purchased from the grid, P_{sell} is the electricity sold to the grid, and C_{buy} and C_{sell} are the purchase and sale prices of electricity, respectively. a and b are the operation and maintenance costs per unit of the PV module and energy storage system.

4.2 Constraints

4.2.1 Energy storage system

Considering that the scenario of this article is the energy storage system for buildings, the current form of energy storage applied in buildings is still mainly battery energy storage, such as lithium battery energy storage. At present, the charging/discharging power of household energy storage is about 5–20 kW (Sonnen Home Energy Storage, 2022; Tesla Powerwall, 2022). The state of charge SOC_t of the energy storage system at moment t is determined by the state of charge at the previous moment SOC_{t-1} and the charge/discharge power. It is also controlled by the upper and lower limits of its own maximum charge/discharge power, as shown in formula Eqs 17–19.

$$SOC_{\min} \leq SOC_t \leq SOC_{\max}, \tag{17}$$

$$SOC_t = SOC_{t-1} + \left(P^c_{t-1}\eta_c - P^d_{t-1}/\eta_d\right)\Delta t \quad \forall t \in [2, 24], \tag{18}$$

$$\begin{cases} 0 \leq P^c_t \leq P^c_{\max} \\ 0 \leq P^c_t \leq Ku \\ 0 \leq P^d_t \leq P^d_{\max} \\ 0 \leq P^d_t \leq K(1-u) \end{cases}, \tag{19}$$

$$E_{store} = E_{store,cal}/\varepsilon, \tag{20}$$

where Δt is the time interval, P^c_{t-1} is the charging power at t-1, P^d_{t-1} is the discharging power at moment t-1, and η_c and η_d is the charging/discharging efficiency of the energy storage system. P^c_{max} and P^d_{max} are the maximum charge/discharge power of the energy storage system, respectively. u is the charge/discharge state, where *1* represents charging and *0* represents discharging. k is a large constant and is used as an auxiliary constraint. E_{store} is the actual capacity of the sPCEB system, and $E_{\text{store,cal}}$ is the calculated capacity. ε is the protection coefficient to avoid over discharging of the storage system; in this article, the protection coefficient is taken as 0.8.

4.2.2 Shared charging service fees

Public EV users need to pay charging service fees M_{charge} for charging at public charging facilities. The sPCEB system can settle specific charging service fees within the upper limit $M_{\text{charge,max}}$:

$$0 \leq M_{\text{charge}} \leq M_{\text{charge, max}}. \tag{21}$$

4.2.3 Area of photovoltaic modules

The area constraint of PV modules S_{pv} is determined according to the building and location; $S_{\text{pv,max}}$ is the maximum area of PV modules that can be installed in the building:

$$0 \leq S_{pv} \leq S_{pv, \max}. \tag{22}$$

4.2.4 Time-of-use tariff

The time-of-use tariff policy is different for each area. Taking a province in the middle and lower reaches of the Yangtze River as an example, the tariff policy is shown as:

$$C(t)_{buy} = \begin{cases} P_b & t = [07{:}\,00, 09{:}\,00] \cup [15{:}\,00, 20{:}\,00] \cup [22{:}\,00, 23{:}\,00] \\ 1.49P_b & t = [09{:}\,00, 15{:}\,00] \\ 1.80P_b & t = [20{:}\,00, 22{:}\,00] \\ 0.48P_b & t = [23{:}\,00, 07{:}\,00] \end{cases}, \tag{23}$$

where C_{buy} represents the electricity tariff. P_{b} represents the price of the electricity in ordinary hours (7:00~9:00 a.m., 15:00 ~ 20:00 p.m., and 22:00–23:00 p.m.).In China, the price of C_{sell} ranges from 0.35 to~ 0.5 yuan/kWh. Because the electricity price varies from different region or area, the aforementioned time-of-use tariff model is used in this article as a reference, it

can be adjusted according to the actual situation in practical application.

4.2.5 Power balance

The power balance equation at moment t of the busbar:

$$P(t)_{\mathrm{PV}} + P(t)_{\mathrm{buy}} + P(t)_{\mathrm{discharge}} = P(t)_{\mathrm{load}} + P(t)_{\mathrm{EV}} + P(t)_{\mathrm{charge}} + P(t)_{\mathrm{sell}}, \tag{24}$$

where $P(t)_{\mathrm{discharge}}$ and $P(t)_{\mathrm{charge}}$ are the charging and discharging power of energy storage system, respectively. $P(t)_{\mathrm{load}}$ and $P(t)_{\mathrm{EV}}$ are the building load and EV's charging power, respectively.

4.2.6 Nearly zero energy system

The sPCEB system has two sources of electricity, that is, the power generated by its PV modules or purchases electricity from the power grid. In order to achieve high clean energy penetration in sPCEB systems, the concept of nearly zero energy in this article is defined as the sPCEB system's annual purchase of non-renewable energy from the power grid cannot be greater than the amount of the electricity sold to the power grid.

$$\sum_{t=1}^{8760} P_{pv}(t) \geq v \sum_{t=1}^{8760} P_{buy}(t), \tag{25}$$

where v is the percentage of non-renewable energy in the local power grid.

4.2.7 Shared charging time limits

Based on the historical load data of the building, the shared charging service can be provided if the charging piles are available.

4.2.8 Other constraints

Shared charging time limitation: based on the historical load data of the building, the shared charging service can be provided if the charging piles are available.

Engineering standard limitation: to avoid the fluctuation caused by the sPCEB system, the calculated operation strategy should meet the actual engineering standards of distributed energy sources (General Administration of Quality Supervision et al., 2009; Pingzhou L et al., 2016; State Grid Corporation of China et al., 2016).

5 Optimal locating method and operation of shared photovoltaic, charging, and energy storage building system

The proposed optimization strategy focuses on the optimal design and improvement of renewable energy equipment (such as PV modules and energy storage system) based on existing common buildings. To sum up, the optimized strategy of the sPCEB system is summarized in the following steps (Figure 2):

Step 1: determining the building type. In this article, we mainly discuss two building types, public buildings, and residential buildings.

Step 2: ranking the importance of locating indexes, according to the needs of decision makers. For residential buildings, the indexes include traffic flow, public transport accessibility, population density, green space accessibility, and housing price; for public buildings, green space accessibility and housing price are not considered, but the attractiveness of the building to users and the cost of the building need to be further considered.

Step 3: analyzing and filtering the data that are needed for decision making.

Step 4: the improved AHP is used for locating; the final optimal location is obtained.

Step 5: obtain basic data of selected building (sPCEB), such as solar energy resources, electricity load, and available charging time.

Step 6: determine objective and constraints. The combined benefit is taken as the optimal objective, and constraints include the shared charging service fees and area constraints of PV module.

Step 7: Solving the problem according to the determined objective function and constraints, the final optimized operation strategy is obtained.

6 Simulation

The analytical object (urban area) in the simulation is a new first-tier city in China. The data are collected from reality, and the existing buildings can be re-designed and modified at the original situation if necessary.

6.1 Residential building

6.1.1 Analysis of locating

This region is divided into 11 districts, D1~D11, one typical residential unit is selected from each district, named as RU1~RU11. The main avenues in this urban area are named as A1~A6, respectively. The population density data of D1~D11 are collected through the national census (National

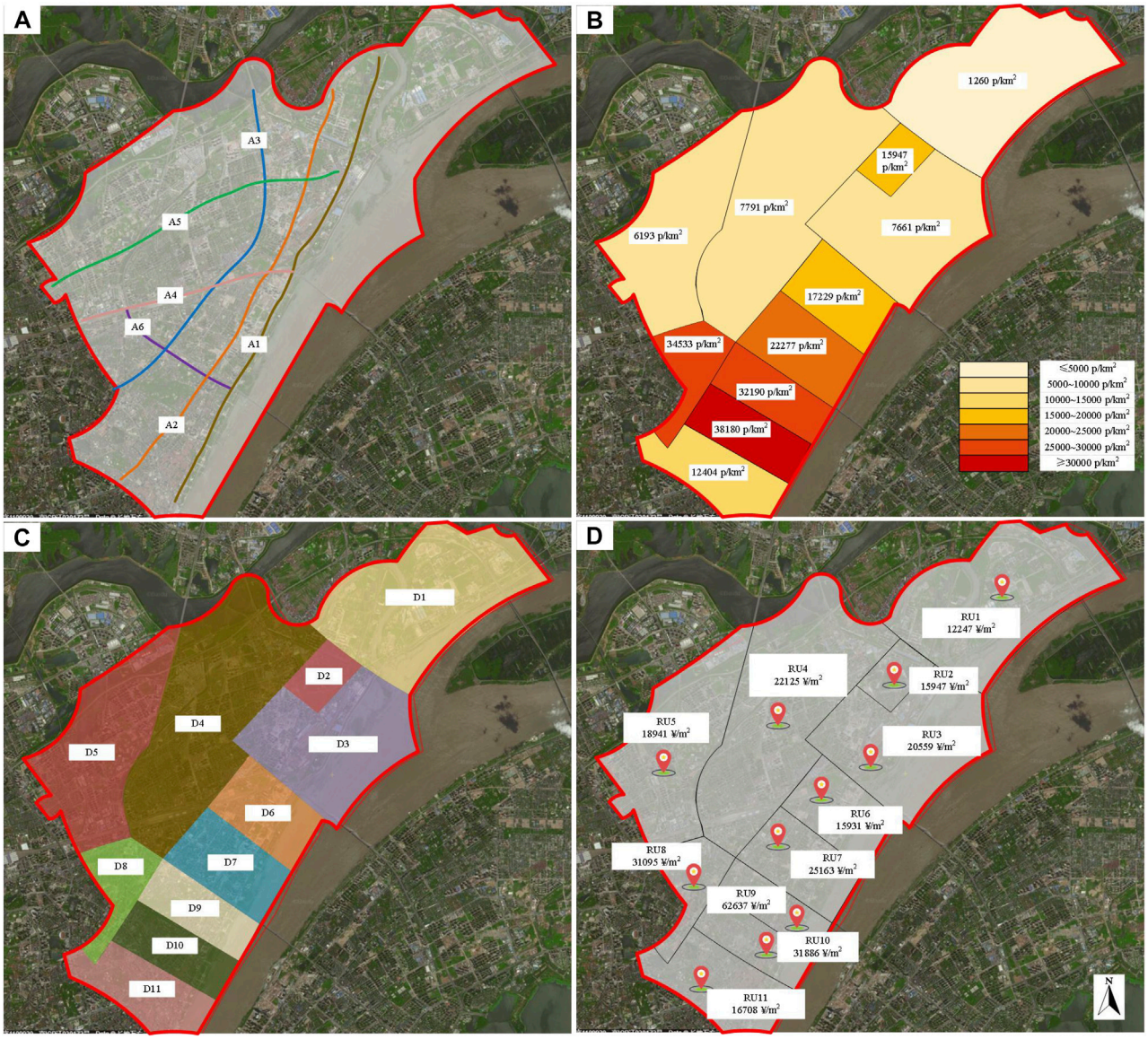

FIGURE 3
Region and statistics **(A)** main avenues (A1~A6); **(B)** population density of each district; **(C)** districts (D1~D11); and **(D)** housing price (RU1~RU11)

Bureau of Statistics of China, http://www.stats.gov.cn/), and the average housing price data are collected by web crawler through Lianjia (http://www.lianjia.com) in 2021 (Figure 3).

Based on the collection of data, several indexes can be calculated for locating the sPCEB system, as shown in Figure 4. The population density, the reciprocals of housing price, public transport accessibility, green space accessibility, and traffic flow are selected as the locating indexes in this part, and all the data are preprocessed to the range of 1–10, named as Index 1~5, respectively. Among the aforementioned five indexes, all of them should be higher, except for the housing price, which should be lower.

The population density and housing price data in Figures 4A,B are obtained directly through the collected data. In Figure 4C, the distance of the nearest subway station and bus stop to each residential unit are measured by digital map software (http://ditu.amap.com, https://map.tianditu.gov.cn/), and the corresponding public transport accessibility is derived by applying Eqs 1, 3. In Figure 4D, the area and distance of the nearest green space to each residential unit are also measured by digital map software, thus the green space accessibility can be calculated. In Figure 4E, the traffic flow data of a main avenue (A1~A6) nearest to it is accumulated by Eq. 1 for each residential unit, and then normalized.

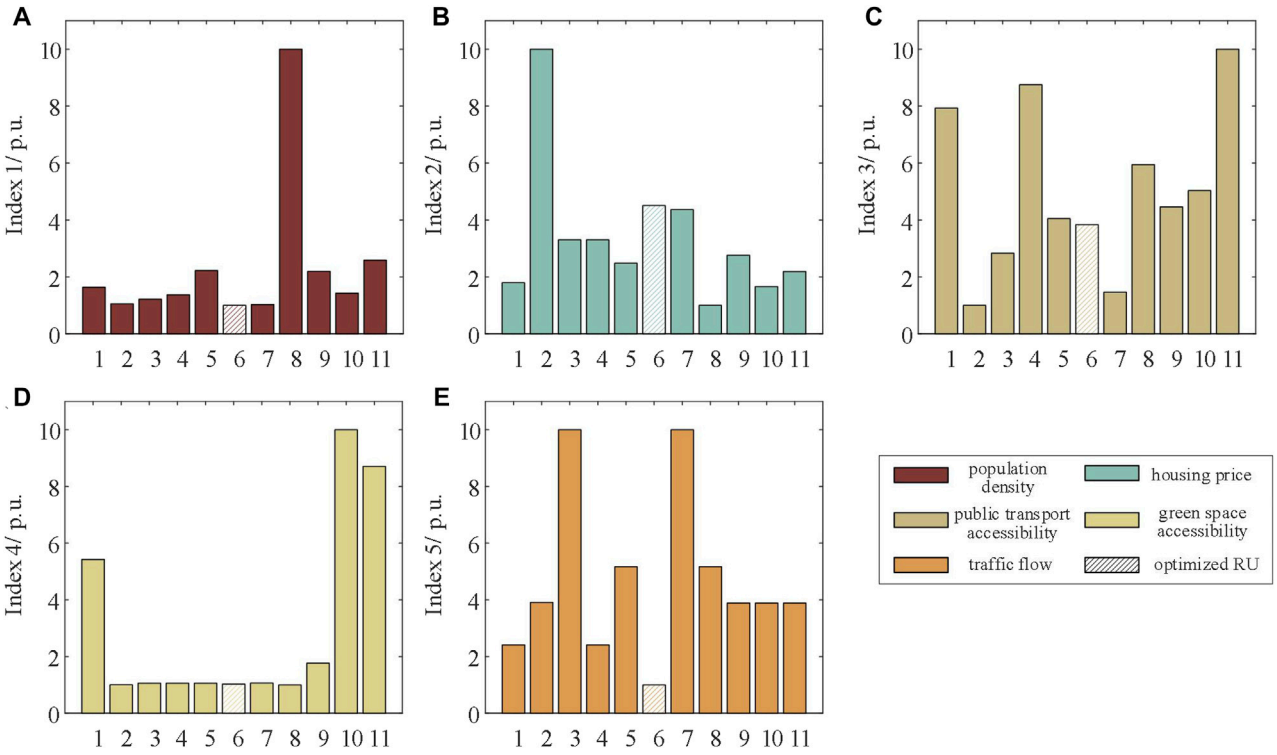

FIGURE 4
Preprocessed data **(A)** population density (Index 1); **(B)** housing price (Index 2); **(C)** public transport accessibility (Index 3); **(D)** green space accessibility (Index 4); and **(E)** traffic flow (Index 5)

The importance rankings of Index 1~5 need to be defined during the decision-making process. Here, we take Index 5 > Index 2 > Index 3 > Index 1 = Index 4 as an example, that is, the traffic flow is the most important index, the population density and the green space accessibility are less important, and the rankings are shown in Table 3.

From Table 4, RU6 achieved the highest ranking of all the 11 residential units in both Index 1 and Index 5. Index 5, the traffic flow, is the most important index in this example, which is also an essential factor in determining the location as a charging station. RU6 ranks first in this index among all the residential units. According to the improved AHP, the RU6 is chosen as the most proper location for the sPCEB system.

6.1.2 Optimal operation

In RU6, the maximum area of PV modules that can be installed on the top surface of the building is 100 m^2, and the maximum area of PV modules on the sunny side is 50 m^2. The building is designed with one EV charging space, and the maximum power of the charging pile is designed as 10 kw per hour. Owners of the building are used to charging their own car every night from 18 to 24 p.m., so the parking space is temporarily closed to public EV users during that time. The service lives of PV, energy storage, and other devices are considered to be 20 years; the prices of devices refer to the existing system (Tesla Powerwall, Sonnen Home Energy Storage system).

If the power generation efficiency of the PV modules at optimum installation angle (installed on the top surface of the building) is 100%, the power generation efficiency of the vertical sunny side is 54.05% by calculating using *PV*syst software. The historical load data of the building and the solar irradiance of the area for a typical day in each of the four seasons of 1 year are shown in Figures 5B,C.

It should be noted that the sum of the electricity of sPCEB every 2 hours is shown in the following figures, so the unit of vertical coordinate is kWh. According to Figures 5B,C, the consumption of electricity is mainly concentrated in 5–8 a.m. and 18–24 p.m., the effective working time of PV modules is mainly concentrated in 6 a.m.–18 p.m. Therefore, it needs to be flexibly regulated by the optimal operation strategy. The strategy is solved by a CPLEX optimizer using MATLAB, and the solutions are shown in Figures 6, 7 and Tables 5, 6.

TABLE 3 Importance ranking and scales.

Most importance → less important

Index 5	*Strong importance*	Index 2	*Moderate importance*	Index 3	*Moderate importance*	Index 1	*Equal importance*	Index 4
				Adjacent scales				
	3		2		1		1	

TABLE 4 Data of the optimal location (RU6).

Index	Population density (Index 1)	Housing price (Index 2)	Public transport accessibility (Index 3)	Green space accessibility (Index 4)	Traffic flow (Index 5)
Data	38,180 p/km2	31,886/m2	0.4762/p.u.	0.5395/p.u	18,356 per day
Ranking	1	10	4	3	1

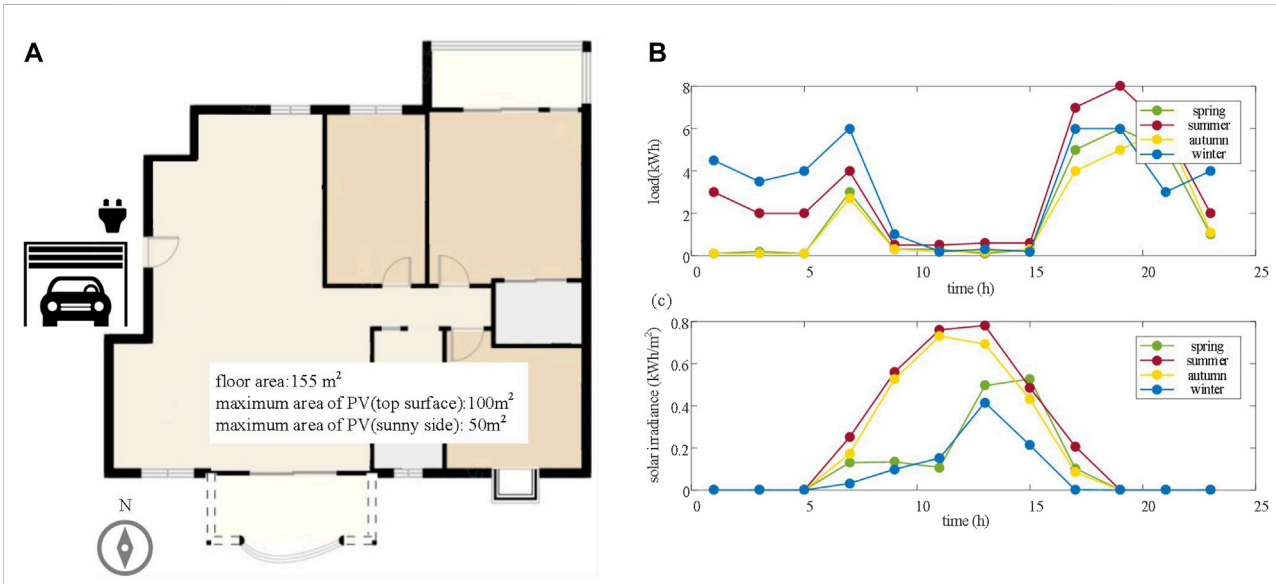

FIGURE 5
Initial data of building **(A)** floor plan; **(B)** historical load; and **(C)** solar irradiance.

In Figure 6A, the value of energy storage greater than zero represents that the energy storage system is charging at this moment, and the value lower than zero represents that the system is discharging. Likewise, in Figure 6B, the value greater than zero represents that the building sells electricity to the power grid, and the value lower than zero represents that the building purchases electricity from the power grid. From Table 5 and Table 6, the combined benefit of the whole four typical days is 542.2 yuan, and the PV module should be installed as much as possible, that is 50 m^2 on sunny side, 100 m^2 on top surface of the building. The capacity of energy storage system should be 23.7 kwh. The shared charging service is available from 6–8 a.m. and 14–18 p.m. on these four typical days.

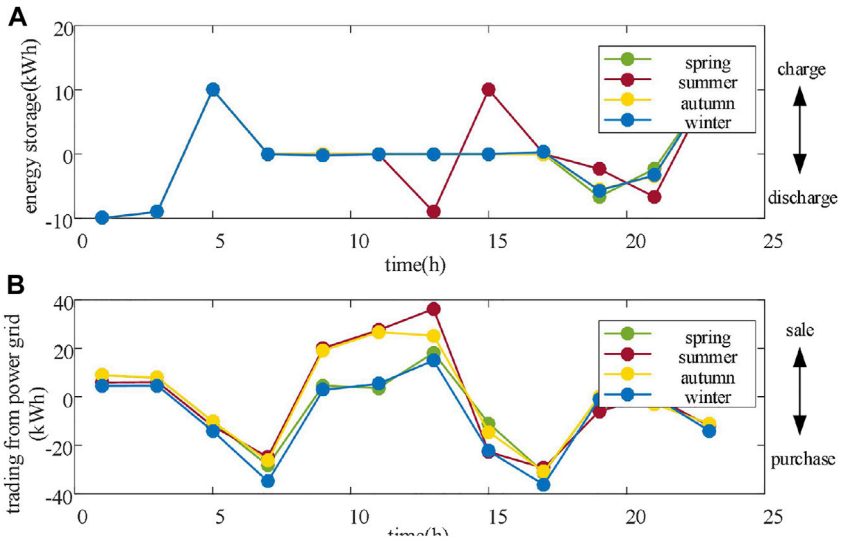

FIGURE 6
Optimal operation **(A)** discharging/charging of energy storage system and **(B)** trading of power grid.

FIGURE 7
Location of public buildings.

In China, distributed energy sources such as photovoltaic and wind power have been vigorously developed in recent years. China has now developed a series of engineering standard for distributed power sources in order to maintain the stability of the power system (Pingzhou L et al., 2016; National Energy Administration et al., 2017). The maximum capacity of

TABLE 5 Parameters of devices.

Combined benefit	542.2 yuan
PV module on sunny side	50 m^2
PV module on the top surface	100 m^2
Minimum capacity of the energy storage system	23.7 kWh

TABLE 6 Available charging time for others.

Time(h)	Charging fee (yuan/kwh)
6–8 and 14–18 (4 typical days)	0.95

TABLE 7 Details of public buildings.

Number	Floor area (m^2)	Type
1	12,500	Commercial
2	44,600	Office
3	9,900	Theater
4	460,000	Commercial
5	36,300	Science and research
6	71,200	Commercial
7	22,430	Museum
8	292,500	Commercial
9	34,100	Commercial
10	33,000	Library

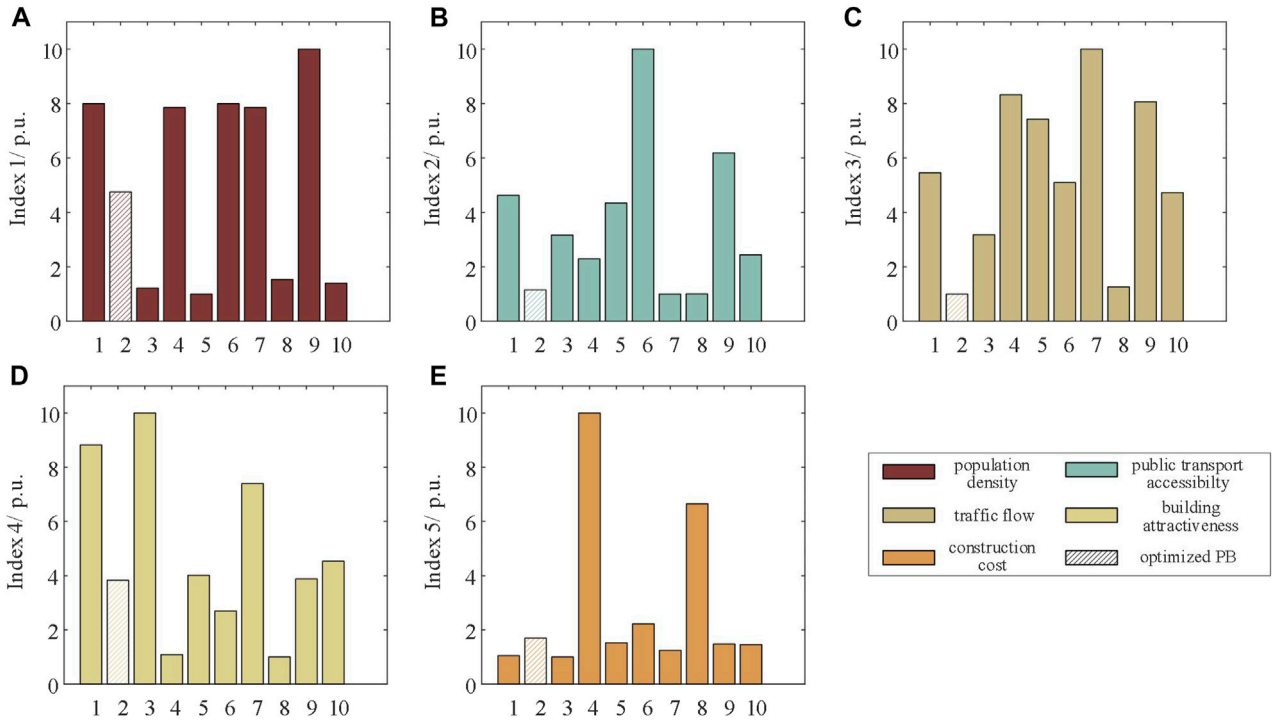

FIGURE 8
Preprocessed data **(A)** population density; **(B)** public transport accessibility; **(C)** traffic flow; **(D)** building attractiveness; and **(E)** construction cost.

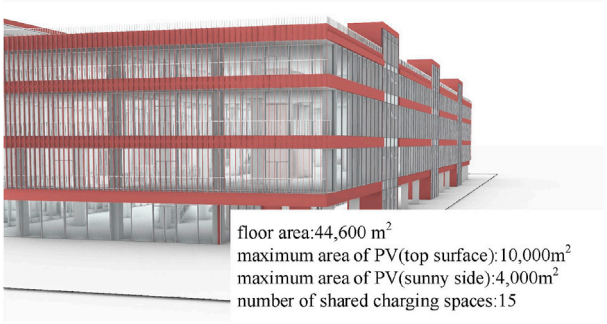

FIGURE 9
Design of the office building.

distributed generation that can be connected to the 380 V grid is 400 kW. The maximum power of this building interaction with the grid does not exceed 20 kW (the line graphs in the manuscript show the power interacted with the grid every 2 hours, the maximum power does not exceed 40 kWh/2 h. Thus, it can be directly connected to the 380 V grid. The length of the line is 0.5 km. The calculated maximum line voltage drop is only 1.749%, which is much lower than the 7% specified in the standard.

6.2 Public building

6.2.1 Analysis of locating

The types of public buildings that can provide shared charging service for public EV users are office buildings, commercial buildings, science, education, culture and health buildings, *etc*. In this article, 10 public buildings (PB1~PB10) containing parking spaces are selected for analysis in this region, and the details of each building are shown in Table 7 and Figure 7.

Five indexes in this section are population density, public transport accessibility, traffic flow, building attractiveness, and construction cost. PB2 is finally chosen as the optimal sPCEB system, and the preprossessed data are shown in Figure 8. The importance rankings of Index 1~5 are the same as Table 3. It can be found that PB2 is the best in Index 3. Although not all of the indexes are optimal, PB2 is still globally optimal from the overall perspective.

6.2.2 Optimal operation

The type of PB2 is office building, the maximum area of installed PV modules on the top surface is 10,000 m^2, and the maximum area of installed PV modules on the sunny side is 4,000 m^2 (Figure 9). The building is designed to contain

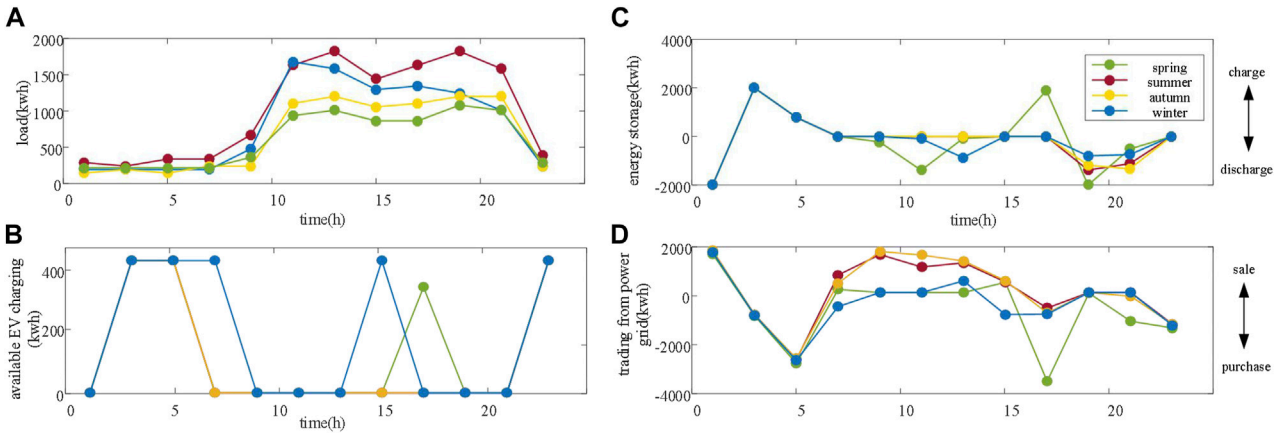

FIGURE 10
Optimal operation **(A)** historical load of PB2; **(B)** available shared charging service; **(C)** discharging/charging of energy storage system; and **(D)** trading of the power grid.

TABLE 8 Parameters of devices.

Combined benefit	**3,0401 yuan**
PV module on sunny side	4,000 m^2
PV module on the top surface	10,000 m^2
Minimum capacity of the energy storage system	3,128 kwh

150 parking spots, with an estimated penetration rate of 10% for EVs, 15 charging piles are available for public EV users all day. The maximum power of the charging piles is 15 kw per hour. By collecting the consumption data of the building for four typical days, the operation strategy of the building is obtained, as shown in Figure 10; Table 8.

The main difference between public building and residential building is: 1) the amount of electricity consumption is large; hence, the demands for energy storage and PV modules are larger; 2) more shared EV charging spaces can be provided throughout all day. In Figures 10A,B, the description of load, storage management, and power trading strategies are similar to the residential building, only the values are different. In Figure 10C, 15 charging piles are all available at 2–6 a.m., 22–24 p.m. (all typical days), 6–8 a.m., and 14–16 p.m. (typical day in winter), 14 charging piles are available at 16–18 p.m. (typical day in spring).

The shared public building in this section will be connected to a 10 kV grid with a line length of 1 km. The maximum power of the proposed optimal operation strategy does not exceed 2 MW per hour, and the maximum line voltage drop is calculated to be 1.436%.

6.3 Additional analysis

6.3.1 Influence on the owner of shared photovoltaic, charging, and energy storage building system

In the previous analysis, the combined benefits of the optimization objectives include the environmental, social, and economic impacts of the sPCEB system. However, from the perspective of the owners of the sPCEB system, the investment costs and the corresponding revenues are the primary concern.

Assuming that the charging piles are full load, Figure 11 presents the comparison between public building PB2 and residential building RU6 in terms of the electricity cost, revenues of shared charging service, and investment costs of devices. Actually, the charging piles are not always in full load, thus the surplus energy can be sold to the power grid. Accordingly, the actual revenue of shared charging service is less than or equal to 342 yuan for RU10 and 6,327 yuan for PB2. Even without the shared charging revenue, the saved electricity fees are still greater than the average device cost.

Figure 11A shows the comparison results for RU6. RU6 saves 80 yuan in electricity costs, and earns the charging revenues for 342 yuan. The average device cost is 64 yuan (service life: 20 years and average time: four typical days). In other words, not only can save some electricity expenses but also can generate an additional benefit of 278 yuan for using the optimal operating strategy in this article.

Figure 11B shows the comparison results for PB2. PB2 saves 28,071 yuan in electricity costs and earns the charging revenues for 6,327 yuan, the device costs are 8,707 yuan. That is, PB2 needs to pay 28,071 yuan for purchasing electricity from the power grid

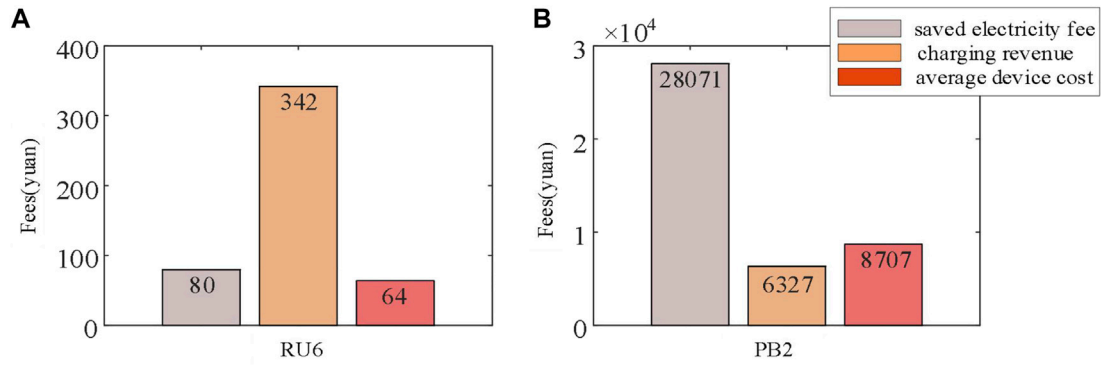

FIGURE 11
Comparison of revenues and costs **(A)** RU6 and **(B)**PB2.

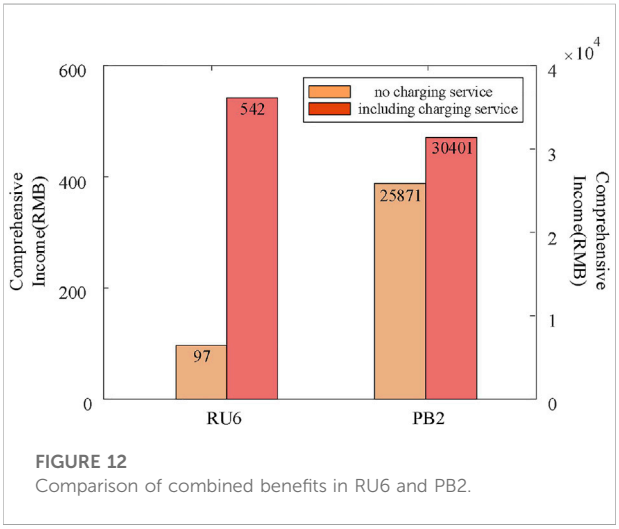

FIGURE 12
Comparison of combined benefits in RU6 and PB2.

if not using the optimization strategy of this article; however, the costs have reduced to 2,380 yuan.

6.3.2 Analysis of combined benefits

This section compares the combined benefits of applying the optimal operating strategy with and without the shared charging service, and the results are shown in Figure 12. For RU6, the combined benefit will be 542 yuan if the shared charging service is included, and the combined benefit will be 97 yuan if the shared charging service is excluded, and the total benefits increased by 445 yuan. For PB2, the total benefits increased by 4,530 yuan.

7 Conclusion

This article proposes a concept of the sPCEB system. More specifically, the location problem of the system is solved by the improved AHP, and the optimal operating strategy with shared charging service is further introduced. The simulation results indicate that:

1) The locating method of sPCEB can objectively give the order of importance of each element based on specific data analysis results, which can overcome the problem that the traditional AHP method cannot pass the consistency test with too many elements on the one hand, and combining the advantages of subjective and objective judgment on the other hand. It makes the decision-making process more user-friendly and more convenient.
2) The optimal operating strategy with shared charging service can not only improve the combined benefits of the building system from the perspective of social, environmental, and economic, but also greatly reduce the cost of purchasing electricity from the power grid for the owners and improve the local energy consumption capacity of the building. In addition, it achieves greater combined benefits comparing to optimal operation without shared charging services

Data availability statement

The original contributions presented in the study are included in the article/Supplementary Material; further inquiries can be directed to the corresponding author.

Author contributions

CL, ZW, and BG contributed to conception and design of the study. HD organized the database. LL performed the statistical analysis. Other authors helped supervised the project. All authors

contributed to manuscript revision, read, and approved the submitted version.

Conflict of interest

The authors declare that the research was conducted in the absence of any commercial or financial relationships that could be construed as a potential conflict of interest.

Publisher's note

References

Albacete, X., Olaru, D., Paül, V., and Biermann, S. (2017). Measuring the accessibility of public transport: A critical comparison between methods in helsinki. *Appl. Spat. Anal. Policy* 10, 161–188. doi:10.1007/s12061-015-9177-8

Bheema, T. L., and June, T. H. M. (2017). A framework for electric vehicle (EV) charging in Singapore. *Energy Procedia* 143, 15–20. doi:10.1016/j.egypro.2017.12.641

Danhong, W., Xiang, L., Julien, M., Carmeliet, J., and Orehounig, K. (2021). Advancing the thermal network representation for the optimal design of distributed multi-energy systems. *Front. Energy Res.* 9. doi:10.3389/fenrg.2021.668124

Feng, D., Ying, W., Bin, S., Hua, Y., and Zhang, Y. (2019). The process of peak CO2 emissions in developed economies: A perspective of industrialization and urbanization. *Resour. Conservation Recycl.* 141, 61–75. doi:10.1016/j.resconrec.2018.10.010

General Administration of Quality Supervision (2009). *Power quality-deviation of supply voltage*. Beijing. GB/T 12325-2008.Inspection and quarantine of the people's republic of China

Hansen, W. G. (1959). How accessibility shapes land use. *J. Am. Inst. Plann.* 25, 73–76. doi:10.1080/01944365908978307

Heinstein, P., Ballif, C., and Perret-Aebi, L. (2013). Building integrated photovoltaics (BIPV): Review, potentials, barriers and myths. *Green* 3, 125–156. doi:10.1515/green-2013-0020

Huanan, L., and Quande, Q. (2019). Challenges for China's carbon emissions peaking in 2030: A decomposition and decoupling analysis. *J. Clean. Prod.* 207, 857–865. doi:10.1016/j.jclepro.2018.10.043

Huff, D. L. (1964). Defining and estimating a trading area. *J. Mark.* 28, 34. doi:10.2307/1249154

Igor, S., Assunta, N., and Karsten, V. (2012). Net zero energy buildings: A consistent definition framework. *Energy Build.* 48, 220–232. doi:10.1016/j.enbuild.2012.01.032

Kapsalaki, M., Leal, V., and Santamouris, M. (2012). A methodology for economic efficient design of Net Zero Energy Buildings. *Energy Build.* 55, 765–778. doi:10.1016/j.enbuild.2012.10.022

Michael, B., Prateek, M., and Sivasathya, B. (2021). "Incorporating residential Smart electric vehicle charging in Home energy management systems," in *IEEE green technologies conference*. doi:10.1109/GreenTech48523.2021.00039

Muhammad, A. S., Mohammad, M. Z., and Adam, T. (2018). *Public transport accessibility: A literature review*. Periodica Polytechnica Transportation Engineering. doi:10.3311/PPtr.12072

Muhammad, Z. (2014). A hybrid approach for reliability analysis based on analytic hierarchy process and Bayesian network. *Front. Energy Res.* 2. doi:10.3389/fenrg.2014.00052

National Energy Administration,National Development and Reform Commission (2017). Notice of the two departments on the pilot market-oriented trading of distributed power generation. Available at: http://www.gov.cn/xinwen/2017-11/14/content_5239535.htm (Accessed November 14, 2017).

Olszewski, P., and Wibowo, S. S. (2005). *Using equivalent walking distance to assess pedestrian accessibility to transit stations in Singapore*. Transportation Research Record, 38–45. doi:10.1177/0361198105192700105

Overview of Greenhouse Gases (2021). *Overview of greenhouse gases*. Available at: https://www.epa.gov/ghgemissions/overview-greenhouse-gases (Accessed November 19, 2021).

Pingzhou, L., Kaisheng, B., and Yuanhui, R. (2016). *Design manual for industrial and civil power supply and distribution*. Beijing: China Electric Power Press.

Qiwei, J., Tingxiang, L., Xiaotao, C., Laijun, C., Yang, S., Shengweio, M., et al. (2021). Optimized regulation of hybrid adiabatic compressed air energy storage system for zero-carbon-emission micro-energy network. *Front. Energy Res.* doi:10.3389/fenrg.2021.745457

Ruike New Energy (2022). *National speed skating oval*. Available at: http://www.rksolar.com.cn/en/.

Sayali, A. J., Sanjay, K. S., and Pushpendra, S. (2021). "Control strategies for electric vehicle charging station: A review," in *2021 2nd international conference for emerging Technology*. doi:10.1109/INCET51464.2021.9456280

Schirmer, P. M., Van Eggermond, M. A. B., and Axhausen, K. W. (2014). The role of location in residential location choice models: A review of literature. *J. Transp. Land Use* 7, 3. doi:10.5198/jtlu.v7i2.740

Sonnen Home Energy Storage (2022). *Power your life with a smart, reliable, and safe home battery from sonnen*. Available at: https://sonnenusa.com/en/.

State Grid Corporation of China (2016). *Technical rule for distributed resources connected to power grid*. Beijing. Q/GDW 1480-2015.

Tesla Powerwall (2022). *Powerwall*. Available at: https://www.tesla.com/powerwall.

The Paris Agreement (2015). *The Paris agreement*. Available at: https://www.un.org/en/climatechange/paris-agreement (Accessed December 12, 2015).

Yandong, W., Mingxuan, D., Senbao, L., Wei, J., and Yanyan, G. (2018). Social media-based site selection study for business districts. *Geospatial Inf.* 16, 34–38. (in Chinese).

Advantages of publishing in Frontiers

OPEN ACCESS
Articles are free to read for greatest visibility and readership

FAST PUBLICATION
Around 90 days from submission to decision

HIGH QUALITY PEER-REVIEW
Rigorous, collaborative, and constructive peer-review

TRANSPARENT PEER-REVIEW
Editors and reviewers acknowledged by name on published articles

Frontiers
Avenue du Tribunal-Fédéral 34
1005 Lausanne | Switzerland

Visit us: www.frontiersin.org
Contact us: frontiersin.org/about/contact

REPRODUCIBILITY OF RESEARCH
Support open data and methods to enhance research reproducibility

DIGITAL PUBLISHING
Articles designed for optimal readership across devices

FOLLOW US
@frontiersin

IMPACT METRICS
Advanced article metrics track visibility across digital media

EXTENSIVE PROMOTION
Marketing and promotion of impactful research

LOOP RESEARCH NETWORK
Our network increases your article's readership